

Low-Melting Cationic Transition Metal Complexes – Developing Spin Crossover Ionic Liquids –



INAUGURALDISSERTATION
zur Erlangung des Doktorgrades
der Fakultät für Chemie und Pharmazie
der Albert-Ludwigs-Universität Freiburg im Breisgau

vorgelegt von
Timo Huxel
aus Sinsheim

2014

Vorsitzender des Promotionsausschusses:	Prof. Dr. Thorsten Koslowski
Referentin:	Dr. Julia Klingele
Korreferent:	Prof. Dr. Philipp Kurz
Tag der mündlichen Prüfung:	04.11.14

Diese Arbeit wurde von Januar 2011 bis August 2014 am Institut für Anorganische und Analytische Chemie der Albert-Ludwigs-Universität Freiburg im Breisgau unter der Leitung von Dr. Julia Klingele angefertigt. Teile der Arbeit enthalten Ergebnisse, die während dem Forschungspraktikum von Christian Göhringer (November bis Dezember 2011), der Bachelorarbeit von Selina Leone (April bis Juli 2012) und der Masterarbeit von Michael Skaisgirski (September 2013 bis März 2014) im Arbeitskreis Klingele unter der Anleitung des Autors entstanden sind.

Publikationen

Timo Huxel, Sebastian Riedel, Jochen Lach, and Julia Klingele
Iron(II) and Nickel(II) Complexes of N-Alkylimidazoles and 1-Methyl-1H-1,2,4-Triazole: X-ray Studies, Magnetic Characterization, and DFT Calculations (Diplomarbeit)
Z. Anorg. Allg. Chem. **2012**, 638 (6), 925–934

Julia Klingele, Dominic Kaase, Timo Huxel, Carla Gotzmann, Yanhua Lan
3-(2-Pyrazyl)-[1,2,4]triazolo[4,3-a]pyridine – A versatile ligand: Ambidenticity and coordination isomerism in mono- and polynuclear 3d transition metal complexes
Polyhedron **2013**, 52, 500–514

Timo Huxel, Selina Leone, Yanhua Lan, Serhiy Demeshko, and Julia Klingele
2-Amino-4-(2-pyridyl)thiazole as Chelating Ligand: A Dinuclear Oxido-Bridged Ferric Complex and Mononuclear 3d Metal Complexes
Eur. J. Inorg. Chem. **2014**, 3114–3124

Timo Huxel and Julia Klingele
Cobalt(II) Complexes of a New Imidazolium-Tagged Thiadiazole Ligand With Bis(trifluoromethylsulfonyl)imide or Tetrakisothiocyanato Cobaltate as Counterion
submitted

Timo Huxel, Serhiy Demeshko, Yanhua Lan, and Julia Klingele
2-Amino-5-(2-pyridyl)-thiadiazole as Ligand – Spin Crossover Close to Room Temperature in preparation

Konferenzbeiträge

Timo Huxel, Sebastian Riedel, and Julia Klingele
Feasible Prediction of Spin Crossover in Azole Based Iron(II) Coordination Compounds (Diplomarbeit)
Poster, 7. Koordinationschemie-Treffen, Stuttgart, **Februar 2011**

Timo Huxel, Sebastian Riedel, Jochen Lach, and Julia Klingele
Prediction of Spin Crossover in Azole Based Iron(II) Coordination Compounds (Diplomarbeit)
Poster, 8. Koordinationschemie-Treffen, Dortmund, **Februar 2012**

Timo Huxel, Sebastian Riedel, Jochen Lach, and Julia Klingele
Prediction of Spin Crossover in Azole Based Iron(II) Coordination Compounds (Diplomarbeit)
Poster, 14. JCF Frühjahrssymposium, Rostock, **März 2012**

Timo Huxel, Selina Leone, Christian Göhringer und Julia Klingele
Neue 3d-Übergangsmetallkomplexe mit funktionalisierbaren Liganden
Poster, Tag der Forschung, Freiburg, **Juli 2012**

Timo Huxel, Selina Leone, Max Schmucker, and Julia Klingele
Transition Metal Compounds with Low Melting Points – Developing Switchable Liquids
Vortrag, 10. Koordinationschemie-Treffen, Kaiserslautern, **März 2014**

Danksagung

Herzlichen Dank an alle, die mich bei der Anfertigung dieser Arbeit unterstützt haben:

Dr. Julia Klingele für die Bereitstellung des interessanten Themas, die Betreuung und die angenehme Arbeitsatmosphäre.

Dankeschön an Dominic Kaase für die gute Laune in R127 und eine hervorragende Zusammenarbeit in all den Jahren.

Prof. I. Krossing für die vielfältige Unterstützung und für die Möglichkeit, Teil seiner Gruppe zu sein.

Prof. P. Kurz für wichtige Diskussionen und Hinweise.

Christian Göhringer, Carla Gotzmann, Selina Leone, Michael Skaisgirski und Max Schmucker für ihre engagierte Mitarbeit.

Dr. Daniel Himmel, Alexander Rupp, Dr. Harald Scherer, Ulf Sachs und Dr. Julia Klingele für das Korrekturlesen dieser Arbeit.

Dr. Safak Bulut, Dr. Philipp Eiden und Alexander Rupp für wichtige Diskussionen und Hinweise zu ionischen Flüssigkeiten.

Dr. Harald Scherer und Fadime Bitgül für das Messen unzähliger NMR-Spektren und Harald Scherer für die Hilfe bei der Interpretation der Spektren.

Carola Sturm für die vielen DSC-Messungen und Alexander Rupp für die Hilfe bei der Interpretation der Ergebnisse.

Christoph Warth für den hervorragenden MS Service und seine unendliche Hilfsbereitschaft bei auftretenden Problemen.

Angelika Siegel für die vielen Elementaranalysen und ihre Eigeninitiative. Sabine Lude und Günter Wünsche für das Messen der externen Proben.

Dr. Serhiy Demeshko für das Aufnehmen von Mößbauerspektren und die Durchführung von SQUID-Messungen und seine Hilfe bei der Interpretation der Messergebnisse. Dr. Yanhua Lan und Frederik Schleife für weitere SQUID-Messungen und Dr. Valeriu Mereacre für das Aufnehmen eines Mößbauerspektrums.

Ulf Sachs für die Einweisung in seine HPLC-Maschine und seine stetige Hilfsbereitschaft.

Dominic Kaase, Boumahdi Benkmil und Miriam Schwab für das Messen der Kristallstrukturen und Dominic Kaase und Dr. Julia Klingele für das Lösen und Verfeinern. Dr. Nils Trapp und Dr. Daniel Kratzert für die Unterstützung bei kristallographischen Problemen.

Susanne Röckel und Bettina Ganter für die unkomplizierte Hilfe bei der Literaturrecherche.

Dominic Kaase und Felix Brosi für die schnelle Hilfe bei IT-Problemen.

Danke an das Team des Chemikalienlagers, insbesondere an Friedbert Jerg, Monika Völker und Winfried Weber für ihr Engagement bei der Besorgung vieler Chemikalien.

Tim Lecke und Martin Walter für die Reparatur vieler Glasgeräte. Danke an Markus Melder und an das Team der Werkstatt, sowie an Harald Große und an das Team der Haustechnik.

Vielen Dank an Brigitte Jörger und Vera Brucksch für die Hilfe mit den vielen Formularen.

Danke allen ehemaligen und aktuellen Mitarbeitern des AK Krossing, AK Jenne, AK Riedel und der anderen Gruppen in der AC für die stetige Hilfsbereitschaft und für die gute Stimmung im Haus.

Alberto Steffani, Alexander Higelin, Daniel Himmel, Dominic Kaase, Felix Brosi, Felix Huff, Heike Haller, Katharina Pütz, Michael Schwarz, Ulf Sachs und Valentin Radtke danke ich für die schöne Zeit am und außerhalb des Instituts.

Abstract

Several approaches for the synthesis of SCO ionic liquids or SCO glasses have been investigated and appropriate ligands for the synthesis of such compounds have been developed. Furthermore, iron(II) triflimide ($\text{Fe}(\text{NTf}_2)_2 \cdot 6\text{H}_2\text{O}$) has been prepared, structurally characterised and successfully used as starting material for complex syntheses. Using 4-(2-pyridyl)-2-amino-thiazole (L^{tz}) and 2-(2-pyridyl)-4-amino-1,3,4-thiadiazole (L^{td}) as ligands a series of syntheses was carried out in order to identify which ligand forms complexes with the general formula $[\text{M}^{\text{II}}(\text{L})_3](\text{X})_2$ and $[\text{M}^{\text{II}}(\text{L})_2(\text{Y})_2]$ ($\text{M} = \text{Fe}, \text{Co}$; $\text{L} = \text{L}^{\text{tz}}, \text{L}^{\text{td}}$; $\text{X} = \text{non-coordinating anion}$; $\text{Y} = \text{coordinating coligand}$). The thiazole L^{tz} forms pure HS complexes with iron(II) and cobalt(II), whereas the thiadiazole L^{td} forms complexes featuring the formula $[\text{M}(\text{L})_3](\text{X})_2$ that comprise the metal ion in the LS state in the case of iron(II) and in the HS state in the case of cobalt(II). Eventually, the iron(II) complex $[\text{Fe}(\text{L}^{\text{td}})_2(\text{NCS})_2]$ (**15**) was prepared featuring a SCO near to rt at $T_{1/2} = 250 \text{ K}$. Besides, it was shown that the formal exchange of the chloride anion in $[\text{Fe}(\text{L}^{\text{td}})_3]\text{Cl}_2$ (**9**) ($T_{\text{dec}} = 210 \text{ }^\circ\text{C}$) for a triflimide anion leads to $[\text{Fe}(\text{L}^{\text{td}})_3](\text{NTf}_2)_2$ (**12**) featuring a melting point at $T_{\text{fus}} = 194 \text{ }^\circ\text{C}$.

Three new ligands for the preparation of low melting complexes with the formula $[\text{M}(\text{L})_3](\text{X})_2$ have been developed. Substitution of the amine function of the thiazole ligand L^{tz} with a methoxyacetyl group leads to the amide L^1 . Since 2-(2-pyridyl)-imidazole (**pi**) is known to form SCO complexes with iron(II) featuring the general formula $[\text{Fe}(\text{L})_3](\text{X})_2$ it was taken as starting point for two further new ligands. Substitution on the N_{im} atom of the imidazole moiety in **pi** with an ethyl group (L^2) or methoxyethyl group (L^3) leads to the ligands L^2 and L^3 , respectively. Another ligand for the preparation of complexes with the formula $[\text{M}(\text{L})_2(\text{Y})_2]$ was developed starting from the thiadiazole L^{td} . Substitution at the amino function of the thiadiazole L^{td} with ω -bromopentanoic acid chloride leads to the formation of the amide **tdBr** which was reacted with 1-ethylimidazole forming the imidazolium bromide L^4Br . Subsequent metathesis with LiNTf_2 leads to the new ligand L^4NTf_2 comprising an imidazolium tag along with the triflimide WCA.

Complex preparation with L^1 was shown to be rather demanding. As expected the complex $[\text{Fe}(\text{L}^1)_3](\text{BF}_4)_2$ (**16**), which decomposes at $218 \text{ }^\circ\text{C}$, comprise the metal ion in the HS state. However, using L^2 and L^3 as ligands complex synthesis becomes much more feasible. Two series of iron(II) LS complexes with the formula $[\text{Fe}(\text{L}^2)_3](\text{X})_2$ ($\text{X} = \text{ClO}_4^-$: **22**; BF_4^- : **23**; NTf_2^- : **24**) and $[\text{Fe}(\text{L}^3)_3](\text{X})_2$ ($\text{X} = \text{ClO}_4^-$: **27**; BF_4^- : **28**) were prepared. Preparing the HS cobalt(II) complexes $[\text{Co}(\text{L})_3](\text{ClO}_4)_2$ ($\text{L} = \text{L}^2$: **25**; L^3 : **29**) permitted the structural characterisation of such compounds *via* single crystal X-ray diffraction analysis. Preparation of the related nickel(II) complexes $[\text{Ni}(\text{L})_3](\text{ClO}_4)_2$ ($\text{L} = \text{L}^2$: **26**; L^3 : **30**) and subsequent examination by UV/Vis spectroscopy revealed similar ligand strengths of L^2 , L^3 and their precursor **pi**. Thus, it is very likely that the iron(II) LS complexes **22–24** and **27–28** switch into the HS state at elevated temperatures. Apart from the perchlorate compounds **22** and **27** the iron(II) complexes comprise melting points in the range of $239\text{--}153 \text{ }^\circ\text{C}$ with $[\text{Fe}(\text{L}^2)_3](\text{NTf}_2)_2$ (**24**, $T_{\text{fus}} = 153 \text{ }^\circ\text{C}$) being the lowest melting compound in this series. It was shown that complexes with the methoxyethyl substituted ligand L^3 generally comprise lower melting points than complexes with the ethyl substituted ligand L^2 and the complex with NTf_2^- as counterion melts significantly lower than related complexes with ClO_4^- or BF_4^- anion.

Preparing complexes with the general formula $[\text{M}(\text{L}^4)_2(\text{NCS})_2](\text{NTf}_2)_2$ ($\text{M} = \text{Fe}, \text{Co}$) using the imidazolium tagged ligand L^4NTf_2 was shown to be quite difficult. With “ $\text{Fe}(\text{NCS})_2$ ” presumably incomplete coordination occurred, as indicated by HPLC chromatography. Using “ $\text{Co}(\text{NCS})_2$ ” lead to the formation of two kinds of crystals identified as $[\text{Co}(\text{L}^4)_2(\text{NCS})_2][\text{Co}(\text{NCS})_4]$ (**31**) and $[\text{Co}(\text{L}^4)_2(\text{NCS})_2](\text{NTf}_2)_2$ (**32**), respectively, by X-ray diffraction analysis. Unfortunately, no bulk material of those compounds could be obtained.

The synthesis of complexes using $\text{Fe}(\text{NTf}_2)_2 \cdot 6\text{H}_2\text{O}$ and six equivalents of the azoles 1-methylimidazole (**mim**) and 1-ethylimidazole (**eim**) as ligands was established. The complexes $[\text{Fe}(\text{mim})_6](\text{NTf}_2)_2$ (**33**) and $[\text{Fe}(\text{eim})_6](\text{NTf}_2)_2$ (**34**) comprise the metal ion in the HS state. Whereas complex **33** decomposes at $183 \text{ }^\circ\text{C}$, complex **34** melts at a remarkably low temperature of $T_{\text{fus}} = 83 \text{ }^\circ\text{C}$.

Kurzzusammenfassung

Mehrere Strategien zur Synthese von Ionischen Flüssigkeiten oder Gläsern mit SCO-Eigenschaften wurden untersucht und geeignete Liganden für die Synthese solcher Verbindungen wurden entwickelt. Außerdem wurde Eisen(II)-triflimid ($\text{Fe}(\text{NTf}_2)_2 \cdot 6\text{H}_2\text{O}$) hergestellt, seine Struktur wurde charakterisiert und es wurde erfolgreich als Ausgangsmaterial für Komplexsynthesen eingesetzt. Mit 4-(2-pyridyl)-2-amino-thiazol (L^{tz}) und 2-(2-pyridyl)-4-amino-1,3,4-thiadiazol (L^{td}) wurde eine Reihe von Komplexsynthesen ausgeführt, um zu evaluieren, welcher Ligand Komplexe mit der allgemeinen Formel $[\text{M}(\text{L})_3](\text{X})_2$ und $[\text{M}(\text{L})_2(\text{Y})_2]$ ($\text{M} = \text{Fe}, \text{Co}$; $\text{L} = \text{L}^{\text{tz}}, \text{L}^{\text{td}}$; $\text{X} =$ nicht koordinierendes Anion; $\text{Y} =$ koordinierender Coligand) bildet. Das Thiazol L^{tz} bildet mit Eisen(II) und Kobalt(II) ausschließlich HS Komplexe, wohingegen das Thiadiazol L^{td} Komplexe mit der allgemeinen Formel $[\text{M}(\text{L})_3](\text{X})_2$ bildet, die das Metall Ion im LS Zustand (im Falle von Fe^{II}) oder im HS Zustand (im Falle von Co^{II}) aufweisen. Schließlich wurde der Eisen(II) Komplex $[\text{Fe}(\text{L}^{\text{td}})_2(\text{NCS})_2]$ (**15**) mit SCO nahe RT bei $T_{1/2} = 250 \text{ K}$ hergestellt. Des Weiteren wurde gezeigt, dass der formale Austausch von Chlorid in $[\text{Fe}(\text{L}^{\text{td}})_3]\text{Cl}_2$ (**9**) ($T_{\text{dec}} = 210 \text{ }^\circ\text{C}$) gegen ein Triflimid Anion zur Verbindung $[\text{Fe}(\text{L}^{\text{td}})_3](\text{NTf}_2)_2$ (**12**) führt, die einen Schmelzpunkt bei $T_{\text{fus}} = 194 \text{ }^\circ\text{C}$ aufweist.

Drei neue Liganden für die Synthese von niedrig schmelzenden Komplexen der allgemeinen Formel $[\text{M}(\text{L})_3](\text{X})_2$ wurden entwickelt. Substitution der Aminofunktion im Thiazol L^{tz} mit einer Methoxyacetyl-Gruppe führt zum Amid L^1 . Da 2-(2-pyridyl)-imidazol (**pi**) bekannt dafür ist, SCO Komplexe mit Eisen(II) der allgemeinen Formel $[\text{Fe}(\text{L})_3](\text{X})_2$ zu bilden, wurde es als Ausgangspunkt für die Synthese von zwei weiteren neuen Liganden gewählt. Substitution am N_{im} Atom des Imidazoliumrings von **pi** mit einer Ethyl-Gruppe (L^2) bzw. einer Methoxyethyl-Gruppe (L^3) führt zu den Liganden L^2 und L^3 . Ein weiterer Ligand für die Synthese von Komplexen mit der Formel $[\text{M}(\text{L})_2(\text{Y})_2]$ wurde ausgehend vom Thiadiazol L^{td} entwickelt. Substitution der Aminofunktion des Thiadiazols L^{td} mit ω -Brompentansäurechlorid führt zum Amid **tdBr** das mit 1-Ethylimidazol weiter zum Imidazoliumbromid L^4Br umgesetzt wurde. Anschließende Metathese mit LiNTf_2 ergibt den neuen Imidazoliumtriflimid Liganden L^4NTf_2 .

Die Schwierigkeit von Komplexsynthesen mit L^1 wurde gezeigt. Wie erwartet weist der Komplex $[\text{Fe}(\text{L}^1)_3](\text{BF}_4)_2$ (**16**) das Metallion im HS Zustand auf und zersetzt sich außerdem bei $218 \text{ }^\circ\text{C}$. Mit den Liganden L^2 und L^3 sind Komplexsynthesen eher machbar. Es wurden zwei Serien von Eisen(II)-Komplexen mit der Formel $[\text{Fe}(\text{L}^2)_3](\text{X})_2$ ($\text{X} = \text{ClO}_4^-$: **22**; BF_4^- : **23**; NTf_2^- : **24**) bzw. $[\text{Fe}(\text{L}^3)_3](\text{X})_2$ ($\text{X} = \text{ClO}_4^-$: **27**; BF_4^- : **28**) hergestellt. Die Darstellung der Kobalt(II)-Komplexe $[\text{Co}(\text{L})_3](\text{ClO}_4)_2$ ($\text{L} = \text{L}^2$: **25**; L^3 : **29**) erlaubte die strukturelle Charakterisierung solcher Komplexe mittels Einkristalldiffraktometrie. Durch die UV/Vis spektroskopische Untersuchung der verwandten Nickel(II)-Komplexe $[\text{Ni}(\text{L})_3](\text{ClO}_4)_2$ ($\text{L} = \text{L}^2$: **26**; L^3 : **30**) konnte bestätigt werden, dass L^2 und L^3 ähnliche starke Liganden wie ihre Vorstufe **pi** sind. Daher ist es sehr wahrscheinlich, dass die Eisen(II) LS Komplexe **22–24** und **27–28** bei höheren Temperaturen in den HS Zustand übergehen. Außer den Perchlorat-Komplexen **22** und **27**, besitzen alle Eisen(II)-Komplexe einen Schmelzpunkt im Bereich von $239\text{--}153 \text{ }^\circ\text{C}$, wobei $[\text{Fe}(\text{L}^2)_3](\text{NTf}_2)_2$ (**24**, $T_{\text{fus}} = 153 \text{ }^\circ\text{C}$) den niedrigsten Schmelzpunkt besitzt. Es wurde außerdem gezeigt, dass Komplexe mit dem Methoxyethyl substituierten Liganden L^3 generell niedrigere Schmelzpunkte aufweisen als Komplexe mit dem Ethyl substituierten Liganden L^2 . Außerdem schmilzt der Komplex mit NTf_2^- als Gegenion bei signifikant niedrigerer Temperatur als verwandte Komplexe mit ClO_4^- oder BF_4^- Anionen.

Es wurde gezeigt, dass die Darstellung von Komplexen der Zusammensetzung $[\text{M}(\text{L}^4)_2(\text{NCS})_2](\text{NTf}_2)_2$ ($\text{M} = \text{Fe}, \text{Co}$) mit Hilfe des Imidazoliumliganden L^4NTf_2 relativ schwierig ist. Mit „ $\text{Fe}(\text{NCS})_2$ “ tritt vermutlich eine unvollständige Komplexierung auf, worauf eine HPLC chromatographische Untersuchung hinweist. Mit „ $\text{Co}(\text{NCS})_2$ “ kam es zur Bildung von zwei verschiedenen Kristallsorten, die röntgenographisch als $[\text{Co}(\text{L}^4)_2(\text{NCS})_2][\text{Co}(\text{NCS})_4]$ (**31**) und $[\text{Co}(\text{L}^4)_2(\text{NCS})_2](\text{NTf}_2)_2$ (**32**) identifiziert wurden. Bulk Material konnte von diesen Verbindungen nicht erhalten werden.

Synthesen mit $\text{Fe}(\text{NTf}_2)_2 \cdot 6\text{H}_2\text{O}$ und sechs Äquivalenten der Azole *N*-Methylimidazol (**mim**) bzw. *N*-Ethylimidazol (**eim**) als Liganden wurden etabliert. Die Komplexe $[\text{Fe}(\text{mim})_6](\text{NTf}_2)_2$ (**33**) und $[\text{Fe}(\text{eim})_6](\text{NTf}_2)_2$ (**34**) weisen das Metallion im HS Zustand auf. Komplex **33** zersetzt sich bei $183 \text{ }^\circ\text{C}$, wohingegen Komplex **34** bei einer bemerkenswert niedrigen Temperatur von $T_{\text{fus}} = 83 \text{ }^\circ\text{C}$ schmilzt.

Abbreviations

10Dq	ligand field splitting in the octahedral coordination geometry
APCI	atmospheric pressure chemical ionisation
ATR	attenuated total reflection
bs	broad singlet
calcd.	calculated
CI	chemical ionisation
CT	charge transfer
d	doublet
DCM	dichloromethane
ddd	doublet of doublet of doublet
ΔE_Q	quadrupole splitting
DMSO	dimethyl sulfoxide
DSC	differential scanning calorimetry
EE	ethyl acetate
EI	electron impact
eim	<i>N</i> -ethylimidazole
ESI	electrospray ionisation
etz	<i>N</i> -ethyltetrazole
<i>fac</i>	facial
fus	fusion
<i>g</i>	Landé <i>g</i> factor
HMBC	Heteronuclear Multiple Bond Correlation
HMQC	Heteronuclear Multiple Quantum Correlation
HPLC	high-performance liquid chromatography
HR	high resolution
HS	high spin
im	imidazole
IR	infrared
<i>J</i>	magnetic coupling constant
L	ligand
L ¹	2-methoxy- <i>N</i> -[4-(2-pyridyl)-2-thiazolyl]-acetamide
L ²	2-(2-pyridyl)-1-ethyl-imidazole
L ³	2-(2-pyridyl)-1-(2-methoxyethyl)-imidazole
L ⁴	pentanoic acid [5-(2-pyridyl)-2-[1,3,4]-thiadiazolyl]-amide-5-[3-ethyl-1-imidazolium]
LS	low spin
L ^{td}	2-amino-5-(2-pyridyl)-1,3,4-thiadiazole
L ^{tz}	2-amino-4-(2-pyridyl)-thiazole
m	mass
m	multiplet
M.p.	melting point
<i>mer</i>	meridional
mim	<i>N</i> -methylimidazole
MS	mass spectrometry
NMR	Nuclear Magnetic Resonance
NTf ₂	bis(trifluoromethylsulfonyl)imide
triflimide	bis(trifluoromethylsulfonyl)imide
PI	paramagnetic impurity
pi	2-(2-pyridyl)-imidazole
ppm	parts per million
ptz	1- <i>n</i> -propyltetrazole

py	pyridyl
pyBr	2-(bromoacetyl)-pyridine hydrobromide
pyNH	pyridine-2-carboximidic acid methyl ester
q	quartet
rt	room temperature
s	singlet/strong
SCO	spin crossover
SQUID	superconducting quantum interference device
T	temperature
t	time
TBME	<i>tert</i> -butyl methyl ether
td	1,3,4-thiadiazole
tdBr	pentanoic acid [5-(2-pyridyl)-2-[1,3,4]-thiadiazoly]-amide-5-bromide
TIP	temperature independent paramagnetism
tz	thiazole
UV	ultraviolet
vap	vaporisation
VdW	van der Waals
Vis	visible
vs	very strong
WCA	weakly coordinating anion
z	charge
Z	number of formula units in the unit cell
Γ	line width
δ	isomeric shift
Δ	difference
η	viscosity
λ	wave length
μ_B	Bohr magneton
χ_M	molar magnetic susceptibility
$\tilde{\nu}$	wavenumber

Content

1	INTRODUCTION	1
1.1	Spin Crossover in Coordination Compounds	1
1.2	The Melting Point of Coordination Compounds	6
1.3	Multifunctional Materials	10
1.4	Objectives of this Work	11
2	RESULTS AND DISCUSSION	12
2.1	Complexes with 2-Pyridyl and Amino Substituted Azoles	12
2.1.1	Ligand Synthesis	12
2.1.2	Complex Synthesis	17
2.2	Complexes with Uncharged Ligands	54
2.2.1	Ligand Synthesis	54
2.2.2	Complexes with L ¹	64
2.2.3	Complexes with L ² and L ³	70
2.3	Complexes with an Imidazolium-Tagged Ligand	103
2.3.1	Synthesis of the Ligand L ⁴ NTf ₂	103
2.3.2	Complexes with L ⁴ NTf ₂	113
2.4	Complexes with <i>N</i> -Alkylimidazoles	125
2.5	Summary and Outlook	133
3	EXPERIMENTAL	137
3.1	General Remarks	137
3.2	Organic Ligand Synthesis	140
3.2.1	Synthesis of L ^{tz}	140
3.2.2	Synthesis of L ¹	140

3.2.3	Synthesis of L^{td}	141
3.2.4	Synthesis of L^4NTf_2	142
3.2.5	Synthesis of pi Based Ligands	144
3.3	Complexation Reactions	145
3.3.1	Complexes with L^{tz}	145
3.3.2	Complexes with L^1	149
3.3.3	Complexes with L^{td}	150
3.3.4	Complexes with L^4NTf_2	153
3.3.5	Complexes with L^2 and L^3	154
3.3.6	Complexes with <i>N</i> -Alkylimidazoles	157
4	REFERENCES	158
5	APPENDIX	163
5.1	NMR Spectra	163
5.2	Mass Spectra	171
5.3	Vibrational Spectra	174
5.4	UV/Vis Spectra	184
5.5	X-Ray Data	186

1 Introduction

1.1 Spin Crossover in Coordination Compounds

Spin crossover (SCO) ^[1] coordination compounds consist of bistable complexes featuring two different ground states with different physical and chemical properties that can be triggered by external stimuli. Thus, SCO compounds are considered to be suitable for functional materials and applications especially in the field of information storage and signal processing. ^[2,3] Bistability is feasible for octahedrally coordinated complexes comprising an ion with a d^4 , d^5 , d^6 or d^7 configuration. Investigators especially focused on SCO complexes featuring iron(II) ions (d^6) ^[4,5,6] as well as cobalt(II) ions (d^7). ^[7] In the case of compounds derived from iron(II) the complexes exhibit a diamagnetic low spin (LS) state ($^5T_2(t_{2g}^4e_g^2)$) with minimal spin multiplicity ($S = 0$) and a paramagnetic high spin (HS) state ($^1A_1(t_{2g}^6)$) with maximal spin multiplicity ($S = 2$) (Figure 1).

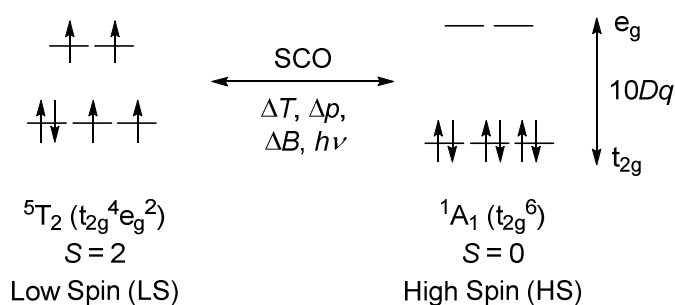


Figure 1: Electronic configuration of the two ground states of iron(II) in an octahedral coordination geometry.

The transition between the two spin states, that is referred to as spin crossover, is commonly triggered by temperature variation, though pressure changes, irradiation or application of an external magnetic field can also result in the occurrence of spin crossover. Such a spin transition or SCO is accompanied by changes of the chemical and physical properties of a certain complex such as its colour, magnetism, metal-donor atom distances, volume of its primitive cell or changes in the ligand field splitting (LFS). ^[1] The latter is an important parameter of SCO complexes. In an ideally octahedral coordinated complex the five nd orbitals of a transition metal split up into two orbital sets. The e_g set includes the d_{z^2} and $d_{x^2-y^2}$ orbitals featuring anti-bonding character whereas the t_{2g} set consists of the d_{xy} , d_{yz} and d_{zx} orbitals basically featuring non-bonding character and therefore lower energies than the e_g orbital set. The splitting between these two orbital sets is referred to as ligand field splitting (LFS) and is quantified by

the ligand field strength symbolised by the parameter $10Dq$ (Figure 1). The value of $10Dq$ depends, as a first approximation, on the electronic properties of the involved ligands. Complexes with a too small $10Dq$ will remain in the HS state even at low temperatures, whereas complexes with a higher value of $10Dq$ can exhibit a LS ground state and cross over into the HS state when heated. The larger the LFS, the higher is the temperature $T_{1/2}$ at which half of the SCO molecules or ions are in the HS state. The progress of such transitions is commonly detected by temperature dependent measurements of the magnetic susceptibility or by Mössbauer spectroscopy and can occur in different manners ranging from incomplete or gradual SCO to complete (multi step) SCO with hysteresis caused by cooperative interactions.

The influence of packing effects in solid material on the SCO properties ^[5,8] of a compound was investigated by Kahn *et al.* who reported on the influence of intramolecular interactions in polymeric SCO compounds on spin transition characteristics. ^[2] More recently, also the influence of intermolecular interactions on SCO characteristics was discussed. ^[9,10] Packing effects, as *e.g.* H-bonds, ^[11] π - π stacking and other short contacts, ^[10] can influence the transition temperature $T_{1/2}$ but especially modify the type of SCO via cooperative interactions. Hence, abrupt and multi-step spin transitions or SCO with hysteresis may be generated. The three related complexes $[\text{Fe}(\text{I})_2(\text{NCS})_2]$ (**A**), $[\text{Fe}(\text{I})_2(\text{NCSe})_2]$ (**B**) and $[\text{Fe}(\text{III})_2(\text{NCS})_2]$ (**E**) (**I** = 2,5-di-(2-pyridyl)-1,3,4-thiadiazole; **III** = 2,5-di-(2-pyridyl)-1,3,4-selenadiazole) (Figure 2) exemplarily show how cooperative interactions influence $T_{1/2}$ as well as the type of SCO. The asymmetric unit in the crystal structure of compound **A** consists of two crystallographically independent molecules, which only vary in the coordination mode of the isothiocyanato coligands. In one molecule, the coligands are coordinated nearly perpendicular to the plane formed by the four donor N atoms of the ligand **I**, whereas in the second molecule NCS^- is coordinated in an inclined manner, which gives rise to a two-step SCO curve. Packing effects in compound **A** presumably lead to the inclined coordination in the second molecule, which causes a smaller LFS and therefore a lower $T_{1/2}$ than in the first molecule featuring perpendicular coordination of NCS^- . ^[12] In contrast, the crystals of the related complex $[\text{Fe}(\text{I})_2(\text{NCSe})_2]$ (**B**) feature an asymmetric unit with only one molecule and therefore **B** exhibits a one-step SCO curve. ^[13] Influence on the type of SCO is observed in the related complex $[\text{Fe}(\text{III})_2(\text{NCS})_2]$ (**E**) which possesses a SCO curve with hysteresis, presumably caused by intermolecular $\text{Se}\cdots\text{S}$ interactions according to the authors. ^[14]

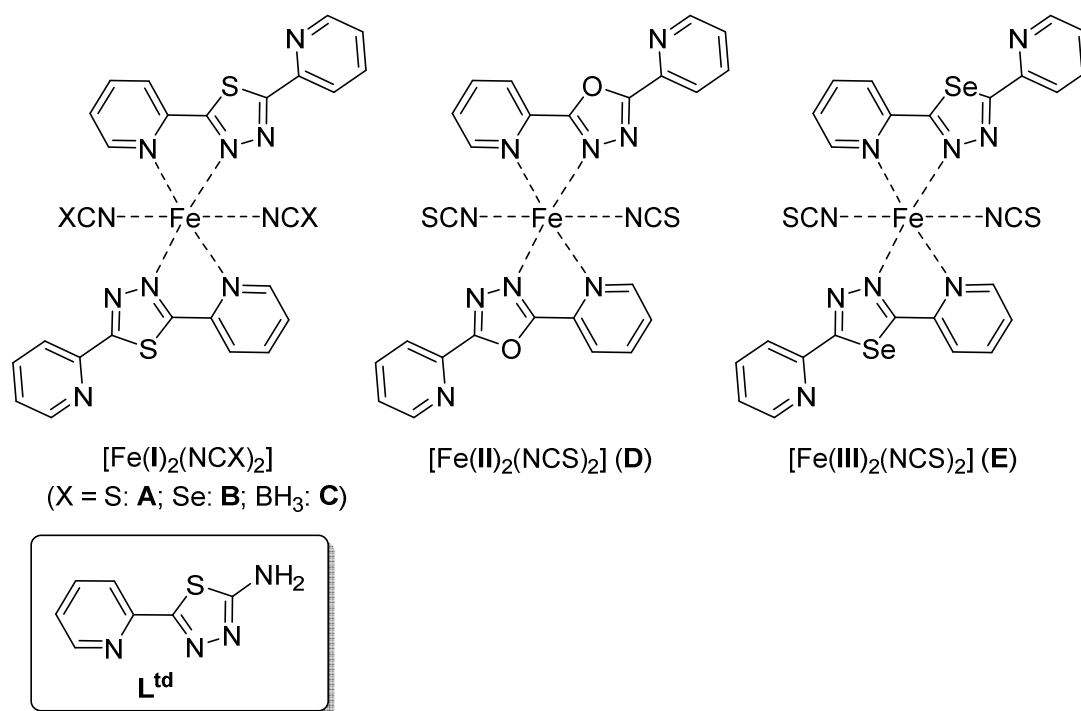


Figure 2: Ferrous 2:1-type SCO complexes with 2,5-di-(2-pyridyl)-1,3,4-chalcadiazole ligands **I–III** and NCX coligands: $[\text{Fe}(\text{I})_2(\text{NCX})_2]$ (**I** = 2,5-di-(2-pyridyl)-1,3,4-thiadiazole, X = S: **A**; Se: **B**; BH₃: **C**)^{[12][13]}, $[\text{Fe}(\text{II})_2(\text{NCS})_2]$ (**II** = 2,5-di-(2-pyridyl)-1,3,4-oxadiazole, **D**),^[14] $[\text{Fe}(\text{III})_2(\text{NCS})_2]$ (**III** = 5-di-(2-pyridyl)-1,3,4-selenadiazole, **E**)^[14]; inset: 2-amino-5-(2-pyridyl)-1,3,4-thiadiazole (**L^{td}**)^[15]

The complexes **A–E**^[12–14] are based on the 1,3,4-chalcadiazole ligands **I–III** acting as bidentate chelates and comprise the general formula $[\text{Fe}^{\text{II}}(\text{L})_2(\text{Y})_2]$ (L = bidentate chelate and Y = anionic coligand) featuring an uncharged chromophore and a ligand to metal ratio (L:M) of 2:1. The related ligand 2-amino-5-(2-pyridyl)-1,3,4-thiadiazole (**L^{td}**) has first been prepared in 1958,^[15] but has not been structurally characterised nor have its complexes been isolated yet (Figure 2). More ferrous SCO complexes are known based on ligands that are 2-pyridyl substituted 1,2,4-triazoles,^[16,17] related chalcadiazoles,^[12–14,18–20] [1,2,4]triazolo[4,3-*a*]pyridines,^[21,22] or pyrazoles.^[23] Some of them form mononuclear complexes featuring an N₆ coordination sphere as well, but comprise the general formula $[\text{Fe}^{\text{II}}(\text{L})_3](\text{X})_2$ (L = bidentate chelate and X = non-coordinating anion) with a ligand to metal ratio (L:M) of 3:1 and a positive charged chromophore. Such 3:1-type iron(II) SCO-complexes (**F**, **G**) have also been prepared with 2-pyridyl substituted ligands featuring a thiazole-moiety (**IV**, **V**).^[24] With the terdentate di-(2-pyridyl) substituted thiazole ligands **VI–VIII** similar ferrous SCO-compounds (**H–J**) with two equivalents of the ligands have been prepared.^{[25–28][29–31][32,33]} With the related ligand 2-amino-4-(2-pyridyl)-thiazole (**L^{tz}**)^[34,35] no complexes have been prepared yet (Figure 3).

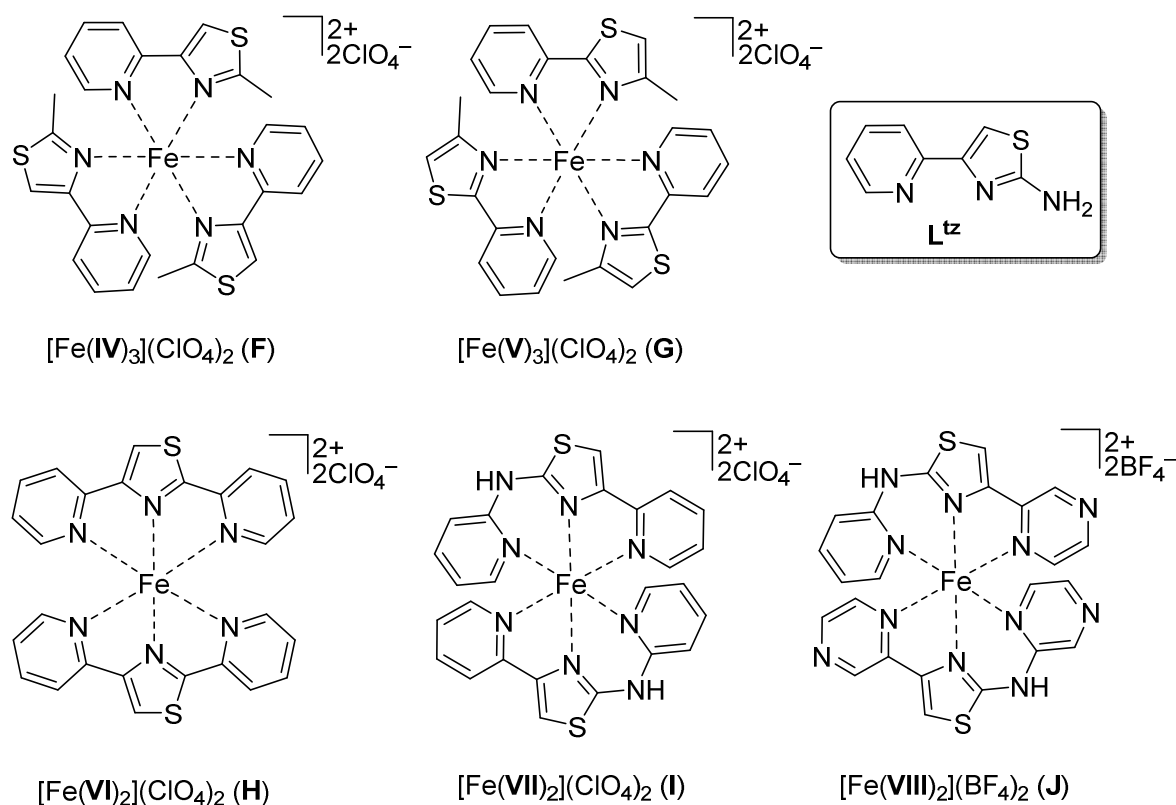


Figure 3: *top*: ferrous 3:1-type SCO complexes with bidentate 2-pyridyl substituted thiazole-ligands **IV** and **V**: $[\text{Fe}(\text{IV})_3](\text{ClO}_4)_2$ (**IV** = 4-(2-pyridyl)-2-methylthiazole, **F**), $[\text{Fe}(\text{V})_3](\text{ClO}_4)_2$ (**V** = 2-(2-pyridyl)-4-methylthiazole, **G**); *bottom*: similar SCO compounds with related terdentate di-(2-pyridyl) substituted thiazole-ligands **VI–VIII**: $[\text{Fe}(\text{VI})_2](\text{ClO}_4)_2$ (**VI** = 2,4-di-(2-pyridyl)-thiazole, **H**), $[\text{Fe}(\text{VII})_2](\text{ClO}_4)_2$ (**VII** = 2-(2-pyridylamino)-4-(2-pyridyl)-thiazole, **I**), $[\text{Fe}(\text{VIII})_2](\text{BF}_4)_2$ (**VIII** = 2-(2-pyrazylamino)-4-(2-pyridyl)-thiazole, **J**); *inset*: 2-amino-4-(2-pyridyl)-thiazole (**L^{tz}**).

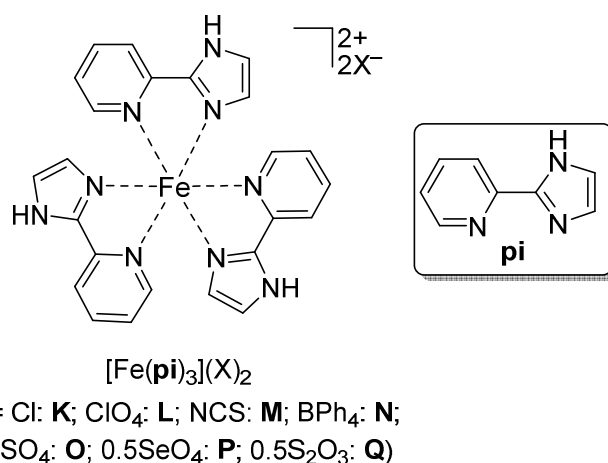


Figure 4: Ferrous 3:1-type SCO-complexes with 2-(2-pyridyl)-imidazole (**pi**) as ligand: $[\text{Fe}(\text{pi})_3](\text{X})_2$ (X = Cl: **K**; ClO_4 : **L**; NCS: **M**; BPh_4 : **N**; 0.5SO_4 : **O**; 0.5SeO_4 : **P**; $0.5\text{S}_2\text{O}_3$: **Q**); *inset*: 2-(2-pyridyl)-imidazole (**pi**).

Further ferrous 3:1-type SCO complexes (**K–Q**) have been prepared using 2-(2-pyridyl)-imidazole (**pi**) and several iron(II) salts (Figure 4).

Apart from ferrous 2:1- and 3:1-type SCO complexes with bidentate ligands, also azoles acting as monodentate ligands have been used to prepare 6:1-type SCO complexes comprising the general formula $[\text{Fe}(\text{L})_6](\text{X})_2$ (L = monodentate azole and X = non-coordinating anion).^[6] Such homoleptic complexes for example have been prepared with isoxazole (**iox**) (**R** and **S**)^[41–44] and 1-alkyl substituted tetrazoles (Rtz) (**T–X**).^[45,46] The 1-*n*-propyl-tetrazole (**ptz**)^[47] ligand is very useful as it forms the ferrous SCO compound **V** featuring an abrupt and complete spin transition whereas analogous complexes with 1-*n*-R-tetrazole (R = Me: **T**, Et: **U**, *i*Pr: **W**) only partly change their spin state^[45] and the complex with 1-*n*-butyltetrazole (**X**) features a more gradual spin crossover^[46] (Figure 5).

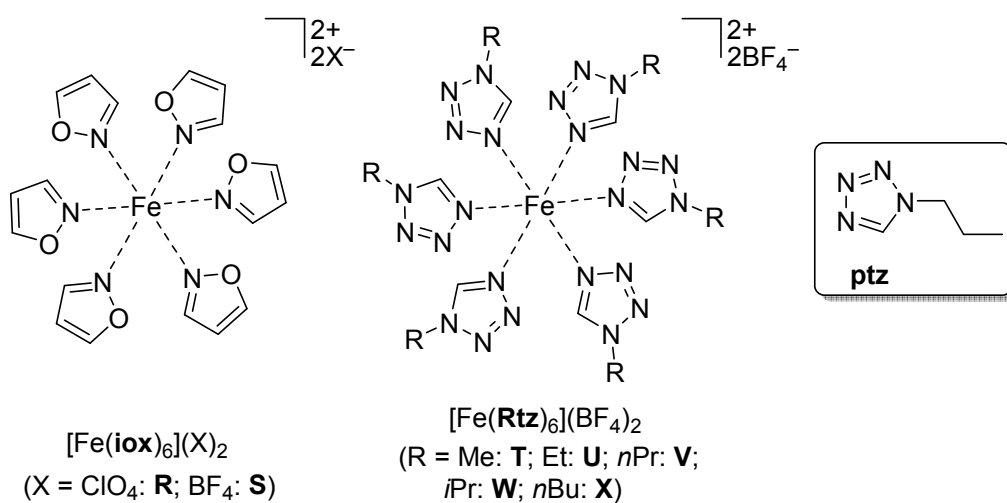


Figure 5: Ferrous 6:1-type SCO complexes with isoxazole (**iox**) and 1-*n*-R-tetrazole (**Rtz**) as ligands: $[\text{Fe}(\mathbf{iox})_6](\text{X})_2$ (X = ClO₄: **R**; BF₄: **S**),^[41–44] $[\text{Fe}(\mathbf{Rtz})_6](\text{BF}_4)_2$ (R = Me: **T**; Et: **U**; *n*Pr: **V**; *i*Pr: **W**; *n*Bu: **X**)^[45]; inset: 1-*n*-propyl-tetrazole (**ptz**)^[47]

1.2 The Melting Point of Coordination Compounds

For the 2:1-type complexes $[\text{Fe}(\text{I})_2(\text{NCSe})_2]$ (**B**) and $[\text{Fe}(\text{I})_2(\text{NCBH}_3)_2]$ (**C**), melting points of 301 °C and 231 °C, respectively were reported (Table 1).^[13] Heating up the ferrous 6:1-type complexes $[\text{Fe}(\text{iox})_6](\text{ClO}_4)_2$ (**R**) and $[\text{Fe}(\text{iox})_6](\text{BF}_4)_2$ (**S**) leads to decomposition of the perchlorate **R** at 120 °C and of the tetrafluoroborate **S** at 136 °C,^[41] whereas the related cobalt(II)- and nickel(II) tetrafluoroborate complexes $[\text{Co}(\text{iox})_6](\text{BF}_4)_2$ (**S^{Co}**) and $[\text{Ni}(\text{iox})_6](\text{BF}_4)_2$ (**S^{Ni}**) melt at 179–183 °C and 208–211 °C, respectively (Table 1). Melting points of the 1-R-tetrazole complexes **T–X** (Figure 5) were not reported. However, the analogous imidazole complexes $[\text{Fe}(\text{mim})_6](\text{ClO}_4)_2$ (**T^{im}**) with **mim** = *N*-methylimidazole and $[\text{Fe}(\text{eim})_6](\text{ClO}_4)_2$ (**U^{im}**) with **eim** = *N*-ethylimidazole exhibit a HS state but feature relatively low melting points at 218 °C (**T^{im}**) and 160 °C (**U^{im}**) (Table 1).^[48]

Table 1: Melting points T_{fus} (°C) of some iron(II) and related Co(II) and Ni(II) complexes.

		$T_{fus} / ^\circ\text{C}$
$[\text{Fe}(\text{I})_2(\text{NCSe})_2]$	(B)	301
$[\text{Fe}(\text{I})_2(\text{NCBH}_3)_2]$	(C)	231
$[\text{Fe}(\text{I})_3](\text{OTf})_2$	(Y)	229
$[\text{Fe}(\text{I})_3](\text{ClO}_4)_2$	(Z)	> 400
$[\text{Fe}(\text{iox})_6](\text{ClO}_4)_2$	(R)	120 (dec.)
$[\text{Fe}(\text{iox})_6](\text{BF}_4)_2$	(S)	139 (dec.)
$[\text{Co}(\text{iox})_6](\text{BF}_4)_2$	(S^{Co})	179–183
$[\text{Ni}(\text{iox})_6](\text{BF}_4)_2$	(S^{Ni})	208–211
$[\text{Fe}(\text{mim})_6](\text{ClO}_4)_2$	(T^{im})	218
$[\text{Fe}(\text{eim})_6](\text{ClO}_4)_2$	(U^{im})	160

Melting points can neither be found for the ferrous 3:1-type complexes **F–G** (Figure 3) featuring 2-pyridyl substituted thiazole ligands (**I**, **II**) or for complexes **K–Q** (Figure 4) comprising the 2-(2-pyridyl)-imidazole (**pi**) ligand nor for complexes **H–J** (Figure 3) possessing terdentate thiadiazole ligands (**III–V**). However, the thiadiazole ligand **I** also forms the 3:1-type LS complexes $[\text{Fe}(\text{I})_3](\text{OTf})_2$ (**Y**) and $[\text{Fe}(\text{I})_3](\text{ClO}_4)_2$ (**Z**). The latter does not melt up to 400 °C, whereas the triflate **Y** indeed melts at 229 °C (Table 1).^[13]

In the case of the overall charge neutral 2:1-type complexes, the melting point is mainly determined by van der Waals interactions and dipole-dipole interactions. In the case of ionic 3:1-type complexes, additional strong and long ranging coulomb interactions have a crucial impact on the melting point. The weaker these intermolecular interactions, the lower are the values of the fusion temperature T_{fus} . The degree of van der Waals and dipole-dipole interactions is given by the molecular structure and the

molecular weight. Thus, it can be assumed as constant for a series of similar coordination compounds. The electrostatic force between two point charges is determined by the magnitudes of charges and the distance between the centres of those two charges. Thus, the coulomb interactions between a cation and anion are directly influenced by the size of the latter. Minimising coulomb interactions is a concept that becomes important in the field of ionic liquids (IL) where often organic monocations (*e.g.* imidazolium, pyridinium, ammonium or phosphonium) with large volumes are combined with weakly coordinating anions (WCA).^[49] Such WCAs additionally minimise ion pair formation between cation and anion as they comprise a periphery consisting of weakly basic atoms.^[50] The fusion temperature T_{fus} is also influenced by the entropy of fusion ΔS_{fus} according to the equation $T_{fus} = \Delta H_{fus} / \Delta S_{fus}$. The entropy of fusion is a function of the molecule's symmetry and its number of torsion angles. The higher the value of ΔS_{fus} , the lower is T_{fus} . Compounds with low symmetry and a high number of torsion angles feature high entropy of fusion.^[51] The cations of ILs often comprise substituents such as ethyl-, propyl- butyl or polyglycol-groups featuring additional torsion angles and providing a relatively high value of ΔS_{fus} .

Both concepts, lowering coulomb interactions and increasing the fusion entropy, have been used to prepare 3:1-type complexes with low melting points. *Masui et al.* obtained the room temperature melts **AA** and **AB** of iron(II)- and cobalt(II)-perchlorate complexes using a polyglycol substituted bipyridine ligand (Figure 6).^[52,53] *Mochida et al.* prepared the iron(III) SCO complex **AC** that is liquid at room temperature using an anionic ligand with a charge of -2 and the WCA bis(trifluoromethylsulfonyl)imide (triflimide, NTf₂), (Figure 6).^[54] In the latter case, apart from weak coulomb interactions between the ferric complex cation and the triflimide WCA, the *n*-butyl substituents at the imidazole coligands and the resulting increase of the entropy of fusion are responsible for the low lying melting point.

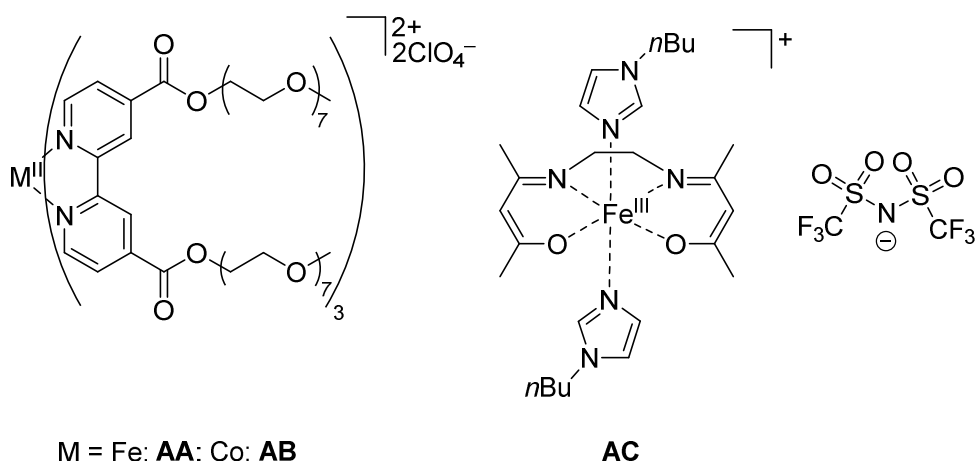


Figure 6: left: structure of rt melts of iron(II)- (**AA**) and cobalt(II)-perchlorate (**AB**) complexes with a polyglycol substituted bipyridine ligand;^[52,53] right: iron(III) SCO complex that is liquid at room temperature (**AC**).^[54]

In order to introduce weak coulomb interactions, charge neutral complexes can be enhanced with an imidazolium moiety that is combined with a WCA. In the field of organometallic catalysis, efforts have been done to enhance the solubility of catalytic active compounds in ionic liquids as reaction media. Therefore complexes with imidazolium tag were prepared. Such compounds also feature low melting points^[55] or are even ionic liquids themselves.^[56,57] For example, *Raubenheimer et al.* prepared the organometallic ionic liquid **AD** consisting of an $\text{Co}_2(\text{CO})_6$ moiety covalently attached to an imidazolium cation (Figure 7) which reversibly melts at 75–77 °C.^[56] In the field of electrochemistry, ferrocene compounds with an imidazolium tag were prepared in order to use the intrinsic electroactivity also in the liquid phase.^[57,58] For example, *Bala et al.* prepared a series of ferrocene compounds featuring an imidazolium tag.^[57] One member of this series, the tetrafluoroborate **AE**, consists of a 1-*n*-butylimidazolium cation that is bound *via* a methylene group to the ferrocene, building a compound which melts at 73°C.

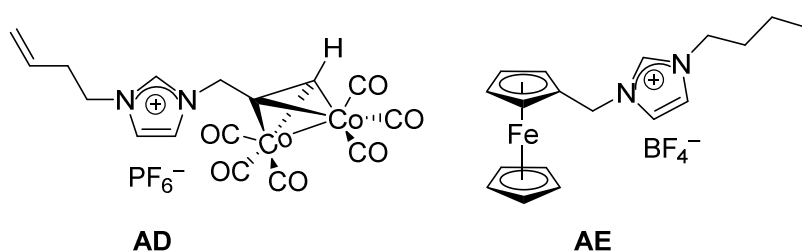


Figure 7: left: catalytic active organometallic ionic liquid (**AD**); right: electroactive organometallic ionic liquid (**AE**).

If cooling of a sample in the liquid state does not lead to the formation of a crystalline solid but rather to the formation of an amorphous solid, the transition is called a glass transition and the solid is referred to as glass or supercooled melt. The specific temperature, at which this process takes place, is the glass transition temperature T_g . The glass transition is accompanied by an increase of the viscosity η . Values of η in a glass normally are $> 10^{12}$ Pa·s which are typical values for solids ($\eta(\text{water at } 25\text{ }^\circ\text{C}) = 0.891 \cdot 10^{-3}$ Pa·s). Furthermore, in glasses the temperature dependence of the volume is rather small as it is the case for crystalline material. The structure of the glassy material only changes marginally in comparison to the liquid state. Thus the glass does not feature a regular lattice, but rather an amorphous and disordered structure. ^[59]

1.3 Multifunctional Materials

In the light of SCO applications, compounds that combine the SCO property with another technological relevant property are of special interest. Efforts have been made to combine SCO with material-,^[60] nano-,^[61] liquid crystalline^[62] and host-guest chemistry.^[63] Applying SCO compounds with a low melting point, SCO compounds that are ionic liquids or SCO compounds that are glasses, could permit the manipulation of magnetic properties, density, viscosity, conductivity or colour by temperature or pressure change or by photoexcitation. Such compounds could be of interest for sensor, magnetism or solar energy research. Furthermore, the liquid and glass state can be seen as a connector between the solid state and a solution. In the latter, intermolecular interactions between the molecules of the dissolved compound can be neglected, whereas in the solid state strong interactions are present. In the liquid or glassy state the intermolecular interactions might be weaker than in related crystalline materials but stronger than in solution. Thus SCO compounds that are liquid or exhibit a glass state could offer new possibilities for the investigation of the SCO phenomenon.

1.4 Objectives of this Work

As a first step on the way to SCO compounds with low melting points, SCO ionic liquids or SCO glasses, suitable ligands that form 2:1-type complexes with charge neutral chromophores and 3:1-type complexes with cationic chromophores should be identified. Therefore 2:1- and 3:1-type complexes with the general formula $[M(L)_3](X)_2$ and $[M(L)_2(Y)_2]$ ($M = Fe^{II}, Co^{II}, Ni^{II}$; $L = L^{tz}, L^{td}$; $X =$ non-coordinating anion, $Y =$ anionic coligand) should be prepared using both ligands L^{tz} and L^{td} . The ligands feature a 4-(2-pyridyl)-thiazole and a 2-(2-pyridyl)-1,3,4-thiadiazole moiety, respectively that are known to form SCO compounds (Figure 2, Figure 3). However, no complexes have been prepared yet using L^{tz} or L^{td} . The obtained complexes should be structurally characterised and especially be investigated on their spin state and melting point.

Based on 2-amino-5-(2-pyridyl)-1,3,4-thiadiazole (L^{td}) a new ligand featuring an imidazolium tag along with the triflimide WCA (L^4NTf_2) should be developed. Using L^4NTf_2 the preparation of 2:1-type complexes with the general formula $[M(L^4)_2(NCS)_2](NTf_2)_2$ ($M = Fe, Co$) featuring charge neutral chromophores should be investigated.

From the ligand 2-(2-pyridyl)-imidazole (**pi**) several 3:1-type SCO complexes are already known (Figure 4). Based on **pi** and 2-amino-4-(2-pyridyl)-thiazole (L^{tz}) new ligands featuring a methoxyacetyl (L^1), ethyl (L^2) or a methoxyethyl (L^3) substituent should be developed. Using these ligands the synthesis of 3:1-type complexes with the general formula $[M(L)_3](X)_2$ ($M = Fe, Co$; $L = L^1, L^2, L^3$; $X =$ non-coordinating anion) featuring cationic chromophores should be examined. The spin states as well as the melting points of the so obtained coordination compounds should be determined.

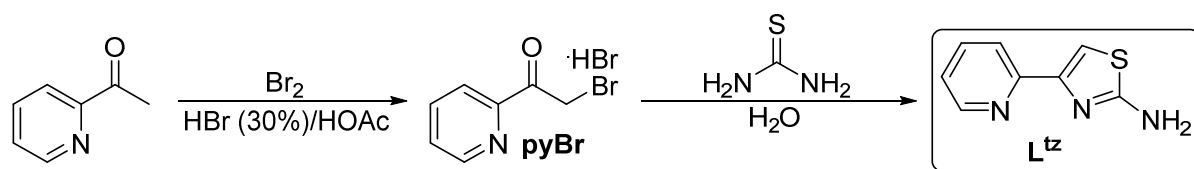
Furthermore, iron(II) triflimide ($Fe(NTf_2)_2$) should be prepared and characterised and used as starting material for complex syntheses. Especially the ability to form 6:1-type complexes with the general formula $[Fe(L)_6](NTf_2)_2$ ($L =$ azole) featuring cationic chromophores with 1-*n*-propyltetrazole (**ptz**) (Figure 5) or related azoles should be investigated. The spin states as well as the melting points of the so obtained coordination compounds should be determined.

2 Results and Discussion

2.1 Complexes with 2-Pyridyl and Amino Substituted Azoles

Ligands, that contain a 2-pyridyl-thiazole or a 2-pyridyl-1,3,4-thiadiazole moiety, are known to form SCO-complexes. The related 2-pyridyl and amino substituted ligands L^{tz} and L^{td} should be investigated on their behaviour towards 3d transition metals as both ligands could be useful instruments for the preparation of multifunctional complexes featuring an amino group that can easily be functionalised.

2.1.1 Ligand Synthesis



Scheme 1: Synthesis of the thiazole ligand L^{tz} .^[64,65]

2-Amino-4-(2-pyridyl)-thiazole (L^{tz}) was synthesized as reported elsewhere^[64,65] by bromination of 2-acetylpyridine and subsequent treatment of the obtained 2-(bromoacetyl)-pyridine hydrobromide ($pyBr$) with thiourea in water. Acetylpyridine was brominated by dropwise addition of bromine to a solution of the educt in hydrogen bromide and acetic acid. Hydrobromide $pyBr$ was obtained as a yellow amorphous powder. Cyclisation of the latter was carried out with thiourea resulting in the formation of L^{tz} . The ligand was obtained analytically pure as a colourless amorphous powder in an overall yield of 62 % (Scheme 1). The 1H -NMR spectrum of L^{tz} shows a broad signal at 7.12 ppm which was assigned to the amino group. A singlet (7.25 ppm) resulting from the 5-tzH hydrogen atom attached to the five membered thiazole ring overlaps with a multiplet (7.23 ppm) resulting from the 5-pyH hydrogen atom of the pyridine ring. Signals resulting from the remaining hydrogen atom can be seen at 7.81 ppm (3-pyH and 4-pyH) and 8.53 (6-pyH) (Figure 8). The CI mass spectrum shows an isotopic pattern with a main peak at $m/z = 178.0$ resulting from the intact, protonated ligand molecule $[L^{tz}\cdot H]^+$ (Figure 9).

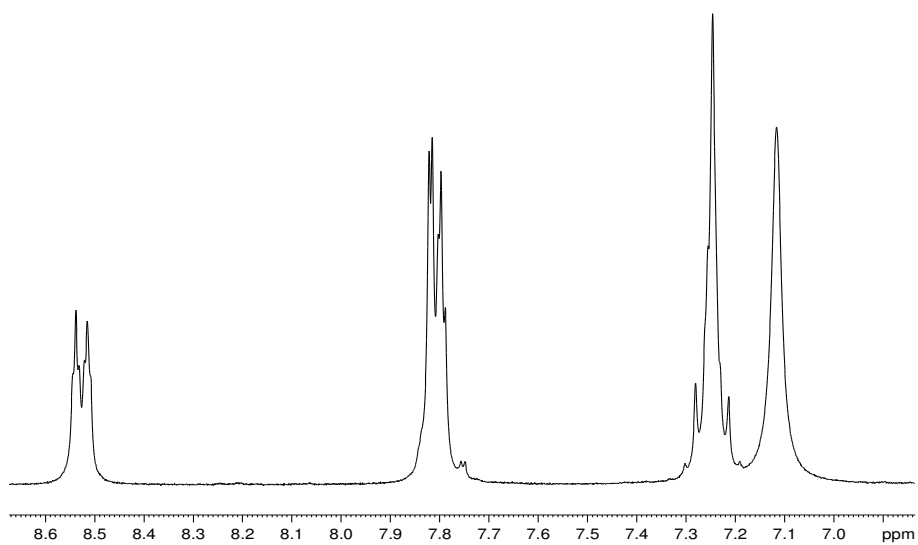


Figure 8: Aromatic region of the $^1\text{H-NMR}$ (200.13 MHz) spectrum of the thiazole ligand L^{tz} in DMSO-d_6 at 298 K.

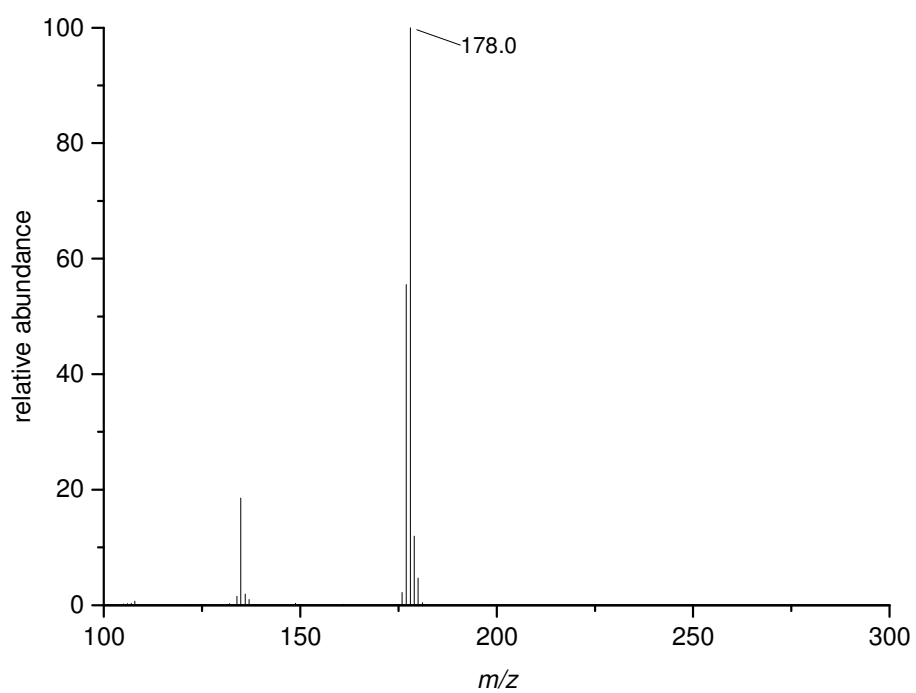
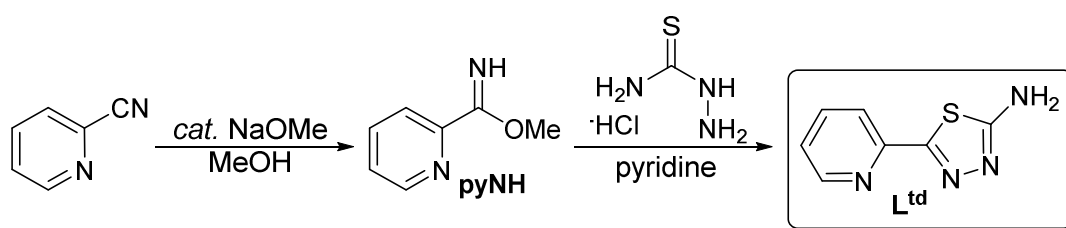


Figure 9: CI mass spectrum of the thiazole ligand L^{tz} .



Scheme 2: Synthesis of the thiadiazole ligand L^{td} .^[66,67]

2-Amino-5-(2-pyridyl)-1,3,4-thiadiazole (L^{td}) was synthesised as reported elsewhere^[66,67] by esterification of 2-pyridinecarbonitrile and subsequent treatment of the obtained pyridine-2-carboximidic acid methyl ester **pyNH** with thiosemicarbazide hydrochloride. The 2-pyridinecarbonitrile was reacted in MeOH and a catalytic amount of NaOMe. Evaporation of the solvent and distillation of the residue gave a colourless liquid of **pyNH**. Cyclisation of the latter was carried out with thiosemicarbazide hydrochloride in pyridine resulting in the formation of L^{td} . The ligand was obtained analytically pure as a slightly yellow amorphous powder (Scheme 2). The $^1\text{H-NMR}$ spectrum of L^{td} shows a broad signal at 7.49 ppm which was assigned to the amino group. Two “doublets” at 8.58 and 8.05 ppm result from the 6-pyH and 3-pyH hydrogen atoms, respectively, whereas the ddd-signals at 7.90 and 7.41 ppm were assigned to the 4-pyH and 5-pyH hydrogen atoms, respectively (Figure 10). The EI mass spectrum shows an isotopic pattern with a main peak at $m/z = 178.0$ resulting from the intact ligand molecule $[L^{td}]^+$ (Figure 11).

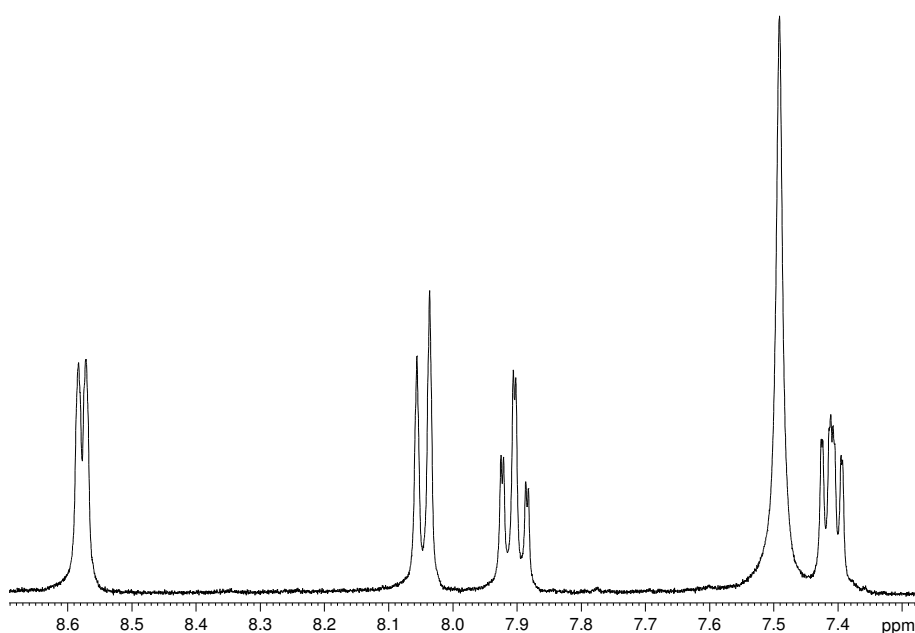


Figure 10: Aromatic region of the $^1\text{H-NMR}$ spectrum (400.17 MHz) of the thiadiazole ligand L^{td} in DMSO-d_6 at 298 K.

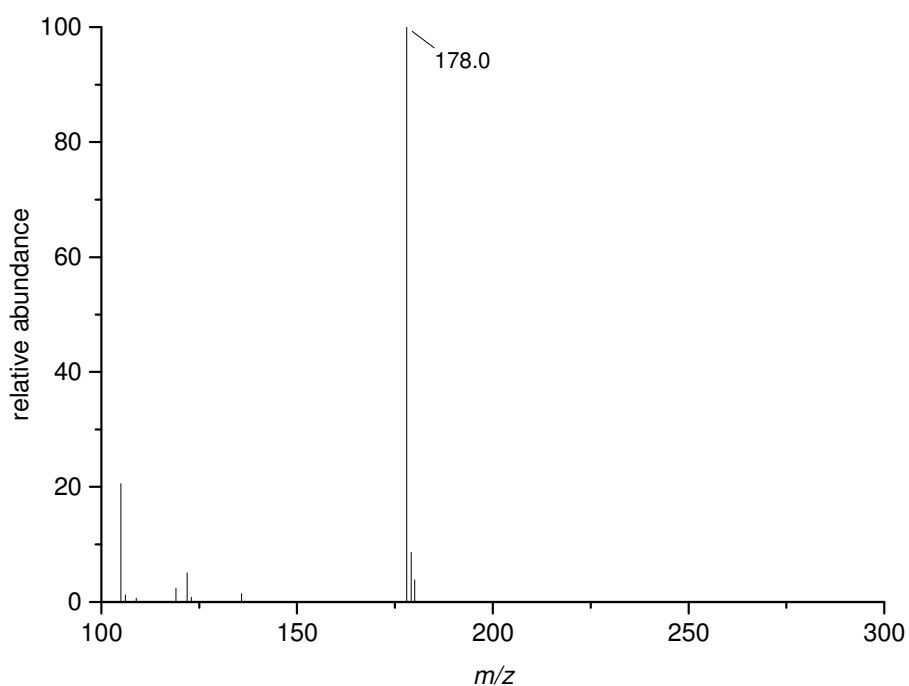


Figure 11: EI mass spectrum of the thiadiazole ligand L^{td} .

Single crystals of the ligand, suitable for X-ray diffraction analysis, were obtained by recrystallisation from MeOH. The ligand crystallises as a colourless block in the orthorhombic space group $Pca2_1$. The asymmetric unit consists of two ligand molecules forming a hydrogen bonded “head-to-tail” pair (Figure 12). These pairs are further hydrogen bonded to form a 3D network (not shown). The crystallographic data for L^{td} are summarised in Table 15.

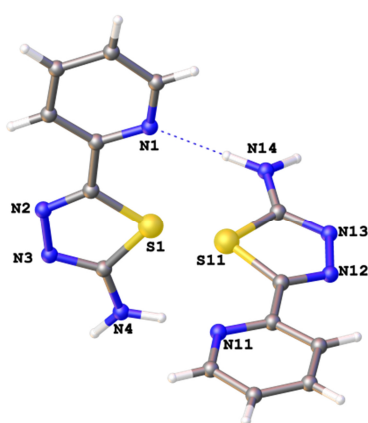


Figure 12: View of the molecular structure of the thiadiazole ligand L^{td} in the asymmetric unit.

A UV/Vis spectrum of the ligand L^{td} was measured in MeOH in order to determine the inner-ligand transitions. The spectrum shows a broad absorption band at 314 nm ($25950 \text{ M}^{-1} \text{ cm}^{-1}$) and rather weak bands at 228 nm ($4940 \text{ M}^{-1} \text{ cm}^{-1}$) and 202 nm ($8750 \text{ M}^{-1} \text{ cm}^{-1}$) which were assigned to $\pi \rightarrow \pi^*$ transitions (Figure 13).

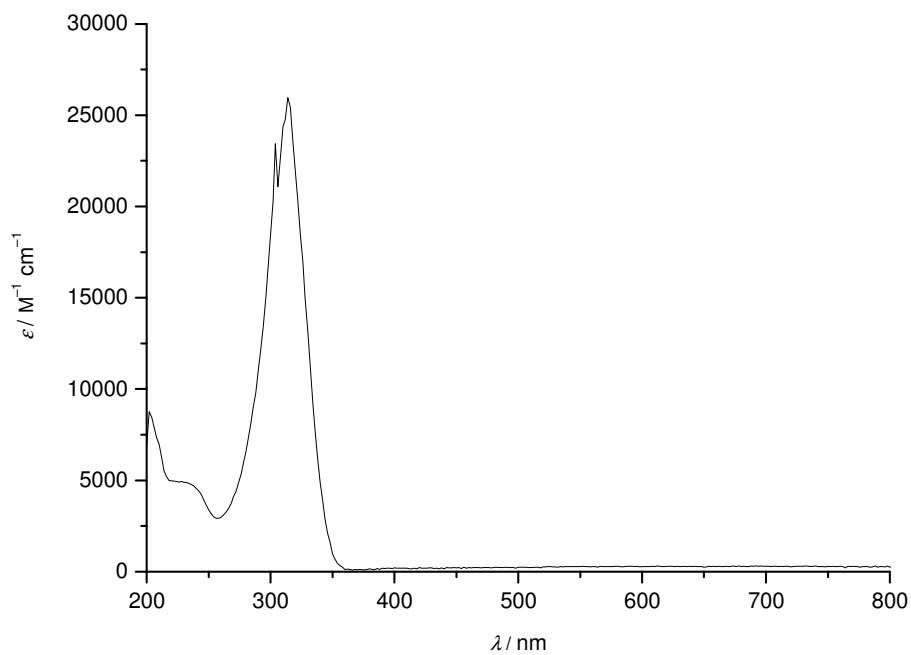
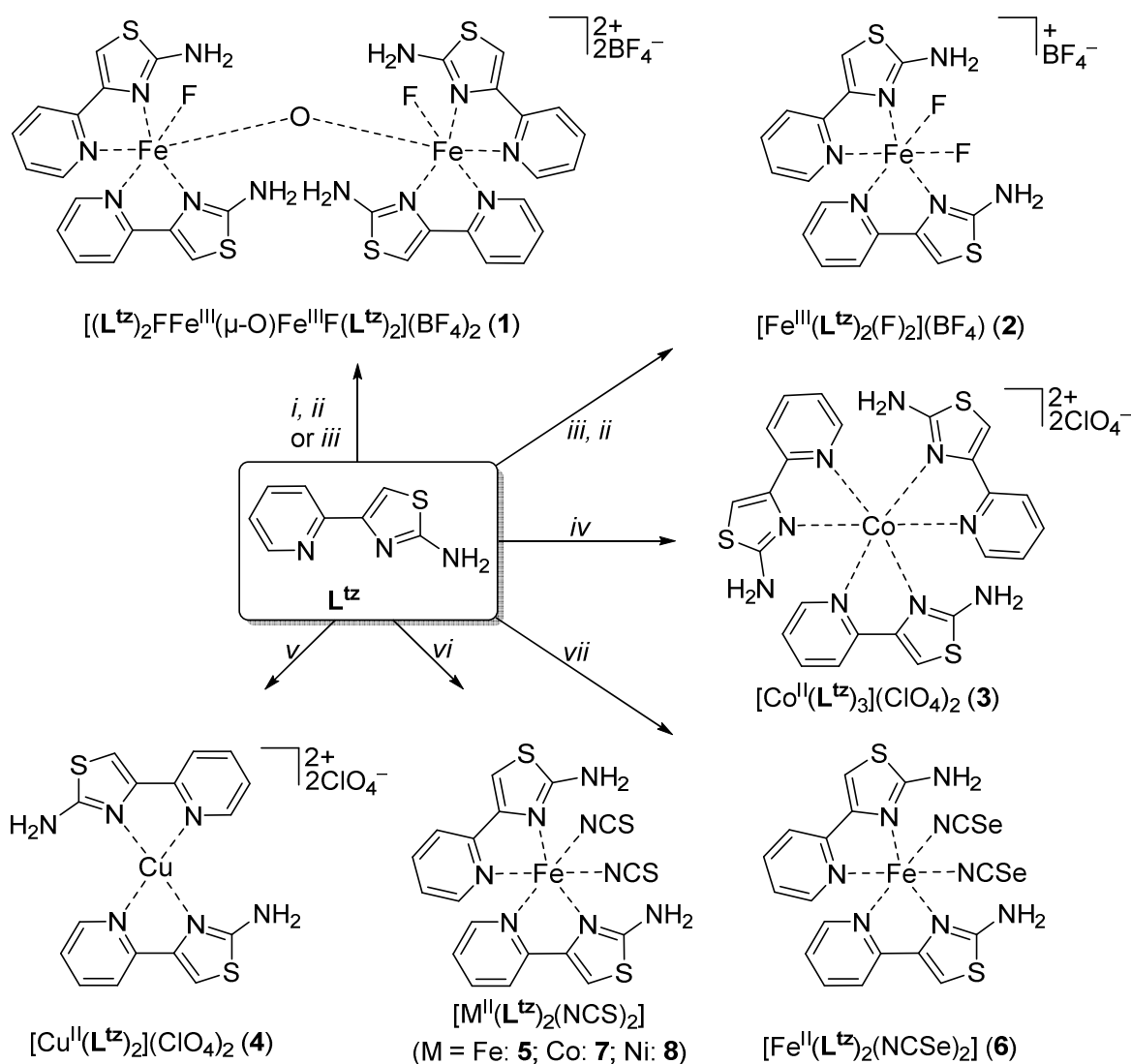


Figure 13: UV/Vis spectrum of L^{td} in MeOH 0.1 mm.

2.1.2 Complex Synthesis

Complexes with thiazole L^{tz}

In this section, complex syntheses with the thiazole ligand L^{tz} are presented. These results were published in: T. Huxel, S. Leone, Y. Lan, S. Demeshko, J. Klingele *Eur. J. Inorg. Chem* **2014**, 3114–3124.^[68]



Scheme 3: Synthesis of complexes $[(L^{tz})_2FFe^{III}(\mu-O)Fe^{III}F(L^{tz})_2](BF_4)_2$ (1), $[Fe^{III}(L^{tz})_2F_2](BF_4)$ (2), $[Co^{II}(L^{tz})_3](ClO_4)_2$ (3), $[Cu^{II}(L^{tz})_2](ClO_4)_2$ (4), $[Fe^{II}(L^{tz})_2(NCS)_2]$ (5), $[Fe^{II}(L^{tz})_2(NCSe)_2]$ (6), $[Co^{II}(L^{tz})_2(NCS)_2]$ (7) and $[Ni^{II}(L^{tz})_2(NCS)_2]$ (8). *i*) $Fe(BF_4)_2 \cdot 6H_2O$, MeCN; *ii*) TBME-vapour diffusion; *iii*) $Fe(BF_4)_2 \cdot 6H_2O$, MeOH; *iv*) $Co(ClO_4)_2 \cdot 6H_2O$, MeOH; *v*) $Cu(ClO_4)_2 \cdot 6H_2O$, MeOH; *vi*) " $M(NCS)_2$ ", MeOH; *vii*) " $Fe(NCSe)_2$ ", MeOH or MeCN.

As shown in the introduction, the thiazole ligands **IV** and **V** (Figure 3) form the 3:1-type SCO complexes $[Fe^{II}(\mathbf{IV})_3]X_2 \cdot nH_2O$ ($X = ClO_4$, $n = 1$: **F**; $X = BF_4$, $n = 0$) and $[Fe^{II}(\mathbf{V})_3]X_2$ ($X = ClO_4$: **G**, BF_4).^[24] In the view of this,

ligand L^{tz} has been reacted with $\text{Fe}(\text{BF}_4)_2 \cdot 6\text{H}_2\text{O}$ in a 3:1 molar ratio. Keeping the MeOH or MeCN reaction mixtures in an inert argon atmosphere for several days did not lead to the formation of any solid. Evaporation of the solvent in air led to the formation of red crystalline solids identified as $[(L^{\text{tz}})_2\text{FFe}^{\text{III}}(\mu\text{-O})\text{Fe}^{\text{III}}\text{F}(L^{\text{tz}})_2](\text{BF}_4)_2 \cdot 1.25\text{MeOH}$ (**1**·1.25MeOH, Figure 16) and **1**·MeCN, respectively by single crystal X-ray diffraction analyses (Scheme 3). For their characteristic spectroscopic and magnetic properties^[69,70] dinuclear μ -oxido-bridged ferric complexes like **1** have attracted much attention in the past. Furthermore, such complexes have also been extensively investigated in the area of bioinorganic chemistry including diiron non-heme proteins like hemeerythrin, methane monooxygenase, ribonucleotide reductase and purple acid phosphatases.^[69,71] Solvent free bulk material of **1** could be obtained from MeCN with help of TBME vapour diffusion and was used for further investigation of the magnetic properties. The formation of the oxido-bridged species was confirmed as well by mass spectrometry (Figure 14) and elemental analysis. The isotopic pattern with the main peak at $m/z = 437.0021$ certainly results from the $[(L^{\text{tz}})_2\text{FFe}^{\text{III}}(\mu\text{-O})\text{Fe}^{\text{III}}\text{F}(L^{\text{tz}})_2]^{2+}$ cation since it is in good agreement with the calculated isotopic pattern.

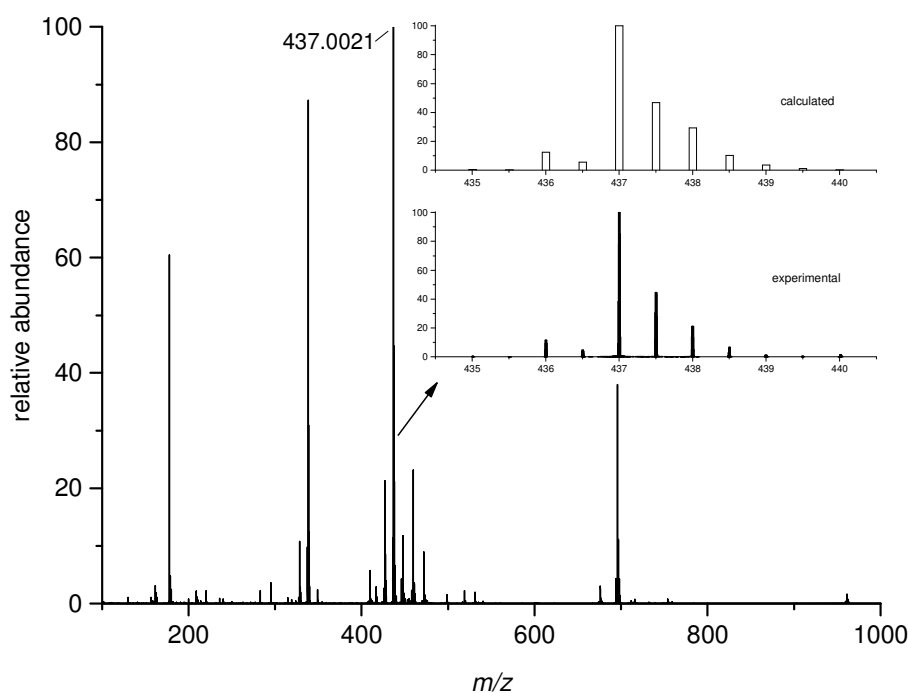


Figure 14: ESI-MS spectrum of $[(L^{\text{tz}})_2\text{FFe}^{\text{III}}(\mu\text{-O})\text{Fe}^{\text{III}}\text{F}(L^{\text{tz}})_2](\text{BF}_4)_2$ (**1**); inset: calculated (top) and experimental (bottom) isotopic pattern of $[(L^{\text{tz}})_2\text{FFe}^{\text{III}}(\mu\text{-O})\text{Fe}^{\text{III}}\text{F}(L^{\text{tz}})_2]^{2+}$.

However, application of TBME vapour diffusion in MeOH solution under otherwise identical reaction conditions lead to the formation of the mononuclear ferric complex $[\text{Fe}^{\text{III}}(\text{L}^{\text{tz}})_2(\text{F})_2](\text{BF}_4) \cdot 1.25\text{MeOH}$ (**2**·1.25MeOH), which was identified by X-ray diffraction analysis (Figure 17, Scheme 3). Drying of the crystals *in vacuo* led to analytically pure bulk material of **2**·1.5H₂O. The formation of a mononuclear complex could be confirmed by mass spectrometry as the isotopic pattern resulting from the complex cation $[\text{Fe}(\text{L}^{\text{tz}})_2\text{F}_2]^+$ is observed at $m/z = 448.0032$ (Figure 15). Surprisingly, fluoride has been abstracted from the tetrafluoroborate anion in both cases while iron(II) has been oxidised forming the latter mononuclear ferric complex **2** or the former dinuclear oxido-bridged ferric complex **1**, respectively. Both complexes also were prepared using the correct 2:1 ligand-to-metal salt stoichiometry, whereas no product could be obtained carrying out the respective reactions in an inert gas atmosphere. The observation that a tetrafluoroborate ion may react with ligand and metal ion, resulting in fluoride abstraction and metal coordination, was reported previously in several publications and was summarised by Reedijk in 1982.^[72]

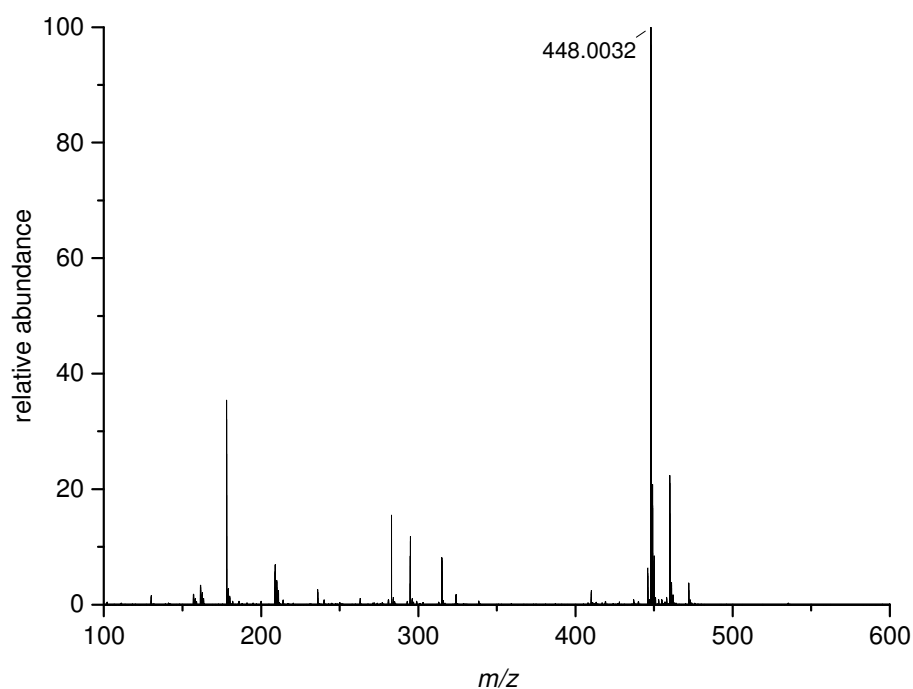


Figure 15: ESI-MS spectrum of $[\text{Fe}^{\text{III}}(\text{L}^{\text{tz}})_2(\text{F})_2](\text{BF}_4) \cdot 1.25\text{MeOH}$ (**2**·1.25MeOH).

Finally, a mononuclear 3:1-type complex of L^{tz} was obtained by reacting $\text{Co}(\text{ClO}_4)_2 \cdot 6\text{H}_2\text{O}$ with 3 equivalents of L^{tz} in MeOH. The resulting crystals were identified as $[\text{Co}^{\text{II}}(\text{L}^{\text{tz}})_3](\text{ClO}_4)_2 \cdot 1.5\text{MeOH} \cdot 0.25\text{H}_2\text{O}$ (**3**·1.5MeOH·0.25H₂O) by X-ray diffraction analysis (Figure 18, Scheme 3). Drying of the orange

crystalline solid *in vacuo* led to analytically pure bulk material of **3**·H₂O. Using Cu(ClO₄)₂·6H₂O under otherwise identical reaction conditions lead to the formation of the 2:1-type complex [Cu^{II}(L^{tz})₂](ClO₄)₂ (**4**, Scheme 3) which was identified by elemental analysis and mass spectrometry (Figure 118, appendix). However, no isolable compound formed using Ni(ClO₄)₂·6H₂O or Fe(ClO₄)₂·6H₂O.

Since SCO complexes of 2-pyridyl substituted azole ligands can also comprise the general formula [Fe^{II}(L)₂(NCX)₂] (X = S or Se), L^{tz} has been reacted with “Fe(NCS)₂” and “Fe(NCSe)₂” in 2:1 molar ratios. Two brown compounds, [Fe^{II}(L^{tz})₂(NCS)₂] (**5**, Figure 19) and [Fe^{II}(L^{tz})₂(NCSe)₂] (**6**, Figure 20), were obtained from MeOH and MeCN solution, respectively. Single crystal X-ray diffraction analyses revealed that both complexes comprise a *cis*-coordination^[12–14,21] of the coligands. Such a coordination mode has not been observed in the studies of the *Klingele* group with related ligands before but is not unknown to 2-pyridyl substituted azole based ligands.^[17] Thus, the complexes [Co^{II}(L^{tz})₂(NCS)₂] (**7**, Figure 21) and [Ni^{II}(L^{tz})₂(NCS)₂] (**8**, Figure 22) were prepared in MeOH solutions. In both cases, X-ray diffraction analyses of the obtained crystals exposed the same *cis*-coordination of the coligands.

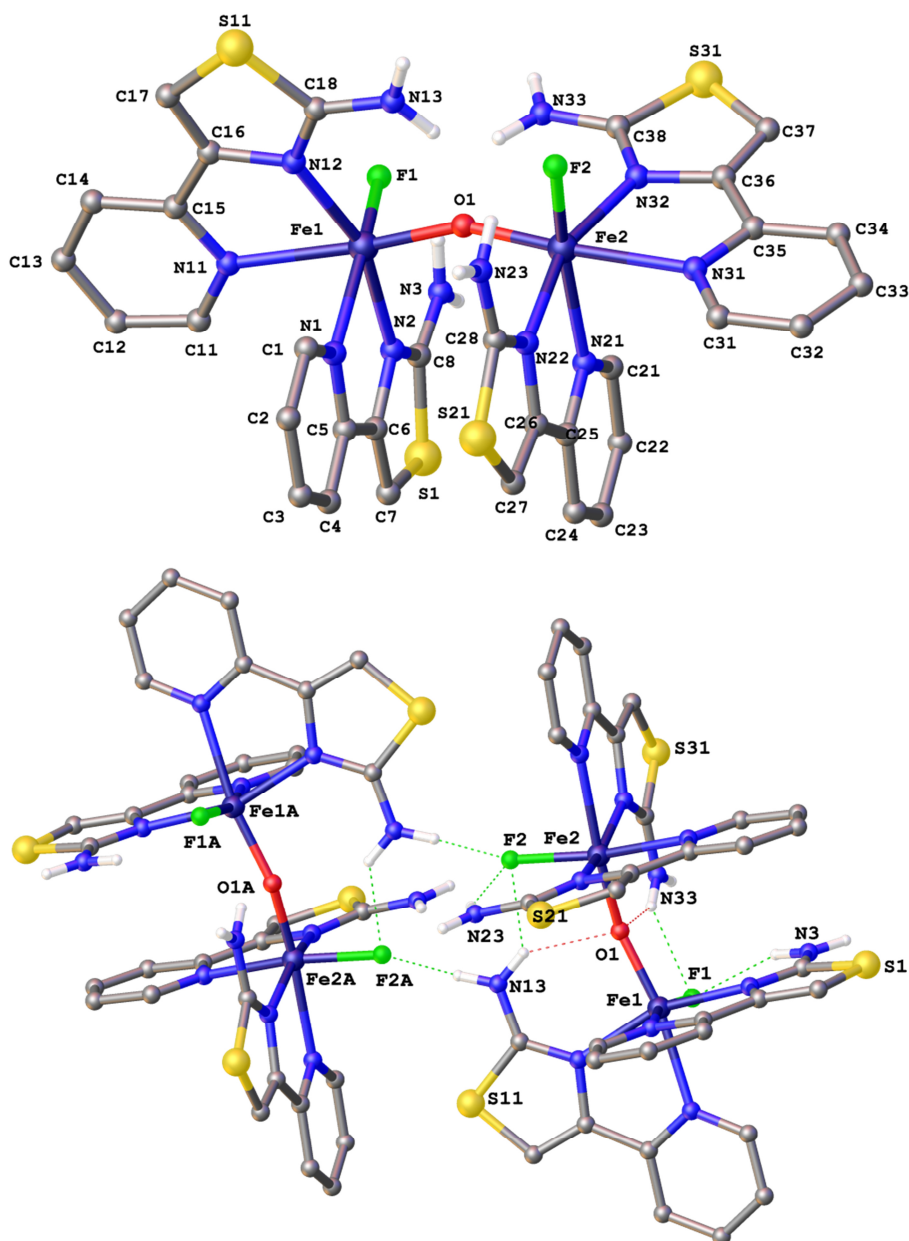


Figure 16: View of the *top*: molecular structure and *bottom*: hydrogen bonding motif of $[(L^{tz})_2Fe^III(\mu-O)Fe^III F(L^{tz})_2]^{2+}$, the complex cation of $[Fe^III_2(L^{tz})_4F_2(\mu-O)](BF_4)_2 \cdot 1.25MeOH$ ($1 \cdot 1.25MeOH$). H-atoms are omitted except for the ones of the amine groups.

Both dinuclear iron(III) complexes $[Fe^III_2(L^{tz})_4F_2(\mu-O)](BF_4)_2 \cdot 1.25MeOH$ ($1 \cdot 1.25MeOH$) and $1 \cdot MeCN$ crystallise in the triclinic space group $P\bar{1}$ with one complex cation, two tetrafluoroborate anions and partially occupied MeOH molecules cumulating to 1.25 or one fully occupied MeCN solvent molecule, respectively. The complex cations $[(L^{tz})_2Fe^III(\mu-O)Fe^III F(L^{tz})_2]^{2+}$ of both compounds are isostructural and feature two oxido-bridged $[Fe^III(L^{tz})_2F]$ -fragments with the ferric iron residing in distorted octahedral N_4OF coordination sphere (Figure 16). Within the fragment two chelating ligands L^{tz} are *cis*-coordinated.

The two fluorido coligands are coordinated *cis* to the oxido-bridge and in a staggered manner regarding the Fe–O–Fe moiety. The F–Fe⋯Fe–F torsion angles are 97.3(1)° (**1**·1.25MeOH) and 100.1(2)° (**1**·MeCN). This is in contrast to both other complexes with a [Fe^{III}N₄F(μ-O)FN₄Fe^{III}] entity known so far. In [(bpmen)FFe^{III}(μ-O)Fe^{III}F(bpmen)](ClO₄)₂ [73] (bpmen = *N,N'*-dimethyl-*N,N'*-bis(2-pyridylmethyl)ethane-1,2-diamine) and [(TPyA)FFe^{III}(μ-O)Fe^{III}F(TPyA)](BF₄)₂ (TPyA = tris(2-pyridylmethyl)amine), [74] a *trans* coordination of the two fluorido coligands regarding to the Fe–O–Fe-moiety is found. Furthermore, in similar complexes of bpmen with other monodentate coligands like chloride, [75,76] acetate [73] or fluoride/acetate, [73] or of TPyA and chloride [77] the coligands as well are usually coordinated *trans* regarding the Fe–O–Fe-moiety. However, a similar staggered coligand coordination is observed in the analogous oxido-bridged ferric complexes [(L)₂ClFe^{III}(μ-O)Fe^{III}Cl(L)₂]²⁺ with L being 2,2'-bipyridine [78] or 4,4'-dimethyl-2,2'-bipyridine. [79] The Fe–O–Fe entity in **1**·1.25MeOH (157.7(1)°) and **1**·MeCN (156.9(3)°) is unusually bend, in comparison to the before mentioned complexes of bpmen, [73,75,76] TPyA, [74,77] 2,2'-bipyridine [78] or 4,4'-dimethyl-2,2'-bipyridine [79], however it is within the range found for other Fe–O–Fe-bridged complexes. [69,70] The Fe^{III}–O bond lengths in both compounds **1**·1.25MeOH and **1**·MeCN are in the range of 1.806(4) – 1.825(2) Å, which are typical values for singly oxido-bridged ferric complexes. [69,70] The Fe^{III}–F bond lengths (1.893(2)–1.918(2) Å) are similar to those of the difluorido complexes of bpmen (1.843(3) Å) [73] and TPyA (1.849(2), 1.892(2) Å). [74] A small *trans* influence is found as the Fe^{III}–N_{py} distances *trans* to the oxido-bridge are a bit longer (2.267(3)–2.290(5) Å) than those *trans* to the fluorido coligands (2.170(3)–2.180(6) Å). Several intramolecular N–H⋯O and N–H⋯F bonds and an intermolecular –(N–H⋯F⋯H–N–H⋯F⋯H) ring motif are observed, the latter leading to the formation of dimers of the dinuclear complexes (Figure 16). In **1**·1.25MeOH those dimeric units are further connected by two S_{tz}⋯S_{tz} short contacts forming chains, whereas in **1**·MeCN a BF₄[–] anion blocks one of the sulphur atoms. Also intramolecular π–π-stacking is found in both complexes **1**·1.25MeOH and **1**·MeCN between the pyridyl ring being *trans* to the fluorido coligand and the thiazole ring of the corresponding ligand of the neighbouring half molecule. Inter- and intramolecular short contacts, H-bonds and π–π-stacking contacts are summarised in Table 2, crystallographic data are summarised in Table 18.

Table 2: Selected distances [Å] and angles [°] for [Fe^{III}(L^{tz})₂F₂(μ-O)](BF₄)₂·1.25MeOH (**1**·1.25MeOH) and **1**·MeCN.

	1 ·1.25MeOH ^[a]	1 ·MeCN ^[b]		1 ·1.25MeOH	1 ·MeCN
Fe1–N1	2.170(3)	2.170(6)	N1–Fe1–N2	75.90(10)	76.3(2)
Fe1–N2	2.124(2)	2.108(5)	N1–Fe1–N11	82.31(9)	82.31(18)
Fe1–N11	2.289(2)	2.290(5)	N1–Fe1–N12	94.98(10)	94.6(2)
Fe1–N12	2.111(2)	2.101(5)	N1–Fe1–F1	162.10(9)	163.18(19)
Fe1–F1	1.893(2)	1.900(4)	N1–Fe1–O1	95.23(9)	94.8(2)
Fe1–O1	1.825(2)	1.819(4)	N2–Fe1–N11	86.87(9)	87.22(19)
Fe2–N21	2.179(3)	2.180(6)	N2–Fe1–N12	160.28(9)	160.5(2)
Fe2–N22	2.134(3)	2.131(8)	N2–Fe1–F1	88.65(9)	89.6(2)
Fe2–N31	2.267(3)	2.283(8)	N2–Fe1–O1	101.77(9)	100.60(19)
Fe2–N32	2.112(3)	2.096(10)	N11–Fe1–N12	74.47(9)	74.33(18)
Fe2–F2	1.918(2)	1.911(4)	N11–Fe1–F1	87.94(8)	87.97(17)
Fe2–O1	1.815(2)	1.806(4)	N11–Fe1–O1	170.22(9)	170.80(18)
			N12–Fe1–F1	96.83(9)	95.92(17)
N3–H...F1	2.731	2.711	N12–Fe1–O1	96.39(9)	97.31(19)
N13–H...O1	2.922	2.911	F1–Fe1–O1	96.76(9)	96.85(19)
N13–H...F2	2.851	2.871	N21–Fe2–N22	75.92(11)	76.1(3)
N23–H...O1	2.974	-/-	N21–Fe2–N31	83.26(10)	83.8(2)
N33–H...O1	-/-	2.962	N21–Fe2–N32	93.61(11)	92.2(3)
N23–H...F2	2.788	2.797	N21–Fe2–F2	162.96(10)	163.3(3)
N33–H...F1	2.829	2.843	N21–Fe2–O1	95.59(9)	96.7(2)
N13–H...F2A	2.746	2.731	N22–Fe2–N31	87.05(11)	86.3(3)
N3–H...F14	3.153	-/-	N22–Fe2–N32	160.36(11)	159.1(3)
N33–H...F14B	-/-	3.028	N22–Fe2–F2	90.39(10)	91.0(3)
N3–H...O50B	2.883	-/-	N22–Fe2–O1	100.23(10)	100.7(2)
N33–H...F12	2.929	-/-	N31–Fe2–N32	75.10(11)	75.1(4)
S1...S1C	3.437(2)	3.420(4)	N31–Fe2–F2	86.00(9)	84.76(19)
S21...S21D	3.475(2)	-/-	N31–Fe2–O1	172.15(10)	173.0(3)
S21...F23D	-/-	3.15(1)	N32–Fe2–F2	96.36(10)	96.5(3)
C _{py1} ...C _{tz2} ^[c]	3.508	3.439	N32–Fe2–O1	97.26(10)	97.9(3)
C _{py2} ...C _{tz1} ^[c]	3.548	3.489	F2–Fe2–O1	96.81(8)	96.22(19)
			Fe1–O1–Fe2	157.72(13)	156.9(3)

^[a] Symmetry operations used to generate equivalent atoms: A) $-x + 1, -y + 2, -z + 1$; B) $-x + 2, -y + 2, -z$; C) $-x + 2, -y + 1, -z$; D) $-x + 2, -y + 2, -z + 1$.

^[b] Symmetry operations used to generate equivalent atoms: A) $-x + 2, -y + 1, -z + 1$; B) $x + 1, y, z$; C) $-x + 1, -y + 2, -z + 2$; D) $-x + 1, -y + 1, -z + 1$.

^[c] C_{py1}: centroid{C1/C2/C3/C4/C5/N1}; C_{py2}: centroid{C21/C22/C23/C24/C25/N21}; C_{tz1}: centroid{C6/(7/S1/C8/N2)}; C_{tz2}: centroid{C27/C28/S21/C28/N22}.

The mononuclear iron(III) complex [Fe^{III}(L^{tz})₂F₂](BF₄)·1.5H₂O (**2**·1.5H₂O) crystallises in the monoclinic space group *P2₁/a*. The asymmetric unit consists of two isostructural [Fe(L^{tz})₂(F)₂]⁺ complex cations, two disordered tetrafluoroborate anions and three water molecules. The iron(III) ion is coordinated in a distorted octahedral manner with a N₄F₂ coordination sphere. The bidentate chelating ligands L^{tz} are *cis* coordinated, with the N_{py} atoms being *cis* and the N_{tz} atoms being *trans* to each other. The two fluoride coligands are *trans* to the N_{py} atoms (Figure 17). Both coligands comprise N–H...F hydrogen bonds. The amine groups are further H-bonded to the BF₄[−] anion and solvent molecules (Table 16, appendix). A chain-like structure caused by intermolecular π–π stacking between symmetry generated molecules

around Fe1 can be observed. The second cationic complex of the asymmetric unit provides a similar π - π stacking motif (Table 16, appendix). Searching for the FeN_4F_2 fragment at the Cambridge Crystallographic Data Centre [80] led to overall 6 structures. None of them comprise bidentate N_2 -ligands or *cis* coordinate F^- coligands. The Fe^{III} -F distances in $\mathbf{2}\cdot 1.5\text{H}_2\text{O}$ (1.854(1)–1.873(1) Å), are similar to those of $\mathbf{1}\cdot 1.25\text{MeOH}$ and $\mathbf{1}\cdot \text{MeCN}$. This extends to the Fe^{III} -N bond lengths with Fe^{III} - N_{py} distances ranging from 2.151(2)–2.211(2) Å and Fe^{III} - N_{tz} distances from 2.087(2)–2.124(2) Å. Table 19 (appendix) summarises the crystallographic data for the above mentioned complex, selected distances and angles are summarised in Table 3.

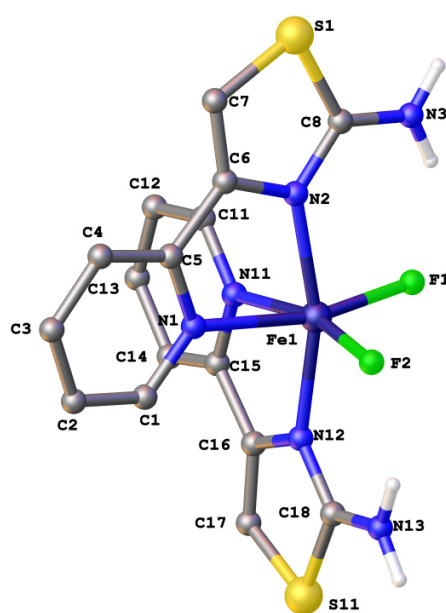


Figure 17: View of the molecular structure of $[\text{Fe}^{\text{III}}(\text{L}^{\text{tz}})_2\text{F}_2]^+$, the complex cation of $\mathbf{2}\cdot 1.5\text{H}_2\text{O}$. Only one complex cation of the two found in the asymmetric unit is shown. H-atoms are omitted except for the ones of the amine groups.

The 3:1-type cobalt(II) complex $[\text{Co}^{\text{II}}(\text{L}^{\text{tz}})_3](\text{ClO}_4)_2\cdot 1.5\text{MeOH}\cdot 0.25\text{H}_2\text{O}$ ($\mathbf{3}\cdot 1.5\text{MeOH}\cdot 0.25\text{H}_2\text{O}$) crystallises in the space group $P2_1/c$. The asymmetric unit consists of one complex cation, two perchlorate counterions and partially occupied solvent molecules cumulating to 1.5MeOH and 0.25H₂O. The cobalt(II) ion is coordinated by three bidentate L^{tz} ligands building up a distorted octahedral N_6 coordination sphere. One of the ligands is disordered in its relative position so that about 78 % of a *fac* isomer and 22 % of a *mer* isomer share the total site occupation. The Co^{II} - N_{py} bond lengths in $\mathbf{3}\cdot 1.5\text{MeOH}\cdot 0.25\text{H}_2\text{O}$ are in the range of 2.107(8)–2.17(3) Å, whereas the Co^{II} - N_{tz} distances lie in the range of 2.127(7)–2.34(2) Å, all typical values for a cobalt(II) HS species. [7] Table 19 summarises the crystallographic data for the above mentioned complexes, selected distances and angles are summarised in Table 3.

Complexes with 2-Pyridyl and Amino Substituted Azoles

Table 3: Selected distances [Å] and angles [°] for [Fe^{III}(L^{tz})₂F₂](BF₄)·1.5H₂O (**2**·1.5H₂O) and [Co^{II}(L^{tz})₃](ClO₄)₂·1.5MeOH·0.25H₂O (**3**·1.5MeOH·0.25H₂O).

	2 ·1.5H ₂ O (M = Fe ^{III}) ^[a]	3 ·1.5MeOH·0.25H ₂ O (M = Co ^{II}) ^[b]
M1–N1	2.211(2) / 2.191(2)	2.107(8) [2.17(3)]
M1–N2	2.0866(19) / 2.1237(19)	2.127(7) [2.34(2)]
M1–N11	2.188(2) / 2.151(2)	2.145(2)
M1–12	2.0892(19) / 2.0959(19)	2.155(2)
Fe1–F1	1.8618(14) / 1.8729(14)	-/-
Fe1–F2	1.8634(14) / 1.8538(14)	-/-
Co1–N21	-/-	2.122(2)
Co1–N22	-/-	2.151(2)
N1–M1–N2	75.71(8) / 74.98(7)	78.7(3) [74.0(7)]
N1–Co1–N1A	-/-	[71.3(7)]
N2–Co1–N2A	-/-	[81.6(6)]
N1–M1–N11	84.39(8) / 82.78(7)	94.1(3) [86.6(9)]
N1–M1–N12	92.29(7) / 96.58(7)	171.2(3) [105.1(6)]
N1–Fe1–F1	166.71(7) / 163.19(7)	-/-
N1–Fe1–F2	88.83(7) / 89.60(7)	-/-
N1–Co1–N21	-/-	93.1(2) [71.3(7)]
N1–Co1–N22	-/-	91.2(3) [99.3(9)]
N2–M1–N11	92.62(8) / 95.99(8)	89.5(3) [90.3(10)]
N2–M1–N12	164.25(9) / 169.55(9)	98.3(2) [167.8(10)]
N2–Fe1–F1	92.25(7) / 89.94(7)	-/-
N2–Fe1–F2	97.97(7) / 95.98(7)	-/-
N2–Co1–N21	-/-	169.5(3) [90.7(6)]
N2–Co1–N22	-/-	96.0(3) [94.7(10)]
N11–M1–N12	75.84(8) / 76.57(7)	77.50(9)
N11–Fe1–F1	90.68(7) / 91.64(7)	-/-
N11–Fe1–F2	165.63(7) / 163.64(7)	-/-
N11–Co1–N21	-/-	97.73(9)
N11–Co1–N22	-/-	173.06(9)
N12–Fe1–F1	98.47(7) / 97.52(7)	-/-
N12–Fe1–F2	91.84(7) / 90.02(7)	-/-
N12–Co1–N21	-/-	90.74(9)
N12–Co1–N22	-/-	97.38(9)
F1–Fe1–F2	98.55(7) / 99.48(7)	-/-
N21–Co1–N22	-/-	77.50(9)

^[a] the second value describes the second complex cation found in the asymmetric unit [Fe2, C21–C28, C31–C38, N21–N23, N31–N33, S21, S31, F3 and F4].

^[b] minor part of the disordered ligand in brackets

The molecular structures of the 2:1-type complexes **5–8** (Figure 19 – Figure 22) are very similar. All structures provide asymmetric units consisting of one bidentate L^{tz} , one coligand NCX ($X = S, Se$) and a metal ion ($Fe^{II}, Co^{II}, Ni^{II}$) with an occupancy of 0.5. The metal(II) ions are distorted octahedrally coordinated residing in an N_6 coordination sphere. The bidentate ligands are *cis* coordinated with the N_{tz} atoms being *trans* to each other, whereas the N_{py} atoms are *cis* to each other and *trans* to the coligands NCX ($X = S, Se$). In **5**, the NCS^- coligand is disordered and the sulphur atom occupies two sites with the major part featuring a site occupancy of 0.80 and leading to an $N-C-S$ -angle of $177.8(3)^\circ$, whereas the $N-C-S$ -angle in the minor part is $173.3(15)^\circ$. The $M-N$ bond lengths in **5–8** follow the sequence $Fe(II) > Co(II) > Ni(II)$, as expected. The $Fe-N$ distances in **5** and **6** are in the range of $2.144(3)$ – $2.196(3)$ Å and $2.155(4)$ – $2.190(4)$ Å, respectively, which are typical values for an iron(II) ion in the HS state.^[81] The $Co-N$ bond lengths in **7** are in the range of $2.110(3)$ – $2.141(3)$ Å, which are typical values for a HS $Co(II)$.^[7] Intermolecular $S_{tz} \cdots S_{tz}$ and $S_{NCS} \cdots S_{NCS}$ (**5, 7, 8**) or $Se_{NCS_e} \cdots Se_{NCS_e}$ (**6**) short contacts are present in the crystal packing of **5–8**. Crystallographic data for $[Fe^{II}(L^{tz})_2(NCS)_2]$ (**5**), $[Fe^{II}(L^{tz})_2(NCSe)_2]$ (**6**) and $[Co^{II}(L^{tz})_2(NCS)_2]$ (**7**), $[Ni^{II}(L^{tz})_2(NCS)_2]$ (**8**) are summarised in Table 20 (appendix) and Table 21 (appendix), respectively, selected distances and angles are presented in Table 4, $S \cdots S$ and $Se \cdots Se$ short contacts are summarised in Table 17 (appendix).

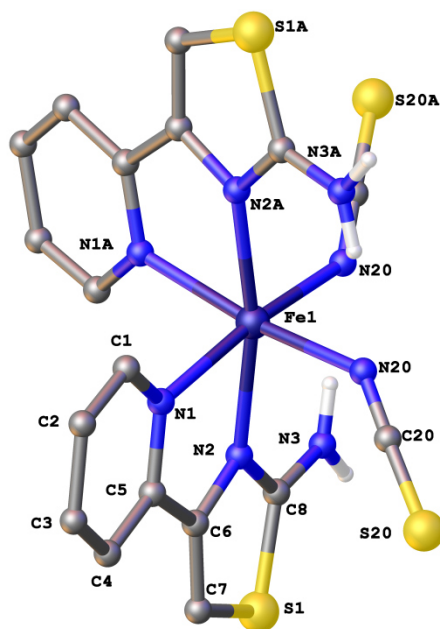


Figure 19: View of the molecular structure of $[Fe^{II}(L^{tz})_2(NCS)_2]$ (**5**). Minor occupancy part of the disordered NCS coligand is not shown. H-atoms are omitted except for the ones of the amine groups. Symmetry operation used to generate equivalent atoms: A) $-x + 1, y, 0.5 - z$.

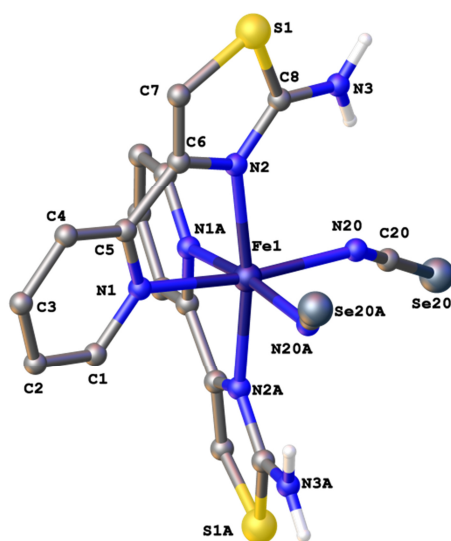


Figure 20: View of the molecular structure of $[\text{Fe}^{\text{II}}(\text{L}^{\text{tz}})_2(\text{NCSe})_2]$ (**6**). H-atoms are omitted except for the ones of the amine groups. Symmetry operation used to generate equivalent atoms: A) $-x, y, 0.5 - z$.

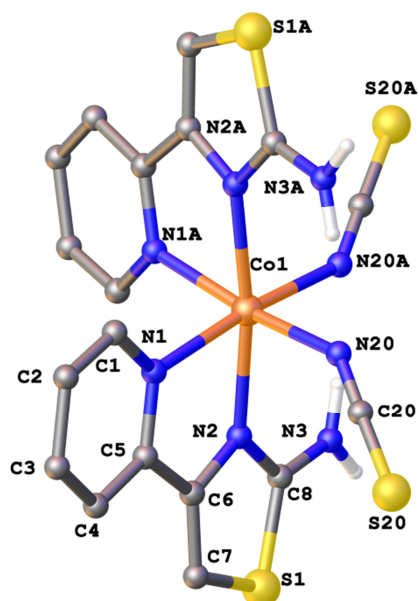


Figure 21: View of the molecular structures of $[\text{Co}^{\text{II}}(\text{L}^{\text{tz}})_2(\text{NCS})_2]$ (**7**). H-atoms are omitted except for the ones of the amine groups. Symmetry operation used to generate equivalent atoms: A) $-x + 1, y, 0.5 - z$.

The Mössbauer spectrum of $[(L^{tz})_2Fe^{III}F(\mu-O)FFe^{III}(L^{tz})_2](BF_4)_2$ (**1**) (recorded at 80 K) shows a symmetrical doublet with an isomeric shift $\delta = 0.48 \text{ mm s}^{-1}$ and small quadrupole splitting $\Delta E_Q = 1.08 \text{ mm s}^{-1}$ which are both typical values for a HS ferric complex.^[82,83] These observations could be confirmed by temperature dependent measurements of the magnetic susceptibility in the range of 295–2 K (Figure 23). The $\chi_M T$ value at 295 K ($1.08 \text{ cm}^3 \text{ mol}^{-1} \text{ K}$) is higher than the spin-only value ($0.75 \text{ cm}^3 \text{ mol}^{-1} \text{ K}$) expected for two independent iron(III) sites in the LS state, but considerably lower than the spin-only value ($8.75 \text{ cm}^3 \text{ mol}^{-1} \text{ K}$) expected for two independent iron(III) sites in the HS ($S = 5/2$) state, hence suggesting strong antiferromagnetic interactions within the $Fe^{III}-O-Fe^{III}$ entity. Upon lowering the temperature the magnetic susceptibility decreases until reaching a plateau at about 35 K and $\chi_M T = 0.07 \text{ cm}^3 \text{ mol}^{-1} \text{ K}$, indicating again antiferromagnetic coupling and the presence of a small amount of uncoupled paramagnetic impurities. Analysis of the magnetic data using the isotropic Heisenberg–Dirac–van Vleck (HDvV) exchange Hamiltonian that includes additional term for Zeeman splitting (Equation 1) indeed leads to a good fit with values $g = 2.02$, $J = -88 \text{ cm}^{-1}$, $PI = 1.6 \%$ and $TIP = 33 \cdot 10^{-6} \text{ cm}^3 \text{ mol}^{-1}$.

$$\hat{H} = -2J\hat{S}_1\hat{S}_2 + \sum_{i=1}^2 g\mu_B\vec{B} \cdot \vec{S}_i \quad \text{Equation 1}$$

The J value indicates strong antiferromagnetic interactions and lies in the range of experimental values for oxido bridged dinuclear iron(III) complexes of $J = -80$ to -130 cm^{-1} .^[69,70,74]

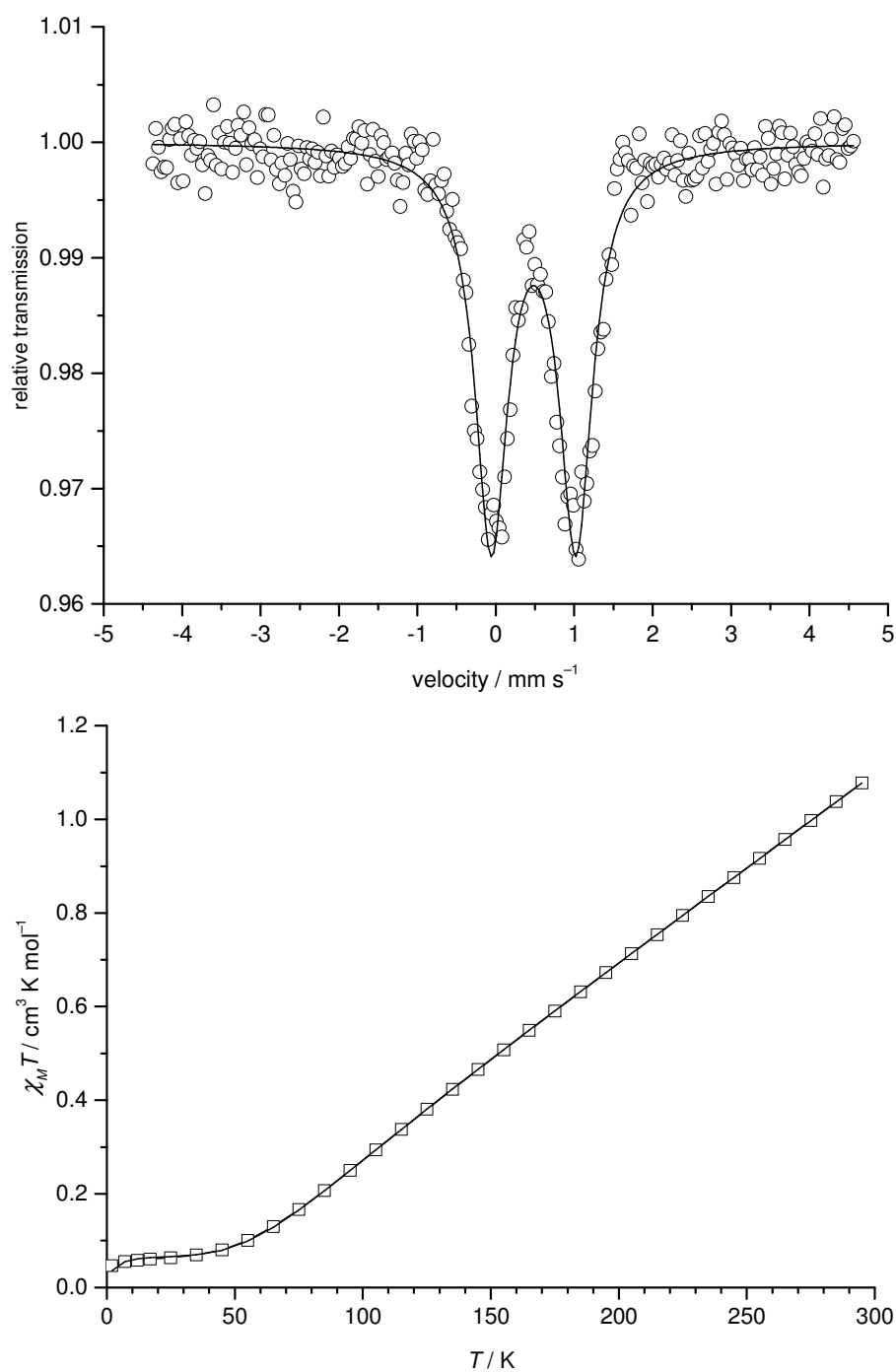


Figure 23: *top:* Mössbauer spectrum of $[(L^{tz})_2Fe^{III}(\mu-O)Fe^{III}F(L^{tz})_2](BF_4)_2$ (**1**) recorded at 80 K. The line represents fitting with Lorentzian doublet. *bottom:* $\chi_M T$ vs. T plot of **1**. The solid line represents the best fit (see text).

Mössbauer spectra of $[\text{Fe}^{\text{III}}(\text{L}^{\text{tz}})_2\text{F}_2](\text{BF}_4)\cdot 1.5\text{H}_2\text{O}$ (**2** $\cdot 1.5\text{H}_2\text{O}$) were recorded at 7, 80 and 200 K and show broad singlets with isomeric shifts in the range of $\delta = 0.31\text{--}0.38 \text{ mm s}^{-1}$ which are typical values for iron(III) compounds (Figure 24).^[82,83] Presumably due to slow paramagnetic relaxation, no quadrupole splitting is observed at any temperature. The lowering of line widths (I) to higher temperatures ($I = 1.74 \text{ mm s}^{-1}$ at 7 K, $I = 1.72 \text{ mm s}^{-1}$ at 80 K and $I = 1.44 \text{ mm s}^{-1}$ at 200 K) additionally confirms the presence of the slow paramagnetic relaxations, since the spin-lattice relaxation becomes faster. Thus, the iron(III) ion is supposed to be in the HS state ($S = 5/2$) at all temperatures. Measurements of the magnetic susceptibility recorded for the same compound over the temperature range of 295–2 K confirmed this suggestion (Figure 24). At 295 K, the $\chi_{\text{M}}T$ value for **2** $\cdot 1.5\text{H}_2\text{O}$ ($4.37 \text{ cm}^3 \text{ mol}^{-1} \text{ K}$) is close to the spin-only value for $S = 5/2$ HS iron(III) ($4.375 \text{ cm}^3 \text{ mol}^{-1} \text{ K}$). Data analysis using a fitting procedure to the spin Hamiltonian for zero-field splitting and Zeeman interaction (Equation 2) and including a term for temperature independent paramagnetism (TIP) provided values $g = 2.0$, $|D| = 1.2 \text{ cm}^{-1}$ and $TIP = 106 \cdot 10^{-6} \text{ cm}^3 \text{ mol}^{-1}$.

$$\hat{H} = D(\hat{S}_z^2 - \frac{1}{3}S(S+1)) + g\mu_B\vec{B} \cdot \vec{S} \quad \text{Equation 2}$$

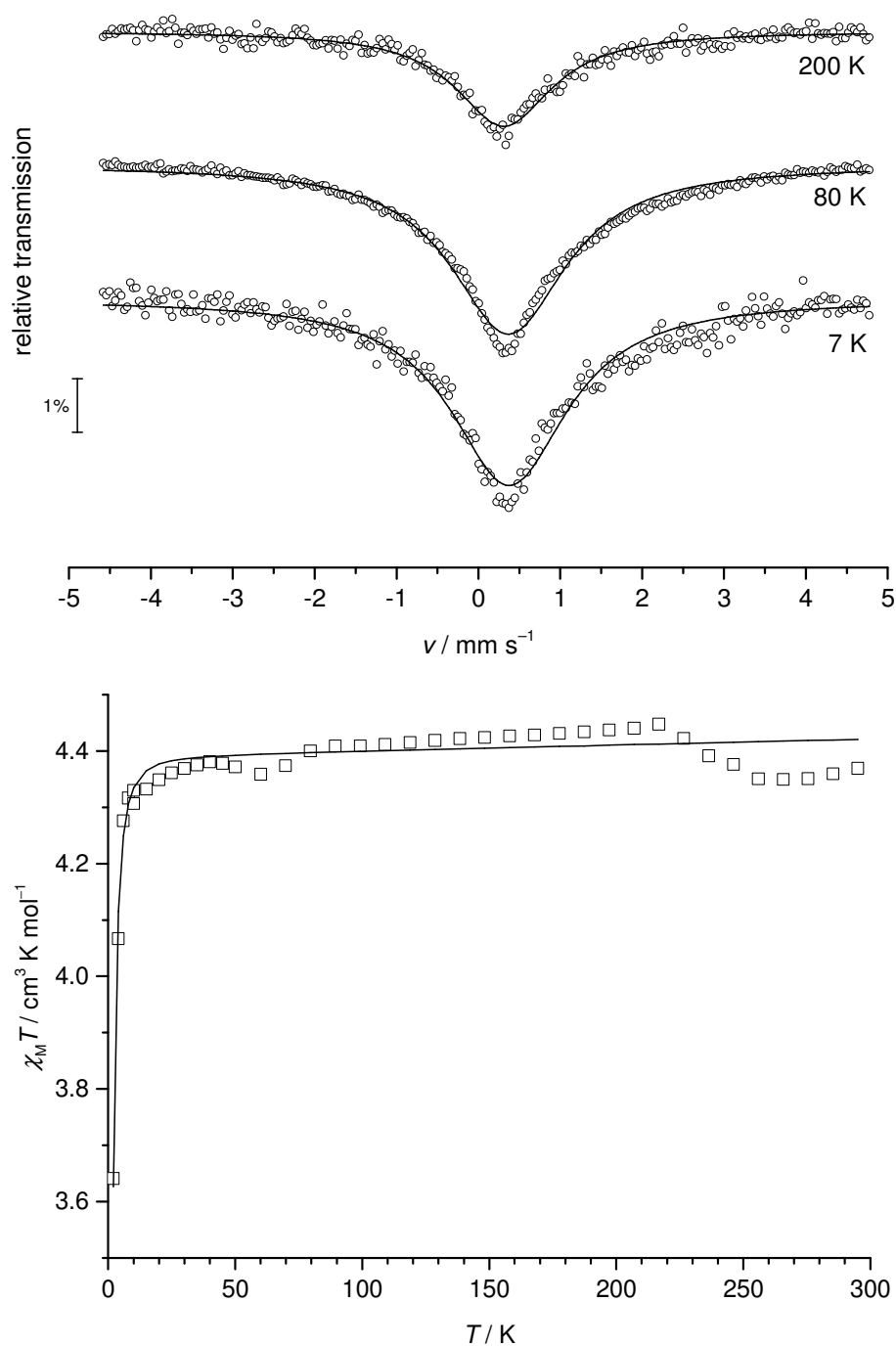


Figure 24: *top:* Mössbauer spectrum of $[\text{Fe}^{\text{III}}(\text{L}^{\text{tz}})_2\text{F}_2](\text{BF}_4) \cdot 1.5\text{H}_2\text{O}$ ($2 \cdot 1.5\text{H}_2\text{O}$), recorded at 7, 80 and 200 K. The lines represent simulations with Lorentzian singlets; *bottom:* $\chi_M T$ vs. T plot of $2 \cdot 1.5\text{H}_2\text{O}$. The solid line represents the best fit (see text).

Both compounds $[\text{Fe}(\text{L}^{\text{tz}})_2(\text{NCS})_2]$ (**5**) and $[\text{Fe}(\text{L}^{\text{tz}})_2(\text{NCSe})_2]$ (**6**) comprise the iron(II) ion in the HS state, as determined by magnetic measurements (Figure 25) and Mössbauer spectroscopy (Figure 26), respectively. At 300 K for **5** the value of $\chi_M T = 4.08 \text{ cm}^3 \text{ mol}^{-1} \text{ K}$ is higher than the spin-only value for a HS iron(II) ($S = 2$; $3.00 \text{ cm}^3 \text{ mol}^{-1} \text{ K}$). However, it is not unexpected as g values for iron(II) are often larger than $g = 2.0$ for the free electron. With a g value of 2.33, a susceptibility value of $\chi_M T = 4.07 \text{ cm}^3 \text{ mol}^{-1} \text{ K}$ is expected. On lowering the temperature, the $\chi_M T$ values remain constant until 80 K, then decrease more and more rapidly to finally reach $1.17 \text{ cm}^3 \text{ mol}^{-1} \text{ K}$ at 1.9 K, indicating large zero field splitting. Data analysis using a fitting procedure to the spin Hamiltonian for axial (D) and rhombic (E) zero-field splitting and Zeeman interaction indeed (Equation 3) provided values $g = 2.33$, $|D| = 17.1 \text{ cm}^{-1}$ and $|E/D| = 0.29$.

$$\hat{H} = D \left[(\hat{S}_z^2 - \frac{1}{3} S(S+1)) + \frac{E}{D} (\hat{S}_x^2 - \hat{S}_y^2) \right] + g \mu_B \vec{B} \cdot \vec{S} \quad \text{Equation 3}$$

The Mössbauer spectrum of **6** (recorded at 8 K) holds a doublet with an isomeric shift of $\delta = 1.15 \text{ mm s}^{-1}$ and a large quadrupole splitting of 1.84 mm s^{-1} which are both typical values for an iron(II) HS complex.

[82,83]

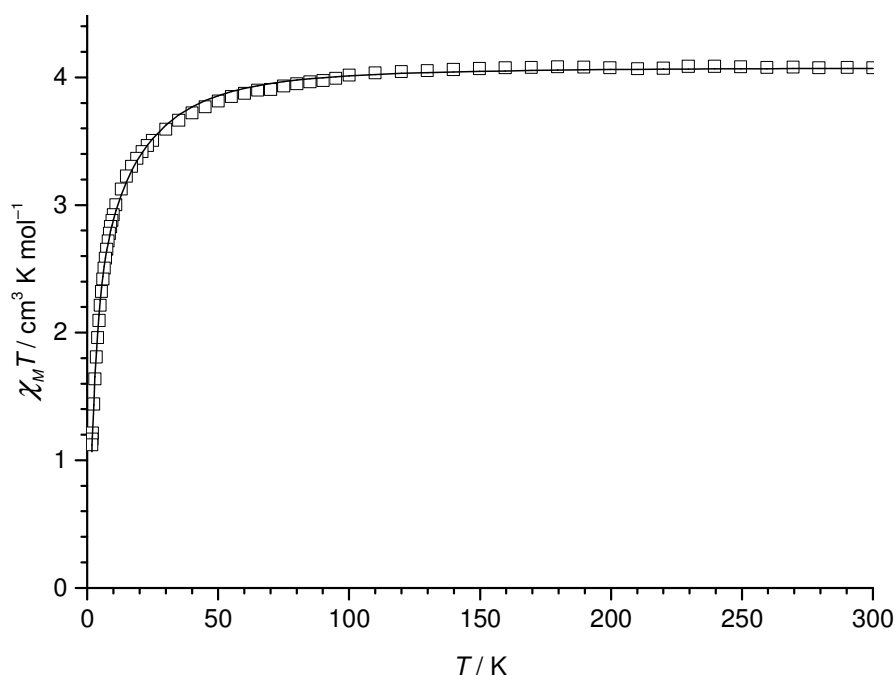


Figure 25: $\chi_M T$ vs. T plot of $[\text{Fe}(\text{L}^{\text{tz}})_2(\text{NCS})_2]$ (**5**). The solid line represents the best fit (see text).

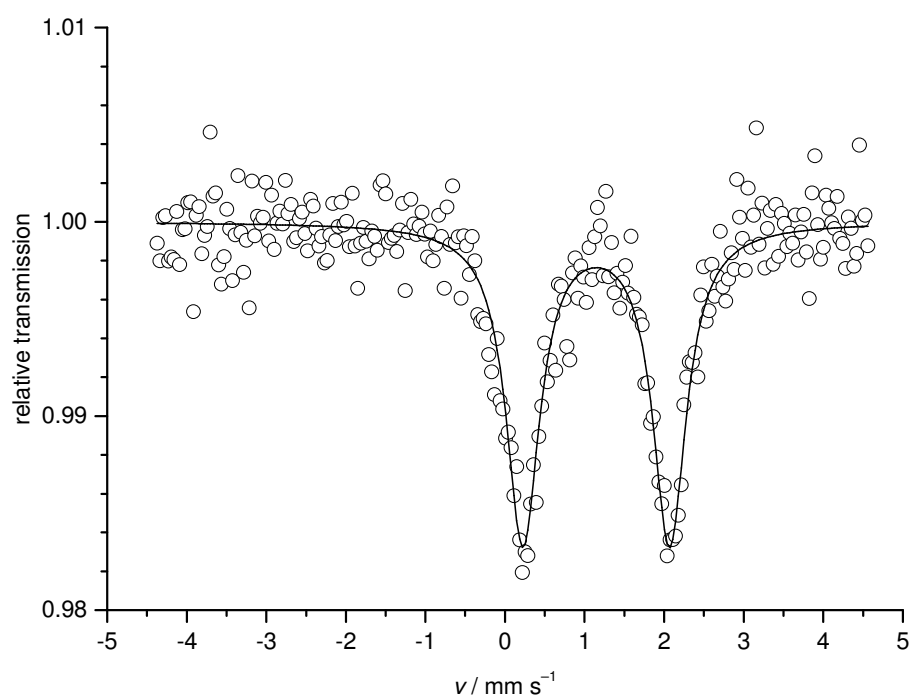
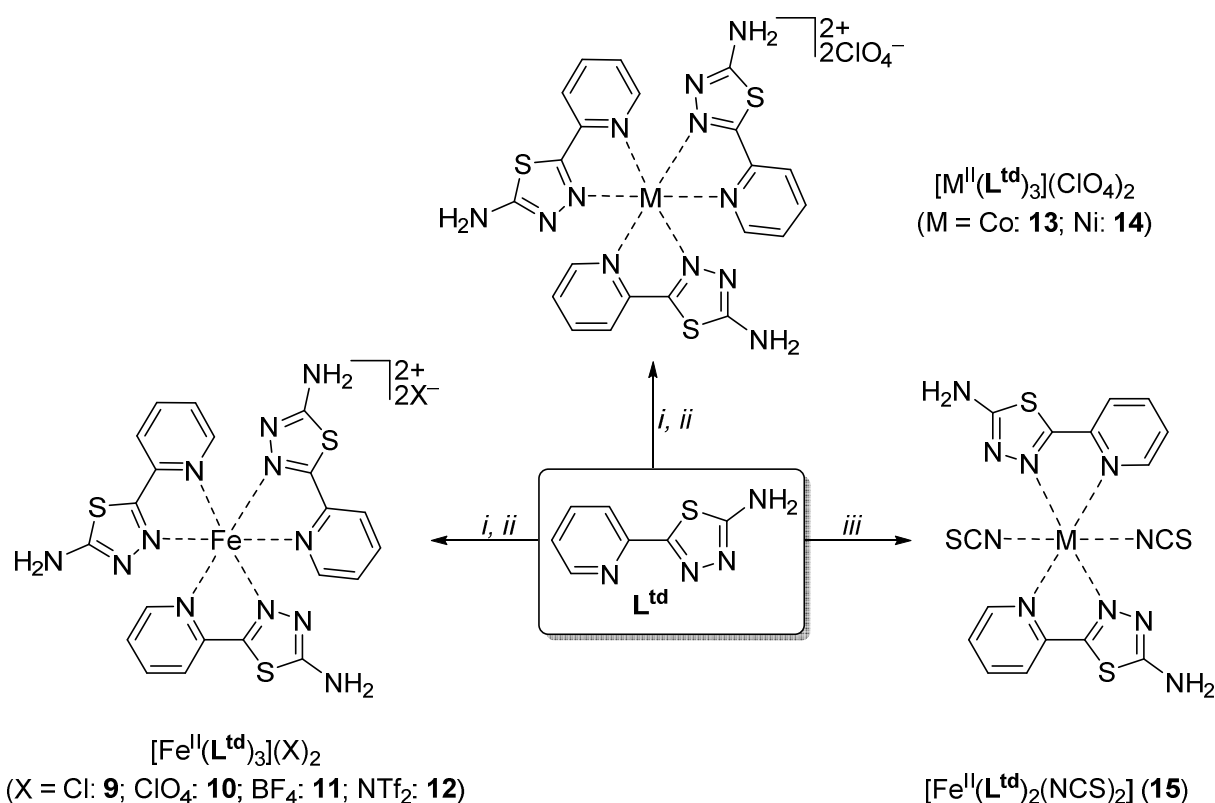


Figure 26: Mössbauer spectrum of $[\text{Fe}^{\text{II}}(\text{L}^{\text{tz}})_2(\text{NCSe})_2]$ (**6**), recorded at 8 K. The line represents fitting with Lorentzian doublet.

Complexes with thiadiazole L^{td}

In this section, complex syntheses with the thiadiazole ligand L^{td} are presented. In the light of the 2:1-type SCO complexes **A–E** ^[12–14] (Figure 2, Introduction), complexations with L^{td} were carried out in a 2:1 molar ratio. Apart from such $[Fe^{II}(L)_2(NCX)_2]$ (L = bidentate chelate and X = S or Se) complexes, SCO complexes of 2-pyridyl substituted azole ligands often follow the composition $[Fe(L)_3]X_2$ (L = bidentate chelate and X = non-coordinating anion). Therefore complexations with L^{td} also were carried out in a 3:1 molar ratio.



Scheme 4: Synthesis of complexes $[Fe^{II}(L^{td})_3](ClO_4)_2$ (**10**), $[Fe^{II}(L^{td})_3](BF_4)_2$ (**11**), $[Fe^{II}(L^{td})_3]Cl_2$ (**9**), $[Fe^{II}(L^{td})_3](NTf_2)_2$ (**12**), $[Co^{II}(L^{td})_3](ClO_4)_2$ (**13**), $[Ni^{II}(L^{td})_3](ClO_4)_2$ (**14**), $[Fe^{II}(L^{td})_2(NCS)_2]$ (**15**). *i*) $FeX_2 \cdot 6H_2O$ (X = ClO_4 , BF_4 , NTf_2) or $FeCl_2 \cdot 4H_2O$ or $M(ClO_4)_2 \cdot 6H_2O$ (M = Co, Ni); *ii*) MeOH; *iii*) “ $Fe(NCS)_2$ ”, MeCN.

Complexations of L^{td} with $Fe(ClO_4)_2 \cdot 6H_2O$ or $Fe(BF_4)_2 \cdot 6H_2O$ in MeOH using a molar stoichiometry of 3:1 (Scheme 4), resulted in dark red reaction solutions and subsequent precipitation of red crystalline materials. The compounds $[Fe^{II}(L^{td})_3](ClO_4)_2 \cdot 0.625MeOH \cdot 0.875H_2O$ (**10**·0.625MeOH·0.875H₂O, Figure 34) and $[Fe^{II}(L^{td})_3](BF_4)_2 \cdot MeOH \cdot H_2O$ (**11**·MeOH·H₂O, Figure 35) were identified by single crystal X-ray diffraction analyses. Compound **10**·0.625MeOH·0.875H₂O crystallises as 1:1 mixture of *mer* and *fac* isomer, whereas only the *mer* complex is found in **11**·MeOH·H₂O. Analytically pure bulk material of

10·2H₂O and **11**·2H₂O were obtained by drying the respective crystalline material *in vacuo*. The red chloride and triflimide compounds [Fe^{II}(L^{td})₃]Cl₂ (**9**) and [Fe^{II}(L^{td})₃](NTf₂)₂·H₂O (**12**·H₂O) (Scheme 4) could not be obtained crystalline, but their compositions were reassured by elemental analysis and mass spectrometry. The mass spectrum of the chloride compound **9** shows a peak at $m/z = 295.0137$ which presumably results from the [Fe^{II}(L^{td})₃]²⁺ dication (Figure 27). The analogous peak is very small in the mass spectrum of the triflimide compound **12**·H₂O. However, a peak assumedly resulting from the fragment [Fe^{II}(L^{td})₂NTf₂]⁺ can be seen at $m/z = 691.9148$ (Figure 120, appendix).

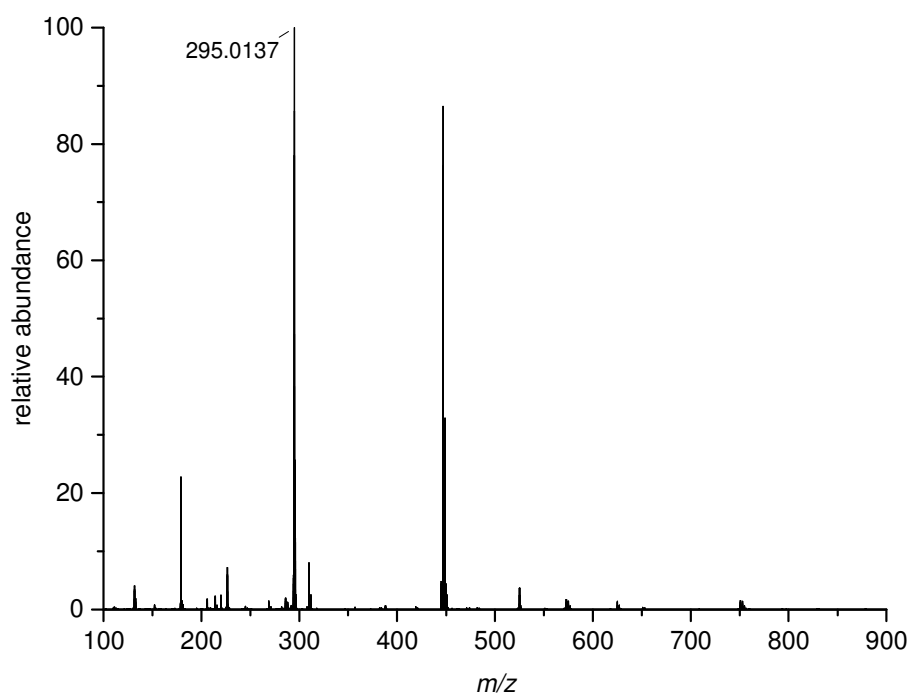
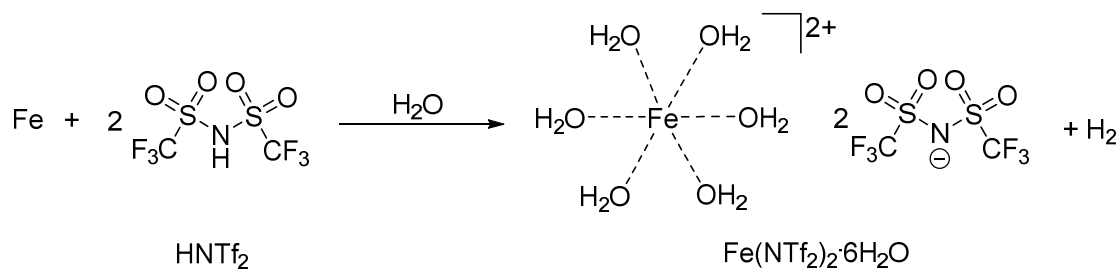


Figure 27: ESI-MS of [Fe^{II}(L^{td})₃]Cl₂ (**9**)

The NTf₂-salt **12**·H₂O was obtained using vacuum-dried Fe(NTf₂)₂·6H₂O, that crystallises as dihydrate of [Fe(H₂O)₆](NTf₂)₂ (Figure 32) from DCM. Bulk material of Fe(NTf₂)₂·6H₂O is accessible *via* treatment of an iron powder suspension in water with an aqueous solution of bis(trifluoromethylsulfonyl)imide acid (HNTf₂) (Scheme 5). Subsequent filtration of unreacted iron and removal of the solvent leads to a blue solid which gets colourless when dried *in vacuo*.



Scheme 5: Synthesis of Fe(NTf₂)₂·6H₂O.

Formation of the anion could be confirmed by mass spectrometry, as in the negative mode a peak resulting from NTf₂⁻ at $m/z = 280.1$ can be seen. The IR spectrum also confirms the presence of the triflimide anion, as it shows strong absorption bands resulting from the asymmetric valence vibration of CF₃ at 1194 cm⁻¹, from the symmetric valence vibration of SO₂ at 1134 cm⁻¹ and from the asymmetric valence vibration of the SNS group at 1041 cm⁻¹ (Figure 33).^[84]

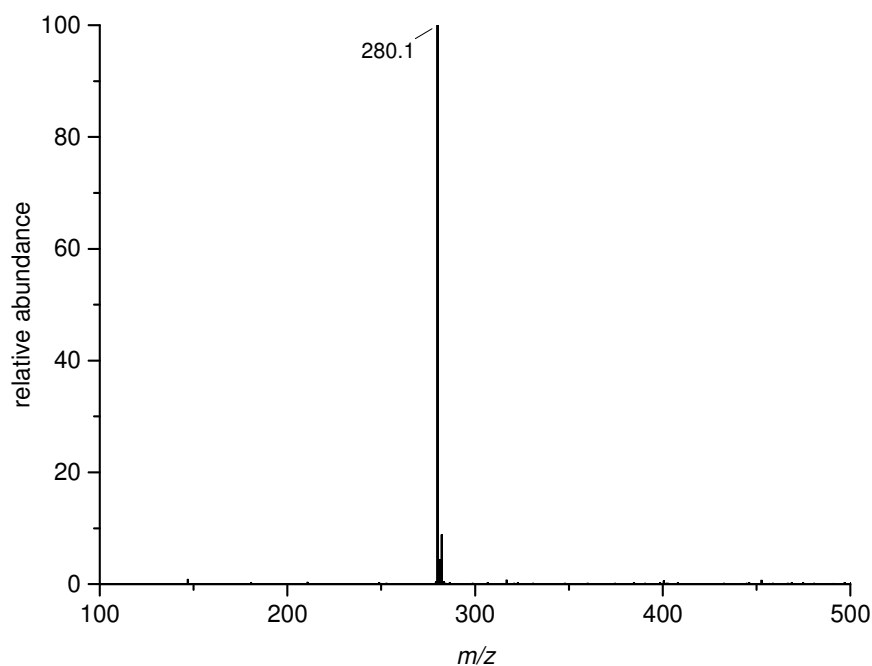


Figure 28: ESI-MS spectrum of $\text{Fe}(\text{NTf}_2)_2 \cdot 6\text{H}_2\text{O}$ in the negative mode.

All 3:1-type iron(II) complexes of \mathbf{L}^{td} isolated in this work assumedly exhibit the metal ion in the LS state, as confirmed by magnetic measurements in the case of $\mathbf{10} \cdot 2\text{H}_2\text{O}$ (Figure 39) and $\mathbf{12} \cdot \text{H}_2\text{O}$ (Figure 38). The chloride compound **9** decomposes at 210 °C and the perchlorate and tetrafluoroborate compounds $\mathbf{10} \cdot 2\text{H}_2\text{O}$ and $\mathbf{11} \cdot 2\text{H}_2\text{O}$ do not melt up to 220 °C, whereas the triflimide compound $\mathbf{12} \cdot \text{H}_2\text{O}$ melts at the remarkably low temperature of 195–201 °C, as confirmed by the second cycle of DSC measurements (Figure 29). The fusion process is represented by the endothermic peak at 201 °C ($T_{\text{onset}} = 195$ °C). Upon cooling, the compound may exhibit a glass transition, although the recorded heat flow in the cooling mode does not permit any secure interpretation. Before melting, the complex presumably changes from the glass state into the solid crystalline state by cold crystallisation resulting in an exothermic peak at 172 °C. The rather small endothermic peak at 92 °C is presumably caused by the loss of solvent and moisture. Thus, by formal metathesis of Cl^- , ClO_4^- or BF_4^- with NTf_2^- a coordination compound with melting point was achieved.

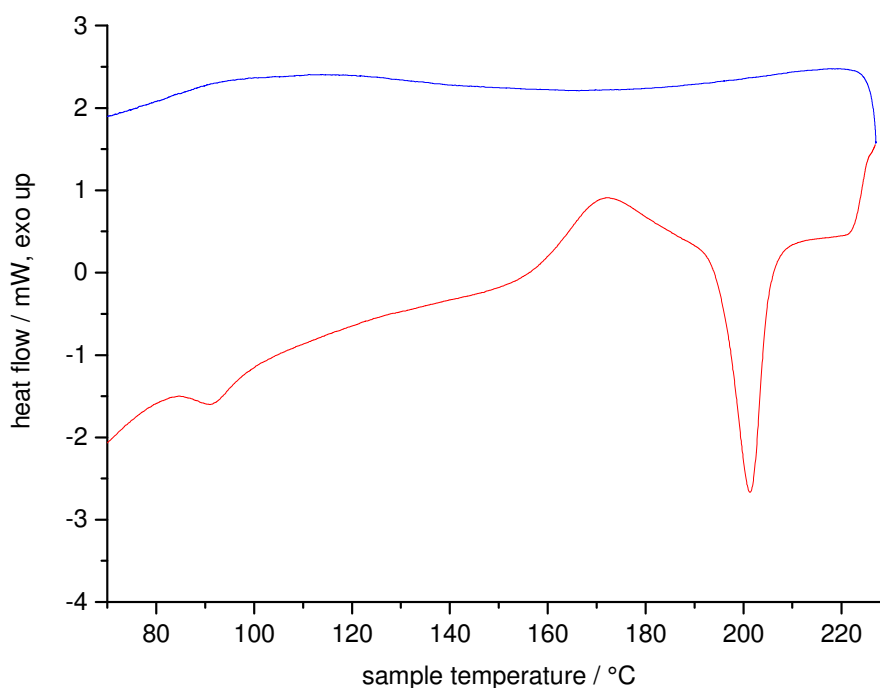


Figure 29: Second cycle of the DSC measurements of $[\text{Fe}^{\text{II}}(\text{L}^{\text{td}})_3](\text{NTf}_2)_2 \cdot \text{H}_2\text{O}$ (**12**· H_2O) with a scan rate of 10 K min^{-1} in the heating (red line) and the cooling (blue line) mode.

Using $\text{Co}(\text{ClO}_4)_2 \cdot 6\text{H}_2\text{O}$ and $\text{Ni}(\text{ClO}_4)_2 \cdot 6\text{H}_2\text{O}$, further 3:1-type complexes with *mer* configuration, namely $[\text{Co}^{\text{II}}(\text{L}^{\text{td}})_3](\text{ClO}_4)_2 \cdot 2\text{H}_2\text{O}$ (**13**· $2\text{H}_2\text{O}$, Figure 36) and $[\text{Ni}^{\text{II}}(\text{L}^{\text{td}})_3](\text{ClO}_4)_2 \cdot \text{MeOH} \cdot \text{H}_2\text{O}$ (**14**· $\text{MeOH} \cdot \text{H}_2\text{O}$, Figure 37) were obtained (Scheme 4). Analytically pure bulk material of **13**· $1.5\text{H}_2\text{O}$ and **14**· $2\text{H}_2\text{O}$ was obtained by drying the respective crystalline material *in vacuo*. The cobalt(II) complex **13**· $1.5\text{H}_2\text{O}$ exhibits the metal ion in the HS state, as confirmed by magnetic measurements (Figure 40) and does not melt up to $220 \text{ }^\circ\text{C}$, neither does the nickel(II) complex **14**· $2\text{H}_2\text{O}$.

To slightly decrease the ligand field, NCS^- was introduced as coligand. In doing so hopefully the occurrence of thermal SCO for an iron(II) complex is enabled. Compound $[\text{Fe}^{\text{II}}(\text{L}^{\text{td}})_2(\text{NCS})_2]$ (**15**) was obtained by using freshly prepared “ $\text{Fe}(\text{NCS})_2$ ” in MeCN solution (Scheme 4). The formation of complex **15** was confirmed by elemental analyses and mass spectrometry, which indicated the presence of the fragment $[\text{Fe}^{\text{II}}(\text{L}^{\text{td}})_2(\text{NCS})_2]^+$ since the spectrum shows a peak at $m/z = 469.9726$ (Figure 30). Furthermore, the IR spectrum of **15** shows an absorption band resulting from the C–N valence vibration of the coligand at $\tilde{\nu} = 2070 \text{ cm}^{-1}$ (Figure 31).^[85] Indeed, the compound features a thermal SCO around 250 K, as confirmed by temperature dependent magnetic measurements (Figure 41).

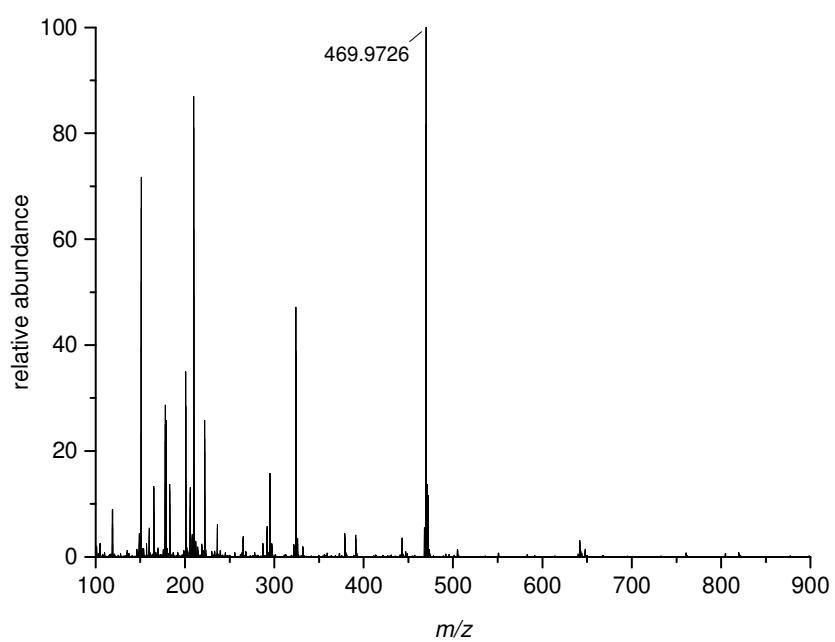


Figure 30: ESI-MS of $[\text{Fe}^{\text{II}}(\text{L}^{\text{td}})_2(\text{NCS})_2]$ (**15**).

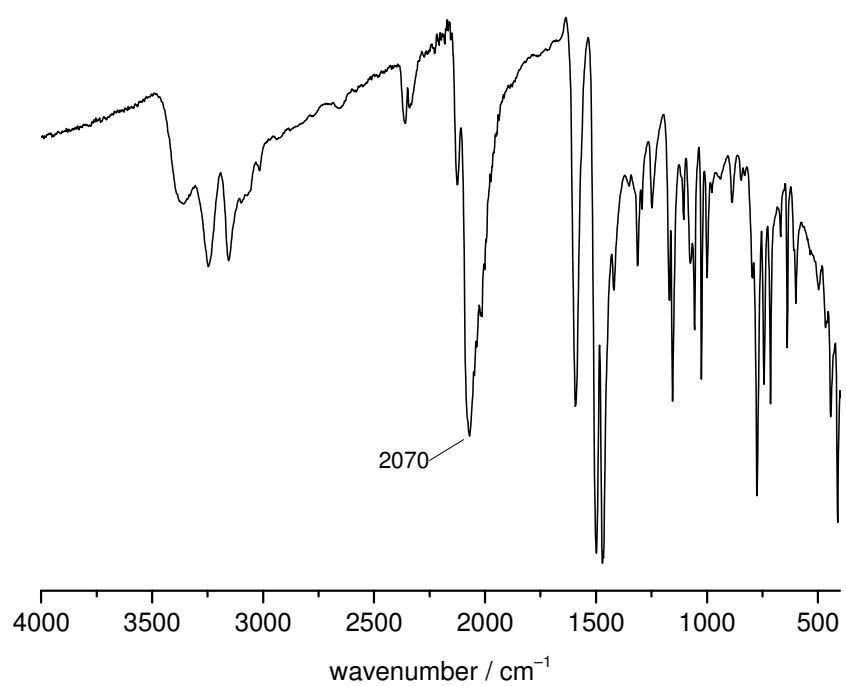


Figure 31: IR spectrum of $[\text{Fe}^{\text{II}}(\text{L}^{\text{td}})_2(\text{NCS})_2]$ (**15**).

The iron salt $[\text{Fe}(\text{H}_2\text{O})_6](\text{NTf}_2)_2 \cdot 2\text{H}_2\text{O}$ crystallises in the tetragonal space group $P4_2/n$. The asymmetric unit consist of half a complex molecule, one triflimide counterion and a water solvent molecule. The iron(II) ion is octahedrally coordinated by six water molecules that are hydrogen bonded to the triflimide counterions and the water solvent molecules (Figure 32). Crystallographic data of $[\text{Fe}(\text{H}_2\text{O})_6](\text{NTf}_2)_2 \cdot 2\text{H}_2\text{O}$ is summarised in Table 22. The coordination of the triflimide anions via its O-atoms could be confirmed by Raman spectroscopy. In 2011 *P. Eiden* found that the SNS vibration is a useful indicator for the coordination behaviour of the triflimide anion. ^[86] The spectrum of $\text{Fe}(\text{NTf}_2)_2 \cdot 6\text{H}_2\text{O}$ shows an intense band at 752 cm^{-1} which is a typical value of the SNS vibration from triflimide that coordinates *via* its O-atoms (Figure 33).

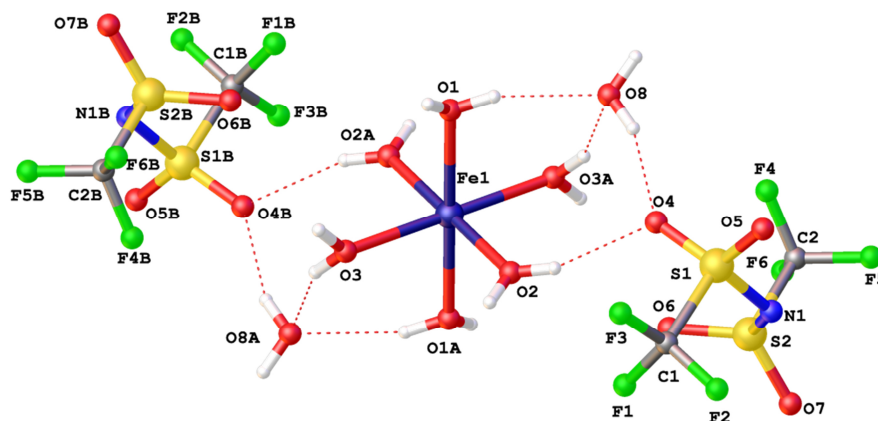


Figure 32: View of molecular structure of $[\text{Fe}(\text{H}_2\text{O})_6](\text{NTf}_2)_2 \cdot 2\text{H}_2\text{O}$ including hydrogen bonding patterns of the asymmetric unit. Selected distances (Å): O1–H···O8 2.762, O2–H···O4 2.970, O3–H···O8A 2.720, O4···O8–H 2.849. Symmetry operations used to generate equivalent atoms: A) $-x, -y, -z + 1$; B) $-y, x - 0.5, z + 0.5$.

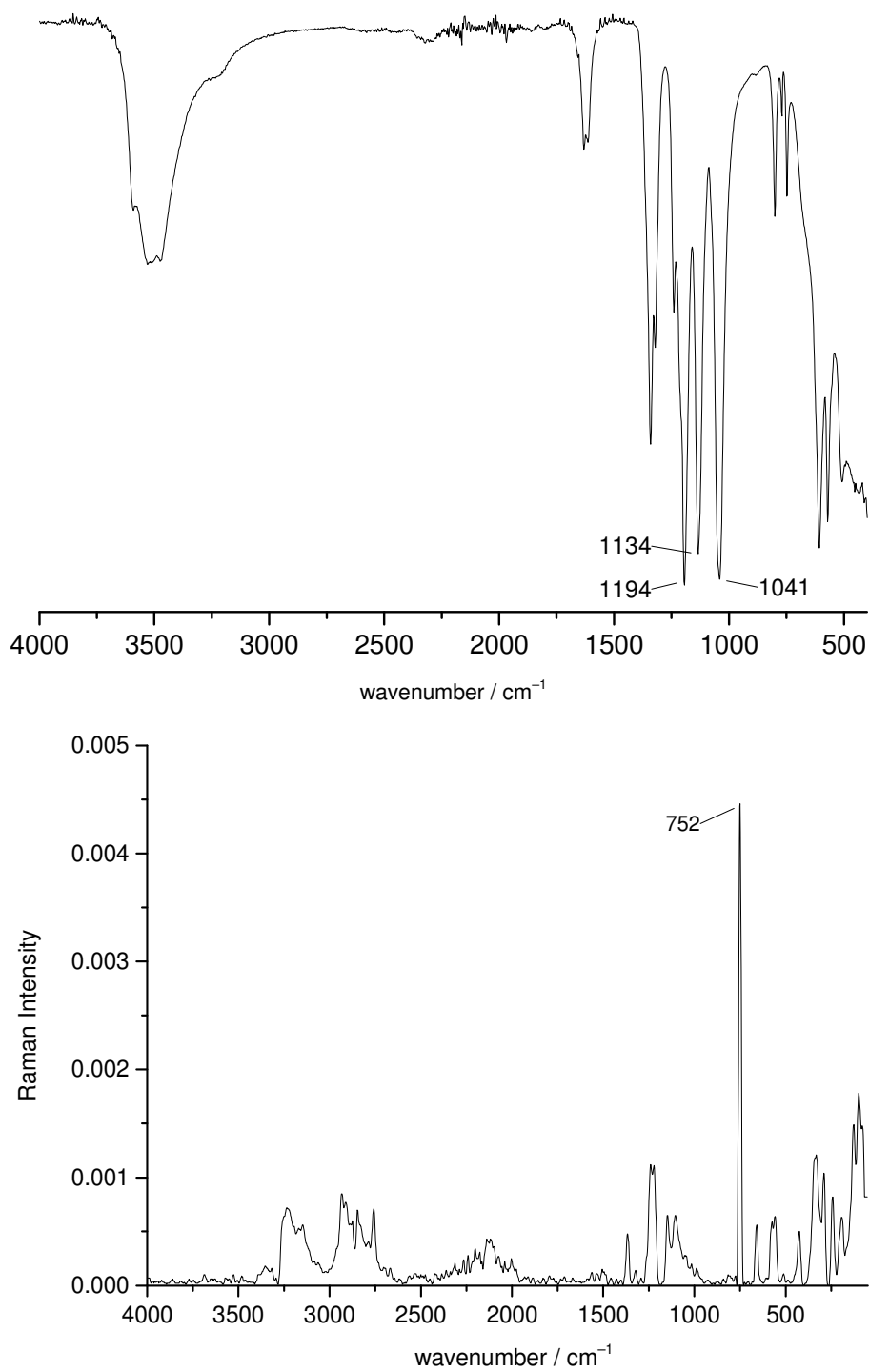


Figure 33: *top:* IR spectrum of $[\text{Fe}(\text{H}_2\text{O})_6](\text{NTf}_2)_2$ and *bottom:* Raman spectrum of $[\text{Fe}(\text{H}_2\text{O})_6](\text{NTf}_2)_2$.

The 3:1-type complexes $[\text{Fe}^{\text{II}}(\text{L}^{\text{td}})_3](\text{ClO}_4)_2 \cdot 0.625\text{MeOH} \cdot 0.875\text{H}_2\text{O}$ (**10**·0.625MeOH·0.875H₂O), $[\text{Fe}^{\text{II}}(\text{L}^{\text{td}})_3](\text{BF}_4)_2 \cdot \text{MeOH} \cdot \text{H}_2\text{O}$ (**11**·MeOH·H₂O), $[\text{Co}^{\text{II}}(\text{L}^{\text{td}})_3](\text{ClO}_4)_2 \cdot 2\text{H}_2\text{O}$ (**13**·2H₂O) and $[\text{Ni}^{\text{II}}(\text{L}^{\text{td}})_3](\text{ClO}_4)_2 \cdot \text{MeOH} \cdot \text{H}_2\text{O}$ (**14**·MeOH·H₂O) crystallise in the triclinic space group *P*-1. The metal ions reside in a distorted octahedral N₆ coordination sphere built by the bidentate chelating ligands, coordinating with an N_{td} atom of the thiadiazole and an N_{py} atom of the pyridyl moiety. The asymmetric unit comprises the *mer* and *fac* isomer in a 1:1 ratio in the case of the perchlorate **10**·0.625MeOH·0.875H₂O (Figure 34), whereas in the tetrafluoroborate compound **11**·MeOH·H₂O mainly the *mer* isomer is found. However, a disorder was modelled for one of the ligands in **11**·MeOH·H₂O resulting in 12 % of the corresponding *fac* isomer (Figure 35). Only the *mer* isomer is found in both, the cobalt complex **13**·2H₂O and the nickel compound **14**·MeOH·H₂O (Figure 35). The bond lengths in the iron(II) complexes **33**·0.625MeOH·0.875H₂O and **34**·MeOH·H₂O lie in the range of 1.958(7)–1.988(5) and 1.966(18)–1.985(2) Å for Fe1–N_{py} and 1.922(6)–1.943(7) and 1.915(15)–1.946(3) Å for Fe1–N_{td}, respectively, and are characteristic values for similar complexes with LS iron(II).^[87] The Co–N distances in the cobalt(II) complex **13**·2H₂O range from 2.116(6)–2.153(6) Å indicating that the cobalt(II) ion is in the HS state.^[7] Selected distances and angles for the above mentioned compounds are summarised in Table 5. The crystallographic data are listed in Table 22 and Table 23 (appendix).

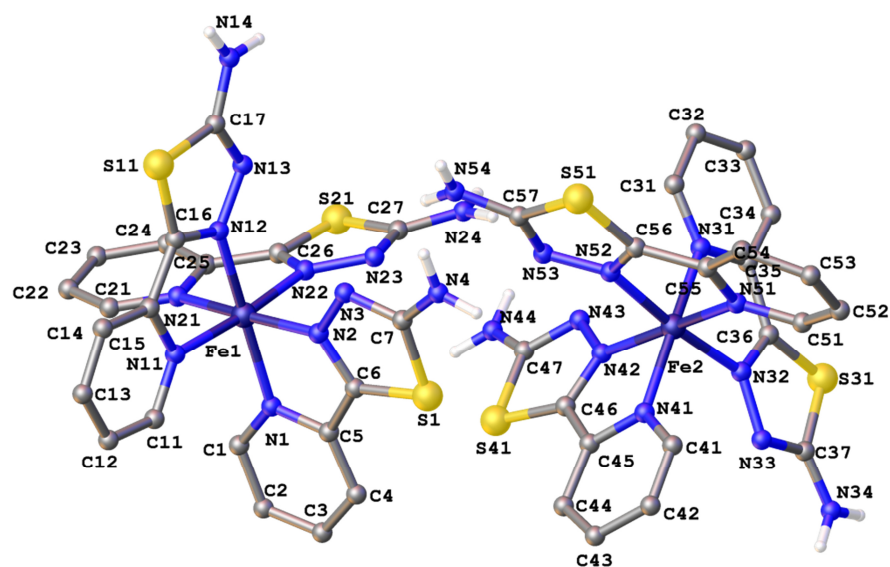


Figure 34: View of the molecular structure of $[\text{Fe}^{\text{II}}(\text{L}^{\text{td}})_3]^{2+}$, the complex cation of $[\text{Fe}^{\text{II}}(\text{L}^{\text{td}})_3](\text{ClO}_4)_2 \cdot 0.625\text{MeOH} \cdot 0.875\text{H}_2\text{O}$. Solvent molecules and hydrogen atoms, except for the ones of the amine group, are omitted. Both isomers of the asymmetric unit are shown (*fac* on the left; *mer* on the right).

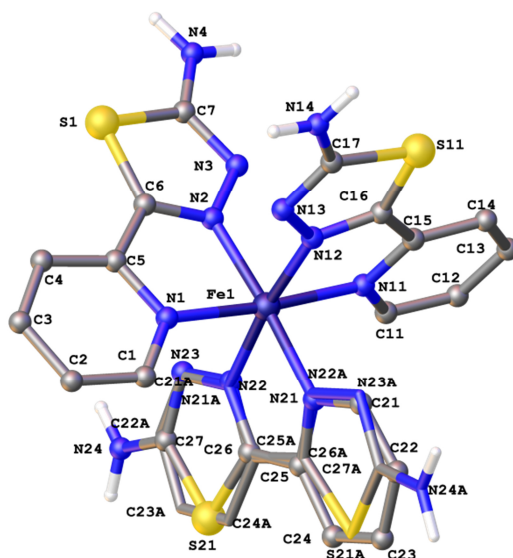


Figure 35: View of the molecular structure of $[\text{Fe}^{\text{II}}(\text{L}^{\text{td}})_3]^{2+}$, the complex cation of $[\text{Fe}^{\text{II}}(\text{L}^{\text{td}})_3](\text{BF}_4)_2 \cdot \text{MeOH} \cdot \text{H}_2\text{O}$ (**11**·MeOH·H₂O). The minor part [(A), occupation 12 %] is drawn in tubes. H-atoms are omitted except for the ones of the amine groups.

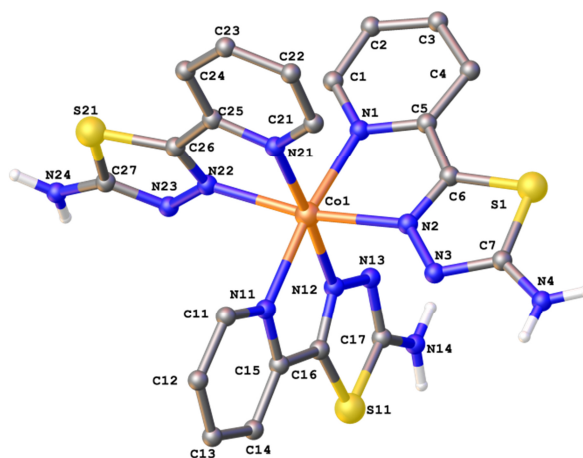


Figure 36: View of the molecular structure of $[\text{Co}^{\text{II}}(\text{L}^{\text{td}})_3]^{2+}$, the complex cation of $[\text{Co}^{\text{II}}(\text{L}^{\text{td}})_3](\text{ClO}_4)_2 \cdot 2\text{H}_2\text{O}$ (**13**·2H₂O). Solvent molecules and hydrogen atoms, except for the ones of the amine group, are omitted.

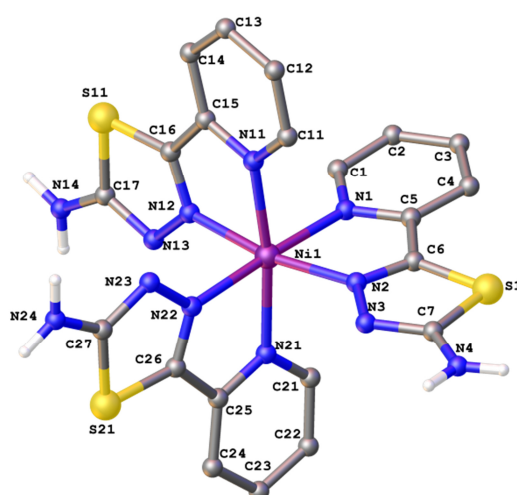


Figure 37: View of the molecular structure of $[\text{Ni}^{\text{II}}(\text{L}^{\text{td}})_3]^{2+}$, the complex cation of $[\text{Ni}^{\text{II}}(\text{L}^{\text{td}})_3](\text{ClO}_4)_2 \cdot \text{MeOH} \cdot \text{H}_2\text{O}$ (**14**·MeOH·H₂O). Solvent molecules and hydrogen atoms, except for the ones of the amine group, are omitted.

Complexes with 2-Pyridyl and Amino Substituted Azoles

Table 5: Selected distances [Å] and angles [°] for [Fe^{II}(L^{td})₃](ClO₄)₂·0.625MeOH·0.875H₂O (**10**·0.625MeOH·0.875H₂O), [Fe^{II}(L^{td})₃](BF₄)₂·MeOH·H₂O (**11**·MeOH·H₂O), [Co^{II}(L^{td})₃](ClO₄)₂·2H₂O (**13**·2H₂O) and [Ni^{II}(L^{td})₃](ClO₄)₂·MeOH·H₂O (**14**·MeOH·H₂O).

	10 ·0.625MeOH·0.875H ₂ O ^[a] (M = Fe)	11 ·MeOH·H ₂ O ^[a] (M = Fe)	13 ·2H ₂ O (M = Co)	14 ·MeOH·H ₂ O (M = Ni)
M1–N1	1.987(5) [Fe2–N31 1.969(7)]	1.983(1)	2.119(7)	2.1151(9)
M1–N2	1.925(5) [Fe2–N32 1.931(7)]	1.944(1)	2.116(6)	2.0728(9)
M1–N11	1.987(6) [Fe2–N41 1.988(6)]	1.974(1)	2.134(6)	2.0902(10)
M1–N12	1.933(5) [Fe2–N42 1.922(6)]	1.942(1)	2.123(6)	2.0662(9)
M1–N21	1.988(5) [Fe2–N51 1.958(7)]	1.985(2) [Fe1–N21A 1.966(18)]	2.153(6)	2.0888(10)
M1–N22	1.937(5) [Fe2–N52 1.943(7)]	1.946(3) [Fe1–N22A 1.915(15)]	2.121(6)	2.0787(9)
N1–M1–N2	81.4(2) [N31–Fe2–N32 81.2(3)]	80.88(5)	77.1(3)	78.81(4)
N1–M1–N11	93.2(2) [N31–Fe2–N41 171.7(3)]	174.91(5)	171.5(2)	89.04(4)
N1–M1–N12	172.1(2) [N31–Fe2–N42 92.5(3)]	95.72(5)	96.0(2)	91.93(4)
N1–M1–N21	94.6(2) [N31–Fe2–N51 94.5(3)]	95.67(19) [N1–Fe1–N21A 87(2)]	87.7(2)	98.47(4)
N1–M1–N22	90.3(2) [N31–Fe2–N52 94.0(3)]	88.8(2) [N1–M1–N22A 93.4(17)]	96.7(2)	176.74(4)
N2–M1–N11	92.5(2) [N32–Fe2–N41 93.3(3)]	94.80(5)	98.6(2)	95.06(4)
N2–M1–N12	92.7(2) [N32–Fe2–N42 91.0(3)]	88.63(5)	89.2(2)	169.20(4)
N2–M1–N21	171.2(2) [N32–Fe2–N51 95.2(3)]	175.94(18) [N2–M1–N21A 98.6(4)]	92.8(2)	90.38(4)
N2–M1–N22	91.3(2) [N32–Fe2–N52 174.3(3)]	96.53(8) [N2–Fe1–N22A 174.1(16)]	168.3(2)	100.83(4)
N11–M1–N12	81.7(2) [N41–Fe2–N42 81.4(2)]	81.43(5)	76.6(2)	79.10(4)
N11–M1–N21	95.4(2) [N41–Fe2–N51 92.2(3)]	88.75(19) [N11–Fe1–N21A 97(2)]	99.9(2)	171.48(4)
N11–M1–N22	175.1(2) [N41–Fe2–N52 91.8(3)]	94.4(2) [N11–Fe1–N22A 90.8(17)]	88.8(2)	94.22(4)
N12–M1–N21	92.0(2) [N42–Fe2–N51 171.2(3)]	93.85(8) [N12–Fe1–N21A 172.7(6)]	176.1(2)	96.53(4)
N12–M1–N22	95.1(2) [N42–Fe2–N52 92.1(2)]	173.63(17) [N12–Fe1–N22A 90.7(5)]	101.3(2)	88.74(4)
N21–M1–N22	80.9(2) [N51–Fe2–N52 82.1(3)]	81.21(8) [N21A–Fe1–N22A 82.2(5)]	77.0(2)	78.29(4)

^[a] values in brackets refer to the *fac* isomer

The Mössbauer spectrum of $[\text{Fe}^{\text{II}}(\text{L}^{\text{td}})_3](\text{NTf}_2)_2 \cdot \text{H}_2\text{O}$ (**12**·H₂O) was recorded at 80 K and shows a symmetrical doublet with an isomeric shift $\delta = 0.37 \text{ mm s}^{-1}$ and a small quadrupole splitting $\Delta E_Q = 0.35 \text{ mm s}^{-1}$, as expected for a ferrous complex in the LS state ^[82,83] (Figure 38). Temperature dependent measurements of the magnetic susceptibility confirm the LS state of **12**·H₂O in the range of 295–2 K. At 295 K the sample possesses a value of $\chi_M T = 0.28 \text{ cm}^3 \text{ K mol}^{-1}$. On slowly cooling, the values decrease marginally until reaching a value of $\chi_M T = 0.12 \text{ cm}^3 \text{ K mol}^{-1}$ at 2 K. Thus, indicating the presence of a LS state over the whole temperature range, taking into account the presence of a paramagnetic impurity with $S = 2.0$ amounting to 8.4 % (Figure 38). Values of around $\chi_M T = 0.005 \text{ cm}^3 \text{ K mol}^{-1}$ are observed for the magnetic susceptibility of the perchlorate compound $[\text{Fe}^{\text{II}}(\text{L}^{\text{td}})_3](\text{ClO}_4)_2 \cdot 2\text{H}_2\text{O}$ (**10**·2H₂O) in the range of 300–2 K (Figure 39), indicating the iron(II) ion to be in the LS state as well. The cobalt(II) perchlorate $[\text{Co}^{\text{II}}(\text{L}^{\text{td}})_3](\text{ClO}_4)_2 \cdot 1.5\text{H}_2\text{O}$ (**13**·1.5 H₂O) instead, is a high spin compound which could be confirmed by susceptibility measurements in the range of 295–2 K (Figure 40). The value of $\chi_M T$ at 295 K ($3.14 \text{ cm}^3 \text{ K mol}^{-1}$) lies in the range of typical observed values for a HS Co(II) ($2.31\text{--}3.38 \text{ cm}^3 \text{ K mol}^{-1}$). ^[81] Upon decreasing the temperature, the $\chi_M T$ values only decline very slightly until at around 100 K an abrupt fall, presumably due to zero field splitting, occurs.

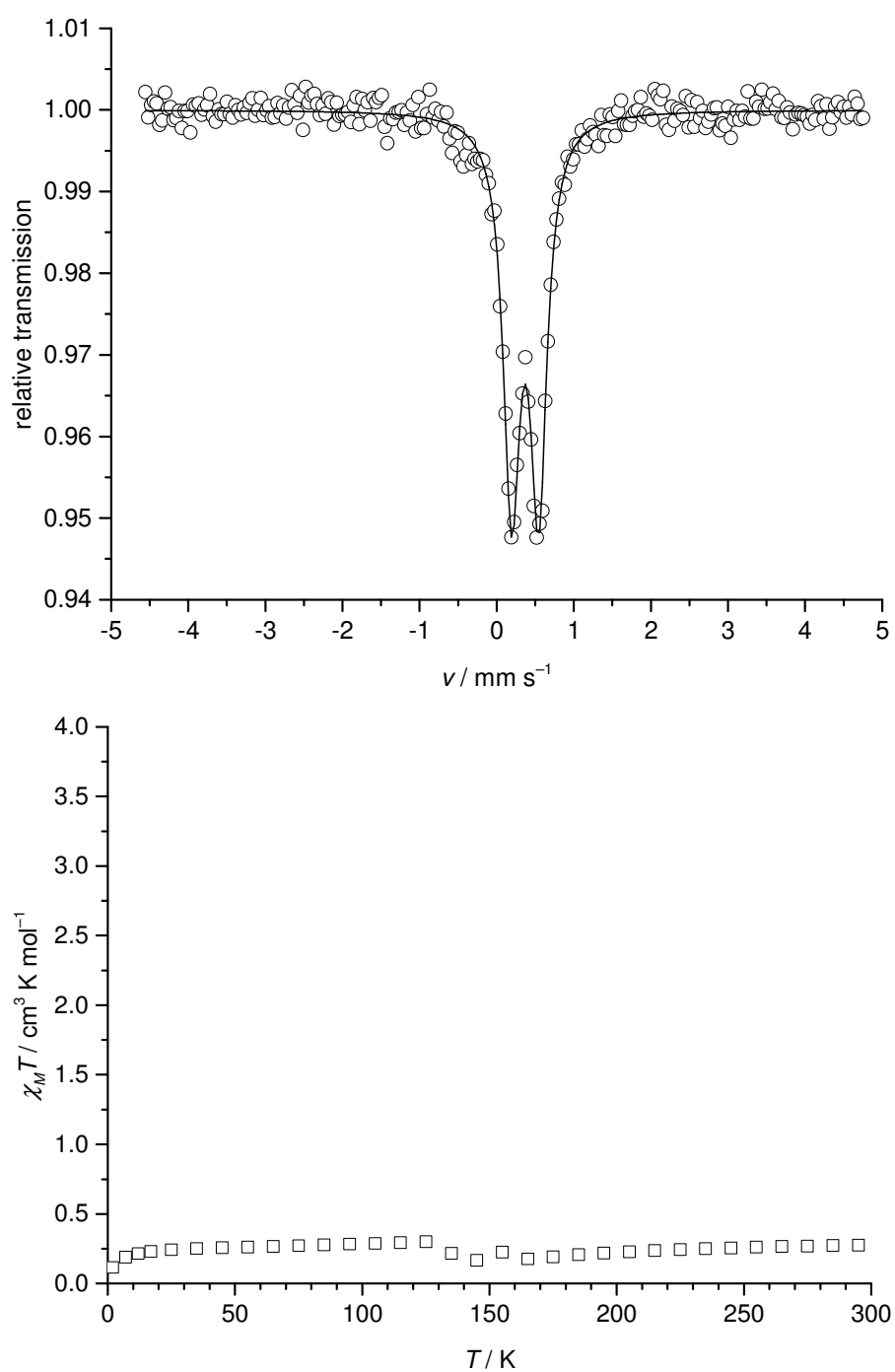


Figure 38: *top:* Mössbauer spectrum of $[\text{Fe}^{\text{II}}(\text{L}^{\text{td}})_3](\text{NTf}_2)_2 \cdot \text{H}_2\text{O}$ (**12**· H_2O), recorded at 80 K. The line represents fitting with Lorentzian doublet; *bottom:* $\chi_M T$ vs. T plot of **12**· H_2O .

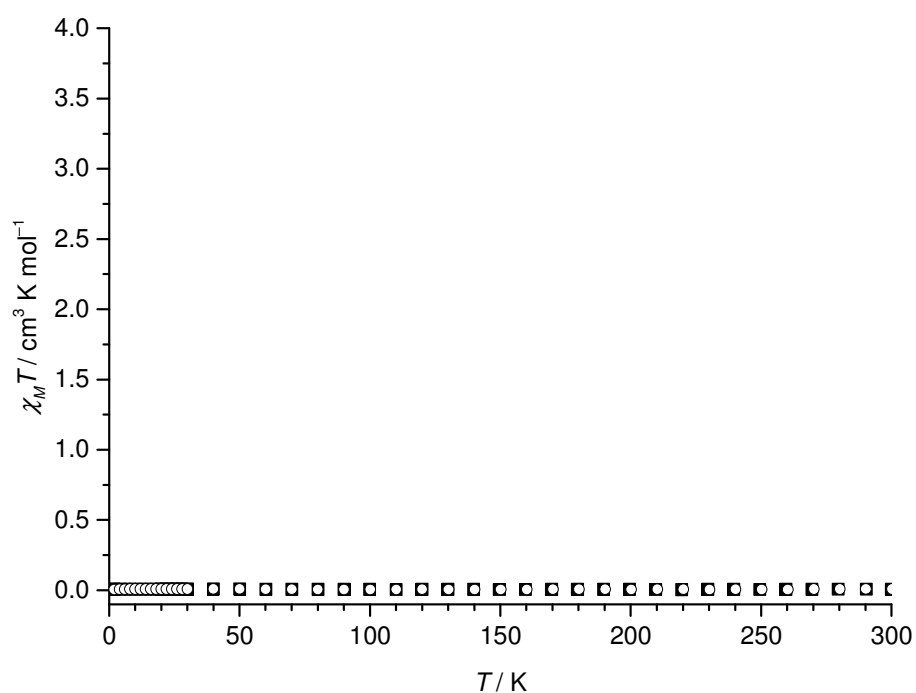


Figure 39: $\chi_M T$ vs. T plot for $[\text{Fe}^{\text{II}}(\text{L}^{\text{td}})_3](\text{ClO}_4)_2 \cdot 2\text{H}_2\text{O}$ (**10** · $2\text{H}_2\text{O}$) in the cooling (\blacksquare) and the heating (\circ) mode.

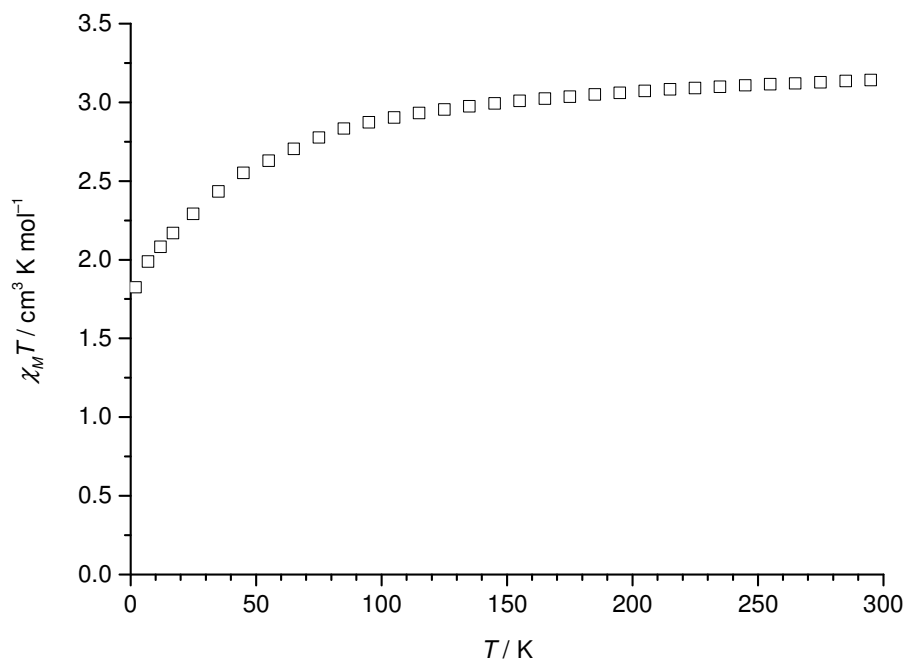


Figure 40: $\chi_M T$ vs. T plot for $[\text{Co}^{\text{II}}(\text{L}^{\text{td}})_3](\text{ClO}_4)_2 \cdot 1.5\text{H}_2\text{O}$ (**13** · $1.5 \text{H}_2\text{O}$).

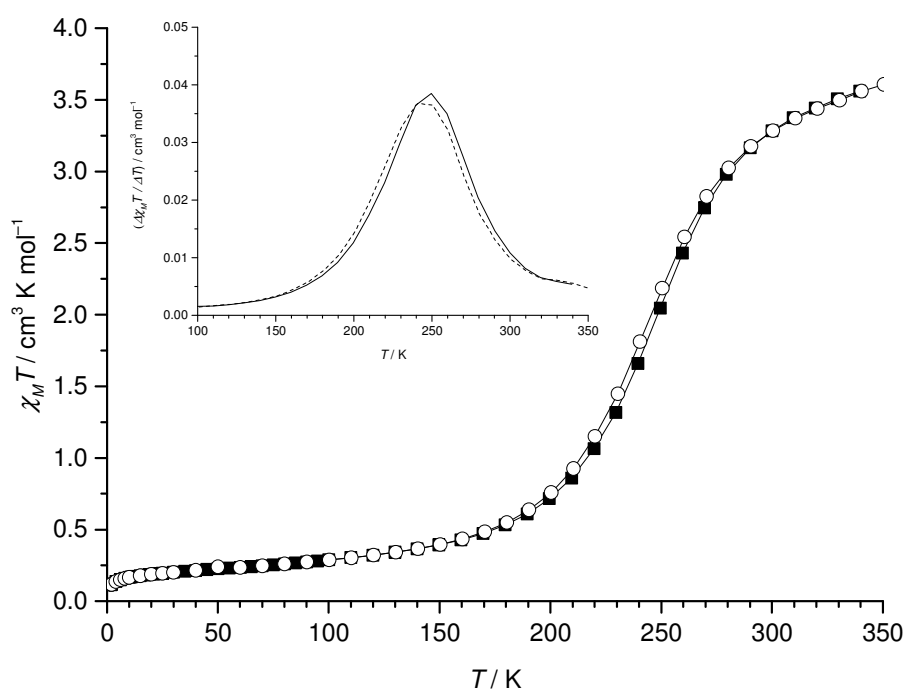


Figure 41: $\chi_M T$ vs. T plots for $[\text{Fe}^{\text{II}}(\text{L}^{\text{td}})_2(\text{NCS})_2]$ (**15**) in the cooling (\blacksquare) and the heating (\circ) mode; the inset shows the first derivatives of the $\chi_M T$ vs. T plots (cooling (—), heating (---)).

Susceptibility measurements of the isothiocyanate compound $[\text{Fe}^{\text{II}}(\text{L}^{\text{td}})_2(\text{NCS})_2]$ (**15**) in the range of 350–2 K indeed revealed that **15** exhibits a spin transition from the $S = 2.0$ (HS) to $S = 0$ (LS). The value of $\chi_M T$ at 350 K ($3.61 \text{ cm}^3 \text{ K mol}^{-1}$) is smaller than usually observed for HS iron(II) (around $4.07 \text{ cm}^3 \text{ mol}^{-1} \text{ K}$),^[81] indicating that the majority of the iron centres is in the HS state, but a small number of iron(II) cores have not yet switched into the HS state at that temperature. On lowering the temperature, the values of $\chi_M T$ decrease somewhat until at ca. 280 K they fall abruptly until reaching a region with a minor decline at about 180 K ($0.55 \text{ cm}^3 \text{ K mol}^{-1}$), thus indicating occurrence of thermal SCO and LS iron(II) at that temperature. The residual value of $\chi_M T = 0.12 \text{ cm}^3 \text{ K mol}^{-1}$ at 2 K presumably results from paramagnetic impurities. Hysteretic behaviour is observed comparing the $\chi_M T$ versus T curves in the cooling and heating mode revealing a small loop of 10 K. The spin transition temperatures $T_{\downarrow} = 250 \text{ K}$ and $T_{\uparrow} = 240 \text{ K}$ were determined from the first derivatives of the $\chi_M T$ versus T curves (Figure 41). Surprisingly, the isothiocyanate compound $[\text{Fe}^{\text{II}}(\text{L}^{\text{td}})_2(\text{NCS})_2]$ (**15**) shows an inverse hysteretic behaviour with $T_{\downarrow} > T_{\uparrow}$. Unfortunately, single crystals of **15**, suitable for X-ray diffraction analyses, could not be obtained up to now, so that no more insight could be gained into the inverse hysteretic behaviour.

The compounds presented in this chapter are summarised in Table 6. The thiazole ligand L^{tz} forms 2:1-type complexes with “ $Fe(NCX)_2$ ” ($X = S$: **5**; Se : **6**) and “ $M(NCS)_2$ ” ($M = Co$: **7**; Ni : **8**) featuring a relatively rare *cis* coordination of the coligands. All iron(II) and the cobalt(II) complexes possess the metal ions in the HS state even at lower temperatures as confirmed by temperature depended measurements of the magnetic susceptibility, Mössbauer spectroscopy or X-ray diffraction analysis. Complexations carried out with a 3:1 molar ratio of ligand and metal salt led to miscellaneous results. With $Co(ClO_4)_2 \cdot 6H_2O$ the 3:1-type HS complex $[Co^{II}(L^{tz})_3](ClO_4)_2$ (**3**) could be prepared as confirmed by X-ray diffraction analysis. A melting point of **3** could not be determined up to 250 °C. Using $Fe(BF_4)_2 \cdot 6H_2O$ leads to the formation of the dinuclear, oxido bridged complex $[(L^{tz})_2FFe^{III}(\mu-O)Fe^{III}F(L^{tz})_2](BF_4)_2$ (**1**) with two antiferromagnetically coupled iron(III) centres. Modification of the reaction set up leads to the formation of the mononuclear iron(III) HS complex $[Fe^{III}(L^{tz})_2F_2](BF_4)$ (**2**) comprising two equivalents ligand. Both complexes **1** and **2** exhibit fluoro ligands generated by fluoride abstraction from the BF_4^- anion. With $Cu(ClO_4)_2 \cdot 6H_2O$ the 2:1-type complex $[Cu^{II}(L^{tz})_2](ClO_4)_2$ (**4**) presumably with a four-fold coordinated environment was obtained which does not melt up to 220 °C.

Table 6: Summary of the compounds prepared in this chapter.

		L:M	spin state	$T_{fus} / ^\circ C$
$[Fe^{II}(L^{tz})_2(NCS)_2]$	(5)	2:1	HS	-
$[Fe^{II}(L^{tz})_2(NCSe)_2]$	(6)	2:1	HS	-
$[Co^{II}(L^{tz})_2(NCS)_2]$	(7)	2:1	HS	-
$[Ni^{II}(L^{tz})_2(NCS)_2]$	(8)	2:1	-	-
$[Co^{II}(L^{tz})_3](ClO_4)_2$	(3)	3:1	HS	>250
$[(L^{tz})_2FFe^{III}(\mu-O)Fe^{III}F(L^{tz})_2](BF_4)_2$	(1)	4:2	HS	-
$[Fe^{III}(L^{tz})_2F_2](BF_4)$	(2)	2:1	HS	-
$[Cu^{II}(L^{tz})_2](ClO_4)_2$	(4)	2:1	-	>220
$Fe(NTf_2)_2 \cdot 6H_2O$	-	-	-	148–151
$[Fe^{II}(L^{td})_3]Cl_2$	(9)	3:1	LS	210 (dec.)
$[Fe^{II}(L^{td})_3](ClO_4)_2$	(10)	3:1	LS	>220
$[Fe^{II}(L^{td})_3](BF_4)_2$	(11)	3:1	LS	>220
$[Fe^{II}(L^{td})_3](NTf_2)_2$	(12)	3:1	LS	194
$[Co^{II}(L^{td})_3](ClO_4)_2$	(13)	3:1	HS	>220
$[Ni^{II}(L^{td})_3](ClO_4)_2$	(14)	3:1	-	>220
$[Fe^{II}(L^{td})_2(NCS)_2]$	(15)	2:1	SCO	-

The compound $Fe(NTf_2)_2 \cdot 6H_2O$ could be prepared by treating iron powder with bis(trifluoromethylsulfonyl)imide acid ($HNTf_2$) in water. The iron(II) triflimide was obtained as a colourless powder that melts at about 150 °C and was successfully used as a reactant for complexation reactions. The molecular structure was determined by X-ray diffraction analysis. The complex features an iron(II)

ion octahedrally coordinated by six water molecules connected *via* H-bonds to the O-atoms of the anions and to two crystal water molecules.

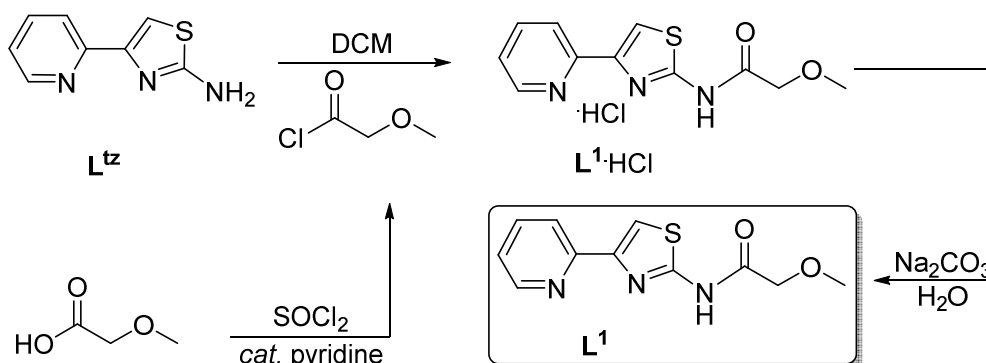
The thiadiazole ligand L^{td} forms several 3:1-type complexes with $Fe^{II}(X)_2 \cdot 6H_2O$ ($X = Cl$: **9**, ClO_4 : **10**, BF_4 : **11**; NTf_2 : **12**), presumably all featuring metal ions in the LS state at rt as confirmed by magnetic measurements. The triflimide $[Fe^{II}(L^{td})_3](NTf_2)_2$ (**12**) melts at 194 °C, whereas the perchlorate **10** and the tetrafluoroborate **11** do not melt up to 220 °C and the chloride **9** even decomposes at 210 °C. Thus, formal metathesis of Cl^- , ClO_4^- or BF_4^- with NTf_2^- leads to the lowering of the melting point. The related cobalt(II) perchlorate compound $[Co^{II}(L^{td})_3](ClO_4)_2$ (**13**) exhibits the metal ion in HS state in the range of 2–295 K and does not melt up to 220 °C, neither does the analogous nickel(II) perchlorate complex **14**. Eventually the 2:1-type SCO complex $[Fe^{II}(L^{td})_2(NCS)_2]$ (**15**) was prepared featuring an inverse hysteresis with $T_{\downarrow} = 250$ K and $T_{\uparrow} = 240$ K which could be confirmed by temperature dependent measurements of the magnetic susceptibility in the heating and cooling mode.

2.2 Complexes with Uncharged Ligands

As shown in chapter 2.1.2, the thiazole ligand L^{tz} features a limited ability to form 3:1-type complexes, whereas from the imidazole ligand **pi** several 3:1-type complexes (Figure 4, **K–Q**) are known. However, both ligands were modified, in order to increase the fusion entropy $\Delta_{fus}S$ of the resulting complexes. The ligand L^{tz} was enhanced with a methoxyacetyl substituent to form L^1 (Scheme 6) and the ligand **pi** was enhanced with a methoxyethyl and an ethyl substituent to form L^2 and L^3 (Scheme 7), respectively. The coordination ability of these enhanced ligands to form 3:1-type complexes with a dicationic chromophore was investigated.

2.2.1 Ligand Synthesis

The methoxyacetyl substituted ligand 2-methoxy-*N*-[4-(2-pyridyl)-2-thiazolyl]-acetamide (L^1) was obtained from its hydrochloride $L^1 \cdot HCl$. The latter was synthesised by coupling of the amine ligand L^{tz} with methoxyacetyl chloride, which is easily accessible through the reaction of the corresponding carboxylic acid with thionyl chloride (Scheme 6).



Scheme 6: Synthesis of the expanded thiazole ligand L^1

The amine L^{tz} was reacted in an inert argon atmosphere with $ClC(O)CH_2OMe$ in dry DCM. The reaction mixture was stirred over night before water was added. The resulting precipitate was washed with Et_2O and dried in vacuo. The hydrochloride $L^1 \cdot HCl$ was obtained as a beige coloured powder (Scheme 6). The 1H -NMR spectrum confirms the successful coupling, as it shows a singlet at 12.40 ppm resulting from the *NH* amide hydrogen atom. In the aromatic region a pattern resulting from the 2-substituted pyridine between 8.73–7.71 ppm and a singlet resulting from the 5-*tzH* proton attached to the five-membered thiazole ring can be seen at 8.40 ppm. At higher field, two singlets at 4.22 and 3.37 ppm are shown, resulting from the methylene- and methoxy group, respectively. The broad peak at 5.91 ppm was

assigned to water, exchanging protons with the hydrochloride. Therefore the signal is relatively broad and shifted to lower field, than expected for water dissolved in DMSO ^[88] (Figure 42).

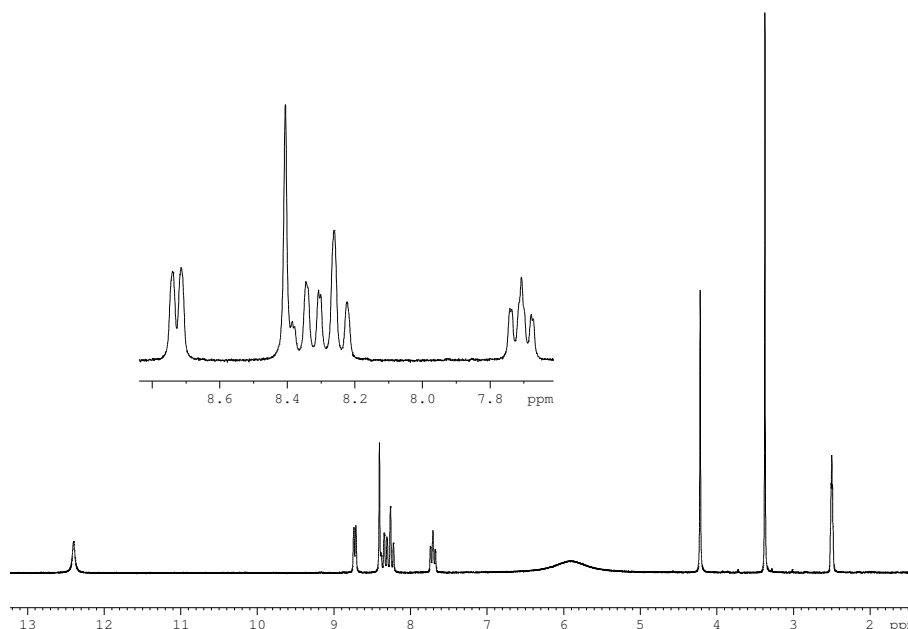


Figure 42: ¹H-NMR spectrum (200.13 MHz) of the hydrochloride of the expanded thiazole ligand $L^1 \cdot HCl$ in $DMSO-d_6$ at 298 K.

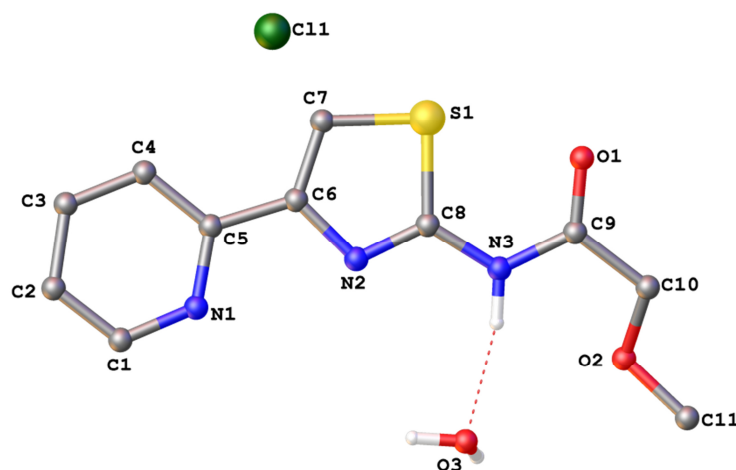


Figure 43: View of the molecular structure of the hydrochloride of the expanded thiazole ligand $L^1 \cdot HCl \cdot H_2O$. H-atoms are omitted except for the ones of the water molecule and the amide group.

Single crystals of the hydrochloride $L^1 \cdot HCl$, suitable for X-ray diffraction analysis, were obtained by recrystallization from MeOH. The ligand crystallises in the monoclinic space group Pc with one ligand molecule, a water molecule hydrogen bonded to the amide group and a chloride anion in the asymmetric unit (Figure 43). The crystallographic data for $L^1 \cdot HCl \cdot H_2O$ are summarised in Table 15.

In order to obtain the free base of the ligand, the hydrochloride $L^1 \cdot HCl$ was dissolved in water and treated with an aqueous solution of Na_2CO_3 . After washing and drying the resulting precipitate, the free base was obtained analytically pure as a beige coloured powder.

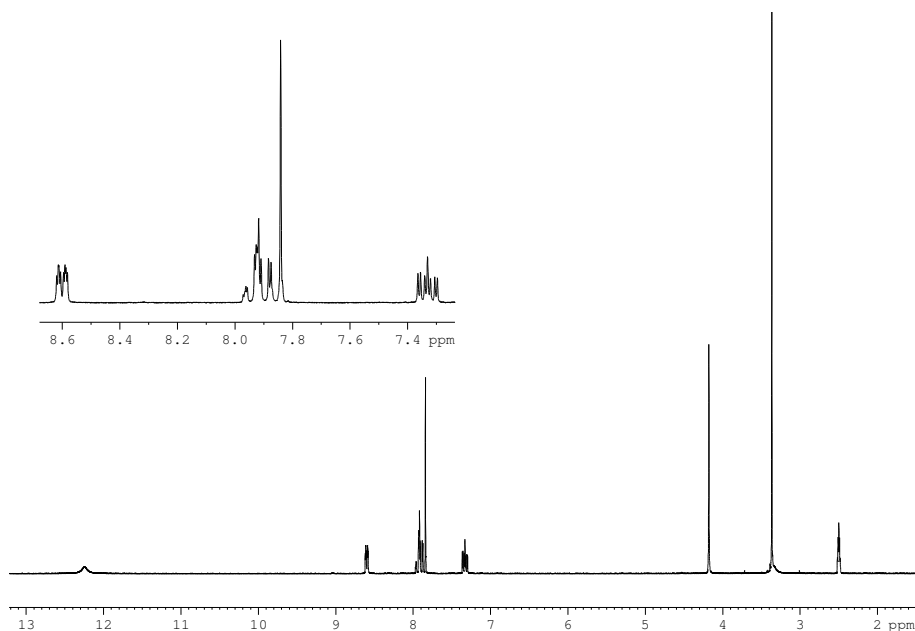


Figure 44: 1H -NMR spectrum (200.13 MHz) of the expanded thiazole ligand L^1 in $DMSO-d_6$ at 298 K.

The 1H -NMR spectrum of the free base L^1 is similar to the spectrum of its hydrochloride. However, no broad signal is observed at 5.91 ppm. Apart from the singlet resulting from the methoxy group (3.37 ppm), all signals of the aromatic groups are shifted to higher field which confirms the presence of an uncharged ligand molecule (Figure 44). The mass spectrum shows a peak resulting from the protonated, intact ligand molecule $[L^1 \cdot H]^+$ at $m/z = 250.1$ with a relative abundance of 100 % (Figure 45). In the IR spectrum absorption bands resulting from the $C=O$ double bond valence vibration at 1692 cm^{-1} and from the $N-H$ deformation vibration at 1554 cm^{-1} can be seen (Figure 46).^[89]

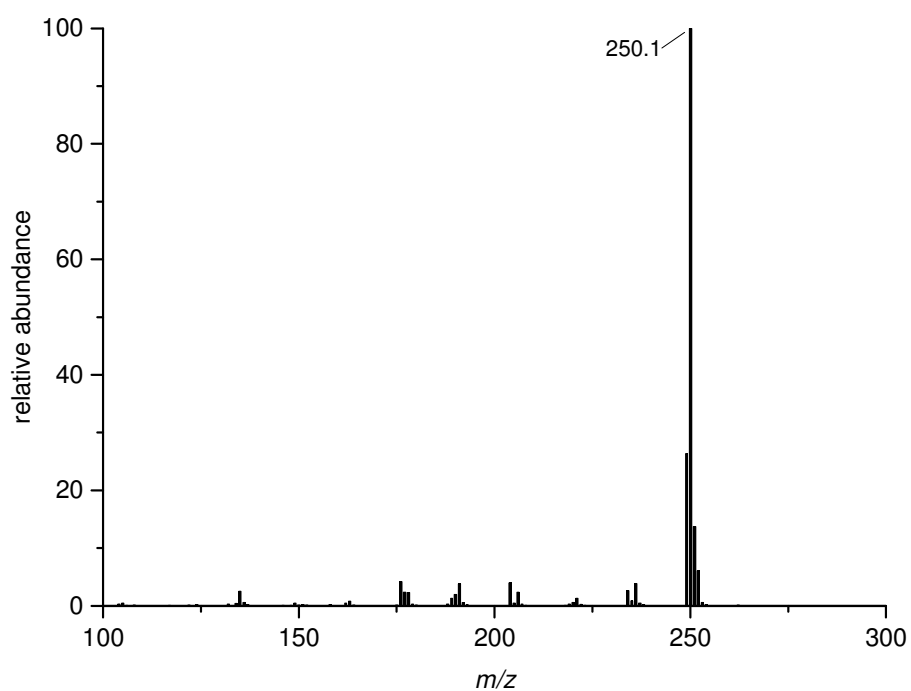


Figure 45: CI-MS spectrum of the expanded thiazole ligand L¹.

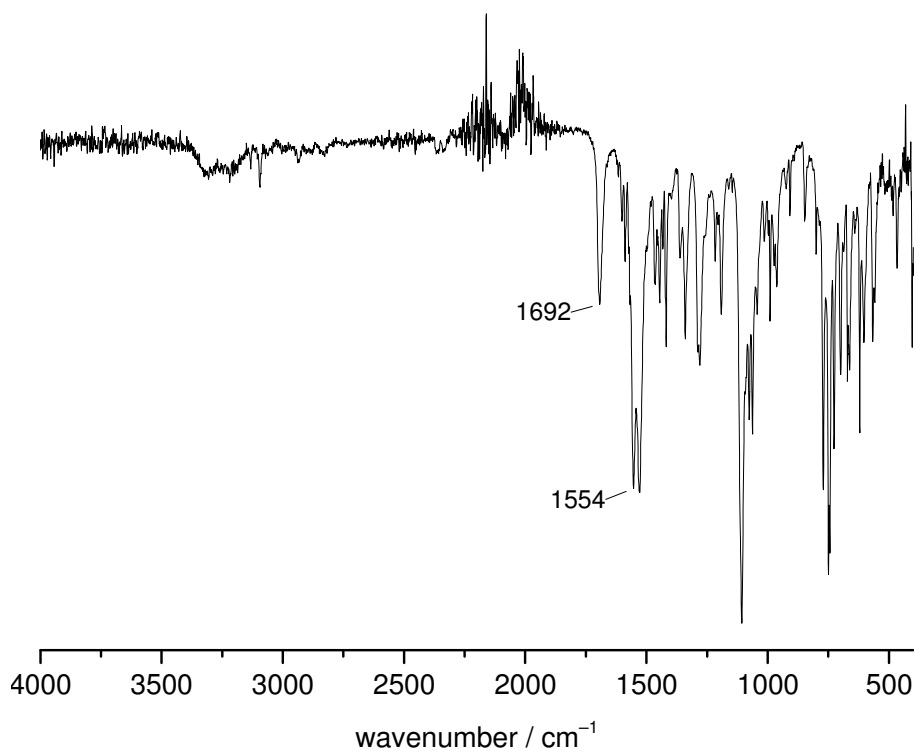
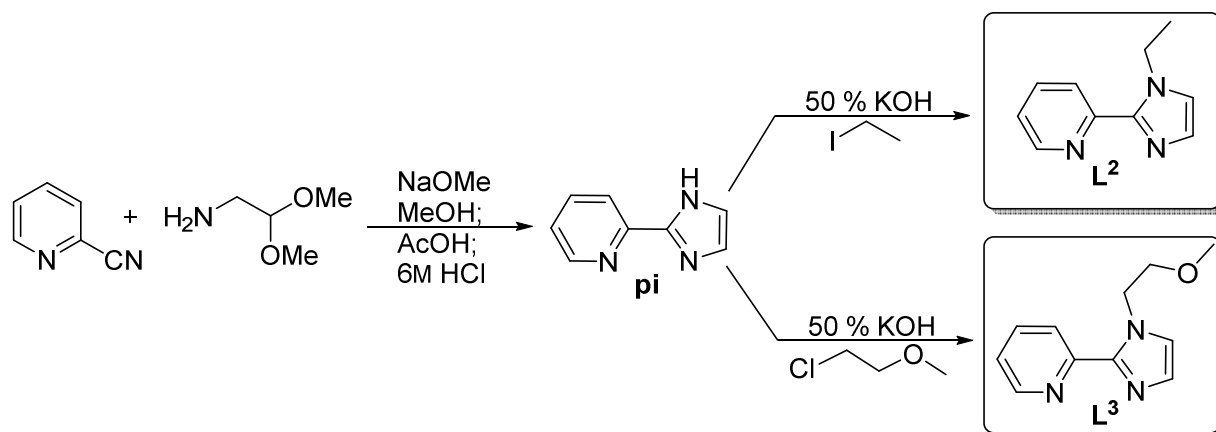


Figure 46: IR spectrum of the expanded thiazole ligand L¹.

The literature known ligand 2-(2-pyridyl)-imidazole (**pi**)^[90] was functionalised at the imidazole HN_{im} nitrogen with an ethyl- and a 2-methoxyethyl substituent in order to obtain the ligands 2-(2-pyridyl)-1-ethyl-imidazole (**L²**) and 2-(2-pyridyl)-1-(2-methoxyethyl)-imidazole (**L³**), respectively (Scheme 7).



Scheme 7: Synthesis of the expanded ligands **L²** and **L³** and the common precursor 2-(2-pyridyl)-imidazole (**pi**).

The common precursor of the herein discussed ligands, **pi**, was synthesised as reported elsewhere^[90] by mixing 2-pyridinecarbonitrile and 2-dimethoxyethylamine in a solution of NaOMe in MeOH. Addition of acid and subsequent alkaline work-up gave the imidazole **pi** as a beige coloured, analytically pure powder (Scheme 7).

The ¹H-NMR spectrum is in good agreement with the already reported data.^[90] The broad signal at 12.78 ppm results from the *NH* hydrogen of the imidazole. In the aromatic region, four signals of the 2-substituted pyridine can be seen in the range of 8.58–7.34 ppm. The signals of the carbon bound 4-*imdH* and 5-*imdH* hydrogen atoms of the imidazole are located at a lower field possessing the chemical shifts 7.22 and 7.08 ppm, respectively (Figure 47). The mass spectrum shows a peak at $m/z = 145.0$ which results from the complete molecule [**pi**]⁺ (Figure 48).

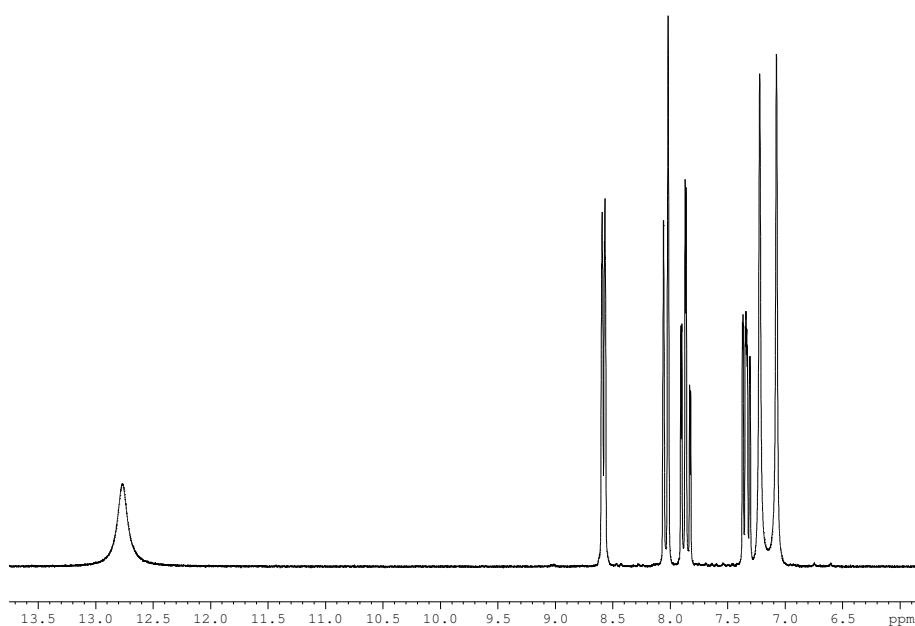


Figure 47: $^1\text{H-NMR}$ spectrum (200.13 MHz) of 2-(2-pyridyl)-imidazole (**pi**) in DMOS-d_6 at 298 K.

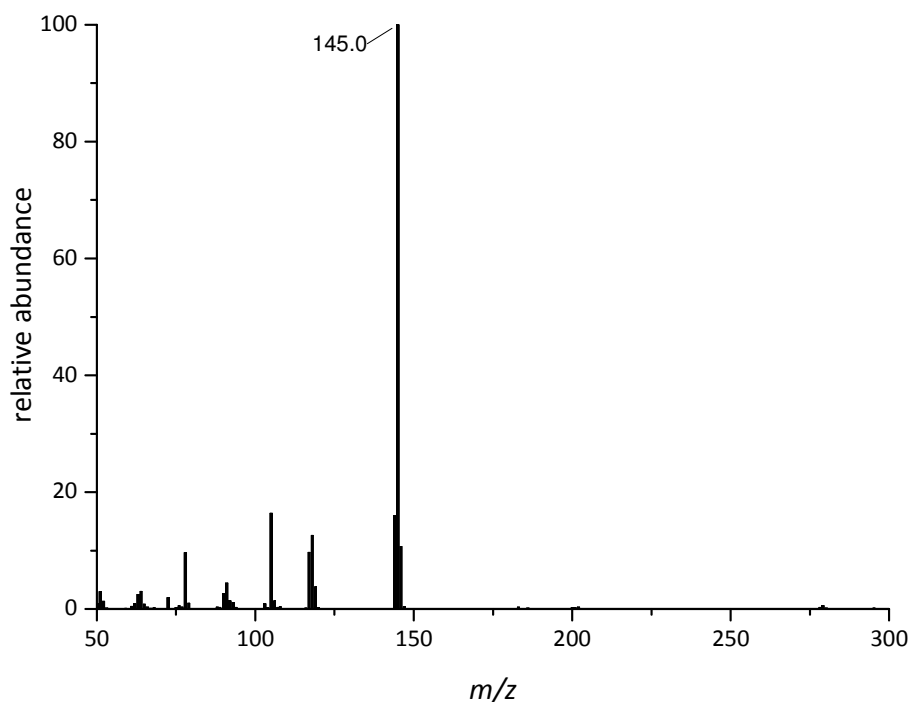


Figure 48: EI-MS spectrum of 2-(2-pyridyl)-imidazole (**pi**).

In the subsequent step, the precursor **pi** was dissolved in 50 % KOH and then reacted with either ethyl iodide or 2-chloroethyl methyl ester to give the ligand **L**² or **L**³, respectively (Scheme 7). Both raw products were purified by column chromatography and were obtained as analytically pure compounds. The $^1\text{H-NMR}$ spectra show additional resonances, compared to the precursor, in the aliphatic region

which were assigned to the substituents of the imidazole rings. Broad signals resulting from imidazole *NH* hydrogen atoms cannot be seen (Figure 49). Thus, the coupling reactions were successful which also could be confirmed by ^1H , ^{13}C -HMBC-correlation experiments. Cross peaks, resulting from the 3J -coupling of the NCH_2 hydrogen atoms of the nitrogen bonded methylene groups with the 2-imdC and 5-imdC carbon atoms of the imidazole, can be seen. Furthermore, cross peaks which result from the 3J -coupling of the 5-imdH hydrogen atoms with the nitrogen bonded NCH_2 carbon atoms, are observed (Figure 50).

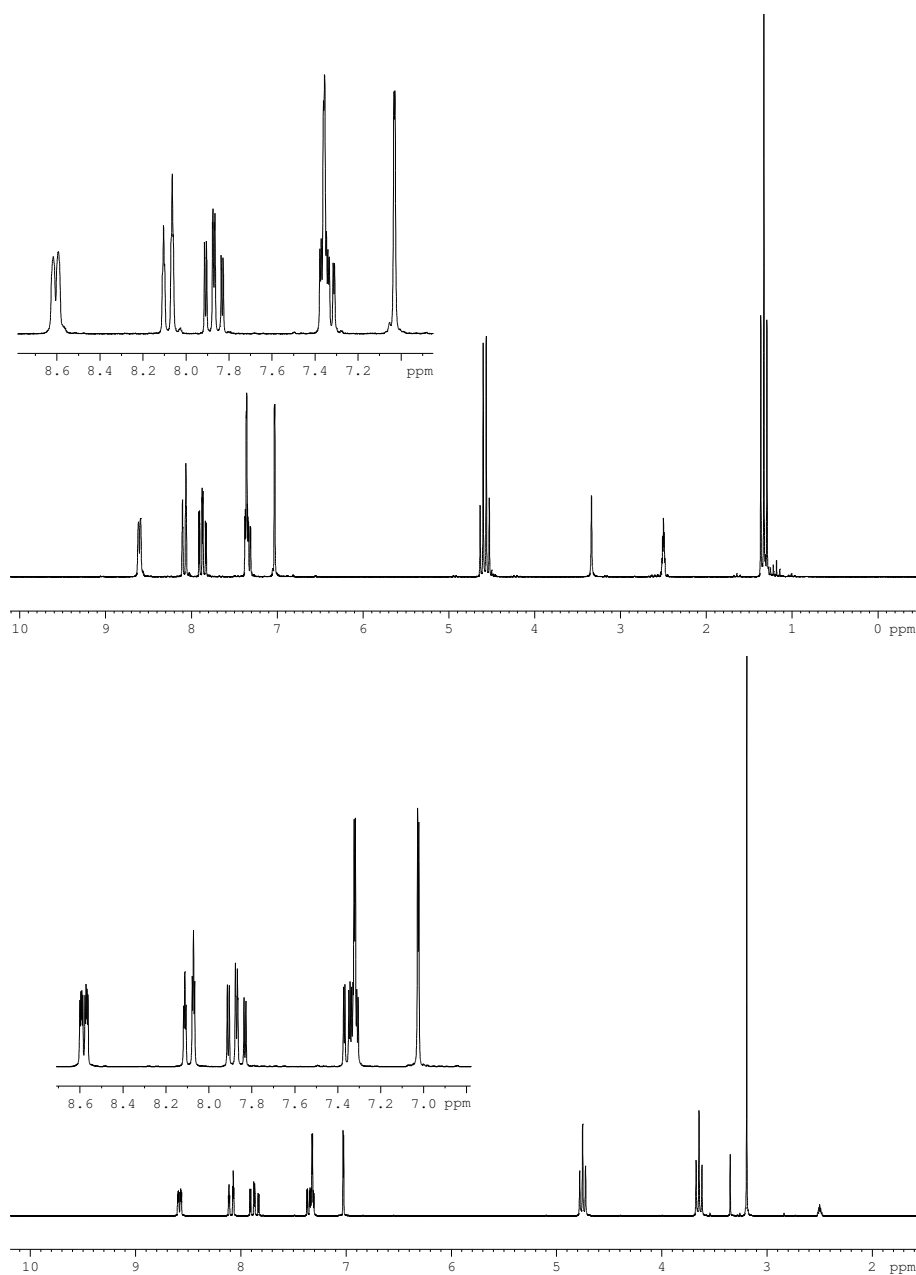


Figure 49: ^1H -NMR spectra (200.13 MHz) of *top*: the ethyl substituted ligand L^2 and *bottom*: the methoxyethyl substituted ligand L^3 in DMSO-d_6 at 298 K.

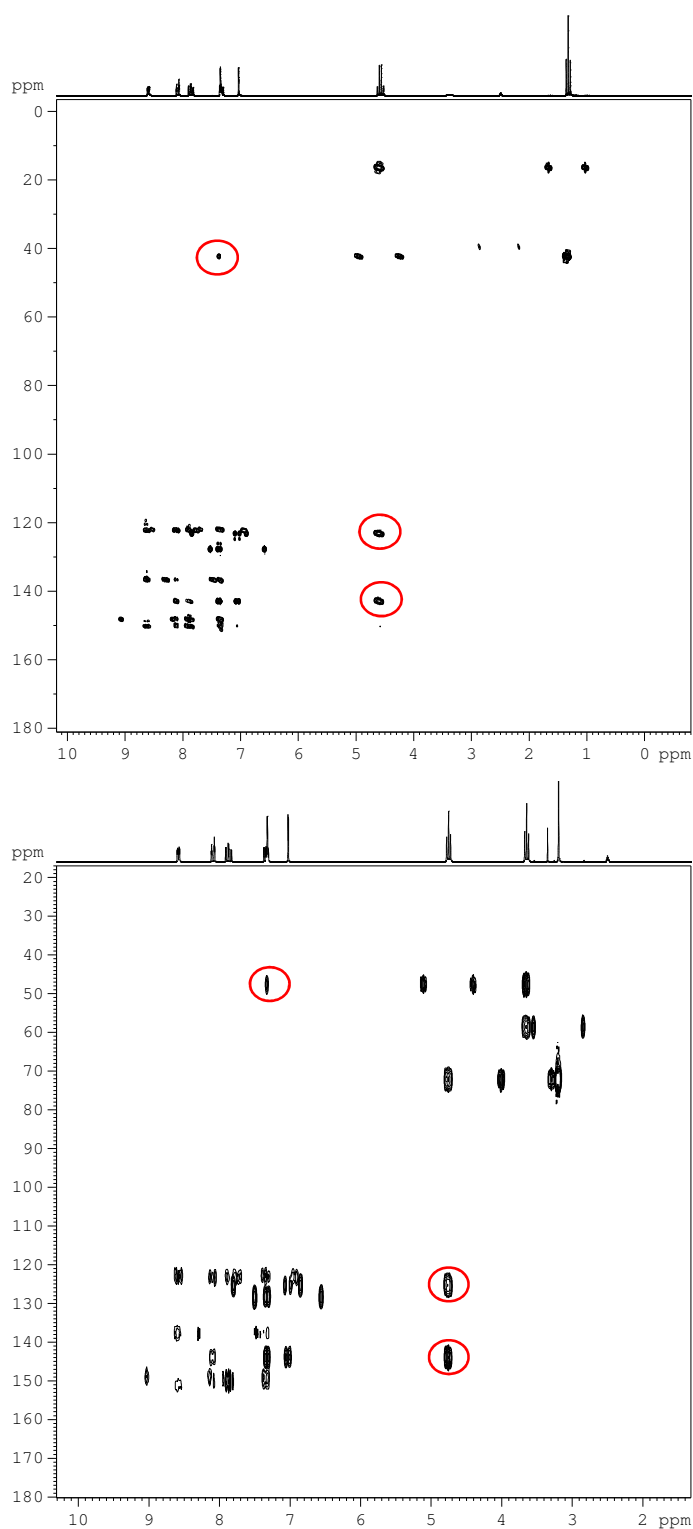


Figure 50: ^1H , ^{13}C -HMBC-correlations (200.13 MHz, optimised for 7 Hz) in DMSO-d_6 at 298 K of the *top*: ethyl substituted ligand L^2 and *bottom*: methoxyethyl substituted ligand L^3 ; the red circles indicate the cross peaks resulting from the 3J -couplings of nitrogen bonded NCH_2 groups with the quaternary 2-imdC carbon atoms and the 5-imdCH groups of the imidazole rings.

The mass spectra of both compounds show peaks resulting from the complete, protonated ligand molecules $[\text{L}^2\cdot\text{H}]^+$ and $[\text{L}^3\cdot\text{H}]^+$ at $m/z = 174.1024$ and 204.1132 (Figure 51), respectively.

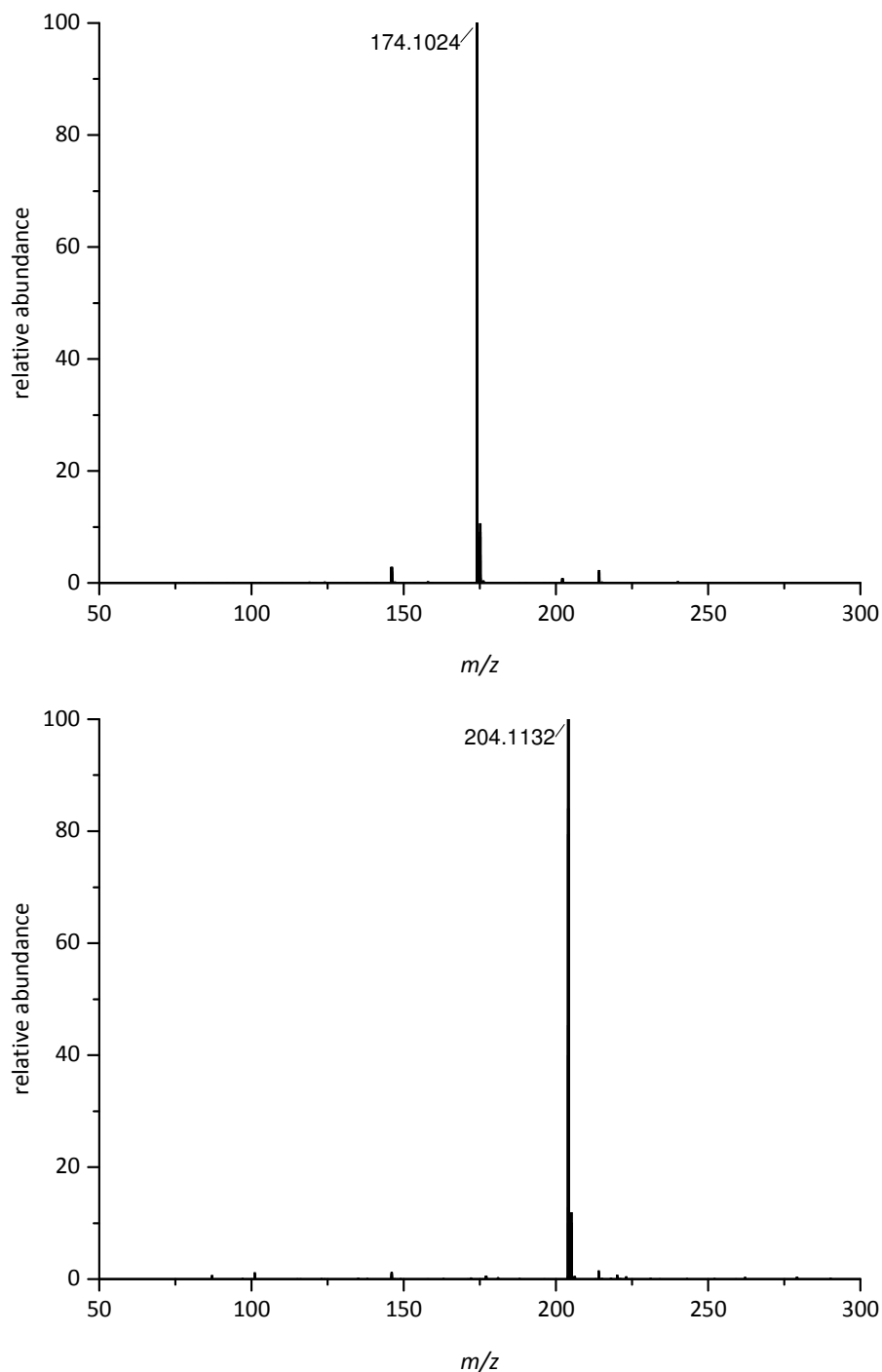


Figure 51: APCI-MS spectra of the *top*: ethyl substituted ligand L^2 and *bottom*: methoxyethyl substituted ligand L^3 .

UV/Vis spectra were recorded in order to determine the inner-ligand transitions. The spectrum of L^2 was measured in MeOH and shows a broad absorption band at 290 nm ($12810 \text{ M}^{-1} \text{ cm}^{-1}$) with a shoulder at 264 nm ($8870 \text{ M}^{-1} \text{ cm}^{-1}$). Rather sharp absorption bands can be seen at 204 and 210 nm (4680 and $5360 \text{ M}^{-1} \text{ cm}^{-1}$). The spectrum of L^3 was measured in MeCN and shows a broad absorptions band at 294 nm ($15850 \text{ M}^{-1} \text{ cm}^{-1}$) with a shoulder at 266 nm ($12010 \text{ M}^{-1} \text{ cm}^{-1}$) (Figure 52).

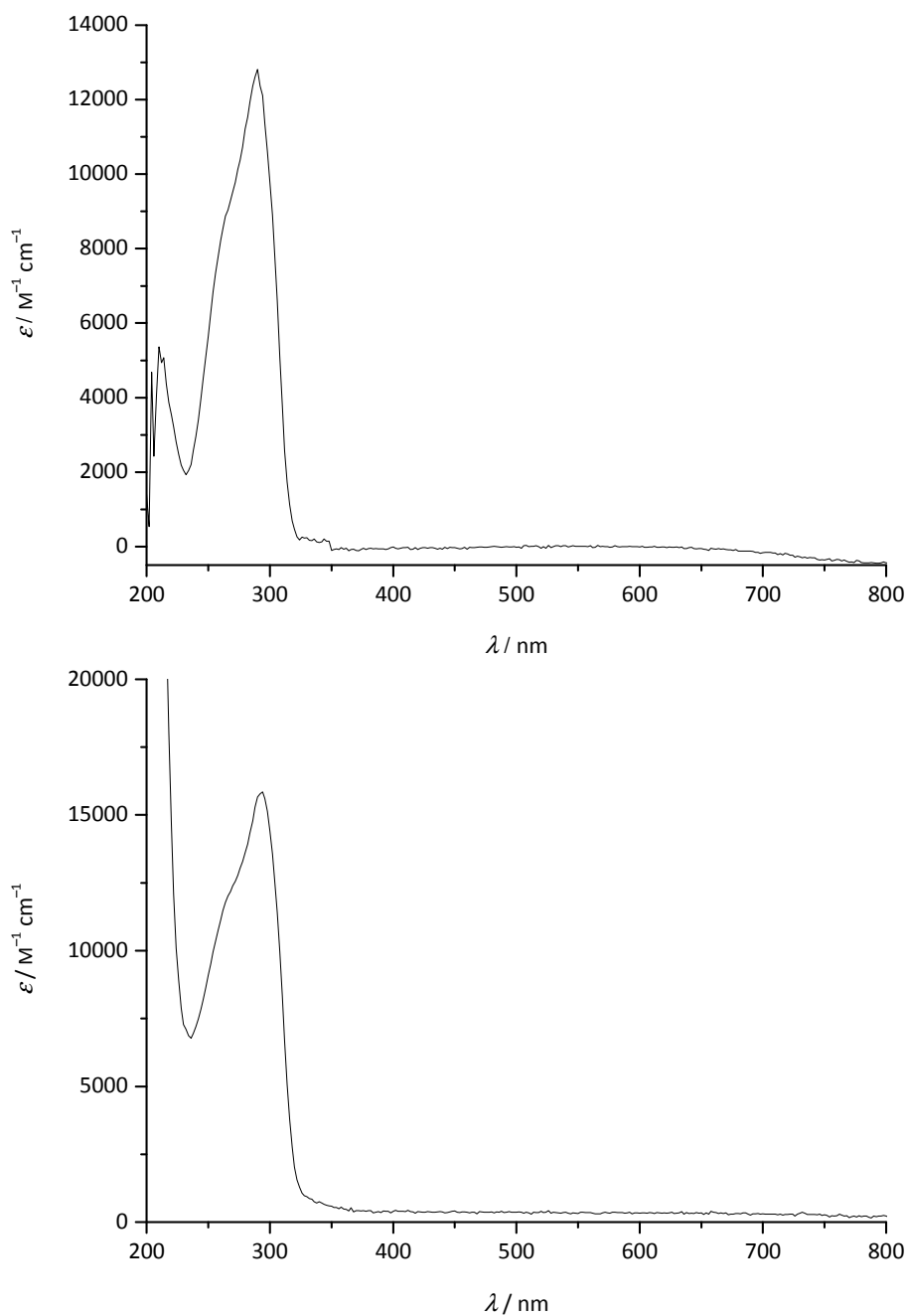
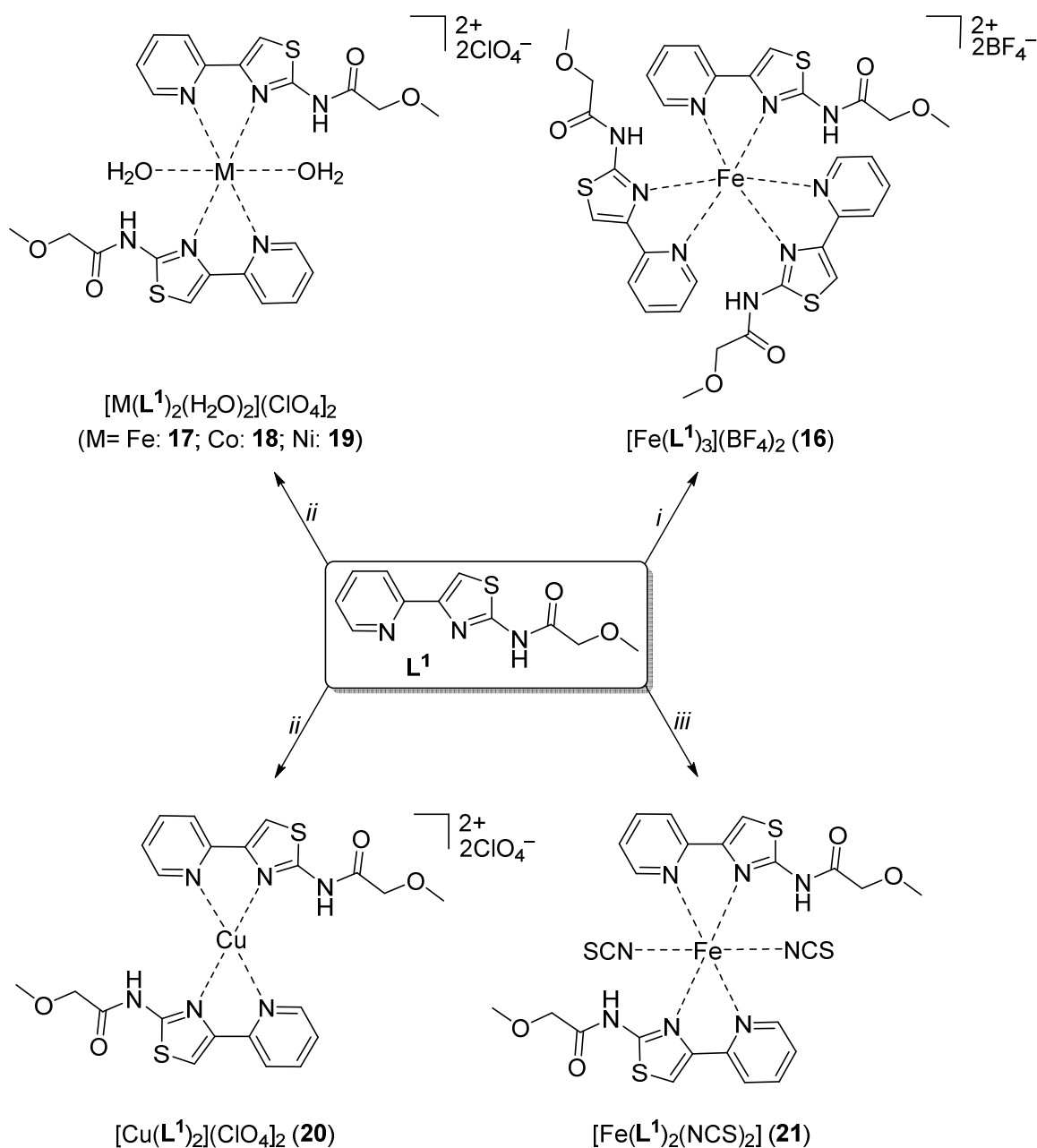


Figure 52: UV/Vis spectra of the *top*: ethyl substituted ligand L^2 in MeOH 0.01 mm and *bottom*: methoxyethyl substituted ligand L^3 in MeCN 0.1 mm.

2.2.2 Complexes with L¹

Scheme 8: Synthesis of the 3:1-type complex $[Fe(L^1)_3](BF_4)_2$ (**16**) and the 2:1-type complexes $[Fe(L^1)_2(H_2O)_2](ClO_4)_2$ (**17**), $[Co(L^1)_2(H_2O)_2](ClO_4)_2$ (**18**), $[Ni(L^1)_2(H_2O)_2](ClO_4)_2$ (**19**), $[Cu(L^1)_2](ClO_4)_2$ (**20**) and $[Fe(L^1)_2(NCS)_2]$ (**21**); i) $Fe(BF_4)_2 \cdot 6H_2O$, ii) $M(ClO_4)_2 \cdot 6H_2O$ (M = Fe, Co, Ni or Cu), iii) " $Fe(NCS)_2$ ".

The ability of the modified thiadiazole ligand L¹ to form 3:1-type complexes was investigated. As the ability was found to be limited, also a 2:1-type complex was prepared in order to gain more insight into the ligand field splitting provided by the ligand. A 3:1-type complex of ligand L¹ only could be obtained

with iron(II) tetrafluoroborate, whereas attempts with iron(II), cobalt(II), or nickel(II) perchlorate resulted in the formation of 2:1-type complexes, presumably possessing two molecules of water as coligands, as indicated by elemental analysis. An attempt with copper(II) perchlorate resulted in the formation of the 2:1-type complex without coligands. A nonionic 2:1-type complex could be obtained with “Fe(NCS)₂” (Scheme 8). Treating the ligand with “Fe(NCSe)₂” or “Fe(NCBH₃)₂” did not lead to the formation of any isolable compound.

Fe(BF₄)₂·6H₂O was reacted with three equivalents of L¹ in MeCN. After removing the solvent, the residue was dissolved in acetone. Upon adding pentane, a yellow precipitate formed which was identified as **16**·2H₂O (Scheme 8) by elemental analysis. When it was heated the complex decomposed at 218 °C. The IR spectrum confirms the presence of the anion and the ligand showing an absorption band resulting from the asymmetric valence vibration of the BF₄⁻ anion at 1054 cm⁻¹.^[91] Bands resulting from the C=O double bond valence vibration at 1697 cm⁻¹ and from the N–H deformation vibration at 1524 cm⁻¹ are observed (Figure 53).^[89] Owing to its low solubility, neither a mass spectrum nor an UV/Vis spectrum could be obtained from this compound.

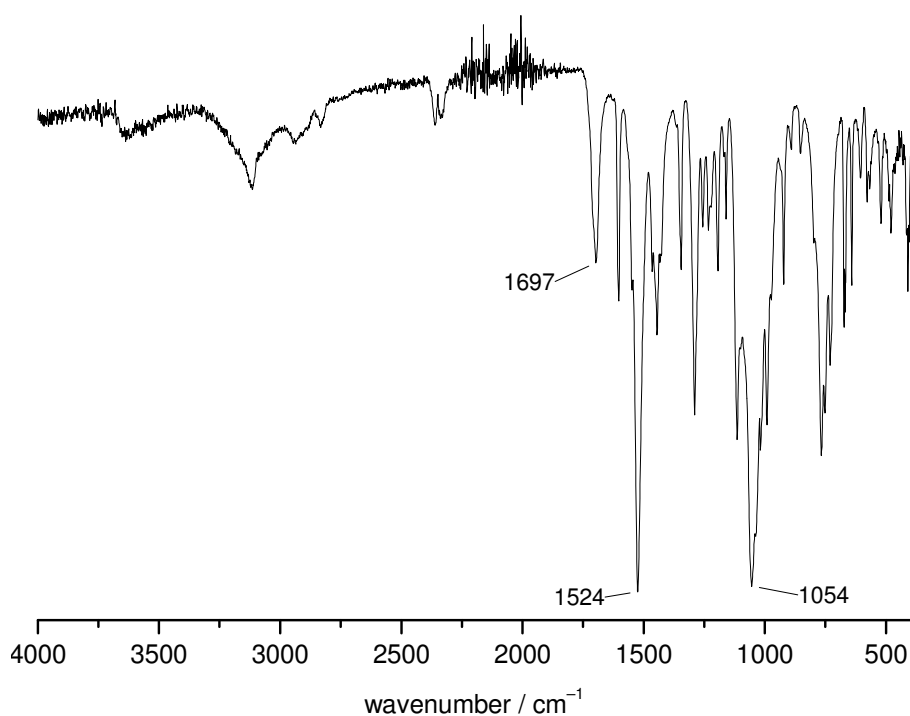


Figure 53: IR spectrum of [Fe(L¹)₃](BF₄)₂·2H₂O (**16**·2H₂O).

Measurements of the magnetic susceptibility were carried out in the range of 330–2 K and reveal that **16**·2H₂O comprises a HS state. The values lie in the range of $\chi_M T = 3.78$ (330 K) and $3.52 \text{ cm}^3 \text{ K mol}^{-1}$ (100 K) which are typical values for an iron(II) species in the HS state.^[81] The further decline between 100 and 2 K probably results from zero field splitting (Figure 54).

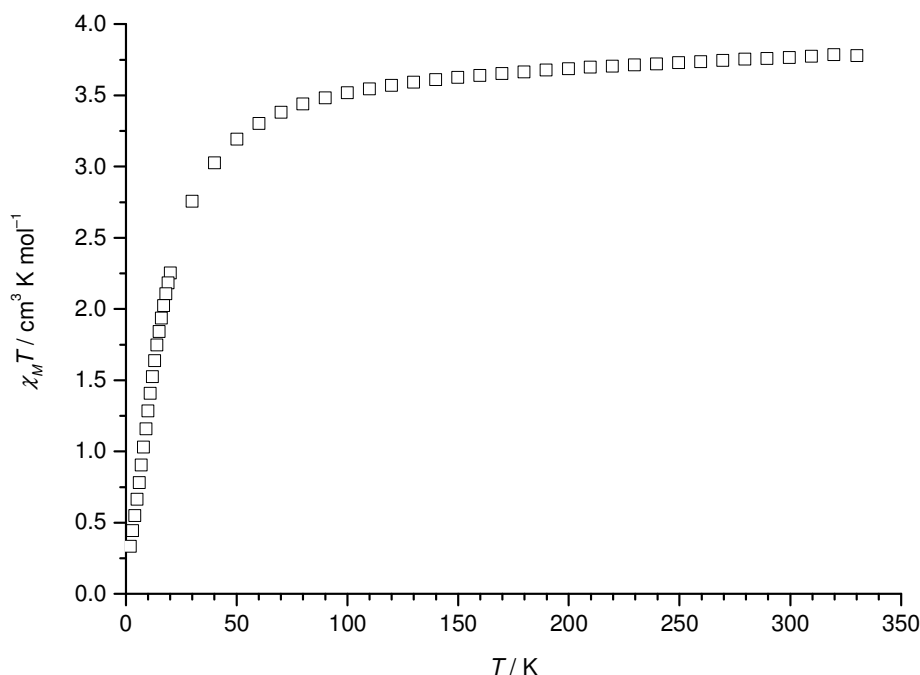


Figure 54: $\chi_M T$ vs. T plot of $[\text{Fe}(\text{L}^1)_3](\text{BF}_4)_2 \cdot 2\text{H}_2\text{O}$ (**16**·2H₂O).

Further attempts to synthesise related complexes with iron(II), cobalt(II) and nickel(II) perchlorate resulted in the formation of 2:1-type complexes with the general formula $[\text{M}(\text{L}^1)_2(\text{H}_2\text{O})_2](\text{ClO}_4)_2$ (M = Fe: **17**; M = Co: **18**; M = Ni: **19**) presumably comprising two molecules of water as coligands, as indicated by elemental analysis. Reactions with $\text{Cu}(\text{ClO}_4)_2 \cdot 6\text{H}_2\text{O}$ led to the formation of the 2:1-type complex $[\text{Cu}(\text{L}^1)_2](\text{ClO}_4)_2 \cdot \text{MeOH}$ (**20**·MeOH) which melts in the range of 158–160 °C (Scheme 8). All compounds have been investigated by elemental analysis and IR spectroscopy (not shown).

Furthermore, a 2:1-type complex with NCS^- coligands was prepared. Adding a ligand solution to a solution of “ $\text{Fe}(\text{NCS})_2$ ” in MeCN, led to the formation of a yellow precipitate which was identified as $[\text{Fe}(\text{L}^1)_2(\text{NCS})_2] \cdot 0.5\text{H}_2\text{O}$ (**21**·0.5 H₂O) by elemental analysis (Scheme 8). The IR spectrum of the latter compound shows a very strong absorption band at $\tilde{\nu} = 2031 \text{ cm}^{-1}$ resulting from the C–N valence vibration^[85] as well as the typical bands resulting from the N–H and C=O bonds at $\tilde{\nu} = 1601$ and 1708 cm^{-1} , respectively (Figure 55).^[89] Owing to the low solubility neither a UV/Vis spectrum nor a mass

spectrum could be obtained from **21**·0.5 H₂O. Measurements of the magnetic susceptibility were carried out in the range of 330–2 K and confirm the expected HS state of the metal ion (Figure 56). The values lie in the range of $\chi_{MT} = 3.54$ (330 K) to $3.22 \text{ cm}^3 \text{ K mol}^{-1}$ (100 K) which are typical values for an iron(II) species in the HS state.^[81] The further decline between 100 and 2 K probably results from zero field splitting.

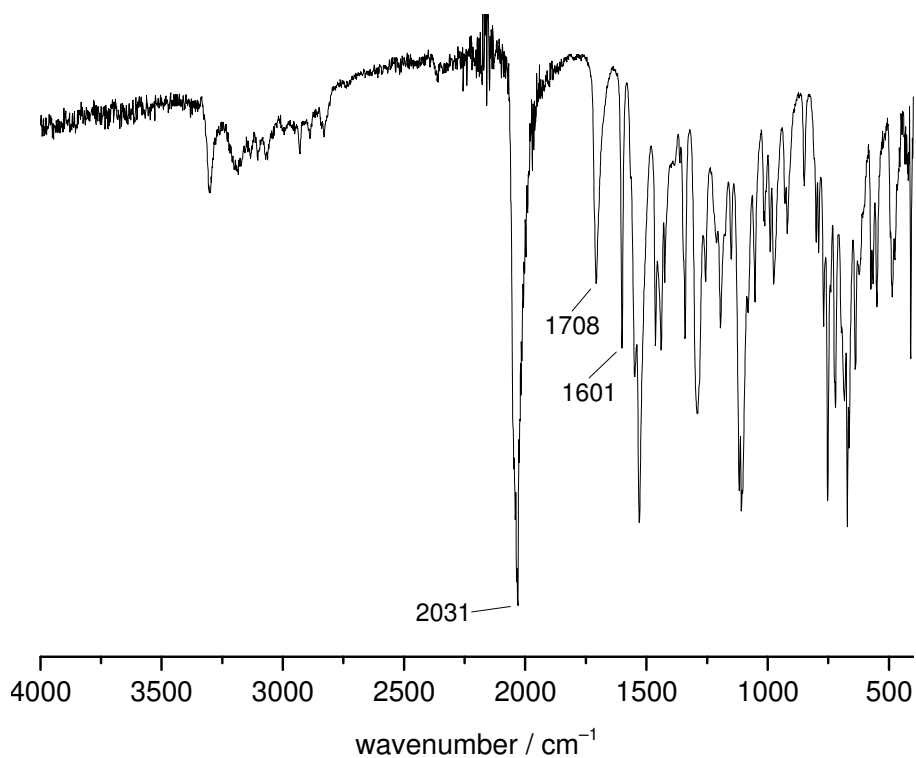


Figure 55: IR spectrum $[\text{Fe}(\text{L}^1)_2(\text{NCS})_2] \cdot 0.5\text{H}_2\text{O}$ (**21**·0.5H₂O).

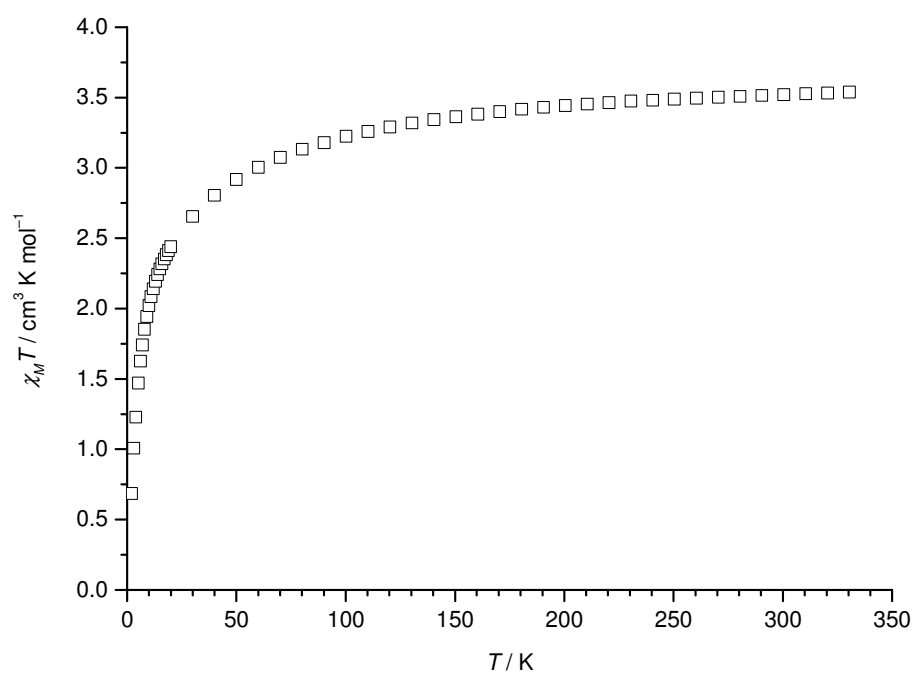


Figure 56: $\chi_M T$ vs. T plot of the magnetic susceptibility of $[\text{Fe}(\text{L}^1)_2(\text{NCS})_2] \cdot 0.5\text{H}_2\text{O}$ (**21**·0.5H₂O).

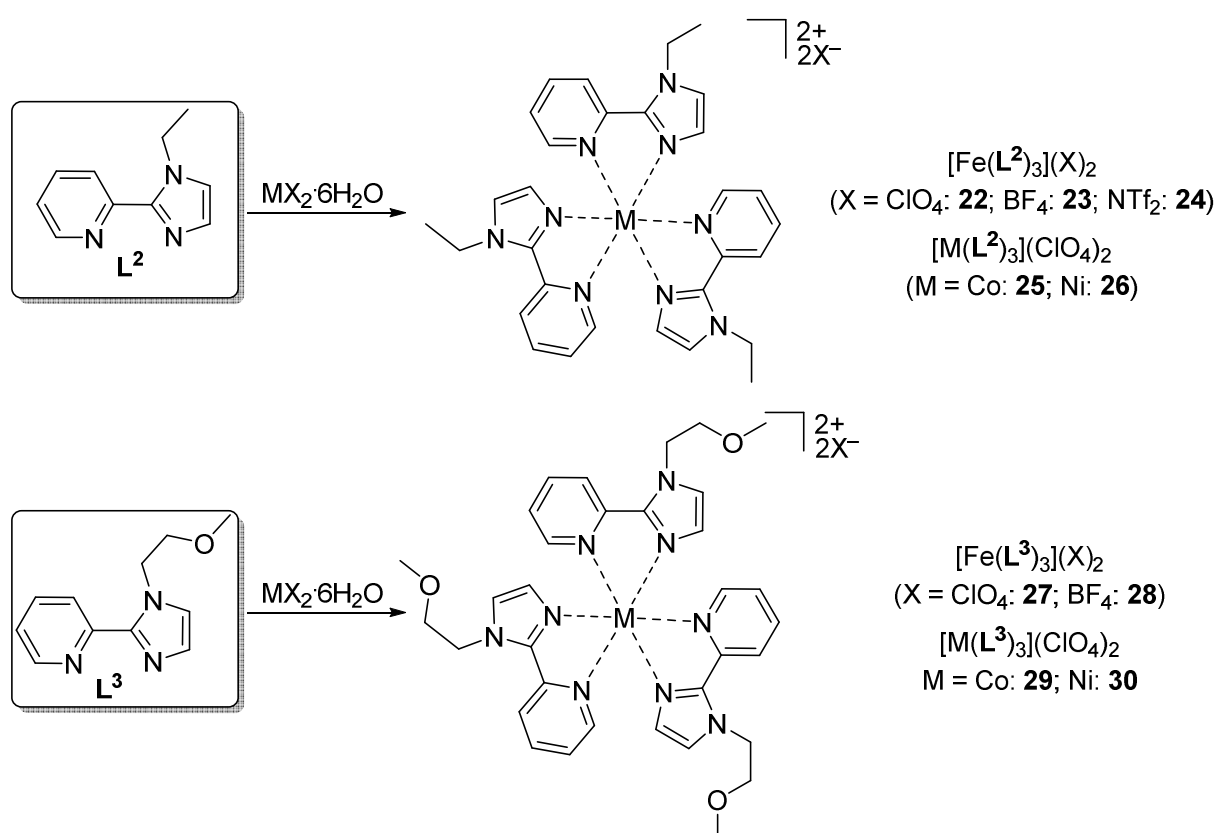
Table 7 summarises the complexes prepared with L^1 . In contrast to its precursor, L^1 forms a 3:1-type complex with $Fe(BF_4)_2 \cdot 6H_2O$. No fluoride abstraction is observed. However, only with the latter metal salt a 3:1-type complex, namely $[Fe(L^1)_3](BF_4)_2 \cdot 2H_2O$ (**16**·2H₂O) could be obtained. Further attempts with iron(II), cobalt(II), or nickel(II) perchlorate resulted in the formation of 2:1-type complexes, presumably possessing two molecules of water as coligands. With “Fe(NCS)₂” the 2:1-type complex $[Fe(L^1)_2(NCS)_2] \cdot 0.5H_2O$ (**21**·0.5H₂O) could be obtained. The iron(II) tetrafluoroborate **16**·2H₂O and the iron(II) isothiocyanate **21**·0.5H₂O exhibit iron(II) in the HS state until 2 K which could be confirmed with temperature dependent magnetic measurements. Hence, the ligand is too weak to form SCO-complexes. Besides, the copper complex $[Cu(L^1)_2](ClO_4)_2 \cdot MeOH$ (**20**·MeOH) was prepared. The tetrafluoroborate **16**·2H₂O decomposes at 218 °C, whereas the copper perchlorate **20**·MeOH melts at 158–160 °C. This indicates that the attachment of methoxyacetyl moiety to ligands can lower the melting points of the resulting complexes, presumably by increasing the entropy of fusion, as the analogous complex with L^{tz} does not melt up to 220 °C.

Table 7: Summary of complexes with L^1 .

		spin state	$T_{fus} / ^\circ C$
$[Fe(L^1)_3](BF_4)_2 \cdot 2H_2O$	(16 ·2H ₂ O)	HS	218 (dec.)
$[Fe(L^1)_2(H_2O)_2](ClO_4)_2$	(17)	-	221–222
$[Co(L^1)_2(H_2O)_2](ClO_4)_2 \cdot H_2O$	(18 ·H ₂ O)	-	> 220
$[Ni(L^1)_2(H_2O)_2](ClO_4)_2$	(19)	-	> 220
$[Cu(L^1)_2](ClO_4)_2 \cdot MeOH$	(20 ·MeOH)	-	158–160
$[Fe(L^1)_2(NCS)_2] \cdot 0.5H_2O$	(21 ·0.5H ₂ O)	HS	> 220

2.2.3 Complexes with L^2 and L^3

The ability of the substituted imidazole ligands L^2 and L^3 to form 3:1-type complexes was investigated. Apart from the substitution at the N_{im} atom of the imidazole moiety (ethyl in the case of L^2 and methoxyethyl in the case of L^3) both ligands are identical. A series of 3:1-type complexes was prepared with L^2 and L^3 , respectively. Using $Fe(ClO_4)_2 \cdot 6H_2O$ (**22**· H_2O , **27**) and $Fe(BF_4)_2 \cdot 6H_2O$ (**23**· H_2O , **28**) as well as $Co(ClO_4)_2 \cdot 6H_2O$ (**25**· $1.5H_2O$, **29**) and $Ni(ClO_4)_2 \cdot 6H_2O$ (**26**· $0.5H_2O$, **30**) complexes were obtained from both ligands. With $Fe(NTf_2)_2 \cdot 6H_2O$ only complex **24** comprising the ethyl substituted ligand L^2 could be obtained (Scheme 9).



Scheme 9: Synthesis of *top*: $[Fe(L^2)_3](ClO_4)_2$ (**22**: M = Fe, X = ClO_4^-), $[Fe(L^2)_3](BF_4)_2$ (**23**), $[Fe(L^2)_3](NTf_2)_2$ (**24**), $[Co(L^2)_3](ClO_4)_2$ (**25**), $[Ni(L^2)_3](ClO_4)_2$ (**26**) and *bottom*: $[Fe(L^3)_3](ClO_4)_2$ (**27**), $[Fe(L^3)_3](BF_4)_2$ (**28**), $[Co(L^3)_3](ClO_4)_2$ (**29**), $[Ni(L^3)_3](ClO_4)_2$ (**30**).

The iron(II) perchlorate compounds $[Fe(L^2)_3](ClO_4)_2 \cdot H_2O$ (**22**· H_2O) and $[Fe(L^3)_3](ClO_4)_2$ (**27**) were prepared by mixing methanolic solutions of the ligands and $Fe(ClO_4)_2 \cdot 6H_2O$. After isolation of the resulting precipitate the compounds were obtained as analytically pure, red amorphous powders. Heating of the two perchlorates did not result in a melting process or a colour change. However, both compounds decomposed at 218 °C (**22**· H_2O) and 187 °C (**27**), respectively. The formation of 3:1-type complexes was

confirmed by ESI mass spectrometry. The spectra show peaks provoked by the dicationic chromophores $[\text{Fe}(\text{L}^2)_3]^{2+}$ and $[\text{Fe}(\text{L}^3)_3]^{2+}$ at $m/z = 287.6095$ and 332.6255 , respectively. Further peaks resulting from the monocationic species $[\text{Fe}(\text{L}^2)_2](\text{ClO}_4)^+$ and $[\text{Fe}(\text{L}^3)_2](\text{ClO}_4)^+$ can be seen at $m/z = 501.0717$ and 561.0955 , respectively. Additionally, signals resulting from the protonated free ligand L^2 and L^3 are observed at $m/z = 174.1029$ and 204.1130 , respectively (Figure 57). The IR spectra confirm the formation of perchlorate compounds as they show characteristic bands resulting from the asymmetric valence vibration of the ClO_4^- anion at 1073 ($\mathbf{22} \cdot \text{H}_2\text{O}$) and 1071 cm^{-1} ($\mathbf{27}$) as well as the bands resulting from the asymmetric deformation vibration at 620 cm^{-1} ($\mathbf{22} \cdot \text{H}_2\text{O}$, $\mathbf{27}$) (Figure 58).^[91]

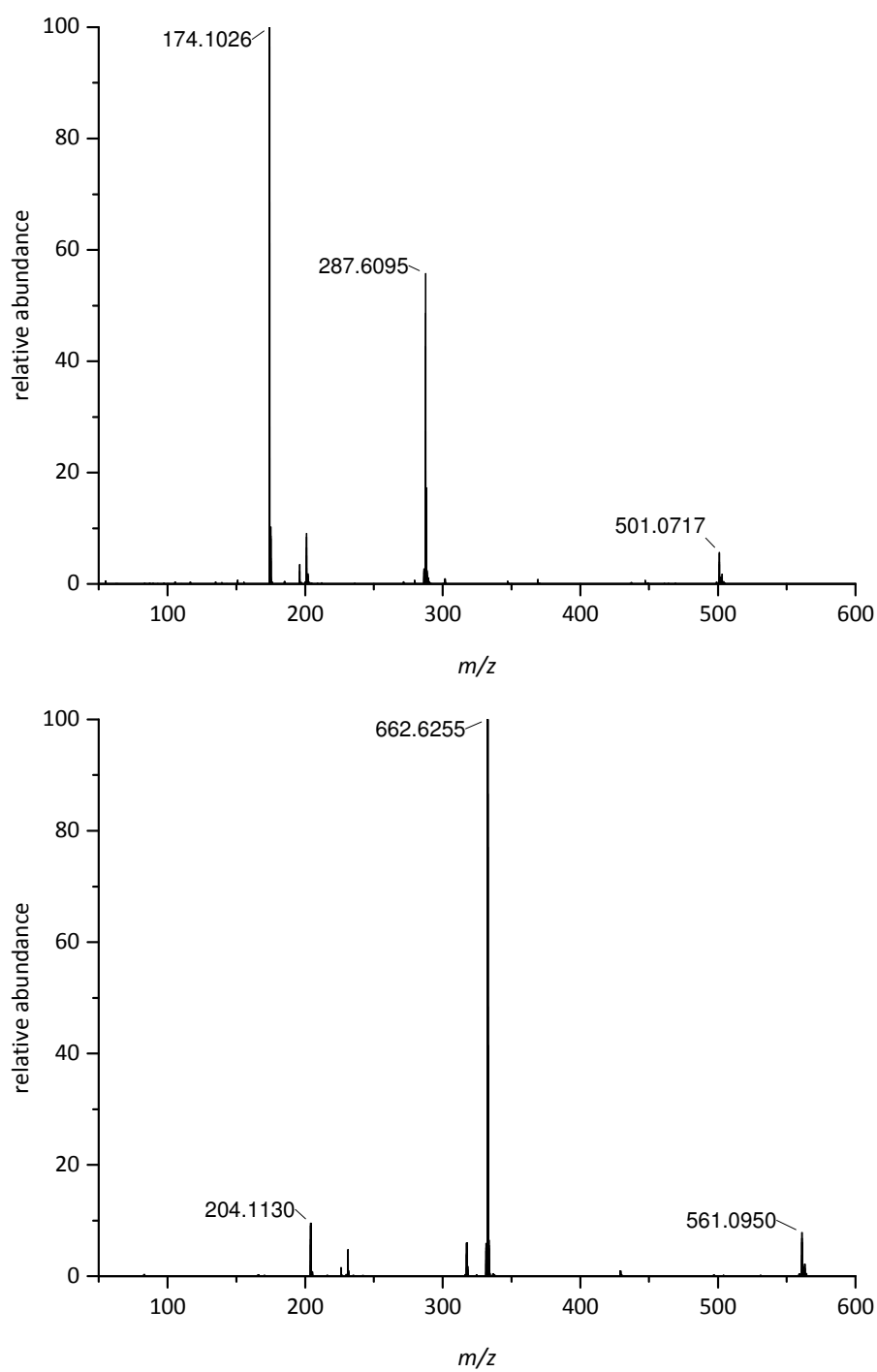


Figure 57: ESI-MS spectra of *top*: $[\text{Fe}(\text{L}^2)_3](\text{ClO}_4)_2 \cdot \text{H}_2\text{O}$ (**22**· H_2O) and *bottom*: $[\text{Fe}(\text{L}^3)_3](\text{ClO}_4)_2$ (**27**).

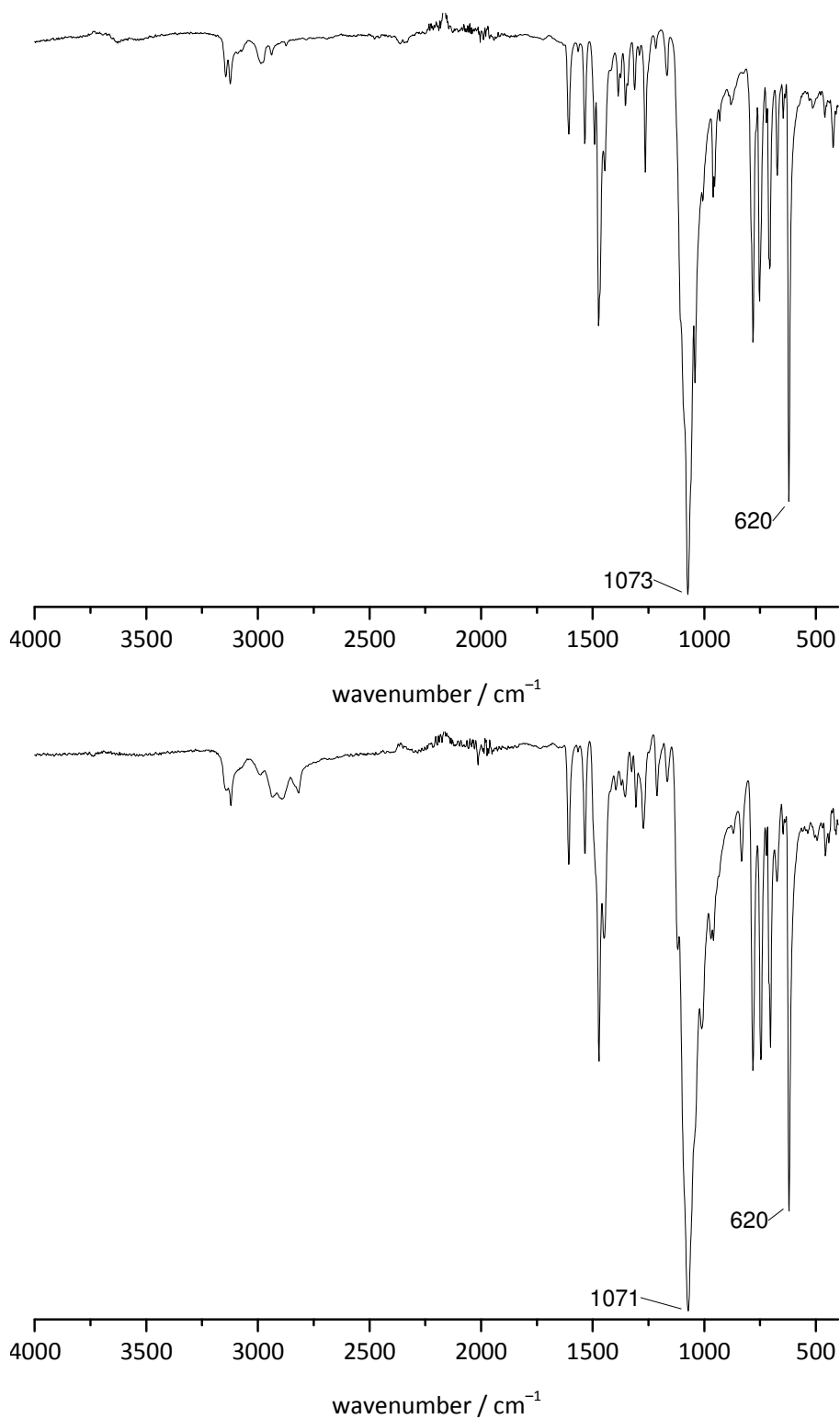


Figure 58: IR spectra of *top*: $[\text{Fe}(\text{L}^2)_3](\text{ClO}_4)_2 \cdot \text{H}_2\text{O}$ (**22**·H₂O) and *bottom*: $[\text{Fe}(\text{L}^3)_3](\text{ClO}_4)_2$ (**27**).

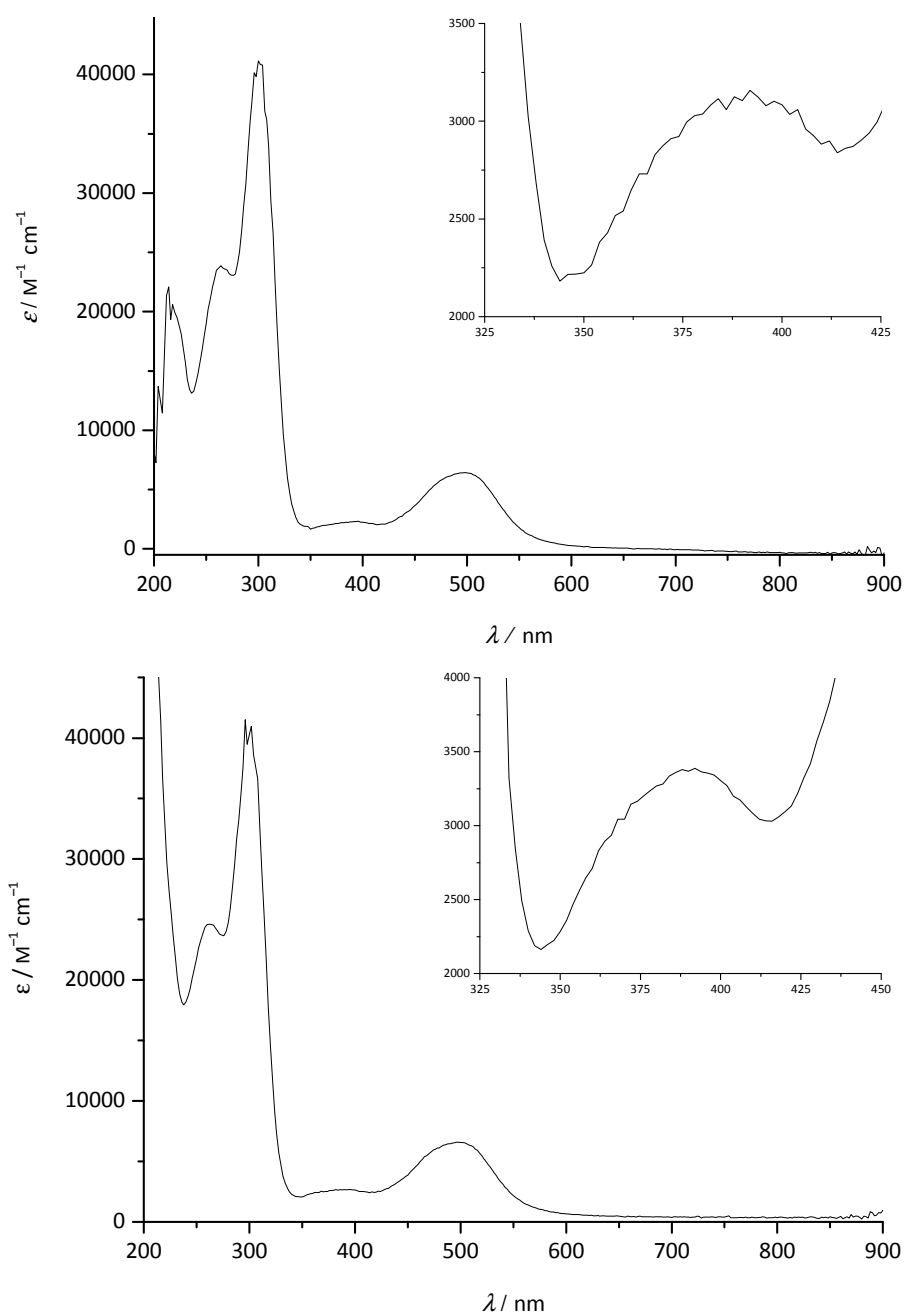


Figure 59: UV/Vis-spectra of *top*: $[\text{Fe}(\text{L}^2)_3](\text{ClO}_4)_2 \cdot \text{H}_2\text{O}$ (**22**· H_2O) in MeOH 0.1mm (inset: 1 mm) and *bottom*: $[\text{Fe}(\text{L}^3)_3](\text{ClO}_4)_2$ (**27**) in MeOH 0.1mm (inset: 1 mm).

The UV/Vis spectra show absorption bands in the UV region, similar to the patterns observed in the spectra of the free ligands, at 204, 214, 264 and 300 nm (**22**· H_2O) and at 262 and 296 nm (**27**). Additionally, both spectra show typical CT absorption bands for an iron(II) LS species at 392 (2310) and 498 nm ($6440 \text{ M}^{-1} \text{ cm}^{-1}$) (**22**· H_2O) and at 392 (3387) and 496 nm ($6600 \text{ M}^{-1} \text{ cm}^{-1}$) (**27**). Absorption bands resulting from d-d-transitions are rather weak and therefore presumably masked by the CT bands (Figure 59).^[38,40,81,92]

The iron(II) tetrafluoroborate compounds $[\text{Fe}(\text{L}^2)_3](\text{BF}_4)_2 \cdot \text{H}_2\text{O}$ (**23**·H₂O) and $[\text{Fe}(\text{L}^3)_3](\text{BF}_4)_2$ (**28**) were prepared by mixing methanolic solutions of the ligands and $\text{Fe}(\text{BF}_4)_2 \cdot 6\text{H}_2\text{O}$. After isolation of the resulting precipitate the compounds were obtained as analytically pure red amorphous powders which melt at 225 °C (**23**·H₂O) and 170 °C (**28**), respectively. No colour change was observed upon heating. ESI mass spectrometry confirmed the formation of a 3:1-type complex in the case of compound **28** featuring the methoxyethyl substituted ligand. The spectrum shows peaks provoked by the dicationic chromophores $[\text{Fe}(\text{L}^3)_3]^{2+}$ and $[\text{Fe}(\text{L}^3)_2]^{2+}$ at $m/z = 332.6253$ and 231.0726 , respectively. A signal resulting from the protonated free ligand can be seen at $m/z = 204.1130$. However, in the mass spectrum of complex **23**·H₂O, featuring the ethyl substituted ligand, such patterns are missing. Instead, signals resulting from the free protonated ligand and from the protonated ligand without ethyl substituent can be seen at $m/z = 174.1021$ and 146.0711 , respectively (Figure 60). The IR spectra confirm the formation of a tetrafluoroborate compound in both cases as they show characteristic bands resulting from the asymmetric valence vibration of the BF_4^- anion at 1034 (**23**·H₂O) and 1027 (**28**) cm^{-1} as well as bands resulting from the asymmetric deformation vibration at 519 cm^{-1} (**23**·H₂O, **28**) (Figure 61).^[91]

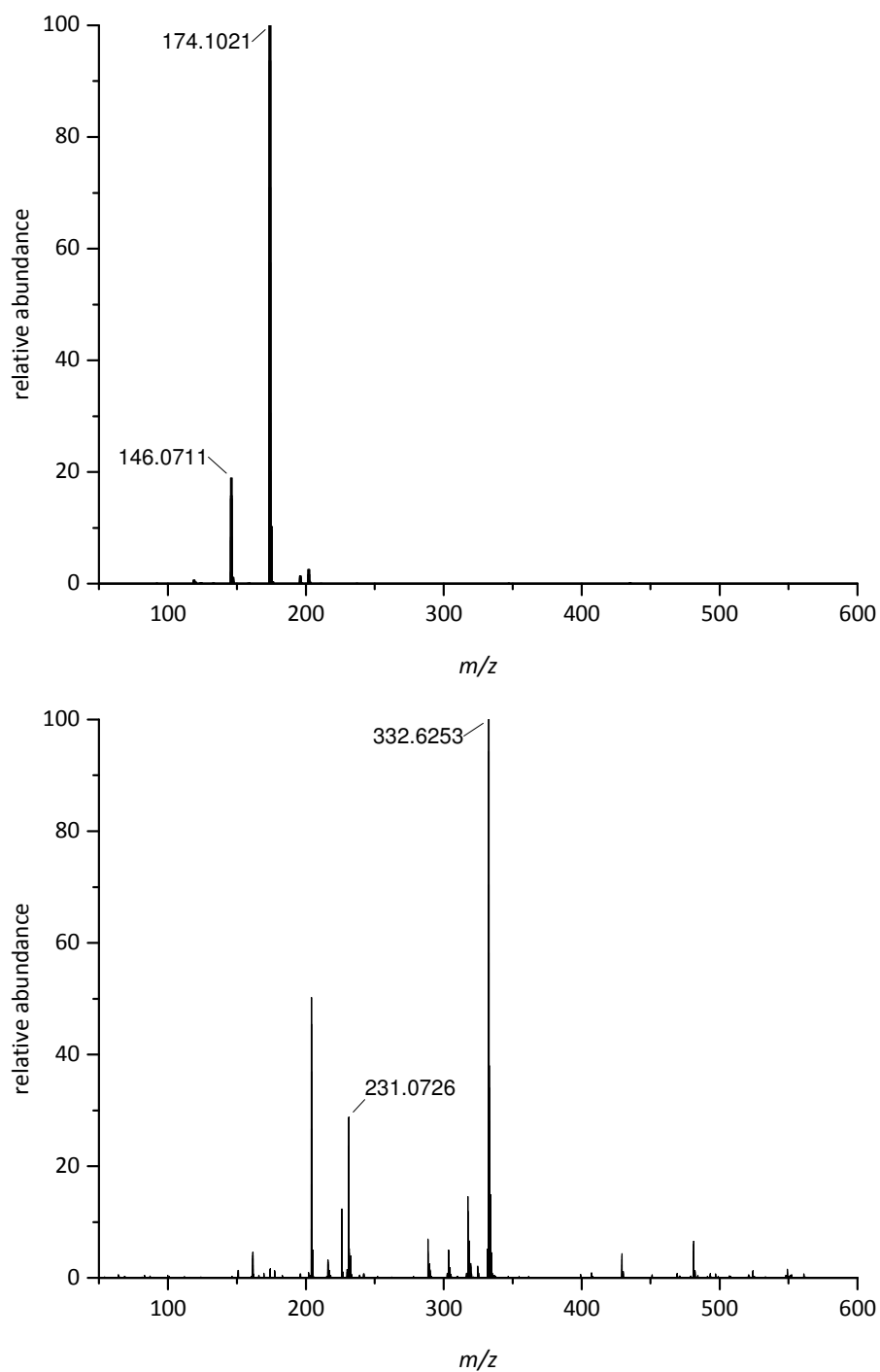


Figure 60: ESI-MS spectra of *top*: $[\text{Fe}(\text{L}^2)_3](\text{BF}_4)_2 \cdot \text{H}_2\text{O}$ (**23**· H_2O) and *bottom*: $[\text{Fe}(\text{L}^3)_3](\text{BF}_4)_2$ (**28**).

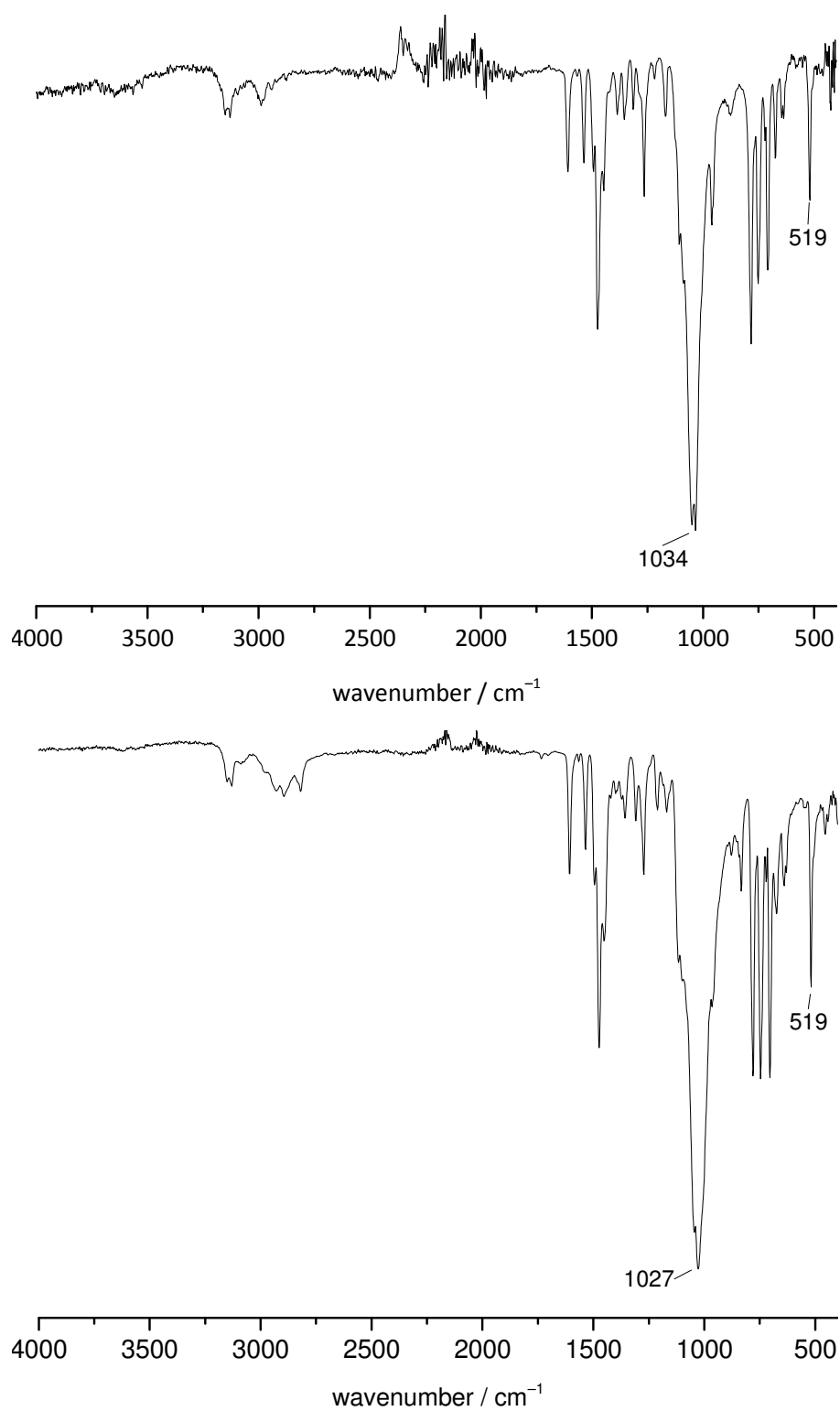


Figure 61: IR spectra of *top*: [Fe(L²)₃](BF₄)₂·H₂O (**23**·H₂O) and *bottom*: [Fe(L³)₃](BF₄)₂ (**28**).

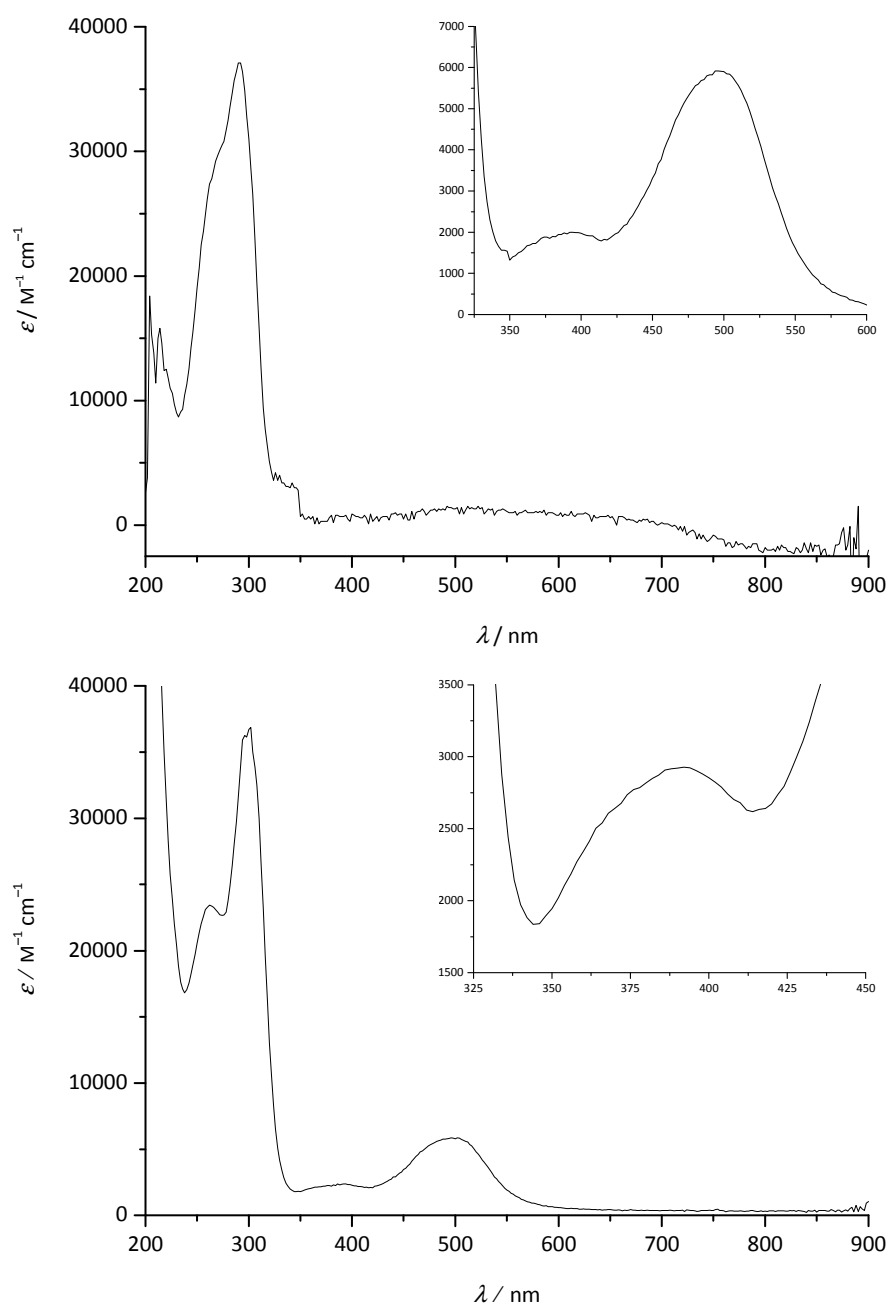


Figure 62: UV/Vis-spectra of *top*: $[\text{Fe}(\text{L}^2)_3](\text{BF}_4)_2 \cdot \text{H}_2\text{O}$ (**23**· H_2O) in MeOH 0.01 mm (inset: 0.1 mm) and *bottom*: $[\text{Fe}(\text{L}^3)_3](\text{BF}_4)_2$ (**28**) in MeOH 0.1 mm (inset: 1mm).

The UV/Vis spectra show absorption bands in the UV region, similar to the patterns observed in the spectra of the free ligands, at 204, 214, 268 and 292 nm (**23**· H_2O) and at 262 and 302 nm (**28**). Additionally, typical CT absorption bands for an iron(II) LS species can be seen at 392 (2000) and 495 nm ($5920 \text{ M}^{-1} \text{ cm}^{-1}$) (**23**· H_2O) and at 392 (2929) and 496 nm ($5860 \text{ M}^{-1} \text{ cm}^{-1}$) (**28**). Absorption bands resulting from d-d-transitions are rather weak and therefore presumably masked by the CT bands (Figure 59).

[38,40,81,92]

DSC measurements of $[\text{Fe}(\text{L}^2)_3](\text{BF}_4)_2 \cdot \text{H}_2\text{O}$ (**23**· H_2O) featuring the ethyl substituted ligand were carried out three times in the heating and the cooling mode with a scan rate of 2 K min^{-1} (Figure 63). The heating curve of the first cycle shows an endothermic peak at $242 \text{ }^\circ\text{C}$ ($T_{\text{onset}} = 239 \text{ }^\circ\text{C}$) resulting from a melting process. The enthalpy of fusion $\Delta H_{\text{fus}} = 36 \text{ kJ mol}^{-1}$ for this process is in the range of usually determined values of compounds consisting of one dication and two monoanions.^[93–95] The cooling curve of the first cycle shows an exothermic peak at $221 \text{ }^\circ\text{C}$ ($T_{\text{onset}} = 224 \text{ }^\circ\text{C}$) resulting from the crystallisation of the compound. The smaller endothermic peak in the heating curve at $181 \text{ }^\circ\text{C}$ ($T_{\text{onset}} = 175 \text{ }^\circ\text{C}$, $\Delta H = 14 \text{ kJ mol}^{-1}$) could result from a solid-solid phase transition or loss of solvent as it is not observed again after the first cycle. In the second cycle the heating curve shows only one endothermic peak at $239 \text{ }^\circ\text{C}$ ($T_{\text{onset}} = 235 \text{ }^\circ\text{C}$) and the cooling curve holds one exothermic peak at $214 \text{ }^\circ\text{C}$ ($T_{\text{onset}} = 216 \text{ }^\circ\text{C}$). Hence, the compound's melting and solidifying process shows a hysteresis of 25 K ($T_{\text{onset}} = 19 \text{ K}$) which is a typical value of ionic compounds.^[93–95] The doublet shape of the exothermic peaks might result from the presence of two isomers with different crystal packing that solidify at distinct temperatures. Further investigations on this issue could for example be made by powder X-ray diffraction analysis at elevated temperatures. The observations of the second cycle also were made in a subsequent third cycle (not shown).

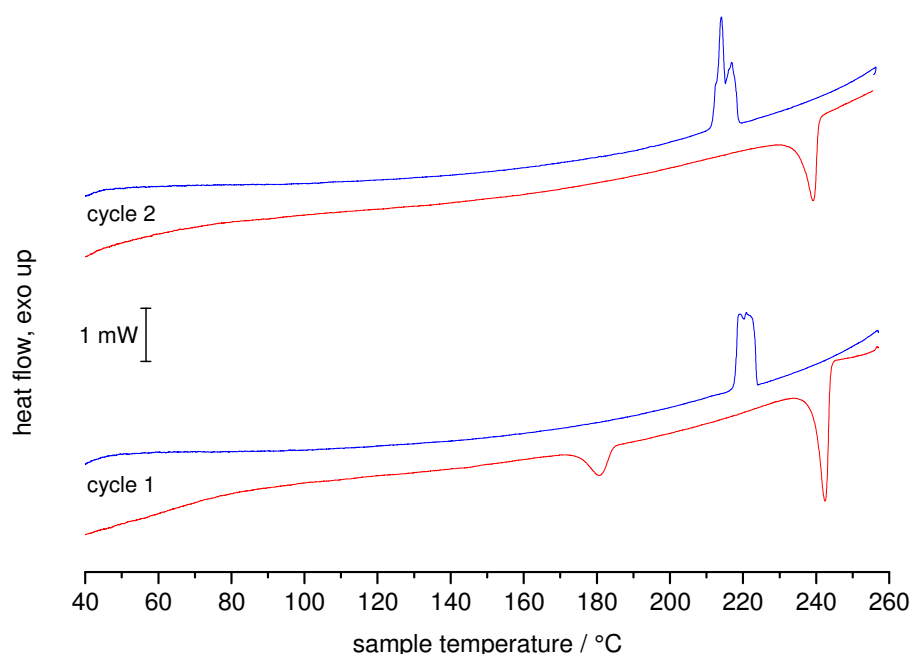


Figure 63: DSC measurements of $[\text{Fe}(\text{L}^2)_3](\text{BF}_4)_2 \cdot \text{H}_2\text{O}$ (**23**· H_2O) with a scan rate of 2 K min^{-1} in the heating (red line) and the cooling (blue line) mode; *top*: cycle 2, *bottom*: cycle 1.

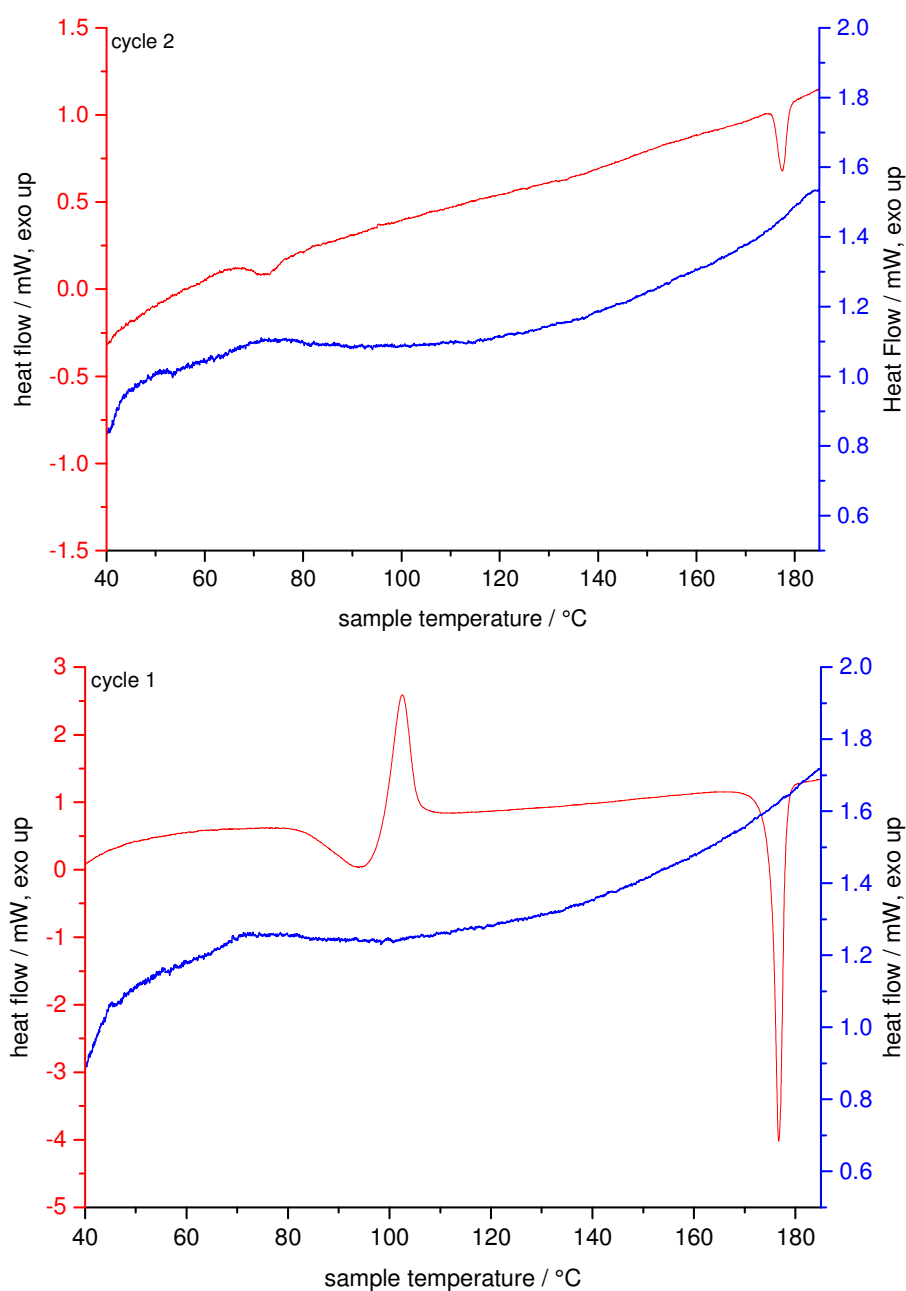


Figure 64: DSC measurements of $[\text{Fe}(\text{L}^3)_3](\text{BF}_4)_2$ (**28**) with a scan rate of 2 K min^{-1} in the heating (red line) and the cooling (blue line) mode; *top*: cycle 2, *bottom*: cycle 1.

DSC measurements of the related complex $[\text{Fe}(\text{L}^3)_3](\text{BF}_4)_2$ (**28**) featuring the methoxyethyl substituted ligand were also carried out three times in the heating and the cooling mode with a scan rate of 2 K min^{-1} (Figure 64). The heating curve of the first cycle shows an endothermic peak at 177 °C ($T_{\text{onset}} = 175 \text{ °C}$) resulting from a melting process. The enthalpy of fusion $\Delta H_{\text{fus}} = 49 \text{ kJ mol}^{-1}$ for this process is in the range of usually determined values of compounds consisting of one dication and two monoanions.^[93–95] Before melting the compound seems to undergo a phase transition as indicated by

an endothermic peak at 95 °C ($\Delta H = 28 \text{ kJ mol}^{-1}$) and a subsequent exothermic peak at 102 °C ($\Delta H = -27 \text{ kJ mol}^{-1}$). The cooling curve of the first cycle could result from a glass transition, although the detected heat flow of the cooling curve does not permit a secure interpretation. In the second cycle the compound presumably underwent a glass transition upon heating, as indicated by the characteristic shape of the heating curve at around 73 °C. However, a residual part of the compound presumably remained in the crystalline state and melted at the same temperature as in the first cycle resulting in a sharp endothermic peak at 178 °C. The subsequent cooling curve is similar to the one of the first cycle. The expected exothermic peak in the cooling curves, resulting from the crystallisation of the residual part of the compound, is assumedly masked by the broad signal of the glass transition and might become visible by applying smaller cooling rates of $< 1 \text{ K min}^{-1}$. The observations of the second cycle also were made in a subsequent third cycle (not shown).

The iron(II) triflimide $[\text{Fe}(\text{L}^2)_3](\text{NTf}_2)_2$ (**24**) could be prepared with the ethyl substituted ligand L^2 by mixing a methanolic solutions of the ligand and $\text{Fe}(\text{NTf}_2)_2 \cdot 6\text{H}_2\text{O}$. Upon the addition of pentane and TBME a precipitate formed. Isolation gave an analytically pure red amorphous powder that melts at 148–151 °C. No colour change was observed during heating up to 220 °C. With the methoxyethyl substituted ligand L^3 analogous reactions have been carried out. However neither crystalline material nor amorphous powders could be isolated.

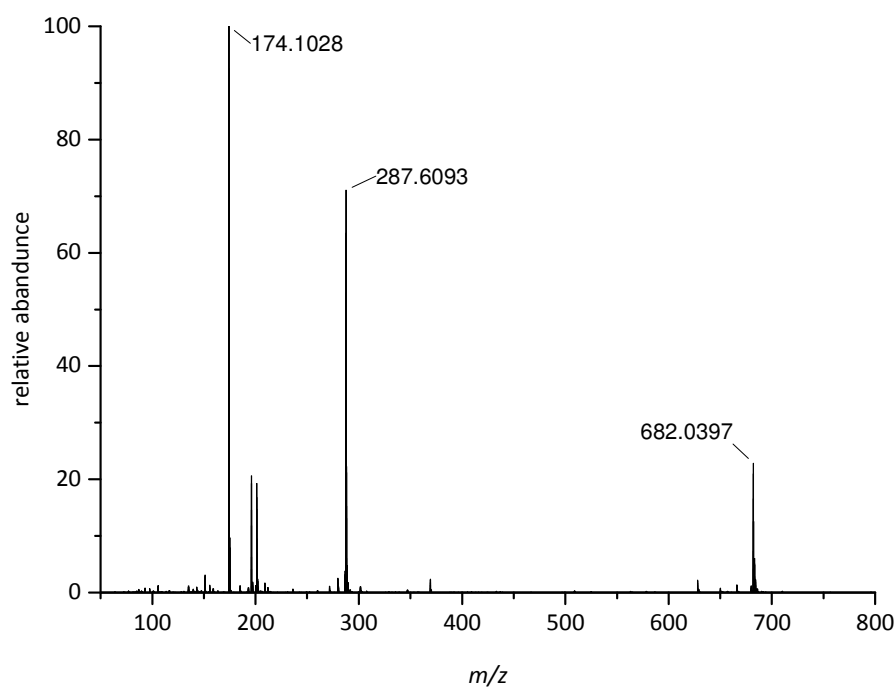


Figure 65: ESI-MS spectrum of $[\text{Fe}(\text{L}^2)_3](\text{NTf}_2)_2$ (**24**).

The formation of a 3:1-type complex in the case of the ethyl substituted ligand L^2 could be confirmed by ESI mass spectrometry. The spectrum shows peaks resulting from the dicationic chromophore $[Fe(L^3)_3]^{2+}$ and the monocationic fragment $[Fe(L^2)_2](NTf_2)^+$ at $m/z = 287.6093$ and 682.0397 , respectively. A signal resulting from the protonated free ligand is observed at $m/z = 174.1028$ (Figure 65). The IR spectrum confirms the formation of an NTf_2^- compound as it shows strong absorption bands resulting from the asymmetric valence vibration of CF_3 at 1178 cm^{-1} , from the symmetric valence vibration of SO_2 at 1132 cm^{-1} and from the asymmetric valence vibration of the SNS group at 1053 cm^{-1} (Figure 66).^[84]

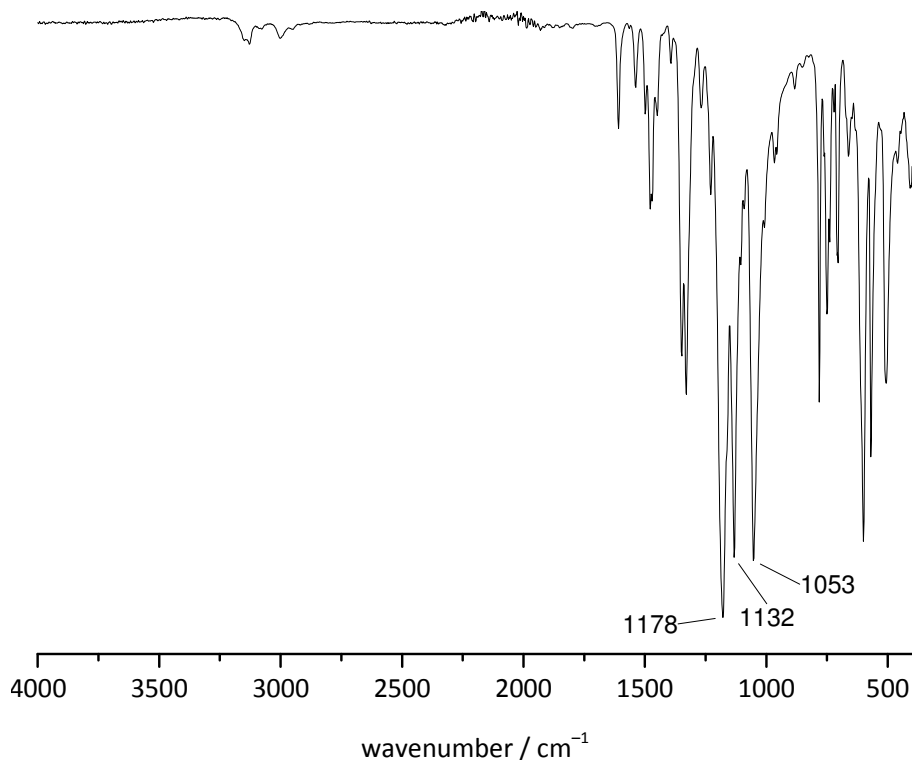


Figure 66: IR spectrum of $[Fe(L^2)_3](NTf_2)_2$ (**24**).

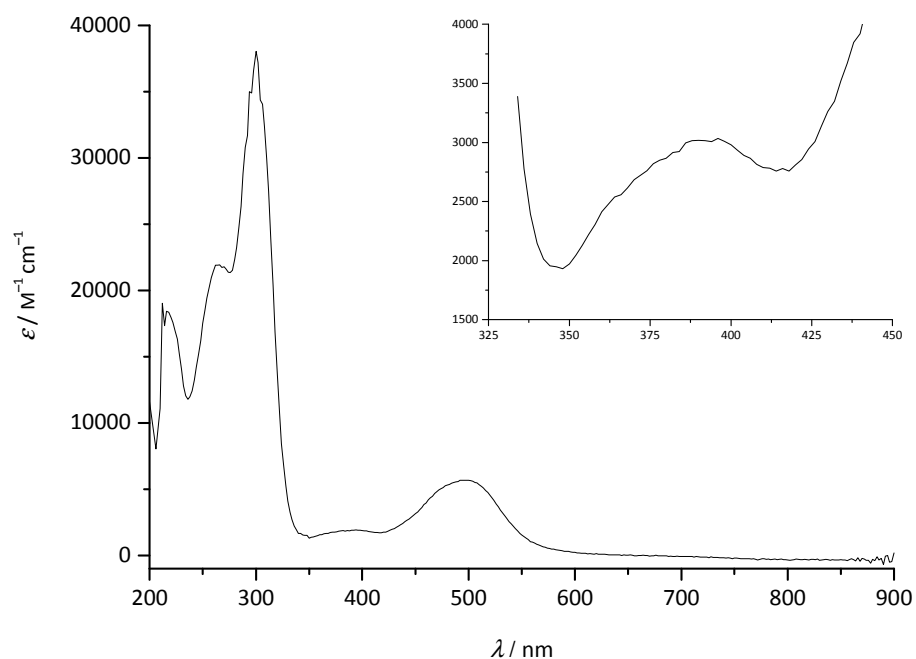


Figure 67: UV-Vis spectrum of $[\text{Fe}(\text{L}^2)_3](\text{NTf}_2)_2$ (**24**) in 0.1 mM MeOH (inset: 1 mM).

The UV/Vis spectrum shows absorption bands in the UV region, similar to the patterns observed in the spectrum of the free ligand, at 216, 262 and 300 nm. Additionally, typical CT absorption bands for an iron(II) LS species can be seen at 396 (3034) and 494 nm (5680 $\text{M}^{-1} \text{cm}^{-1}$). Absorption bands resulting from d-d-transitions are rather weak and therefore presumably masked by the charge-transfer bands (Figure 67).^[38,40,81,92]

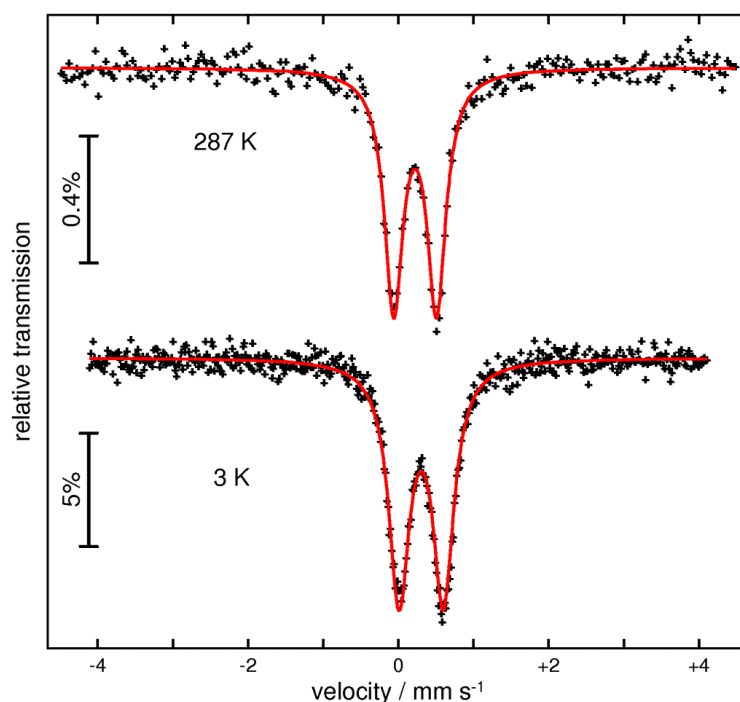


Figure 68: Mössbauer spectra of $[\text{Fe}(\text{L}^2)_3](\text{NTf}_2)_2$ (**24**) recorded at *top*: 287 K and *bottom*: 3 K; the red line represents fitting with Lorentzian doublet.

Mössbauer spectra of $[\text{Fe}(\text{L}^2)_3](\text{NTf}_2)_2$ (**24**) confirm the LS state of the compound at 3 K and at 287 K. The spectra show symmetrical doublets with isomeric shifts $\delta = 0.40$ (3 K) and 0.32 mm s^{-1} (287 K) as expected for a ferrous complex in the LS state.^[82,83] The observed quadrupole splittings $\Delta E_Q = 0.59$ (3 K) and 0.57 (287 K) mm s^{-1} are relatively small and also characteristic for an iron(II) LS core (Figure 68).

In order to confirm the melting point, DSC measurements of **24** were carried out five times in the heating and the cooling mode with a scan rate of 2 K min^{-1} . The heating curve of the first cycle shows an endothermic peak at $155 \text{ }^\circ\text{C}$ ($T_{\text{onset}} = 153 \text{ }^\circ\text{C}$) resulting from a melting process. The enthalpy of fusion $\Delta H_{\text{fus}} = 55 \text{ kJ mol}^{-1}$ is in range of usually determined values of compounds consisting of one dication and two monoanions.^[93–95] The cooling curve of the first cycle presumably results from fluctuations of the baseline which assumedly prevent the detection of a glass transition. This is supported by the fact, that in the second cycle the compound recrystallised upon heating before it melted again at $155 \text{ }^\circ\text{C}$. This cold crystallisation is indicated by an exothermic peak at $58 \text{ }^\circ\text{C}$ ($T_{\text{onset}} = 51 \text{ }^\circ\text{C}$). The subsequent cooling curve is similar to the one of the first cycle. (Figure 69). The latter behaviour of cycle number two was also observed in three subsequent heating-cooling cycles (not shown).

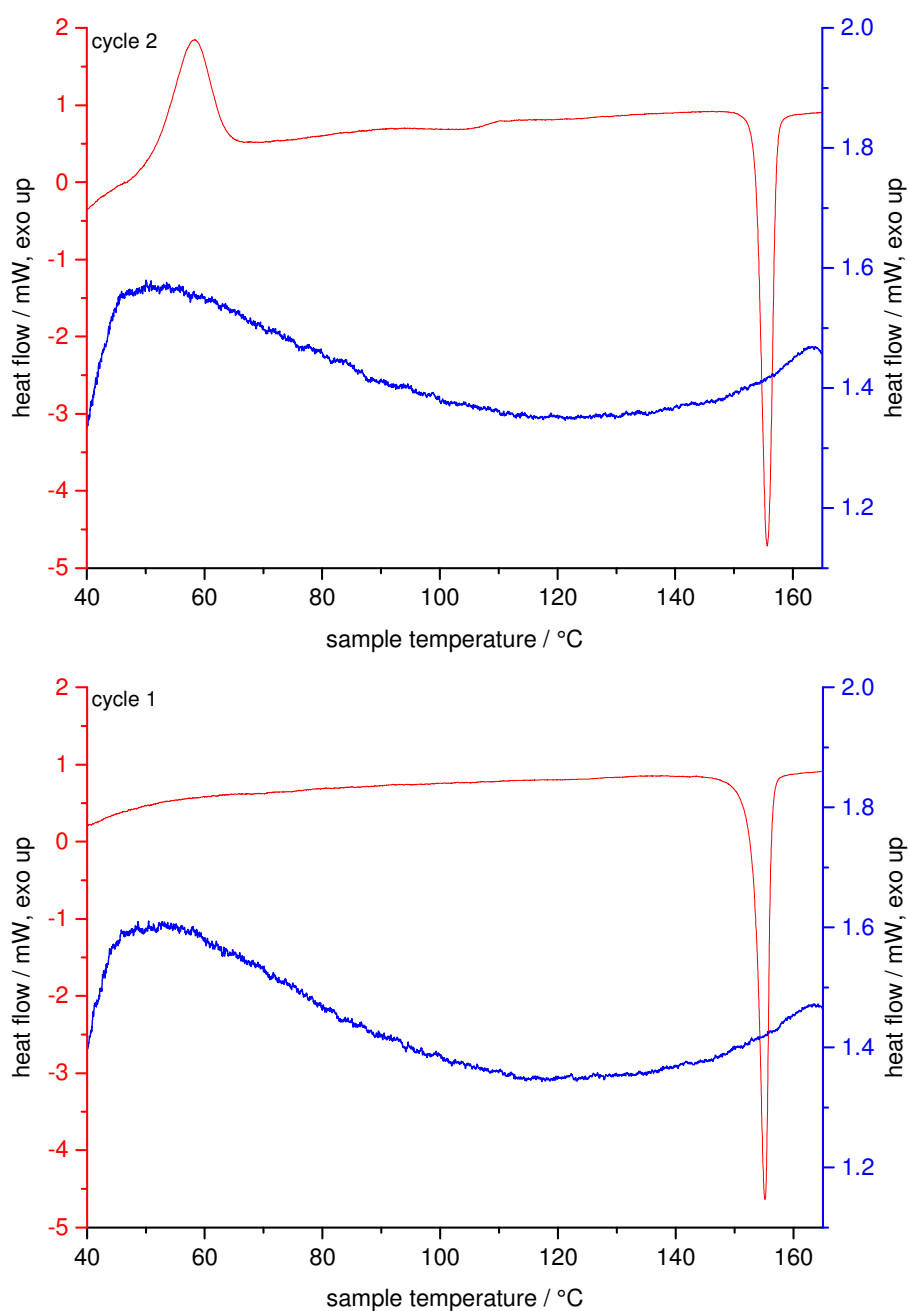


Figure 69: DSC measurements of $[\text{Fe}(\text{L}^2)_3](\text{NTf}_2)_2$ (**24**) with a scan rate of 2 K min^{-1} in the heating (red line) and the cooling (blue line) mode; *top*: cycle 2, *bottom*: cycle 1.

As the ligands L^2 and L^3 form LS complexes with iron(II), using cobalt(II) they may form a SCO complex. With the d^7 metal ion generally stronger ligands are needed to obtain a SCO compound than for iron(II).^[7] Besides, preparing the analogous nickel(II) complex could allow the evaluation of the ligand's strength by examination of the d-d bands in the UV/Vis spectra. The preparation of cobalt(II) and nickel(II) complexes with both ligands could further allow the investigation of the molecular structure of such

3:1-type complexes. Experience has shown that single crystals of nickel(II) and cobalt(II) complexes are sometimes obtained more readily than the respective iron(II) complexes.

The cobalt(II) perchlorate compounds $[\text{Co}(\text{L}^2)_3](\text{ClO}_4)_2 \cdot 1.5\text{H}_2\text{O}$ (**25**·1.5H₂O) and $[\text{Co}(\text{L}^3)_3](\text{ClO}_4)_2$ (**29**) were prepared by slow diffusion of methanolic solutions of the ligands and $\text{Co}(\text{ClO}_4)_2 \cdot 6\text{H}_2\text{O}$. Indeed, orange coloured crystalline material of **25**·2MeOH and **29** had formed after 20 h and 72 h, respectively. The molecular structures could be determined by single crystal X-ray diffraction analyses. Analytically pure bulk material from both compounds could be obtained by isolation of the crystalline material. Heating the sesquihydrate $[\text{Co}(\text{L}^2)_3](\text{ClO}_4)_2 \cdot 1.5\text{H}_2\text{O}$ (**25**·1.5H₂O) up to 235 °C neither led to a melting process nor to a colour change of the compound. The melting point of $[\text{Co}(\text{L}^3)_3](\text{ClO}_4)_2$ (**29**), featuring the methoxyethyl substituted ligand, lies in the range of 180–183 °C. ESI mass spectrometry confirmed the formation of 3:1-type complexes in both cases. The spectra show peaks resulting from the dicationic chromophores $[\text{Co}(\text{L}^2)_3]^{2+}$ and $[\text{Co}(\text{L}^3)_3]^{2+}$ at $m/z = 289.1094$ (**25**·1.5H₂O) and 334.1248 (**29**). Further peaks resulting from the monocationic species $[[\text{Co}(\text{L}^2)_2](\text{ClO}_4)]^+$ and $[[\text{Co}(\text{L}^3)_2](\text{ClO}_4)]^+$ can be seen at $m/z = 504.0728$ and 564.0910, respectively. Additionally, signals resulting from the protonated free ligand **L**² and **L**³ are observed at $m/z = 174.1022$ and 204.1133, respectively (Figure 70). The IR spectra show characteristic bands resulting from the asymmetric valence vibration of ClO_4^- at 1072 cm^{-1} (**25**·1.5H₂O) and 1070 cm^{-1} (**29**) as well as the bands resulting from the asymmetric deformation vibration at 620 cm^{-1} confirming the formation of a perchlorate compound (**25**·1.5H₂O, **29**) (Figure 71).

[91]

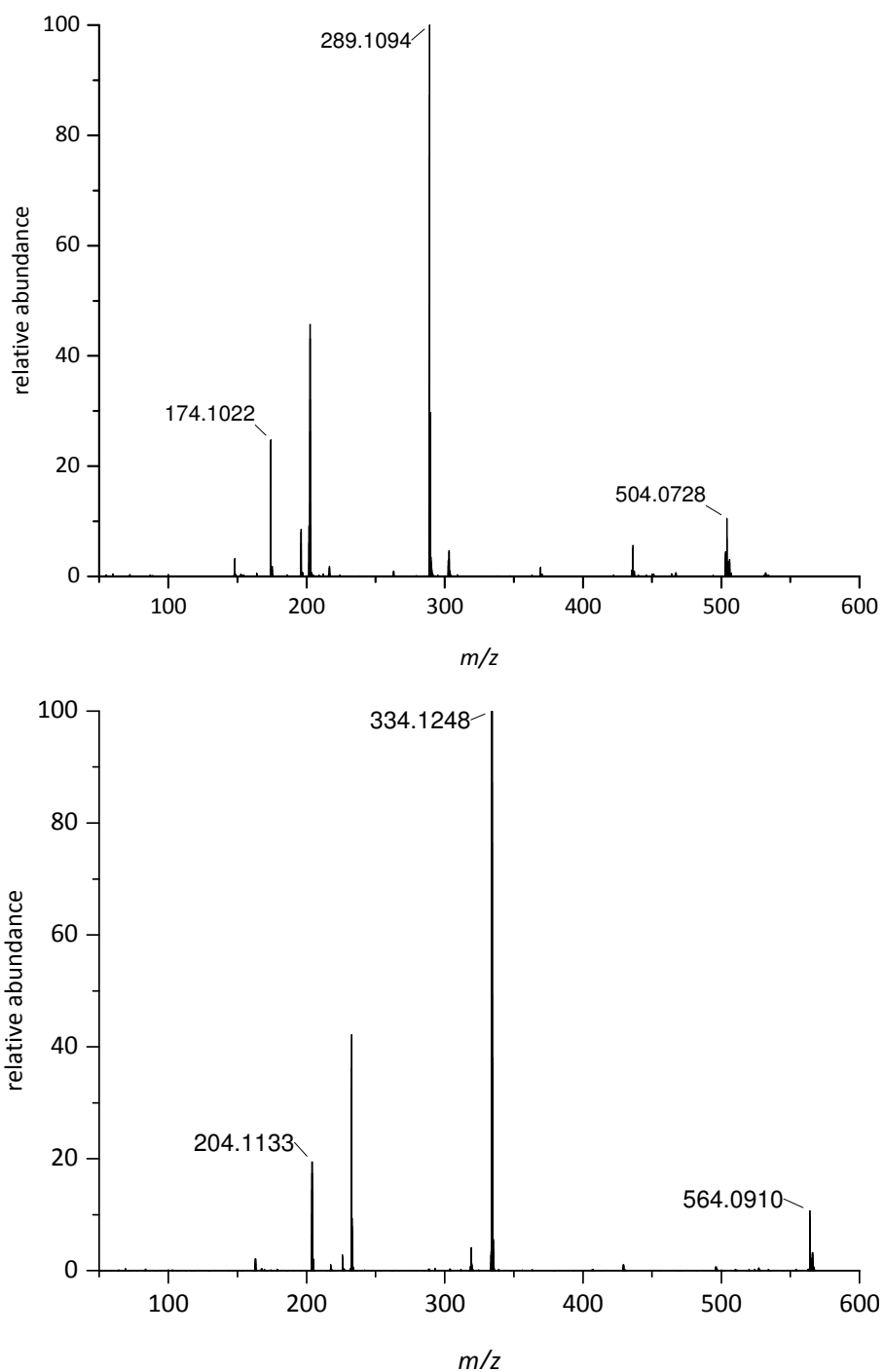


Figure 70: ESI-MS spectra of *top*: $[\text{Co}(\text{L}^2)_3](\text{ClO}_4)_2 \cdot 1.5\text{H}_2\text{O}$ (**25**·1.5H₂O) and *bottom*: $[\text{Co}(\text{L}^3)_3](\text{ClO}_4)_2$ (**29**).

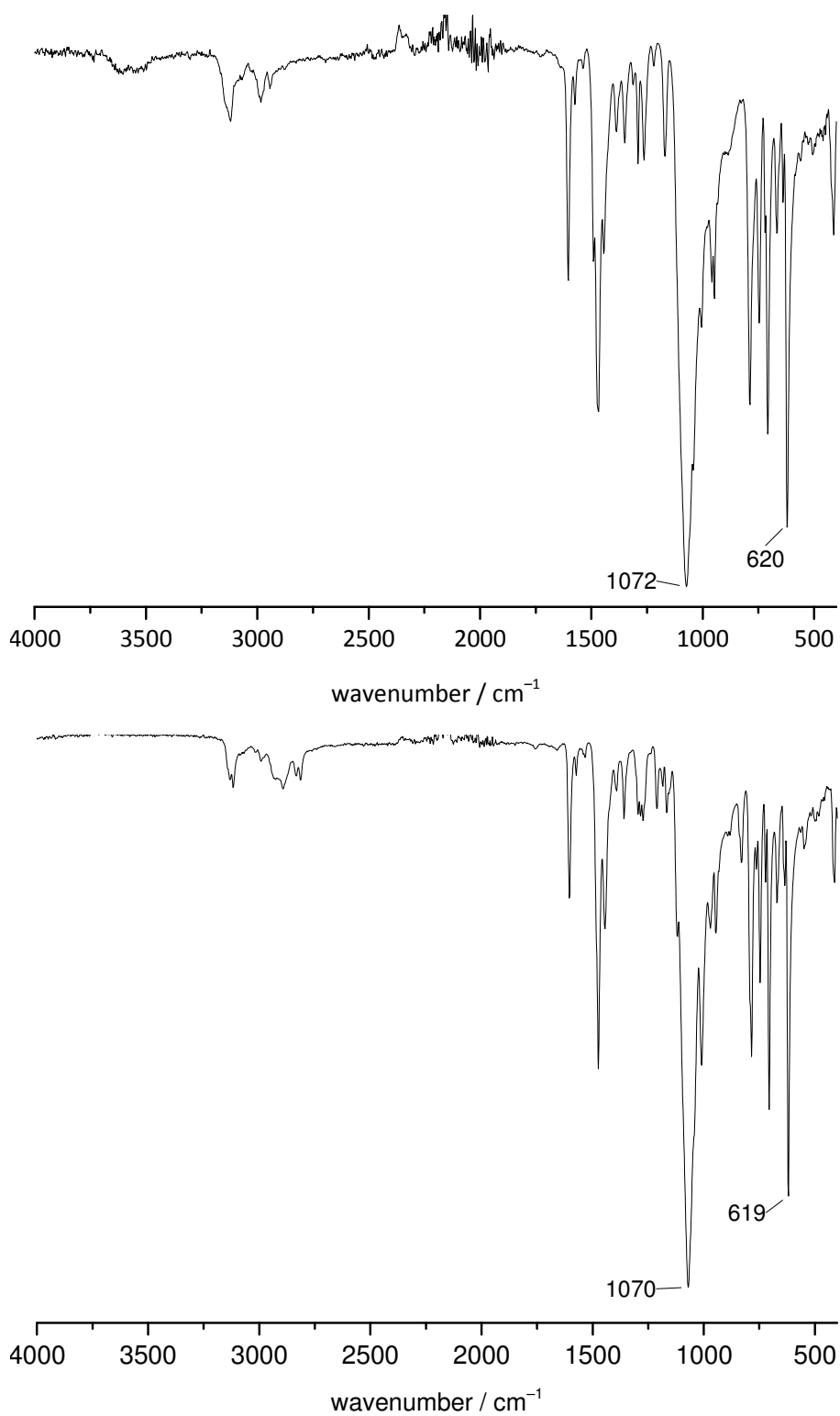


Figure 71: IR spectra of *top*: $[\text{Co}(\text{L}^2)_3](\text{ClO}_4)_2 \cdot 1.5\text{H}_2\text{O}$ (**25**·1.5H₂O) and *bottom*: $[\text{Co}(\text{L}^3)_3](\text{ClO}_4)_2$ (**29**).

The 3:1-type complexes $[\text{Co}(\text{L}^2)_3](\text{ClO}_4)_2 \cdot 1.5\text{H}_2\text{O}$ (**25**·1.5H₂O) and $[\text{Co}(\text{L}^3)_3](\text{ClO}_4)_2$ (**29**) crystallise in the monoclinic space group $P2_1/n$ and in the triclinic space group $P\bar{1}$, respectively. In both compounds a *mer*-isomer is found in the asymmetric unit. The ligands act as bidentate chelate coordinating with an N_{im} atom of the imidazole and the N_{py} atom of the pyridyl moiety. The cobalt atoms are coordinated by the ligands in a distorted octahedral manner (Figure 72). The bond lengths range from 2.077(2)–2.159(2) Å (**25**·1.5H₂O) and 2.100(2)–2.163(2) Å (**29**) and are typical values for complexes with HS Co(II).^[7] Selected distances and angles of the complexes are summarised in Table 8, crystallographic data are summarised in Table 24 (appendix).

Table 8: Selected bond lengths (Å) and angles (°) for $[\text{Co}(\text{L}^2)_3](\text{ClO}_4)_2 \cdot 1.5\text{H}_2\text{O}$ (**25**·1.5H₂O) and $[\text{Co}(\text{L}^3)_3](\text{ClO}_4)_2$ (**29**).

25 ·1.5H ₂ O		29	
Co1–N1	2.159(2)	2.138(2)	Co1–N1
Co1–N2	2.088(2)	2.102(2)	Co1–N2
Co1–N11	2.148(2)	2.146(2)	Co1–N21
Co1–N12	2.077(2)	2.106(2)	Co1–N22
Co1–N21	2.156(2)	2.163(2)	Co1–N41
Co1–N22	2.080(2)	2.100(2)	Co1–N42
N12–Co1–N22	95.81(8)	96.91(7)	N42–Co1–N2
N12–Co1–N2	170.80(8)	93.18(7)	N42–Co1–N22
N22–Co1–N2	92.85(8)	168.25(7)	N2–Co1–N22
N12–Co1–N11	77.32(8)	96.40(6)	N42–Co1–N1
N22–Co1–N11	95.35(8)	77.25(7)	N2–Co1–N1
N2–Co1–N11	98.82(8)	95.68(7)	N22–Co1–N1
N12–Co1–N21	96.88(8)	166.57(7)	N42–Co1–N21
N22–Co1–N21	77.05(8)	94.24(7)	N2–Co1–N21
N2–Co1–N21	88.06(8)	76.64(7)	N22–Co1–N21
N11–Co1–N21	170.07(8)	93.34(7)	N1–Co1–N21
N12–Co1–N1	94.90(8)	76.57(6)	N42–Co1–N41
N22–Co1–N1	169.28(8)	100.69(7)	N2–Co1–N41
N2–Co1–N1	76.44(9)	87.49(7)	N22–Co1–N41
N11–Co1–N1	86.81(8)	172.47(7)	N1–Co1–N41
N21–Co1–N1	101.85(8)	94.04(7)	N21–Co1–N41

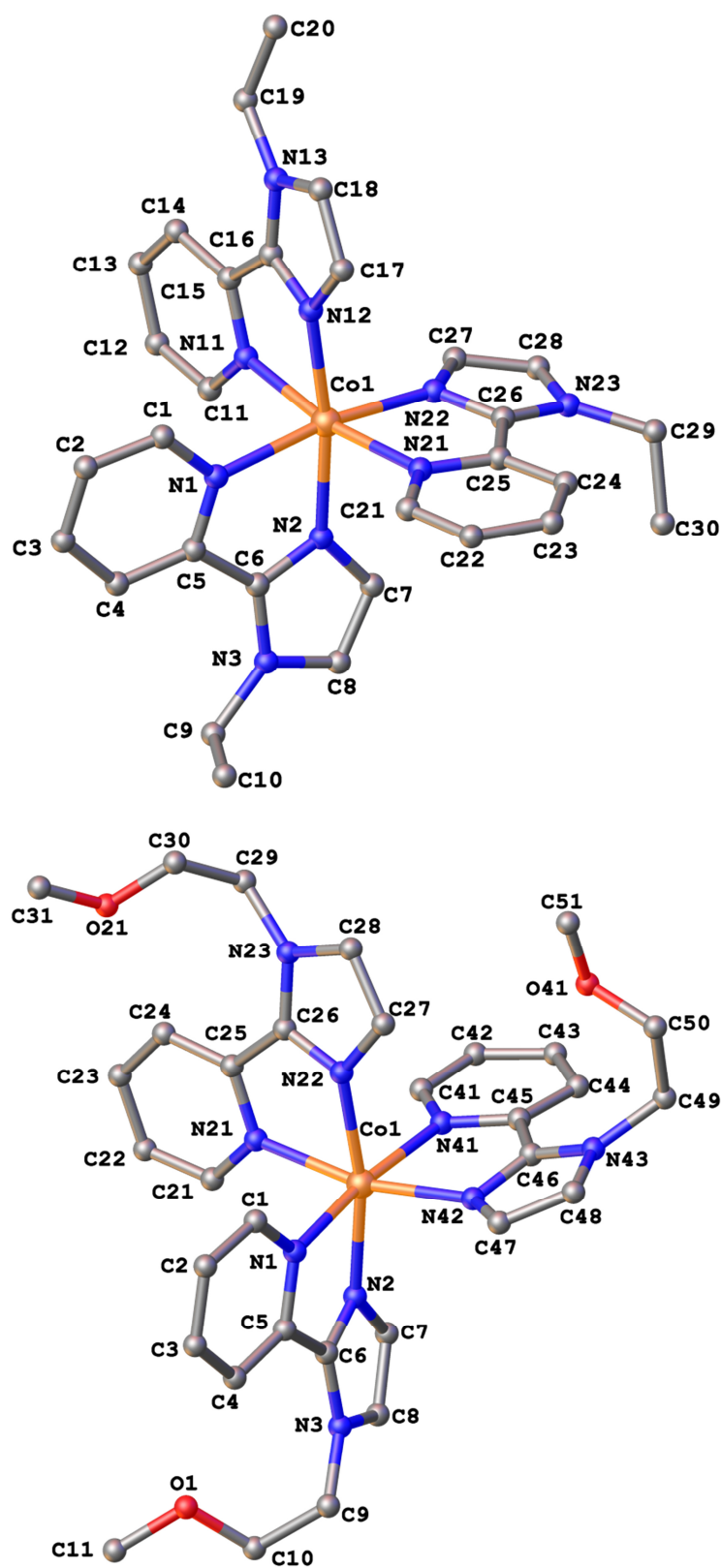


Figure 72: View of the molecular structure at 100 K of *top*: $[\text{Co}(\text{L}^2)_3]^{2+}$ (complex cation of **25**-2MeOH) and *bottom*: $[\text{Co}(\text{L}^3)_3]^{2+}$ (complex cation of **29**); H-atoms, anions and solvent molecules are omitted.

In the UV/Vis spectrum of **25**·1.5H₂O one absorption band in the UV region is observed at 288 nm. The spectrum of **29** shows absorption bands in the UV region similar to the patterns observed in the spectrum of the free ligand, at 266 and 302 nm. Additionally, both spectra show rather weak bands at 474 (38) and 542 nm (16 M⁻¹ cm⁻¹) (**25**·1.5H₂O) and at 476 (39) and 544 nm (17 M⁻¹ cm⁻¹) (**29**) which are presumably provoked by d-d transitions of the cobalt(II) core.^[81] For a d⁷ ion in the HS state absorption bands corresponding to the transitions $\nu_1[{}^4T_{1g}(F) \rightarrow {}^4T_{2g}(F)]$, $\nu_2[{}^4T_{1g}(F) \rightarrow {}^4A_{2g}(F)]$ and $\nu_3[{}^4T_{1g}(F) \rightarrow {}^4T_{1g}(P)]$ are expected. As the sequence of the transition energies is $\nu_1 < \nu_2 < \nu_3$ the absorption band of ν_1 is supposed to lie in the infrared region.^[81] Thus ν_2 and ν_3 , lying in the visible region, were assigned to the absorption bands at 474 (38) and 542 nm (16 M⁻¹ cm⁻¹) (**25**·1.5H₂O) and 476 (39) and 544 nm (17 M⁻¹ cm⁻¹) (**29**), respectively.

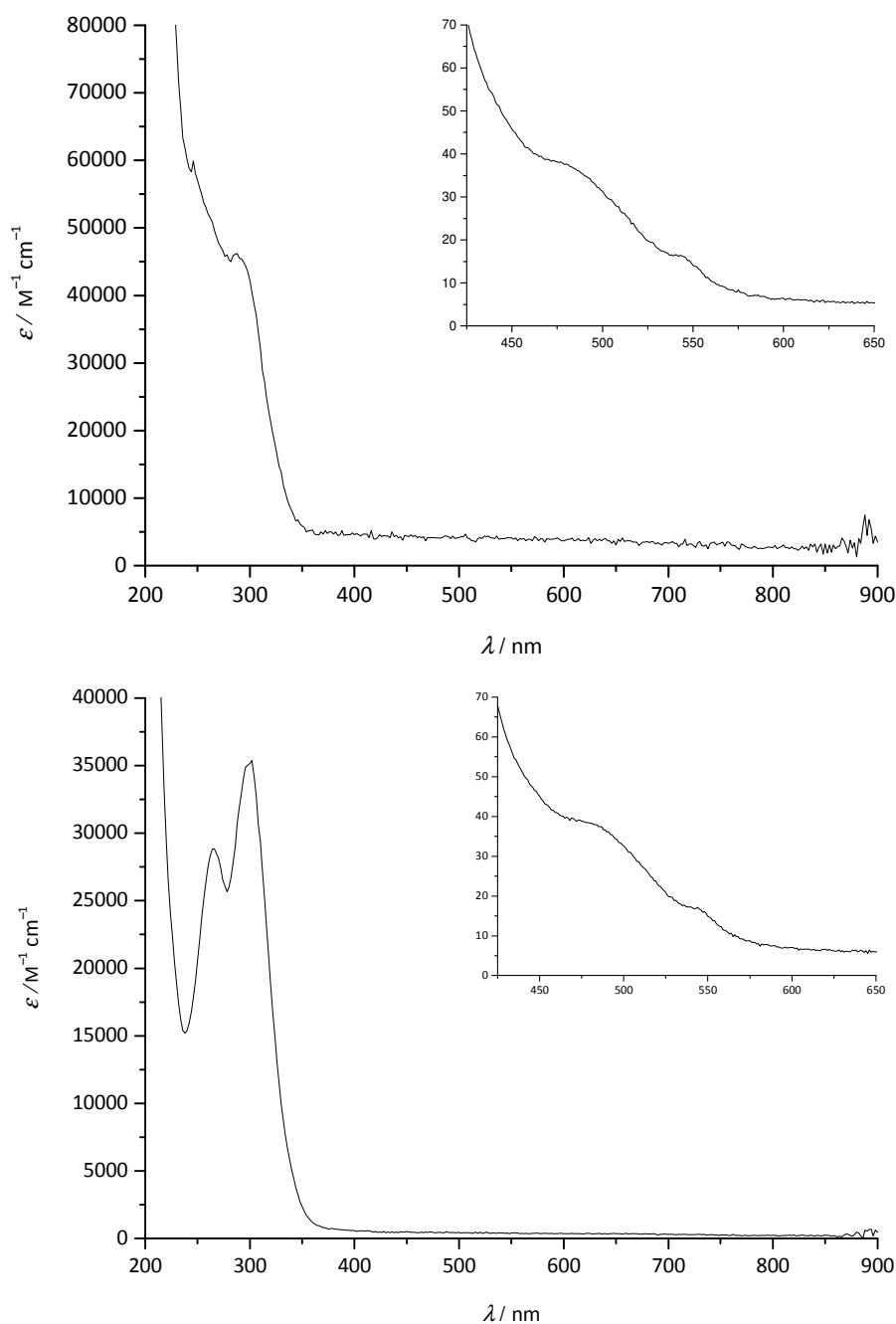


Figure 73: UV/Vis spectra in MeCN of *top*: $[\text{Co}(\text{L}^2)_3](\text{ClO}_4)_2 \cdot 1.5\text{H}_2\text{O}$ (**25**·1.5H₂O) 0.01 mM (inset: 10 mM) and *bottom*: $[\text{Co}(\text{L}^3)_3](\text{ClO}_4)_2$ (**29**) 0.1 mM (inset: 10 mM).

In order to confirm the melting point of $[\text{Co}(\text{L}^3)_3](\text{ClO}_4)_2$ (**29**), featuring the methoxyethyl substituted ligand, DSC measurements were carried out with a scan rate of 2 K min^{-1} . In the first heating-cooling cycle the compound melted at $183 \text{ }^\circ\text{C}$ ($T_{\text{onset}} = 181 \text{ }^\circ\text{C}$) which is represented by the endothermic peak in the heating curve. The enthalpy of fusion $\Delta H_{\text{fus}} = 58 \text{ kJ mol}^{-1}$ is in the range of usually determined values of compounds consisting of one dication and two monoanions.^[93–95] The cooling curve of the first cycle

presumably results from fluctuations of the baseline which prevent the detection of a glass transition. In the second cycle the compound assumedly fulfilled a glass transition with relaxation upon heating as indicated by a small endothermic peak at 66 °C. The subsequent cooling curve is similar to the one of the first cycle (Figure 74). The observations of the second cycle also were made in a subsequent third cycle (not shown).

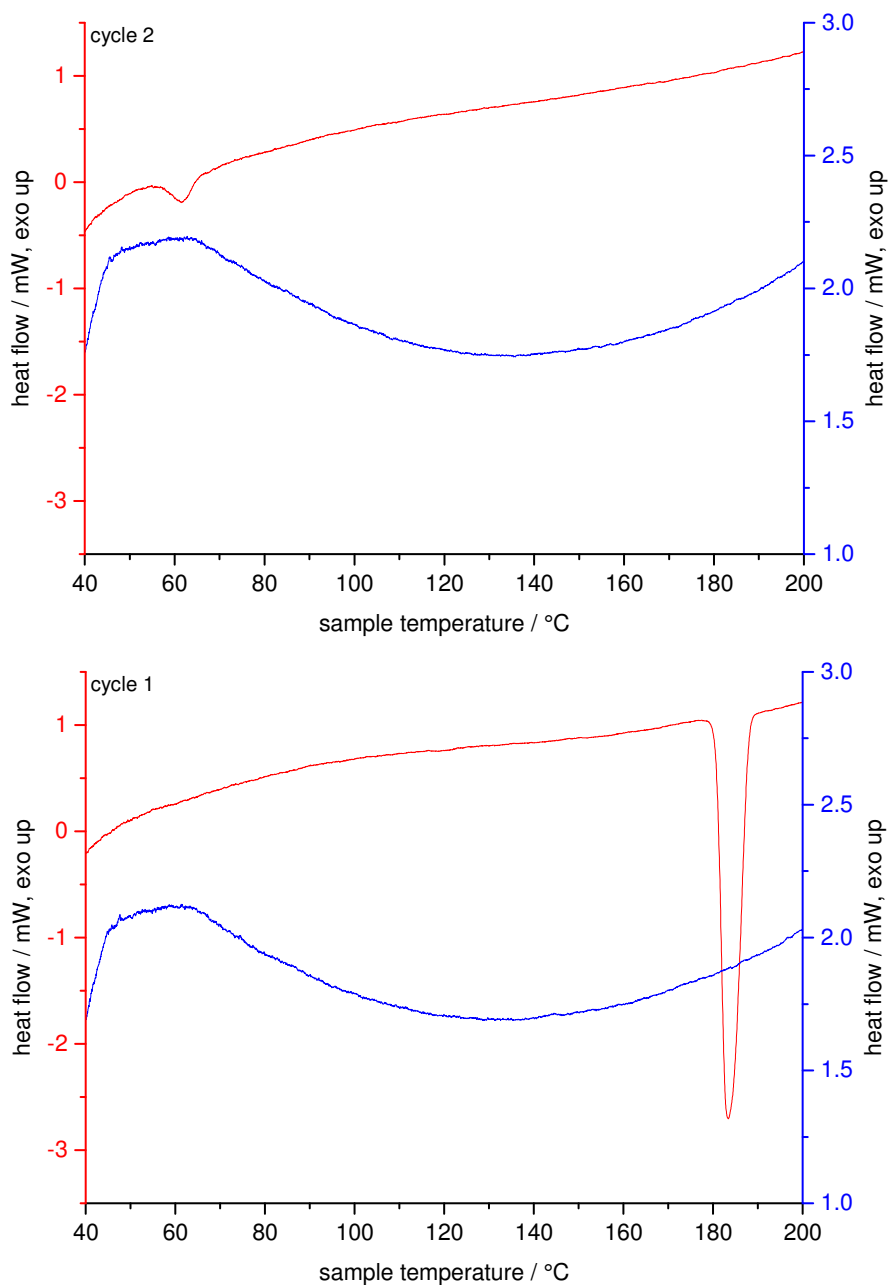


Figure 74: DSC measurements of $[\text{Co}(\text{L}^3)_3](\text{ClO}_4)_2$ (**29**) with a scan rate of 2 K min^{-1} in the heating (red line) and the cooling (blue line) mode; *top*: cycle 2, *bottom*: cycle 1.

The nickel(II) perchlorate compounds $[\text{Ni}(\text{L}^2)_3](\text{ClO}_4)_2 \cdot 0.5\text{H}_2\text{O}$ (**26** $\cdot 0.5\text{H}_2\text{O}$) and $[\text{Ni}(\text{L}^3)_3](\text{ClO}_4)_2$ (**30**) were prepared by slow diffusion of methanolic solutions of the ligands and $\text{Ni}(\text{ClO}_4)_2 \cdot 6\text{H}_2\text{O}$. Purple crystals had formed after 20 h (**26** $\cdot 0.5\text{H}_2\text{O}$) and 72 h (**30**), respectively but unfortunately were not suitable for X-ray diffraction analyses. Analytically pure bulk material from both compounds could be obtained by isolation of the crystalline material. The complex with the ethyl substituted ligand **26** $\cdot 0.5\text{H}_2\text{O}$ does not melt up to 235 °C, whereas the analogous complex with methoxyethyl substituted ligand **30** melts at 188–191 °C. ESI mass spectrometry confirmed the formation of 3:1-type complexes. The spectra show peaks provoked by the dicationic chromophores $[\text{Ni}(\text{L}^2)_3]^{2+}$ and $[\text{Ni}(\text{L}^3)_3]^{2+}$ at $m/z = 288.6099$ (**26** $\cdot 0.5\text{H}_2\text{O}$) and 333.6255 (**30**), respectively. Additionally, the spectra possess peaks resulting from the fragments $[\text{Ni}(\text{L}^2)_2]^{2+}$ and $[\text{Ni}(\text{L}^3)_2]^{2+}$ at $m/z = 202.0622$ and 232.0728, respectively. Further signals resulting from the monocationic species $[[\text{Ni}(\text{L}^2)_2](\text{ClO}_4)]^+$ and $[[\text{Ni}(\text{L}^3)_2](\text{ClO}_4)]^+$ can be seen at $m/z = 503.0732$ (**26** $\cdot 0.5\text{H}_2\text{O}$) and 563.0946 (**30**), respectively. Peaks resulting from the protonated free methoxyethyl substituted ligand **L**³ can be seen at $m/z = 204.1133$ (Figure 75). The IR spectra show characteristic bands resulting from the asymmetric valence vibration of ClO_4^- at 1071 cm^{-1} (**26** $\cdot 0.5\text{H}_2\text{O}$; **30**) as well as the bands resulting from the asymmetric deformation vibration at 619 cm^{-1} (**26** $\cdot 0.5\text{H}_2\text{O}$) and 620 cm^{-1} (**30**) confirming the formation of a perchlorate compound (Figure 76).^[91]

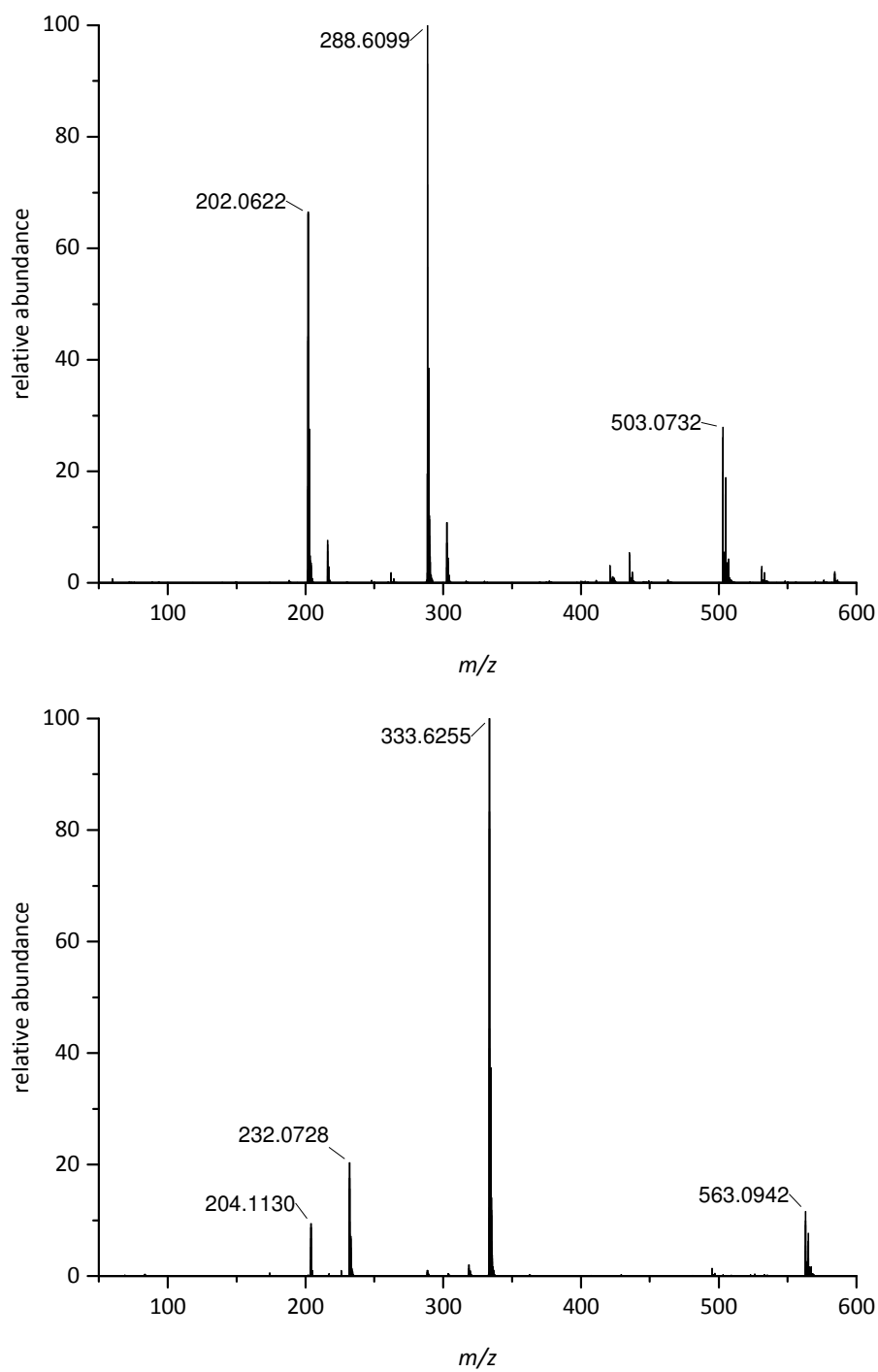


Figure 75: ESI-MS spectra of *top*: $[\text{Ni}(\text{L}^2)_3](\text{ClO}_4)_2 \cdot 0.5\text{H}_2\text{O}$ (**26** $\cdot 0.5\text{H}_2\text{O}$) and *bottom*: $[\text{Ni}(\text{L}^3)_3](\text{ClO}_4)_2$ (**30**).

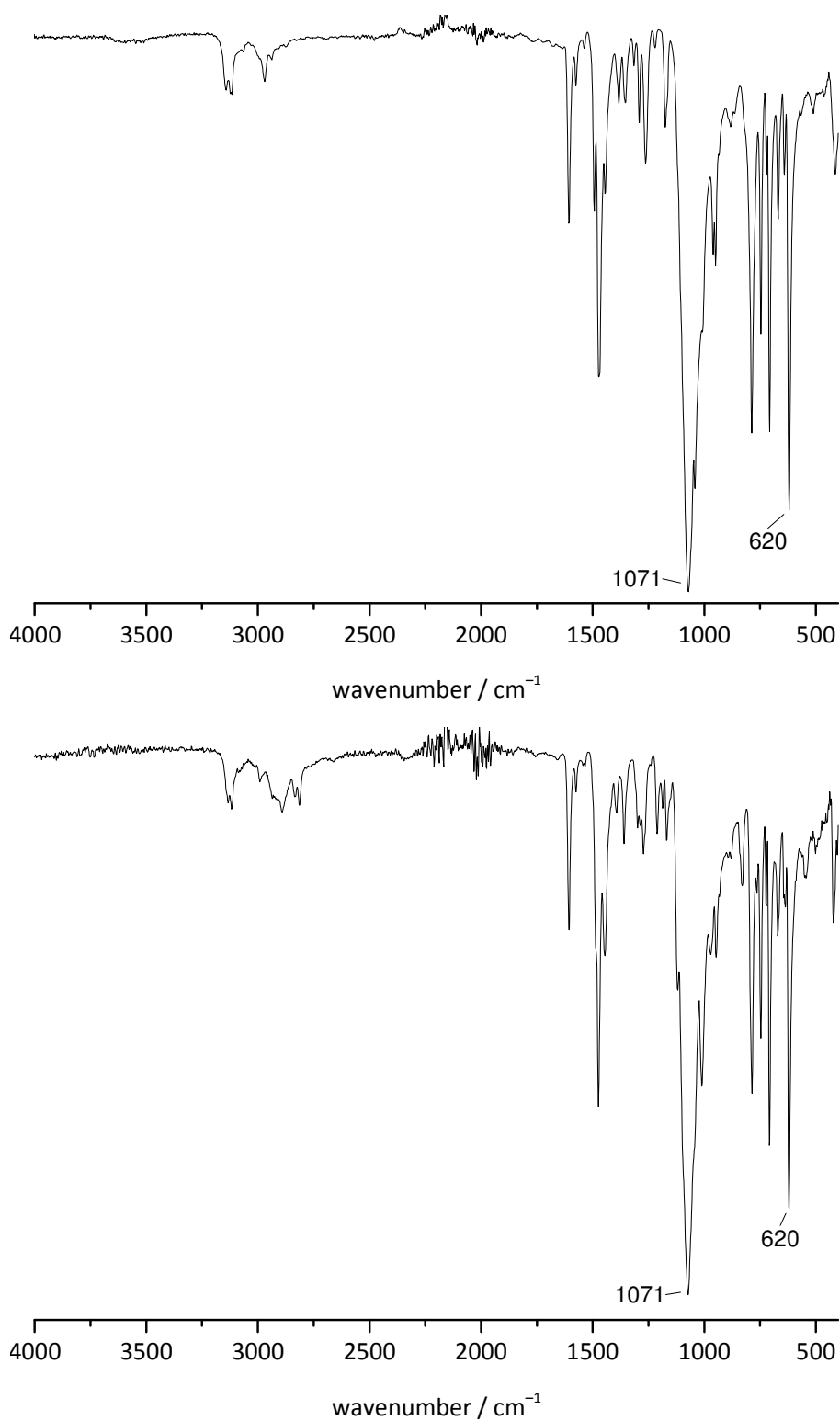


Figure 76: IR spectra of *top*: [Ni(L²)₃](ClO₄)₂·0.5H₂O (**26**·0.5H₂O) and *bottom*: [Ni(L³)₃](ClO₄)₂ (**30**).

The UV/Vis spectrum of the nickel(II) complex **26**·0.5H₂O, featuring the ethyl substituted ligand, shows one absorption band in the UV region at 302 nm. The spectrum of the analogous complex **30**, featuring the methoxyethyl substituted ligand, shows absorption bands in the UV region, similar to the pattern observed in the spectrum of the free ligand, at 262 and 304 nm. Additionally, both spectra show rather weak bands at 536 nm (21 M⁻¹ cm⁻¹) (**26**·0.5H₂O) and at 538 (15 M⁻¹ cm⁻¹) (**30**) which are presumably provoked by d-d transitions of the nickel(II) ion.^[81] For a d⁸ ion absorption bands corresponding to the transitions $\nu_1[{}^3A_{2g}(F) \rightarrow {}^3T_{2g}(F)]$, $\nu_2[{}^3A_{2g}(F) \rightarrow {}^3T_{1g}(F)]$ und $\nu_3[{}^3A_{2g}(F) \rightarrow {}^3T_{1g}(P)]$ are expected. The typically observed values of ν_2 lie in the range of 13000–19000 cm⁻¹. Thus, ν_2 was assigned to the absorption bands at 530 nm (18868 cm⁻¹) (21 M⁻¹ cm⁻¹) (**26**·0.5H₂O) and 538 nm (18587 cm⁻¹) (15 M⁻¹ cm⁻¹) (**30**). The absorption bands resulting from ν_1 are lying in the infrared region and were not detected in the herein presented spectra, whereas the absorption bands resulting from ν_3 are presumably masked by the inner-ligand bands in the UV region.^[81] The observed d-d transitions of the nickel(II) complexes [Ni(L²)₃](ClO₄)₂·0.5H₂O (**26**·0.5H₂O) and [Ni(L³)₃](ClO₄)₂ (**30**) at 530 nm and 538 nm, respectively indicate that both ligands L² and L³ provoke ligand field splittings similar to their precursor 2-(2-pyridyl)-imidazol (**pi**), since the analogues nickel(II) chromophore [Ni(**pi**)₃]²⁺ provokes a d-d band at 538 nm (7 M⁻¹ cm⁻¹).^[92]

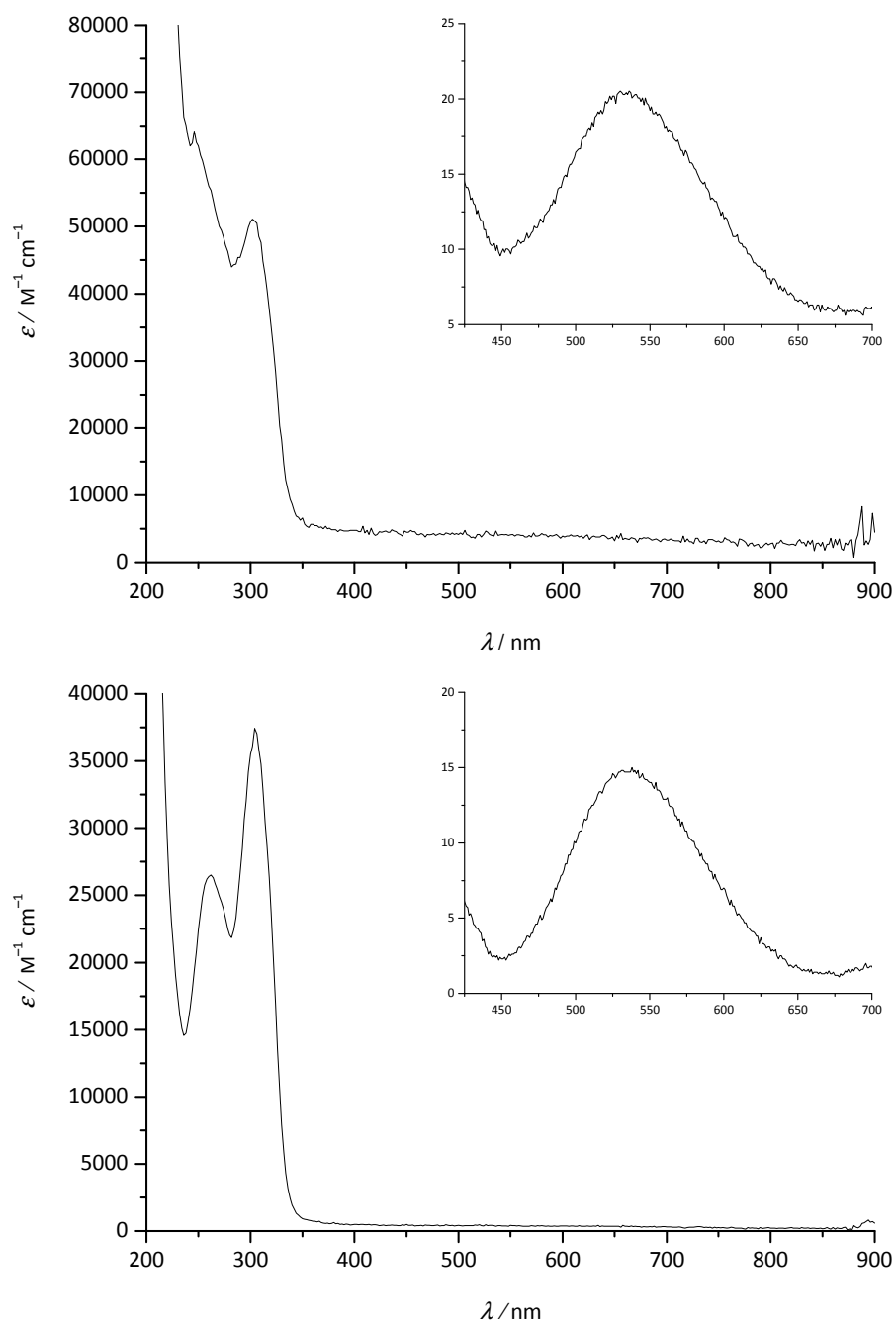


Figure 77: UV/Vis spectra of *top*: $[\text{Ni}(\text{L}^2)_3](\text{ClO}_4)_2 \cdot 0.5\text{H}_2\text{O}$ (**26**·0.5H₂O) in MeOH 0.01 mm (inset: 10 mm) and *bottom*: $[\text{Ni}(\text{L}^3)_3](\text{ClO}_4)_2$ (**30**) in MeCN 0.1 mm (inset: 10 mm).

In order to confirm the melting point of $[\text{Ni}(\text{L}^3)](\text{ClO}_4)_2$ (**30**) DSC measurements were carried out with a scan rate of 2 K min^{-1} . In the first heating-cooling cycle the compound melted at $192 \text{ }^\circ\text{C}$ ($T_{\text{onset}} = 189 \text{ }^\circ\text{C}$) which is represented by the endothermic peak in the heating curve. The fusion enthalpy $\Delta H_{\text{fus}} = 48 \text{ kJ mol}^{-1}$ is in the range of usually determined values of compounds consisting of one dication and two monoanions.^[93–95] The cooling curve of the first cycle could result from a glass transition, although the detected heat flow of the cooling curve does not allow a secure interpretation. The sharp endothermic peak at $164 \text{ }^\circ\text{C}$ results from the beginning argon flow that was switched on during the measurements and does not represent any characteristics of the sample. In the second cycle the compound assumedly fulfilled a glass transition with relaxation upon heating as indicated by a small endothermic peak at 72°C . The cooling curve is similar to one of the first cycle (Figure 78). The latter behaviour of cycle number two was also observed in a subsequent third cycle (not shown).

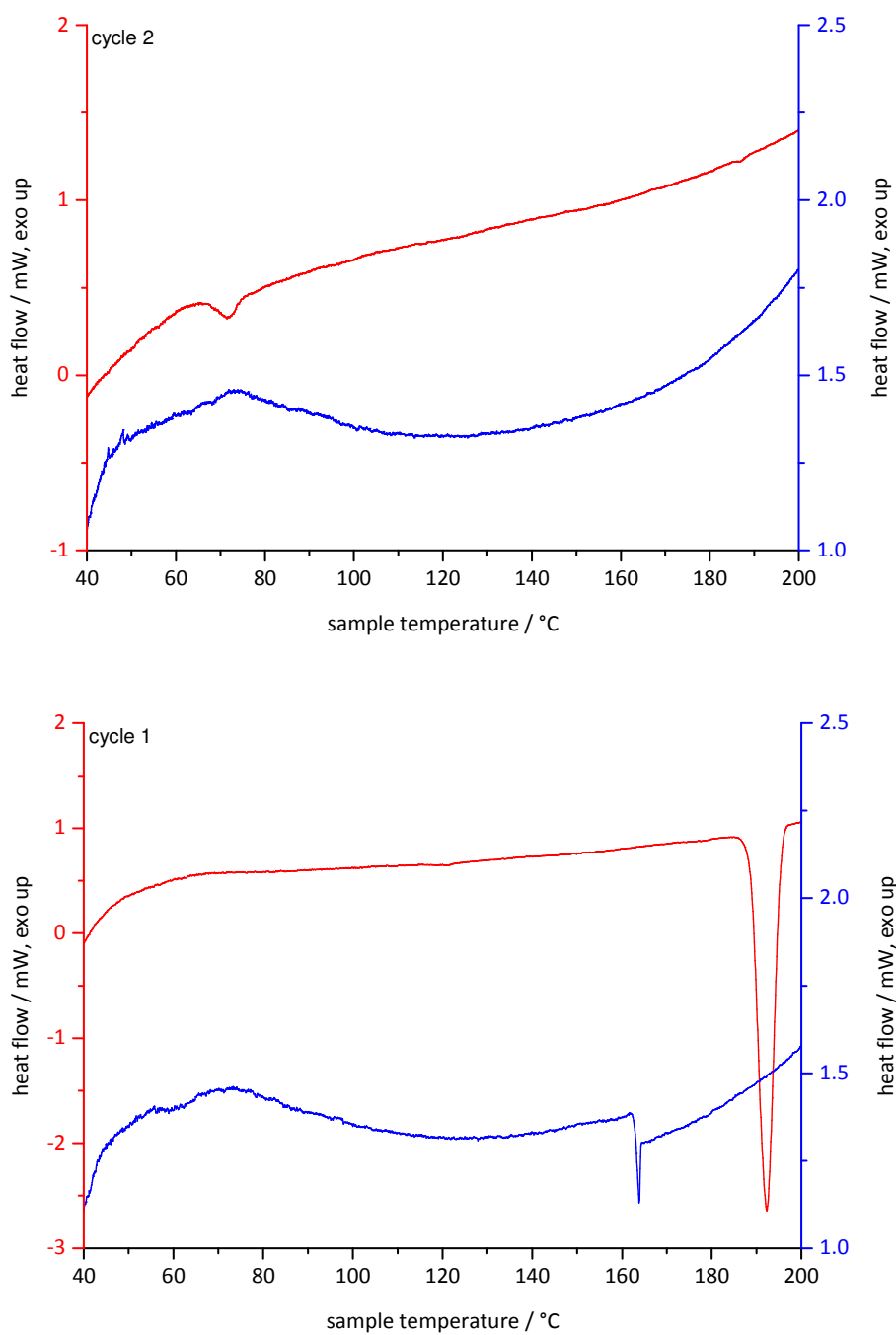


Figure 78: DSC measurements of $[\text{Ni}(\text{L}^3)_3](\text{ClO}_4)_2$ (**30**) with a scan rate of 2 K min^{-1} in the heating (red line) and the cooling (blue line) mode; *top*: cycle 2, *bottom*: cycle 1.

The results of this chapter are summarised in Table 9. The ligands L^2 and L^3 form several ($22 \cdot H_2O$, **27**, $23 \cdot H_2O$, **28**, **24**) 3:1-type coordination compounds with iron(II). Apart from one experiment all approaches to synthesise 3:1-complexes were successful. Only the attempt with $Fe(NTf_2)_2 \cdot 6H_2O$ and the methoxyethyl substituted ligand L^3 did not lead to the formation of any isolable compound. Thus, it seems that with both ligands complex synthesis is feasible in many cases. All prepared iron(II) complexes comprise a metal ion in the LS state at rt as their UV/Vis spectra show typical CT bands or as confirmed by Mössbauer spectroscopy in the case of the triflimide $[Fe(L^2)_3](NTf_2)_2$ (**24**). As the analogous cobalt(II) complexes $[Co(L^2)_3](ClO_4)_2 \cdot 1.5H_2O$ (**25**·1.5H₂O) and $[Co(L^3)_3](ClO_4)_2$ (**29**) feature the metal ion in the HS state it is very likely that the LS iron(II) compounds switch into the HS state at elevated temperatures. Generally, a stronger ligand field is needed to cause spin pairing in such cobalt(II) complexes in comparison to related iron(II) complexes.^[7] Furthermore, the ligand strengths of L^2 and L^3 are similar to the ligand strength of their precursor **pi** which indeed forms the 3:1-type iron(II) SCO complexes **K–Q** (Figure 4). Similar ligand strengths of L^2 , L^3 and **pi** are indicated by the fact that the observed d-d transitions of the nickel(II) complexes $[Ni(L^2)_3](ClO_4)_2 \cdot 0.5H_2O$ (**26**·0.5H₂O) and $[Ni(L^3)_3](ClO_4)_2$ (**30**) at 530 nm and 538 nm, respectively, comprise wavelengths similar to the d-d transition observed at 538 nm ($7 \text{ M}^{-1} \text{ cm}^{-1}$) in the spectrum of $[Ni(\text{pi})_3]^{2+}$.^[92] Although the DSC measurements of the respective iron(II) complexes do not indicate SCO in the examined temperature ranges, spin transition cannot be excluded and further investigations on SCO should be done by SQUID magnetometry or NMR spectroscopy at elevated temperatures.

Table 9: Summary of the complexes with L^2 and L^3 .

		spin state	$T_{fus} / ^\circ\text{C}$	$T_G / ^\circ\text{C}$
$[Fe(L^2)_3](ClO_4)_2 \cdot H_2O$	(22 ·H ₂ O)	LS	218 (dec.)	-
$[Fe(L^3)_3](ClO_4)_2$	(27)	LS	187 (dec.)	-
$[Fe(L^2)_3](BF_4)_2 \cdot H_2O$	(23 ·H ₂ O)	LS	239	-
$[Fe(L^3)_3](BF_4)_2$	(28)	LS	175	73
$[Fe(L^2)_3](NTf_2)_2$	(24)	LS	153	-
$[Co(L^2)_3](ClO_4)_2 \cdot 1.5H_2O$	(25 ·1.5H ₂ O)	HS	> 235	-
$[Co(L^3)_3](ClO_4)_2$	(29)	HS	181	66
$[Ni(L^2)_3](ClO_4)_2 \cdot 0.5H_2O$	(26 ·0.5H ₂ O)	-	> 235	-
$[Ni(L^3)_3](ClO_4)_2$	(30)	-	189	72

Both of the iron(II) perchlorate compounds $22 \cdot H_2O$ and **27** decompose at elevated temperatures presumably favoured by the redox character of iron(II) and the perchlorate anion. This is supported by the fact that both analogous iron(II) tetrafluoroborate complexes $[Fe(L^2)_3](BF_4)_2 \cdot H_2O$ (**23**·H₂O) and $[Fe(L^3)_3](BF_4)_2$ (**28**) are stable before melting at 239 °C and 175 °C, respectively. The iron(II) triflimide

complex of L^2 $[Fe(L^2)_3](NTf_2)_2$ (**24**) exhibits the smallest fusion temperature of all herein presented complexes at 153°C presumably due to small coulomb interactions between the cationic chromophore and the triflimide anion. Thus, a formal exchange of the tetrafluoroborate anion for the triflimide anion results in a decrease of the fusion temperature in the amount of 86 K. Although an additional influence of the presence of solvent molecules on the fusion temperature of the respective complexes cannot be excluded, the difference between the fusion temperatures assumedly arises from different magnitudes of coulomb interactions in **23**·H₂O and **24**. Upon cooling complex **24** converts into a glass before undergoing cold crystallisation when heated up another time. This behaviour was reproducible in overall five heating-cooling cycles. The cobalt(II) and nickel(II) perchlorate complexes $[Co(L^2)_3](ClO_4)_2 \cdot 1.5H_2O$ (**25**·1.5H₂O) and $[Ni(L^2)_3](ClO_4)_2 \cdot 0.5H_2O$ (**26**·0.5H₂O) with the ethyl substituted ligand L^2 neither melt nor decompose until 235 °C, whereas the analogous complexes with the methoxyethyl substituted ligand L^3 $[Co(L^3)_3](ClO_4)_2$ (**29**) and $[Ni(L^3)_3](ClO_4)_2$ (**30**) melt at 181 °C and 189 °C, respectively. Hence, all complexes with the methoxyethyl substituted ligand L^3 exhibit lower melting points than the analogous complexes with the ethyl substituted ligand L^2 . In the case of the two iron(II) tetrafluoroborate compounds **23**·H₂O and **28** the difference amounts to 64 K. Although neither in this case additional influence of the presence of solvent molecules can be excluded, the differences between the fusion temperatures presumably arise from the different substituents of the ligands L^2 and L^3 . Ligand L^2 comprises additional conformational degrees of freedom provided by the methoxyethyl substituent in comparison to ligand L^2 with the ethyl substituent. Furthermore, the rotational energy barrier for a methoxy group is less than for an ethyl group. Hence, the methoxyethyl complexes presumably possess higher entropies of fusion and therefore lower fusion temperatures. ^[51]

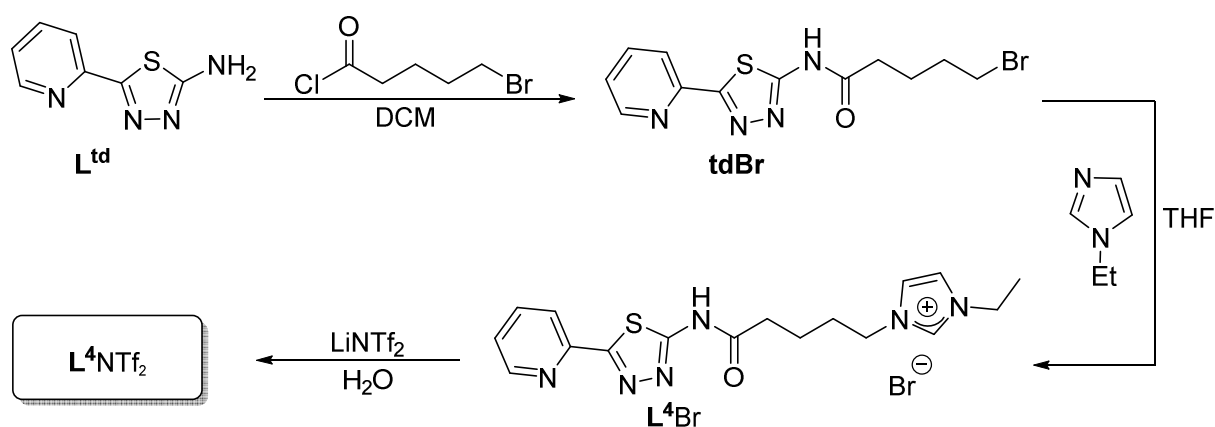
2.3 Complexes with an Imidazolium-Tagged Ligand

Parts of the results of this chapter were included in the following manuscript: Timo Huxel and Julia Klingele, *Cobalt(II) Complexes of a New Imidazolium-Tagged Thiadiazole Ligand With Bis(trifluoromethylsulfonyl)imide or Tetrakisothiocyanato Cobaltate as Counterion, submitted.*

As shown in chapter 2.1.2, the thiadiazole ligand L^{td} forms the 2:1-type SCO complex $[Fe(L^{td})_2(NCS)_2]$ (**15**) possessing a charge neutral chromophore. In order to prepare cationic 2:1-type complexes featuring an uncharged chromophore, the ligand L^{td} was enhanced with an imidazolium tag forming the new ligand L^4NTf_2 .

2.3.1 Synthesis of the Ligand L^4NTf_2

The ligand L^{td} was enhanced with an *N*-ethylimidazolium triflimide moiety to form the expanded ligand L^4NTf_2 . In the first step, the linker molecule ω -bromopentanoic acid chloride was attached to L^{td} using its amino function. The resulting amide **tdBr** possesses a bromine attached to a sp^2 carbon atom, thus it is able to functionalise *N*-ethylimidazole resulting in the imidazolium bromide species L^4Br . In $(L^4)^+$ the cationic imidazolium moiety is separated by four methylene groups and the amide function from the coordinating heterocycles. Finally, the anion was exchanged resulting in the formation of pentanoic acid [5-(2-pyridyl)-2-[1,3,4]-thiadiazolyl]-amide-5-[3-ethyl-1-imidazolium] bis(trifluoromethylsulfonyl)imide (L^4NTf_2) (Scheme 10).



Scheme 10: Synthesis of the imidazolium ligand L^4NTf_2

The ligand L^{td} was reacted under an inert argon atmosphere with ω -bromopentanoic acid chloride in dry DCM forming a colourless powder of **tdBr** with a yield of 76 %. The work up procedure included washing with water, MeOH and DCM. No addition of base was required to prevent the isolation of a

hydrochloride. Elemental analysis revealed that the compound was obtained as free base. $^1\text{H-NMR}$ spectroscopy and $^1\text{H},^{13}\text{C-HMBC}$ -correlation confirmed the formation of an amide species. The signal of the *NH* amide hydrogen atom is shown at 12.67 ppm in the proton spectrum. In the aromatic region, only signals resulting from the 2-substituted pyridine are observed in the range of 8.67–7.52 ppm. At higher field, the spectrum shows signals resulting from the hydrogen atoms of the methylene groups next to the bromine (3.56 ppm) and next to the amide function (2.56 ppm). Two overlapping multiplets resulting from the $\text{COCH}_2\text{CH}_2\text{CH}_2\text{CH}_2\text{Br}$ and $\text{COCH}_2\text{CH}_2\text{CH}_2\text{CH}_2\text{Br}$ hydrogen atoms can be seen at 1.85 and 1.76 ppm, respectively (Figure 110, appendix). The $^1\text{H},^{13}\text{C-HMBC}$ correlation spectrum shows two cross peaks resulting from the 2J -coupling of the *NH* amide hydrogen atom (12.67 ppm) with the quaternary 2-tdC carbon atom (160.1 ppm) of the thiadiazole ring and the CO carbonyl atom (171.4 ppm) of the amide, respectively (Figure 112, appendix). The APCI mass spectrum of **tdBr** shows an isotopic pattern featuring two main peaks at $m/z = 341.0$ and 343.0 with relative abundances of 53 % and 51 % which were assigned to $[\text{td}^{79}\text{Br}]^+$ and $[\text{td}^{81}\text{Br}]^+$, respectively, confirming the presence of the two bromine isotopes ^{79}Br and ^{81}Br . Furthermore, a signal of the **tdBr** molecule without bromide can be seen at $m/z = 261.2$ (Figure 79). Thus, mass spectrometry confirms the formation of **tdBr**.

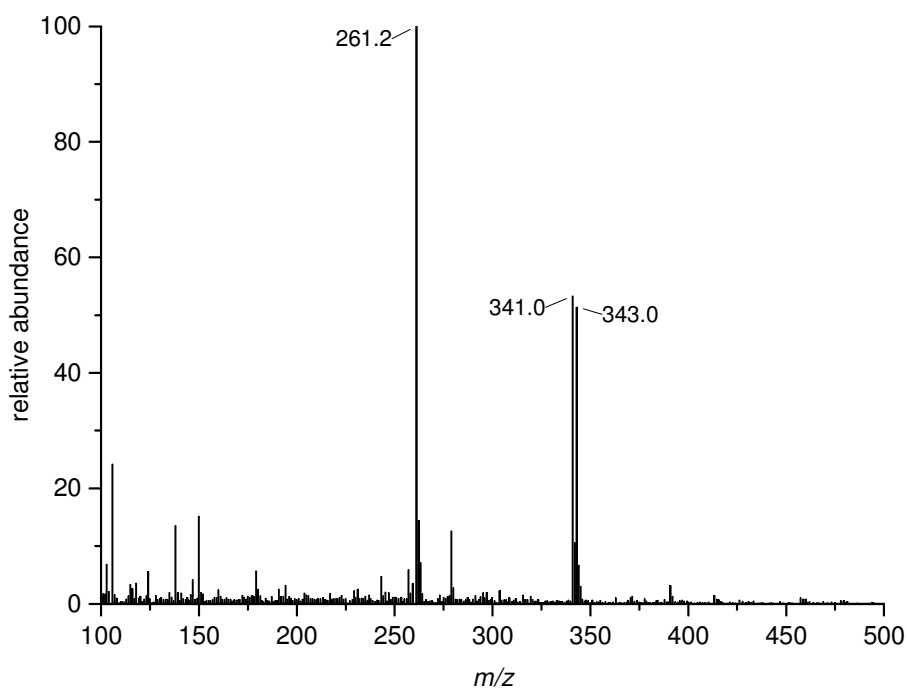


Figure 79: ESI-MS spectrum of precursor **tdBr**.

Reaction with *N*-ethylimidazole was carried out by treating **tdBr** with an excess of imidazole in THF to form the imidazolium compound **L⁴Br**. In MeCN as solvent reaction did not occur, presumably due to the poor solubility of the starting material. The reaction, performed in toluene, was accompanied by the formation of an unidentified byproduct. Thus, the best result was achieved from THF using a huge excess of *N*-ethylimidazole. The imidazolium bromide **L⁴Br** was obtained as a colourless powder. The ¹H-NMR spectrum shows signals of the imidazolium hydrogen atoms at 9.23 ppm (2-imdH) and 7.82 ppm (4-imdH, 5-imdH). Owing to the positive charge of the imidazolium moiety, the signals are shifted to lower field in comparison to the spectrum of *N*-ethylimidazole (Figure 114, appendix). A quartet and a triplet resulting from the ethyl substituent of the imidazolium moiety can be seen at 4.19 and 1.43 ppm, respectively. The quartet overlaps with the triplet resulting from the COCH₂CH₂CH₂CH₂N hydrogen atoms of the linker moiety. The multiplets resulting from the COCH₂CH₂CH₂CH₂N and COCH₂CH₂CH₂CH₂N hydrogen atoms (1.85 ppm, 1.62 ppm) of the linker moiety are clearly separated from each other (Figure 80). The ¹H,¹³C-HMBC correlation confirms the successful attachment of *N*-ethylimidazole as the spectrum shows a cross peak resulting from a ³J-coupling of COCH₂CH₂CH₂CH₂N hydrogen atoms (4.20 ppm) of the linker moiety with the 5-imdC carbon atom (122.0 ppm) of the imidazolium ring (Figure 81).

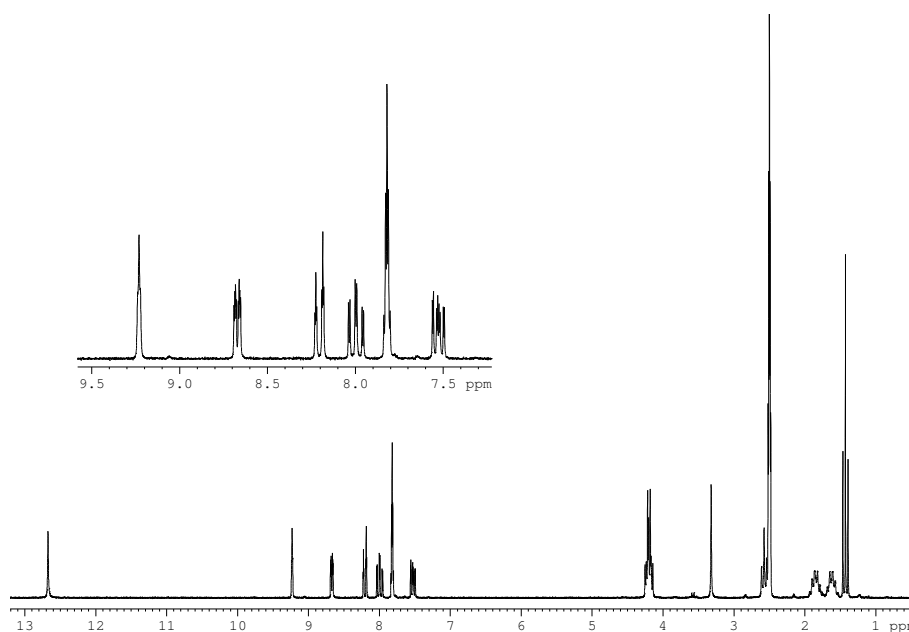


Figure 80: ¹H-NMR spectrum (200.13 MHz) of the imidazolium bromide ligand **L⁴Br** in DMSO-d₆ at 298 K.

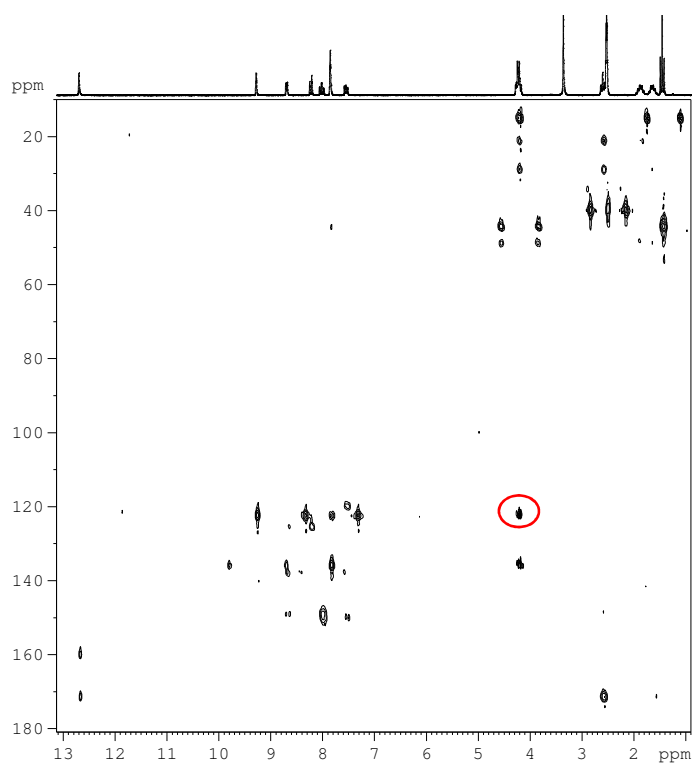


Figure 81: ^1H , ^{13}C -HMBC correlation (200.13 MHz, optimised for 7 Hz) of the imidazolium bromide ligand L^4Br in DMSO-d_6 at 298 K. The red circle indicates the cross peak resulting from the 3J -coupling of the $\text{COCH}_2\text{CH}_2\text{CH}_2\text{CH}_2\text{N}$ hydrogen atoms (4.20 ppm) of the linker moiety with the 5-imC carbon atom (122.0 ppm) of the imidazolium ring.

The ESI mass spectrum of L^4Br shows a peak resulting from the complete cationic part (L^4)⁺ of the ligand at $m/z = 357.1492$. Besides, signals resulting from the fragment without *N*-ethylimidazole ($m/z = 261.0805$) and of from the protonated ligand precursor [$\text{L}^{\text{td}}\cdot\text{H}$]⁺ ($m/z = 179.1179$) are observed. The presence of bromide is clearly indicated in the mass spectrum of the negative mode by the isotopic pattern consisting of two main peaks at $m/z = 80.9165$ and 78.9185 with relative abundances of 100 % and 93.6 %, respectively (Figure 82).

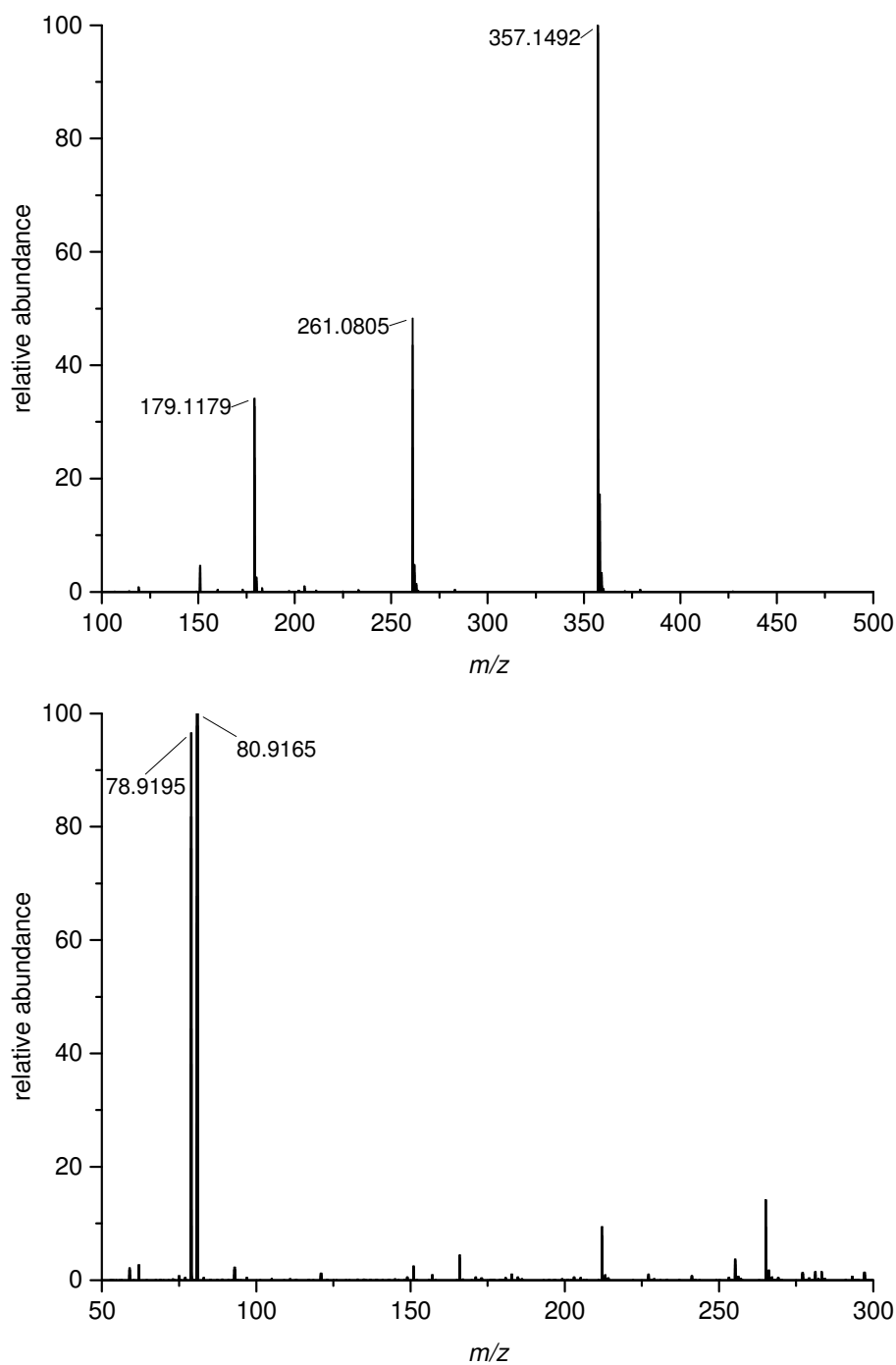


Figure 82: ESI-MS spectra of the imidazolium bromide ligand L^4Br in the *top*: positive mode and *bottom*: negative mode.

In order to obtain a lower melting ligand featuring small coulomb interactions, the anion was exchanged by a metathesis reaction. The bromide L^4Br was reacted with one equivalent of $LiNTf_2$ in water to form the triflimide L^4NTf_2 . Although neither the ligands L^4Br and L^4NTf_2 nor the sodium salt $LiNTf_2$ are water soluble, the metathesis could successfully be carried out this way. Presumably because of the very good

solubility of the byproduct LiBr in water the reaction proceeds quantitatively. The triflimide L^4NTf_2 was obtained analytically pure as a colourless amorphous powder. The 1H -NMR spectrum of L^4NTf_2 shows the same pattern as the spectrum of L^4Br (Figure 83). ^{19}F -NMR spectroscopy reveals that the compound exhibits one fluorine species. The spectrum shows one singlet at -78 ppm. Comparison with the literature confirms that this is a typical value for the NTf_2^- anion (Figure 84).^[86]

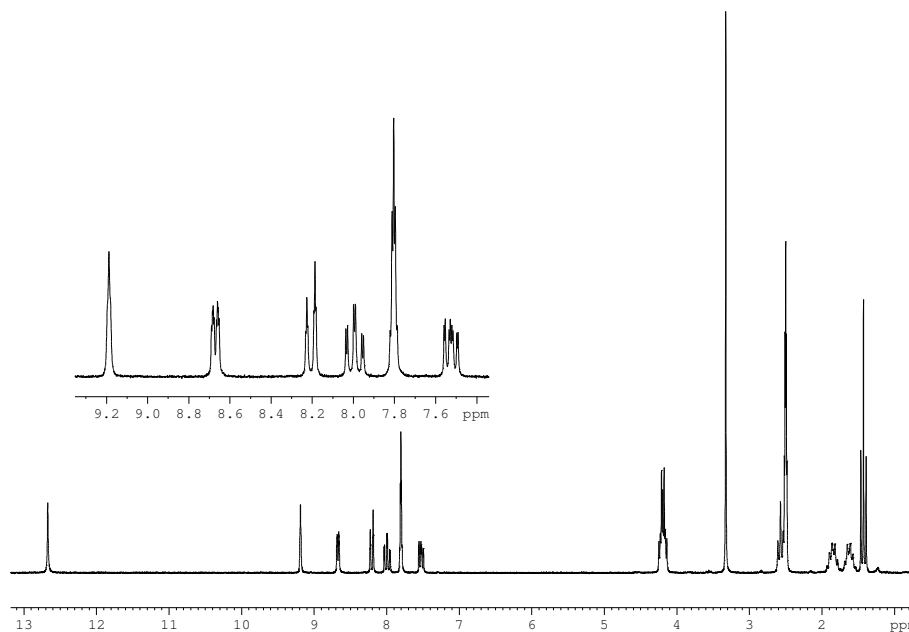


Figure 83: 1H -NMR spectrum (200.13 MHz) of imidazolium triflimide ligand L^4NTf_2 in $DMSO-d_6$ at 298 K.

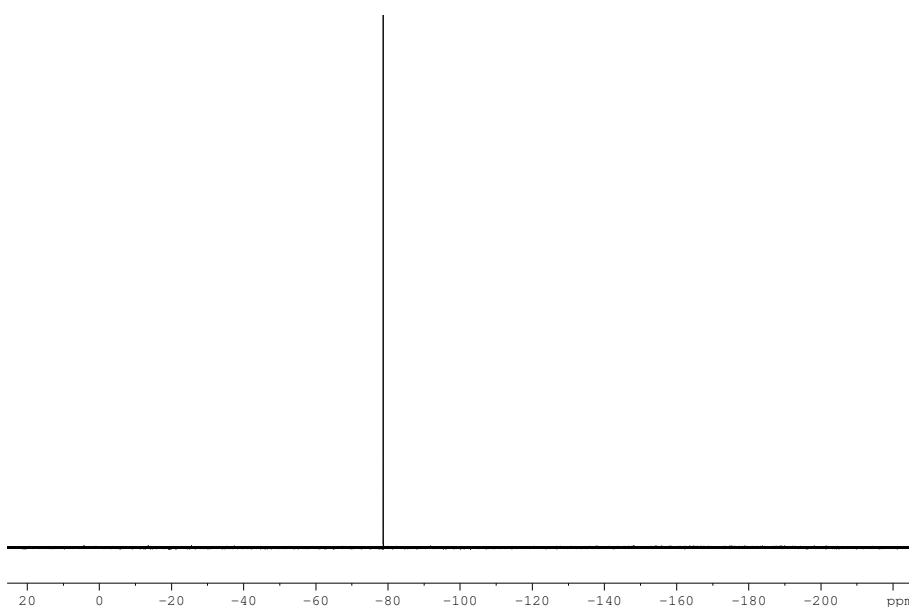


Figure 84: ^{19}F -NMR spectrum (188.29 MHz) of imidazolium triflimide ligand L^4NTf_2 in $DMSO-d_6$ at 298 K.

The cationic part of the ligand has not changed as the mass spectrum of L^4NTf_2 shows the identical isotopic pattern in the positive mode as the mass spectrum of the precursor L^4Br . However, the mass spectrum in the negative mode shows no peaks resulting from bromide. Instead, a signal resulting from the NTf_2^- anion at $m/z = 279.9180$ and a relative abundance of 100 % can be observed. Besides, isotopic patterns resulting from fragments of the anion are observed at $m/z = 146.9608$ ($CF_3SO_2N^-$) and 77.9652 (SO_2N^-) (Figure 85), confirming complete metathesis.

Complexes with an Imidazolium-Tagged Ligand

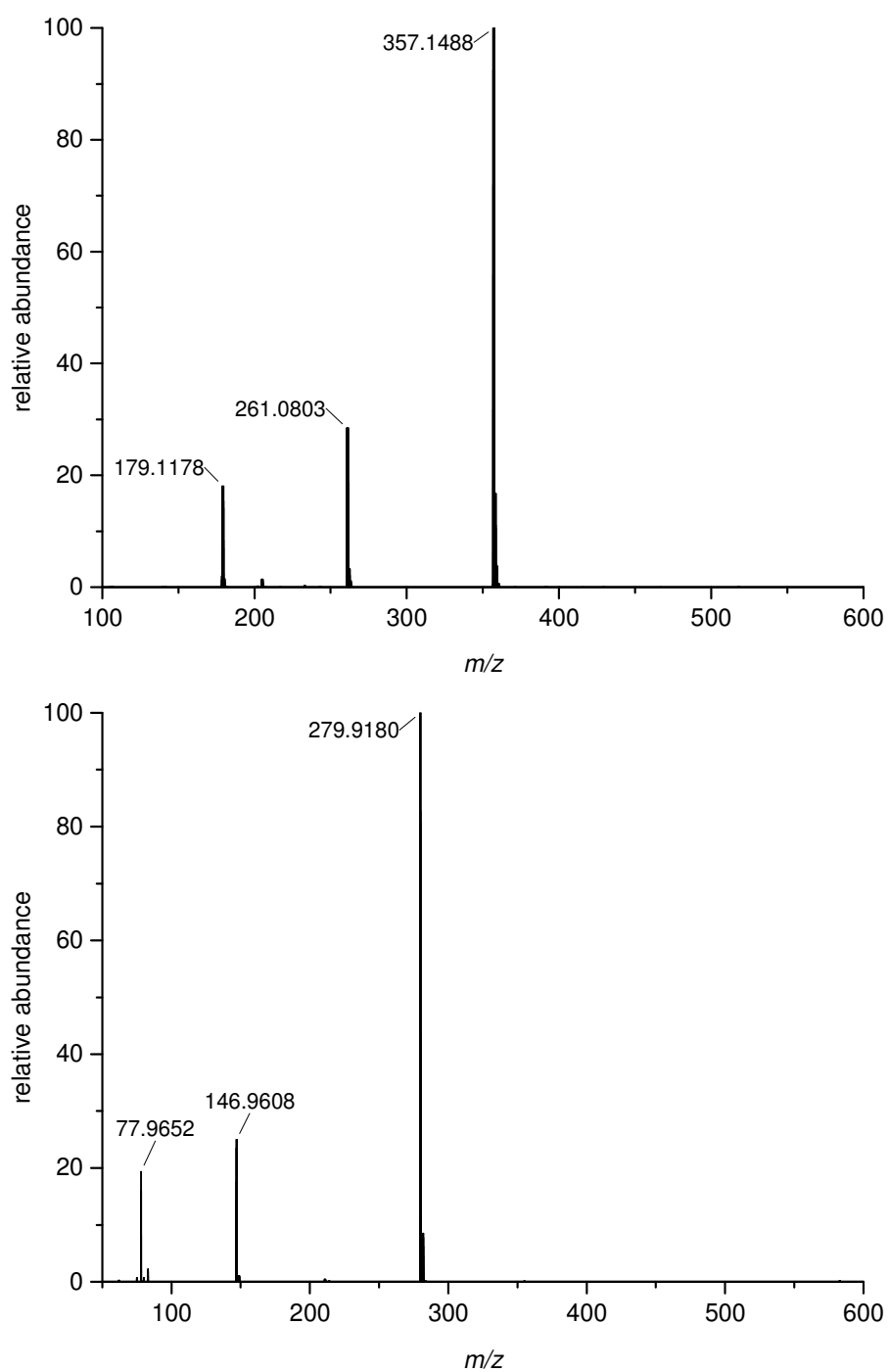


Figure 85: Mass spectra of the imidazolium triflimide ligand L^4NTf_2 in the *top*: positive mode and *bottom*: negative mode.

The IR spectrum of L^4NTf_2 also confirms the presence of the triflimide anion as it shows strong absorption bands resulting from the asymmetric valence vibration of CF_3 at 1175 cm^{-1} , from the symmetric valence vibration of SO_2 at 1131 cm^{-1} and from the asymmetric valence vibration of the SNS group at 1052 cm^{-1} (Figure 86).^[84] The bromide L^4Br melts at $220\text{--}222\text{ }^\circ\text{C}$ whereas the triflimide L^4NTf_2 already melts at $155\text{--}157\text{ }^\circ\text{C}$. Thus the exchange with a weakly coordinating anion remarkably lowers the fusion temperature in the amount of $65\text{ }^\circ\text{C}$, presumably due to weaker coulomb interactions. The UV-Vis spectrum of L^4NTf_2 shows a similar pattern as the ligand L^{td} . The spectrum exhibits a broad absorption band at 301 nm ($17340\text{ M}^{-1}\text{ cm}^{-1}$) which was assigned to inner-ligand transitions (Figure 87).

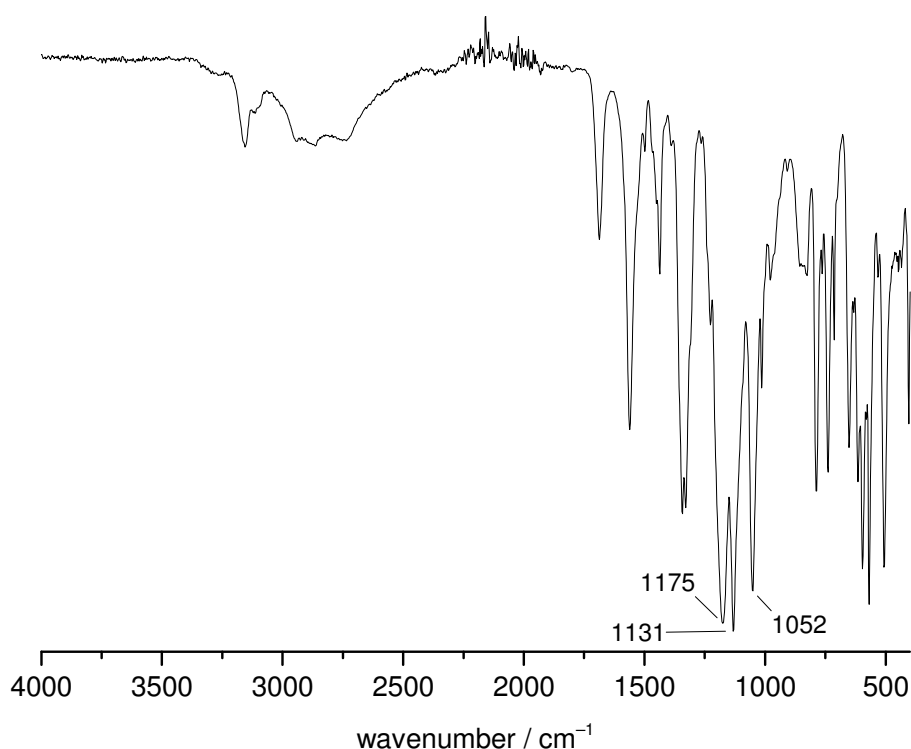


Figure 86: IR spectrum of the imidazolium triflimide ligand L^4NTf_2 .

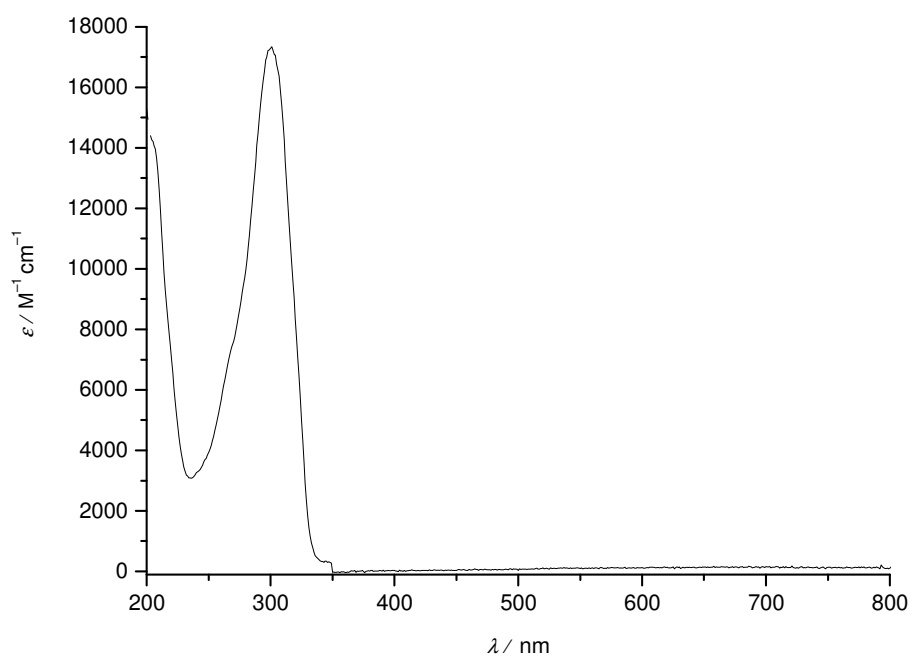
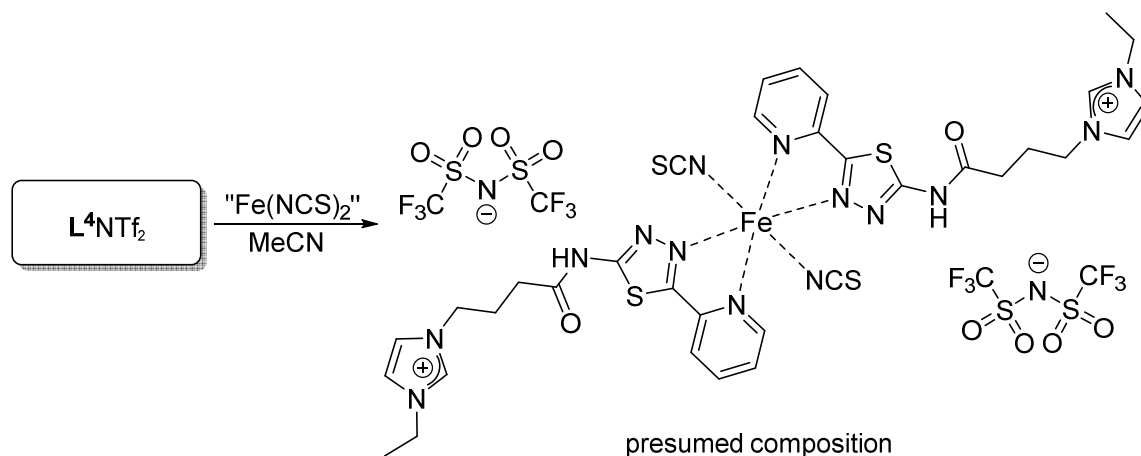


Figure 87: UV/Vis spectrum of the imidazolium triflimide ligand L⁴NTf₂ in MeCN 0.1 mm.

2.3.2 Complexes with L^4NTf_2

In the light of the SCO complex $[Fe(L^{td})_2(NCS)_2]$ (**15**), attempts to synthesise 2:1-type complexes using the imidazolium ligand L^4NTf_2 were carried out. As with “ $Fe(NCS)_2$ ” no analytically pure compound could be obtained, attempts were made using “ $Co(NCS)_2$ ”. In doing so the cobalt(II) isothiocyanate complexes $[Co(L^4)_2(NCS)_2][Co(NCS)_4]$ (**31**) and $[Co(L^4)_2(NCS)_2](NTf_2)_2$ (**32**) were obtained.



Scheme 11: Attempted synthesis of a 2:1-type complex with the imidazolium triflimide ligand L^4NTf_2 .

The imidazolium ligand L^4NTf_2 was reacted with freshly prepared “ $Fe(NCS)_2$ ”. Adding a ligand solution in MeCN to a solution of iron(II) thiocyanate resulted in a deeply red coloured reaction mixture. Neither crystalline material nor amorphous powder could be obtained by cooling, slow evaporation of the solvent or addition of Et_2O and pentane. Instead, the entire solvent was evaporated under reduced pressure and a dark red amorphous powder was obtained (Scheme 11). As expected, elemental analysis of the resulting substance is in accordance with the presumed composition. The IR spectrum confirms the presence of the NTf_2^- anion, as it shows strong absorption bands resulting from the asymmetric valence vibration of CF_3 at 1177 cm^{-1} , from the symmetric valence vibration of SO_2 at 1130 cm^{-1} and from the asymmetric valence vibration of the SNS group at 1050 cm^{-1} .^[84] Furthermore, the spectrum shows the typical peak resulting from the C–N stretching vibration of the isothiocyanato coligand at 2047 cm^{-1} ^[85] (Figure 88).

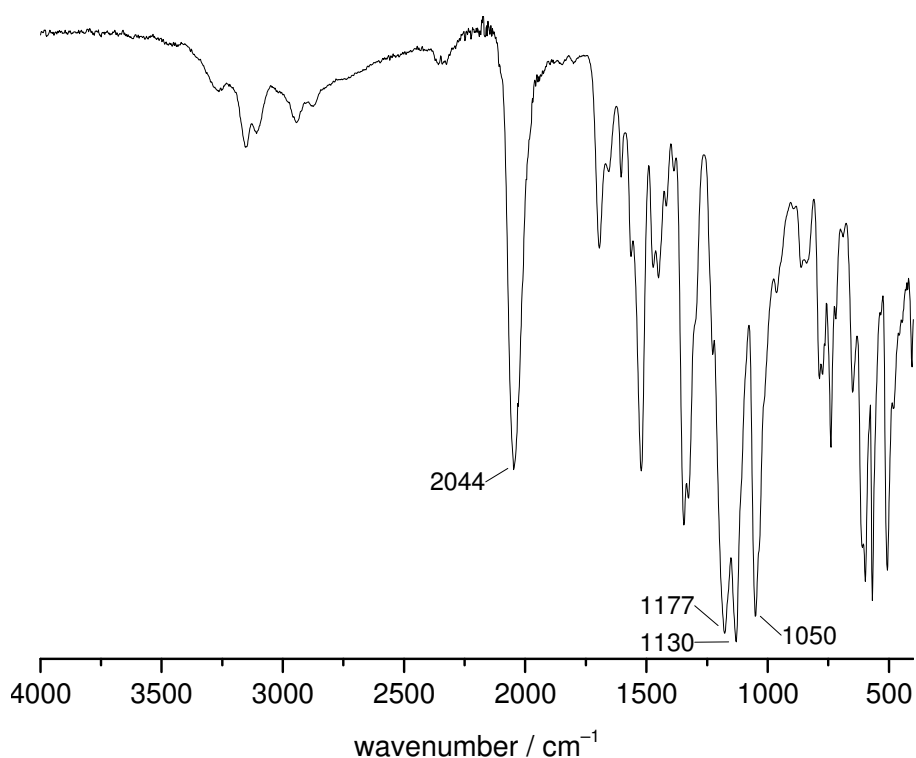


Figure 88: IR spectrum of the dark red powder.

Mass spectrometry, even under inert conditions, only showed peaks resulting from the ligand. No reproducible peaks of higher masses could be observed. Mössbauer spectroscopy of the powder led to an ambiguous result. The isomeric shift $I.S. = 0.37 \text{ mm s}^{-1}$ and the quadrupole splitting of $\Delta E_Q = 0.38 \text{ mm s}^{-1}$ can both be assigned to an iron(II) LS species as well as to an iron(III) HS species (Figure 89).^[82,83] Thus, additional measurements of the magnetic susceptibility have been carried out in the range of 2-295 K. Values lie in the range of $\chi_M T = 1.48$ (295 K) and $1.35 \text{ cm}^3 \text{ K mol}^{-1}$ (55 K) presumably resulting from an iron(II) LS species and a paramagnetic impurity. Indeed fitting the experimental data taking into account 32 % of an impurity with $S = 2.5$ confirms this presumption. The further decline between 50 and 2 K probably results from zero field splitting of the paramagnetic impurity (Figure 90). The impurity might be an iron(III) species resulting from oxidised, uncoordinated “Fe(NCS)₂”.

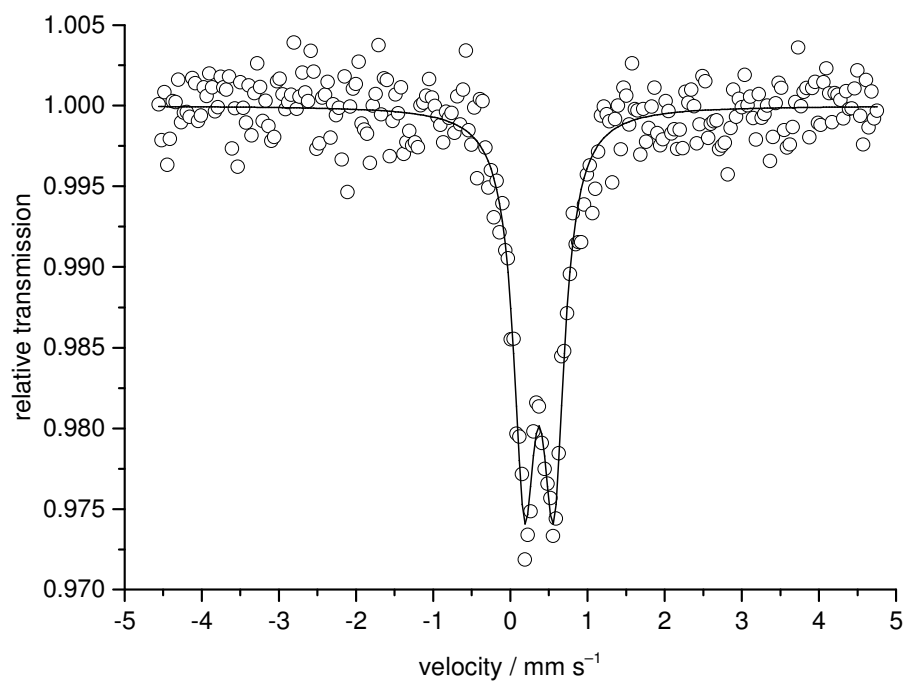


Figure 89: Mössbauer spectrum of the dark red powder.

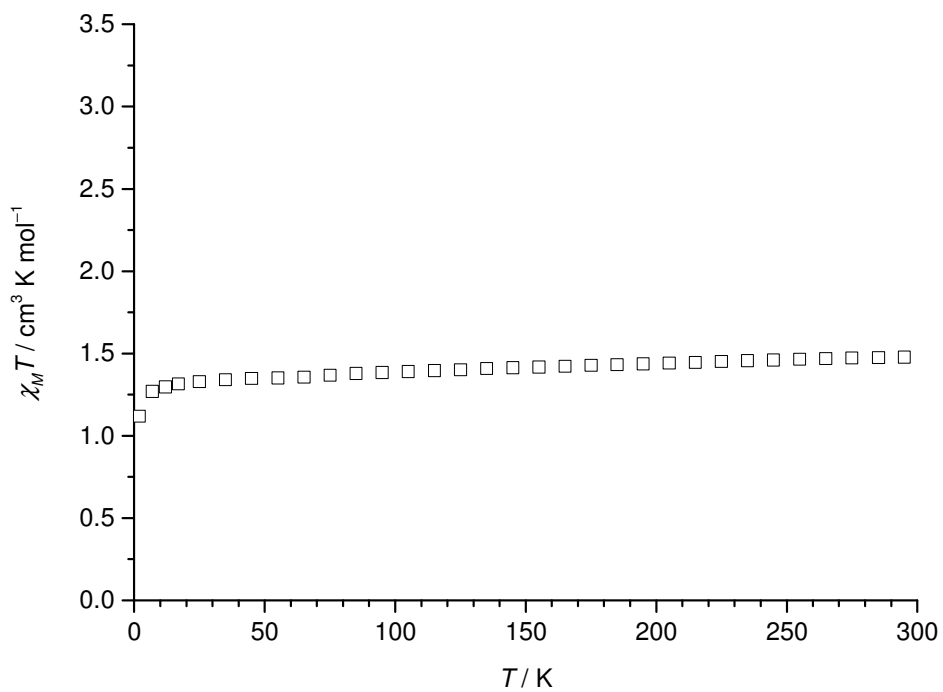


Figure 90: Measurements of the magnetic susceptibility of the dark red powder.

In order to confirm the above mentioned presumption, UV/Vis spectroscopy and HPLC chromatography have been carried out. The UV/Vis spectrum of the freshly prepared, red complex solution in MeCN shows an absorption band at 300 nm which was assigned to inner-ligand transitions. Additionally a broad band at 514 nm ($5800 \text{ M}^{-1} \text{ cm}^{-1}$) with a shoulder at 423 nm ($2720 \text{ M}^{-1} \text{ cm}^{-1}$), presumably resulting from CT transitions, can be seen (Figure 91). HPLC-UV analysis was carried out with a flow rate of 0.3 ml/min and 100 % MeCN as solvent. The chromatogram of the free ligand detected at 300 nm shows one sharp peak at a retention time of 7.88 min. The chromatogram of the red complex solution detected at 500 nm instead, shows one sharp peak at a retention time of 7.46 min. Hence, the ligand and the red substance exhibit different retention times. Detecting the red complex solution at 300 nm reveals that it presumably contains uncoordinated ligand. The chromatogram shows a sharp peak with a retention time of 7.51 min which exhibits a shoulder in the upper region of the peak with a retention time of 7.80 min, assumedly resulting from free ligand. The small deviations between the retention times of the free ligand in chromatogram a) (7.88 min) and b) (7.80 min) and between the retention times of the red substance in chromatogram c) (7.46 min) and b) (7.51 min) could result from mutual interference of the free ligand and the red substance upon recording chromatogram b). The same results have been obtained applying a flow rate of 0.5 ml min^{-1} . No indication for a decomposition of the complex during the separation process is found in the chromatograms, as in this case broad bands would be expected (Figure 92). Thus, the red complex solution is very likely to contain uncoordinated ligand as well as free "Fe(NCS)₂". The latter presumably oxidises to an iron(III) species. Further attempts to obtain a pure compound were carried out in MeOH and in a MeOH/DCM mixture. However, no product could be isolated.

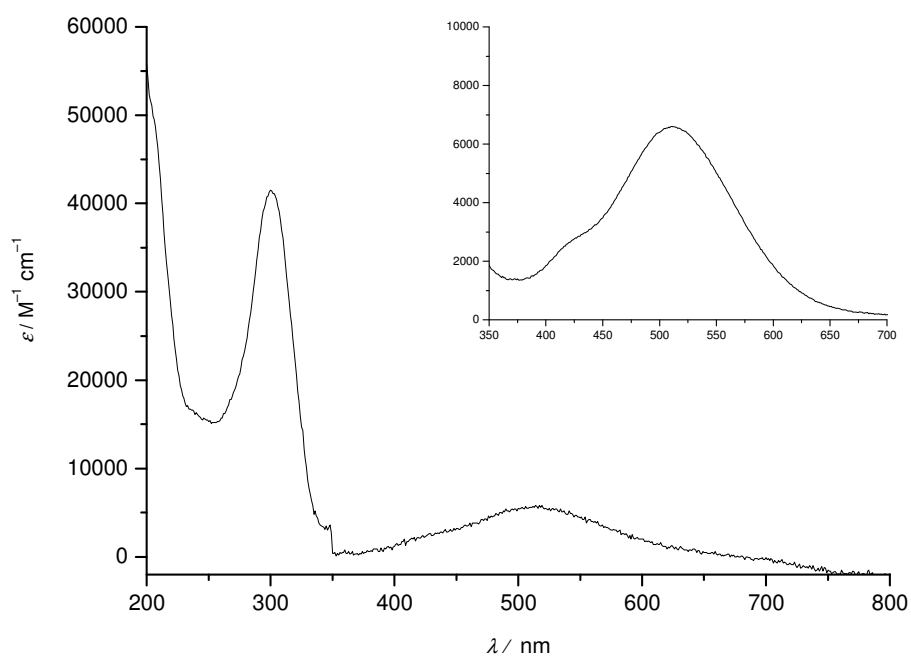


Figure 91: UV/Vis spectrum of the red complex solution 0.01 mm in MeCN (inset: 0.1 mm).

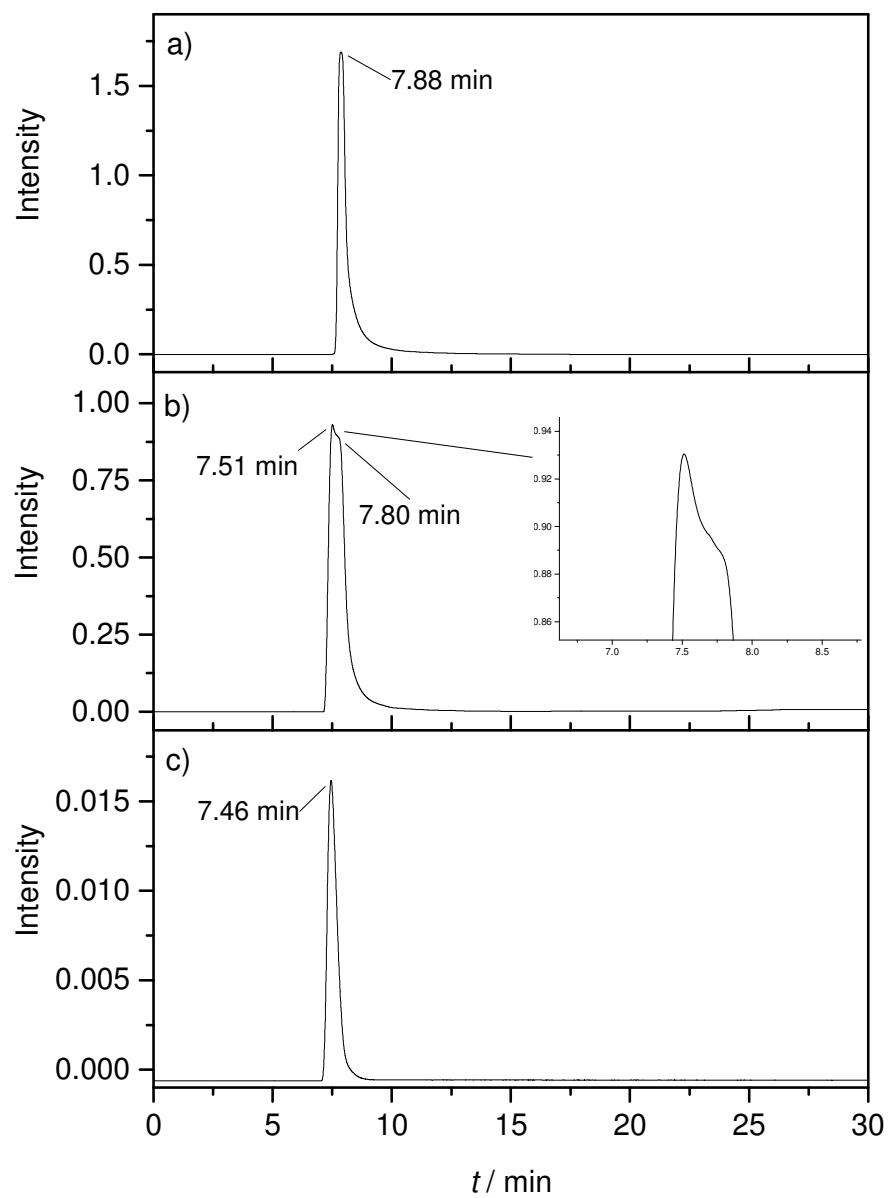
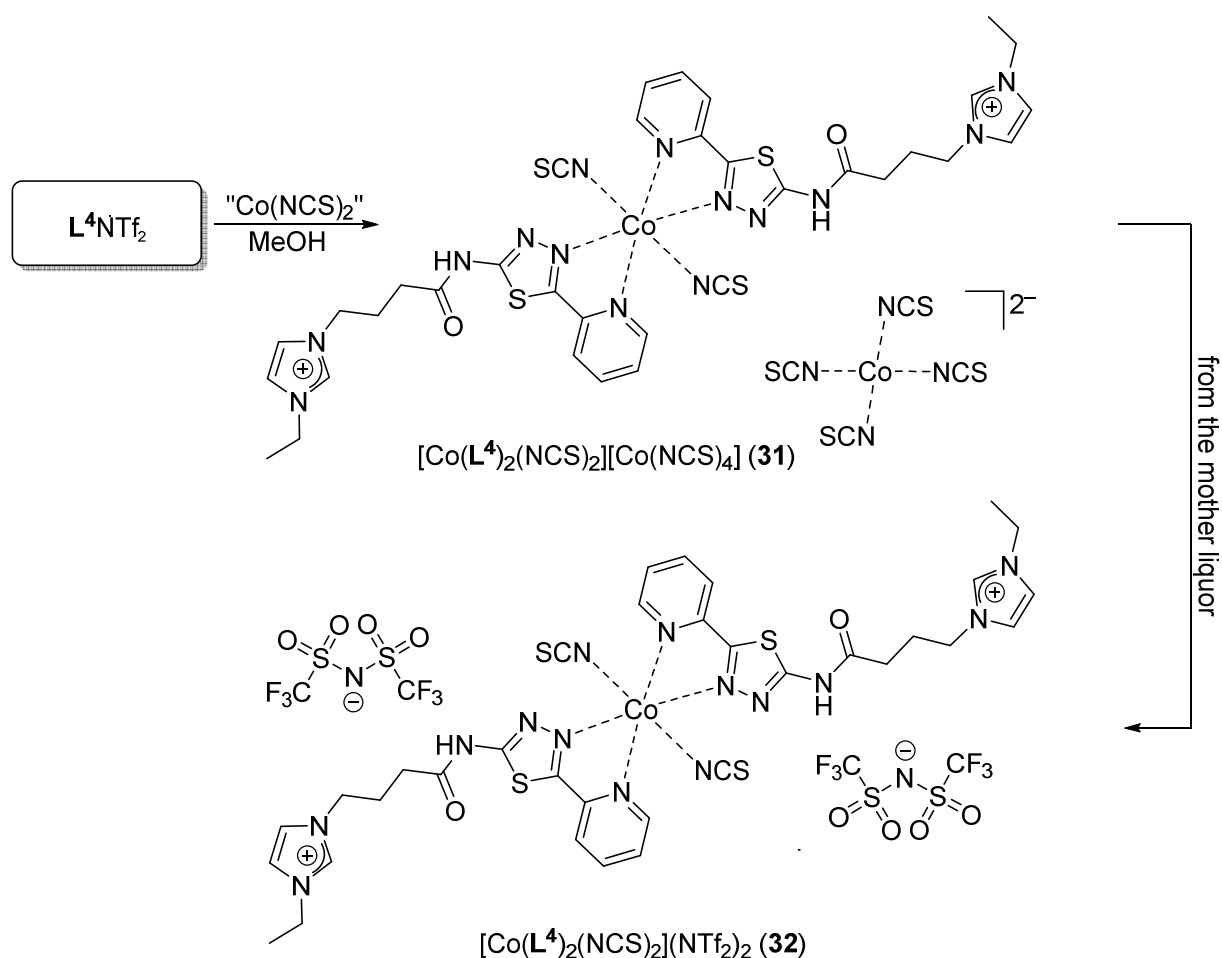


Figure 92: HPLC-UV chromatograms of a) the free ligand L^4NTf_2 (3 mM) detected at 300 nm, b) the red complex solution (6 mM) detected at 300 nm and c) the red complex solution (6 mM) detected at 500 nm; flow rate 0.3 ml min^{-1} , 100 % MeCN.



Scheme 12: Synthesis of $[Co(L^4)_2(NCS)_2][Co(NCS)_4]$ (**31**) and $[Co(L^4)_2(NCS)_2](NTf_2)_2$ (**32**).

As no analytically pure compound could be isolated with “ $Fe(NCS)_2$ ”, the imidazolium ligand L^4NTf_2 was reacted with freshly prepared “ $Co(NCS)_2$ ”. Adding a methanolic ligand solution to a solution of cobalt(II) thiocyanate, resulted in a brown reaction mixture from which after several days some blue coloured crystals formed. The crystals could be identified as $[Co(L^4)_2(NCS)_2][Co(NCS)_4]$ (**31**) by single crystal X-ray diffraction analysis (Scheme 12). Filtration of the blue crystalline compound washing with MeOH and drying *in vacuo* did not lead to analytically pure bulk material. The brown mother liquor was allowed to stand. Slow evaporation of the solvent resulted in the formation of brown crystals which could be identified as $[Co(L^4)_2(NCS)_2](NTf_2)_2$ (**32**) by single crystal X-ray diffraction analysis (Scheme 12). Unfortunately, neither in this case analytically pure bulk material could be obtained. Attempts with “ $Ni(NCS)_2$ ” did not lead to the formation of any identifiable compound. The IR spectra of both compounds **31** and **32** were recorded using several single crystals picked out of the reaction flask. The spectrum of $[Co(L^4)_2(NCS)_2][Co(NCS)_4]$ (**31**) shows the typical peak at 2056 cm^{-1} resulting from the C–N

stretching vibration of the NCS^- coligands (Figure 93).^[85] The IR spectrum of $[\text{Co}(\text{L}^4)_2(\text{NCS})_2](\text{NTf}_2)_2$ (**32**) confirms the presence of the triflimide anion NTf_2^- , as it shows strong absorption bands resulting from the asymmetric valence vibration of CF_3 at 1177 cm^{-1} , from the symmetric valence vibration of SO_2 at 1130 cm^{-1} and from the asymmetric valence vibration of the SNS group at 1052 cm^{-1} .^[84] Besides, the spectrum also shows the typical peak resulting from the C–N stretching vibration of the isothiocyanate coligands at 2079 cm^{-1} (Figure 93).^[85]

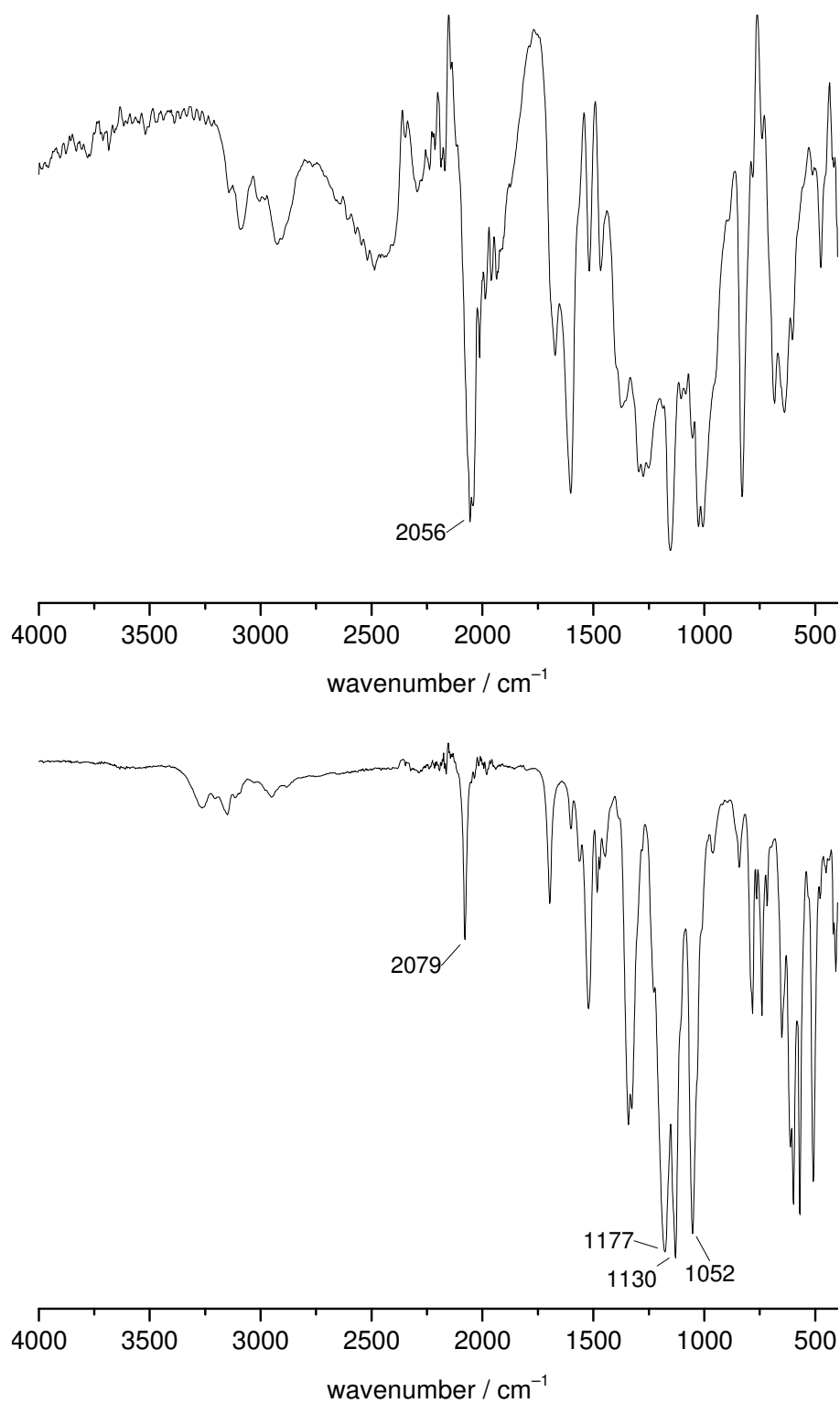


Figure 93: IR spectrum of *top*: [Co(L⁴)₂(NCS)₂][Co(NCS)₄] (**31**) and *bottom*: [Co(L⁴)₂(NCS)₂](NTf₂)₂ (**32**).

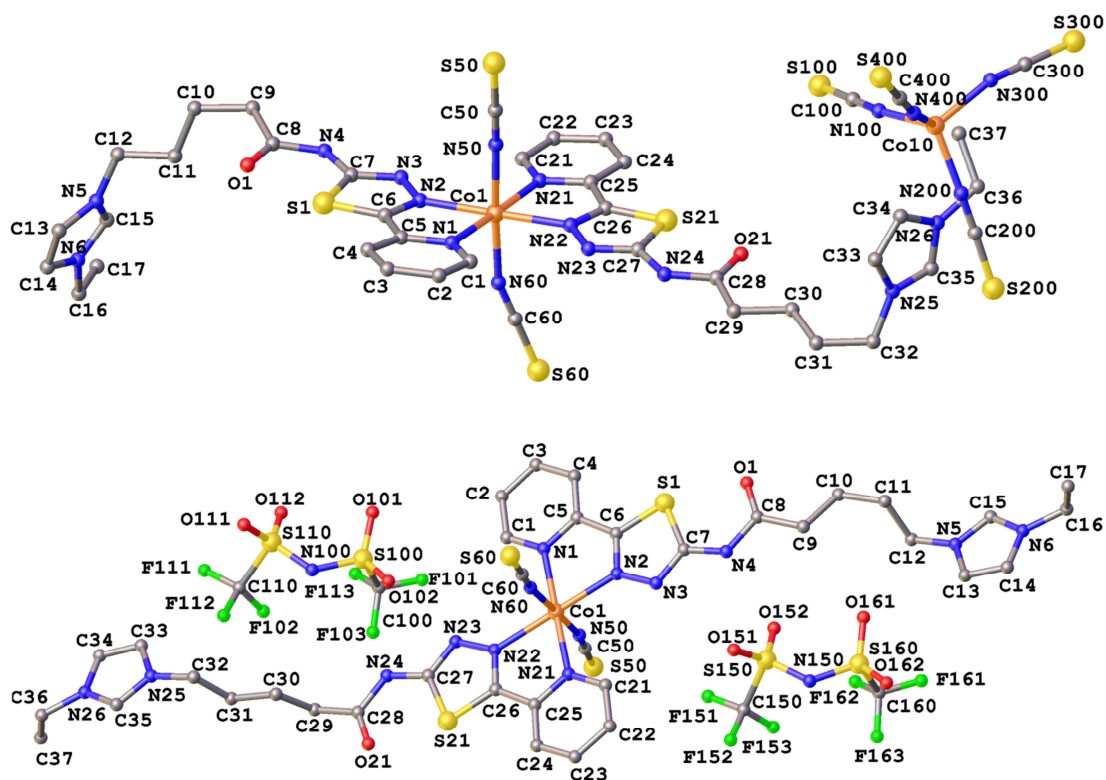


Figure 94: View of the molecular structure at 100 K of *top*: $[\text{Co}(\text{L}^4)_2(\text{NCS})_2][\text{Co}(\text{NCS})_4]$ (**31**) and *bottom*: $[\text{Co}(\text{L}^4)_2(\text{NCS})_2](\text{NTf}_2)_2$ (**32**); H-atoms are omitted for clarity.

Table 10: Selected bond lengths (Å) and angles (°) of $[\text{Co}(\text{L}^4)_2(\text{NCS})_2][\text{Co}(\text{NCS})_4]$ (**31**) and $[\text{Co}(\text{L}^4)_2(\text{NCS})_2](\text{NTf}_2)_2$ (**32**).

	31	32
Co1–N1	2.160(3)	2.138(1),
Co1–N2	2.105(4)	2.179(1)
Co1–N21	2.148(3)	2.141(1)
Co1–N22	2.102(4)	2.185(1)
Co1–N50	2.054(4)	2.058(1)
Co1–N60	2.067(4)	2.059(1)
N1–Co1–N2	76.92(14)	76.63(4)
N1–Co1–N21	177.42(13)	179.13(4)
N1–Co1–N22	102.38(14)	103.67(4)
N1–Co1–N50	88.06(13)	87.70(5)
N1–Co1–N60	92.69(13)	91.28(5)
N2–Co1–N21	103.98(14)	102.73(4)
N2–Co1–N22	178.84(13)	179.60(4)
N2–Co1–N50	90.00(14)	92.87(5)
N2–Co1–N60	92.75(14)	88.63(5)
N21–Co1–N22	76.68(14)	76.96(4)
N21–Co1–N50	89.52(13)	92.93(5)
N21–Co1–N60	89.69(13)	88.11(5)
N22–Co1–N50	89.05(14)	87.41(5)
N22–Co1–N60	88.21(14)	91.09(5)
N50–Co1–N60	177.25(16)	177.93(4)

The complexes $[\text{Co}(\text{L}^4)_2(\text{NCS})_2][\text{Co}(\text{NCS})_4]$ (**31**) and $[\text{Co}(\text{L}^4)_2(\text{NCS})_2](\text{NTf}_2)_2$ (**32**) crystallise in the monoclinic space group $P2(1)/n$ and in the triclinic space group $P-1$, respectively. The asymmetric units consist of one complex $[\text{Co}^{\text{II}}(\text{L}^4)_2(\text{NCS})_2](\text{X})$ ($\text{X} = [\text{Co}^{\text{II}}(\text{NCS})_4]^{2-}$ or 2NTf_2^-). The former complex comprises a tetrakisothiocyanato cobaltate(II) counterion, whereas the latter one features the expected NTf_2^- anion (Figure 94). Bond lengths and angles around the cobalt(II) are similar and are summarised in Table 10. The cobalt(II) resides in a distorted octahedral coordination environment being coordinated by two ligands $(\text{L}^4)^+$ and two NCS^- coligands. The imidazolium ligands act as bidentate chelates coordinating with an N_{py} and N_{td} atom. The coligands coordinate in a *trans* manner to the cobalt(II) completing the N_6 coordination sphere. The coordination octahedron is slightly compressed to the $\text{SCN}-\text{Co}-\text{NCS}$ direction. As often found in complexes with a 2-pyridyl-1,3,4-thiadiazole moiety^[12–14,19,20,96] in **31** the $\text{Co}-\text{N}_{\text{py}}$ bond lengths (2.160(3), 2.148(3) Å) are a bit larger than the $\text{Co}-\text{N}_{\text{td}}$ bond lengths (2.105(4), 2.102(4) Å). However, in the triflimide **32** the opposite is the case with shorter $\text{Co}-\text{N}_{\text{py}}$ (2.138(1), 2.141(1) Å) distances than $\text{Co}-\text{N}_{\text{td}}$ distances (2.179(1), 2.185(1) Å). Nevertheless, with $\text{Co}-\text{N}$ distances ranging from 2.054(4)–2.160(3) (**31**) and 2.058(1)–2.185(1) (**32**) both cobalt(II) centres presumably comprise a HS state.^[7] The NCS^- coligands in **31** are coordinated featuring $\text{Co}-\text{N}-\text{C}$ angles of 159.9(4) and 168.9(4)° whilst the triflimide **32** comprises $\text{Co}-\text{N}-\text{C}$ angles of 168.5(1) and 170.4(1)° with one of the coligands being straightened further. In both compounds the amide oxygen atoms point towards that side of the thiadiazole ring featuring the sulphur atom. In the cobaltate compound **31** both side chains are folded towards a NCS^- coligand. One side chain is disordered beginning with the carbon atom next to the amide and an occupation of the minor part of 0.44. In the triflimide **32** only the side chain comprising the C9-C10-C11-C12 carbon atoms exhibits such a bend.

The complex cations in the crystal structure of **31** are constrained to a close packing by an intermolecular $\text{C}_{\text{im}}-\text{H}\cdots\text{O}_{\text{amide}}$ hydrogen bond and $\text{N}_{\text{amide}}-\text{SCN}$ short contacts forming a stepwise stacking. The cobaltate counterions are located in interspaces surrounded by imidazolium ions. In the crystal structure of the triflimide **32** hydrogen bonding between the complex cation and the NTf_2^- anion and an intermolecular $\text{C}_{\text{im}}-\text{H}\cdots\text{SCN}$ hydrogen bond leads to close packing. Neither $\pi-\pi$ stacking nor $\text{S}\cdots\text{S}$ short contacts with a value of $\text{distance}-\Sigma(\text{vdW-radii}) < 0.05$ Å are found in the structure of **31** or **32**. Selected short contacts are listed in Table 11, crystallographic data are summarised in Table 25 (appendix).

Table 11: Selected short contacts in the crystal structure of $[\text{Co}(\text{L}^4)_2(\text{NCS})_2][\text{Co}(\text{NCS})_4]$ (**31**) and $[\text{Co}(\text{L}^4)_2(\text{NCS})_2](\text{NTf}_2)_2$ (**32**) with a value of $\text{distance} - \sum(\text{VdW-radii}) < -0.2 \text{ \AA}$.

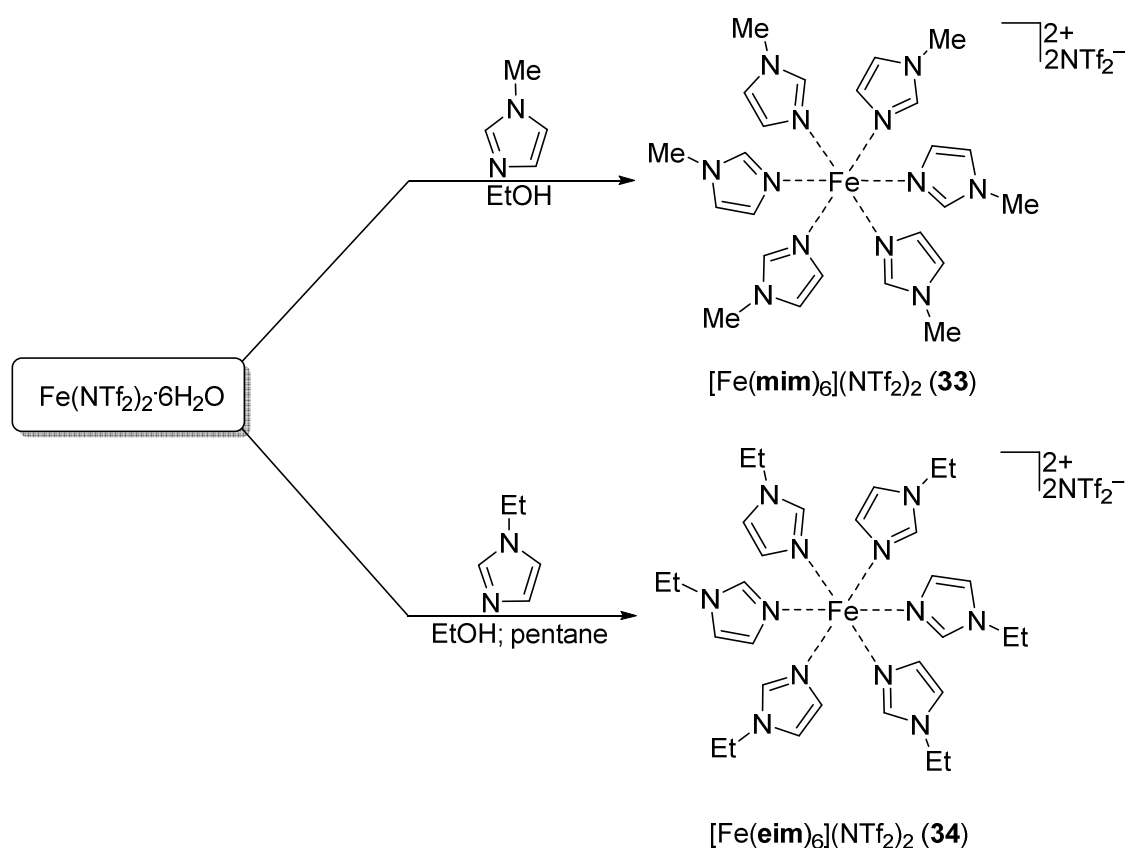
31			
atom1	atom2	distance / \AA	$\text{distance} - \sum(\text{VdW-radii}) / \text{\AA}$
O21	S21	2.628	-0.692
O1	S1	2.688	-0.632
H _{NH} 24	S50A	2.504 (N...S: 3.325)	-0.260
H _{NH} 4	S60B	2.544 (N...S: 3.320)	-0.456
H _{im} 33	O1A	2.362 (C...O: 3.115)	-0.358
H _{im} 34	N100	2.543 (C...N: 3.490)	-0.207
32			
atom1	atom2	distance / \AA	$\text{distance} - \sum(\text{VdW-radii}) / \text{\AA}$
O1	S1	2.615	-0.705
O21	S21	2.574	-0.746
H _{NH} 4	O152	2.047 (N...O: 2.870)	-0.673
H _{NH} 24	O112C	2.107 (N...O: 2.911)	-0.613
H _{py} 1	F111C	2.354 (C...F: 3.028)	-0.316
H _{im} 35	O162D	2.460 (C...O: 3.205)	-0.260
H _{im} 33	O101C	2.488 (C...O: 3.287)	-0.232
H _{im} 14	S50E	2.775 (C...S: 3.508)	-0.225

Symmetry operations used to generate equivalent atoms: A) $-x, 1-y, -z$; B) $-x, 1-y, 1-z$; C) $1-x, 2-y, 1-z$; D) $1-x, 1-y, 1-z$; E) $1-x, -y, -z$.

Owing to the imidazolium tag, both complexes **31** and **32** feature a coordination entity with an overall charge of +2 though the chromophores are charge neutral. The results of this chapter indicate that the capability of the ligand L^4NTf_2 to form coordination compounds is very limited. Presumably the positive charge of the imidazolium moiety might prevent the bond formation to the positive charged transition metals. Nevertheless both compounds **31** and **32** are rare examples of such Werner-type 3d transition metal complexes. As far as known, only a small number of such compounds were prepared yet, such as iron complexes of 3-hydroxy-pyran-4-one^[97], salen-type complexes of manganese^[98], cobalt,^[99] copper,^[100] nickel complexes of bis-salicyldimine^[101] and copper complexes with bis-salicylaloxime.^[100]

2.4 Complexes with N-Alkylimidazoles

In the light of the 6:1-type SCO complexes $[\text{Fe}(\text{etz})_6](\text{BF}_4)_2$ (**U**, Figure 5) and $[\text{Fe}(\text{ptz})_6](\text{BF}_4)_2$ (**V**, Figure 5) with **etz** = 1-ethyltetrazole and **ptz** = 1-*n*-propyltetrazole both ligands were reacted with $\text{Fe}(\text{NTf}_2)_2 \cdot 6\text{H}_2\text{O}$ in order to obtain low melting SCO complexes. The tetrafluoroborate complexes **U** and **V** are solid at rt and as far as known, melting points have not been determined yet. The ligands **etz** and **ptz** were synthesised according to a procedure from *Nishiyama et al.* ^[47] Unfortunately no identifiable compound ^[47] could be isolated from attempts in MeOH, EtOH, MeCN, H₂O or DCM. As with the imidazole ligands *N*-methylimidazole (**mim**) and *N*-ethylimidazole (**eim**) a series of 6:1-type iron(II) complexes was previously synthesised by the author, ^[48,102] the latter ligands were used in order to investigate the ability of $\text{Fe}(\text{NTf}_2)_2 \cdot 6\text{H}_2\text{O}$ to form 6:1-type iron(II) complexes.



Scheme 13: Synthesis of $[\text{Fe}(\text{mim})_6](\text{NTf}_2)_2$ (**33**) and $[\text{Fe}(\text{eim})_6](\text{NTf}_2)_2$ (**34**).

The 6:1-type complexes $[\text{Fe}(\text{mim})_6](\text{NTf}_2)_2$ (**33**) and $[\text{Fe}(\text{eim})_6](\text{NTf}_2)_2$ (**34**) were prepared using $[\text{Fe}(\text{NTf}_2)_2] \cdot 6\text{H}_2\text{O}$ and *N*-methylimidazole (**mim**) or *N*-ethylimidazole (**eim**) as ligands (Scheme 13). The compounds were obtained by mixing ethanolic solutions of the ligand and $\text{Fe}(\text{NTf}_2)_2 \cdot 6\text{H}_2\text{O}$. The

methylimidazole complex $[\text{Fe}(\text{mim})_6](\text{NTf}_2)_2$ (**33**) precipitated immediately as a colourless powder whereas the ethylimidazole complex $[\text{Fe}(\text{eim})_6](\text{NTf}_2)_2$ (**34**) precipitated upon the addition of pentane as beige coloured powder. Elemental analyses revealed that both complexes **33**·0.5EtOH·0.5H₂O and **34**·0.5EtOH·0.5H₂O contain half a solvent molecule EtOH and H₂O. The methylimidazole complex decomposes at 183–185 °C whereas the ethylimidazole compound exhibits a melting point at 83–85 °C. ESI-MS spectra show one peak provoked by a monocationic iron(II) species comprising two ligand molecules and one NTf_2^- anion at $m/z = 499.9577$ (**33**·0.5EtOH·0.5H₂O) and 527.9890 (**34**·0.5EtOH·0.5H₂O) (Figure 95). The IR spectra also confirm the presence of the triflimide anion NTf_2^- , as they show strong absorption bands resulting from the asymmetric valence vibration of CF_3 at 1174 cm^{-1} (**33**·0.5H₂O·0.5EtOH, **34**·0.5EtOH·0.5H₂O), from the symmetric valence vibration of SO_2 at 1140 cm^{-1} (**33**·0.5H₂O·0.5EtOH) and 1133 cm^{-1} (**34**·0.5EtOH·0.5H₂O) and from the asymmetric valence vibration of the SNS group at 1052 cm^{-1} (**33**·0.5H₂O·0.5EtOH) and 1060 cm^{-1} (**34**·0.5EtOH·0.5H₂O) (Figure 96).^[84]

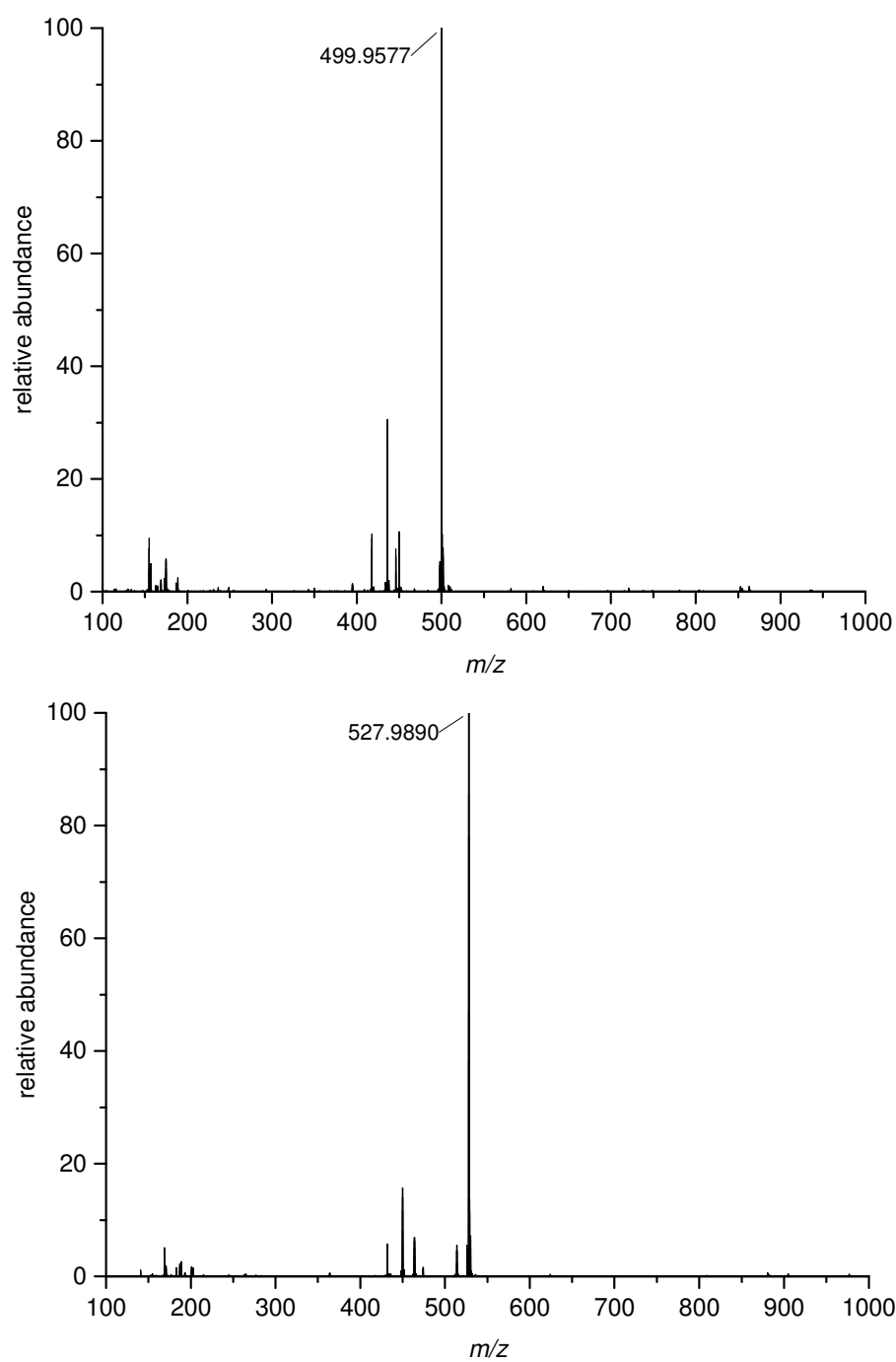


Figure 95: ESI-MS spectra of *top*: $[\text{Fe}(\text{mim})_6](\text{NTf}_2)_2 \cdot 0.5\text{H}_2\text{O} \cdot 0.5\text{EtOH}$ (**33**·0.5H₂O·0.5EtOH) and *bottom*: $[\text{Fe}(\text{eim})_6](\text{NTf}_2)_2 \cdot 0.5\text{H}_2\text{O} \cdot 0.5\text{EtOH}$ (**34**·0.5H₂O·0.5EtOH).

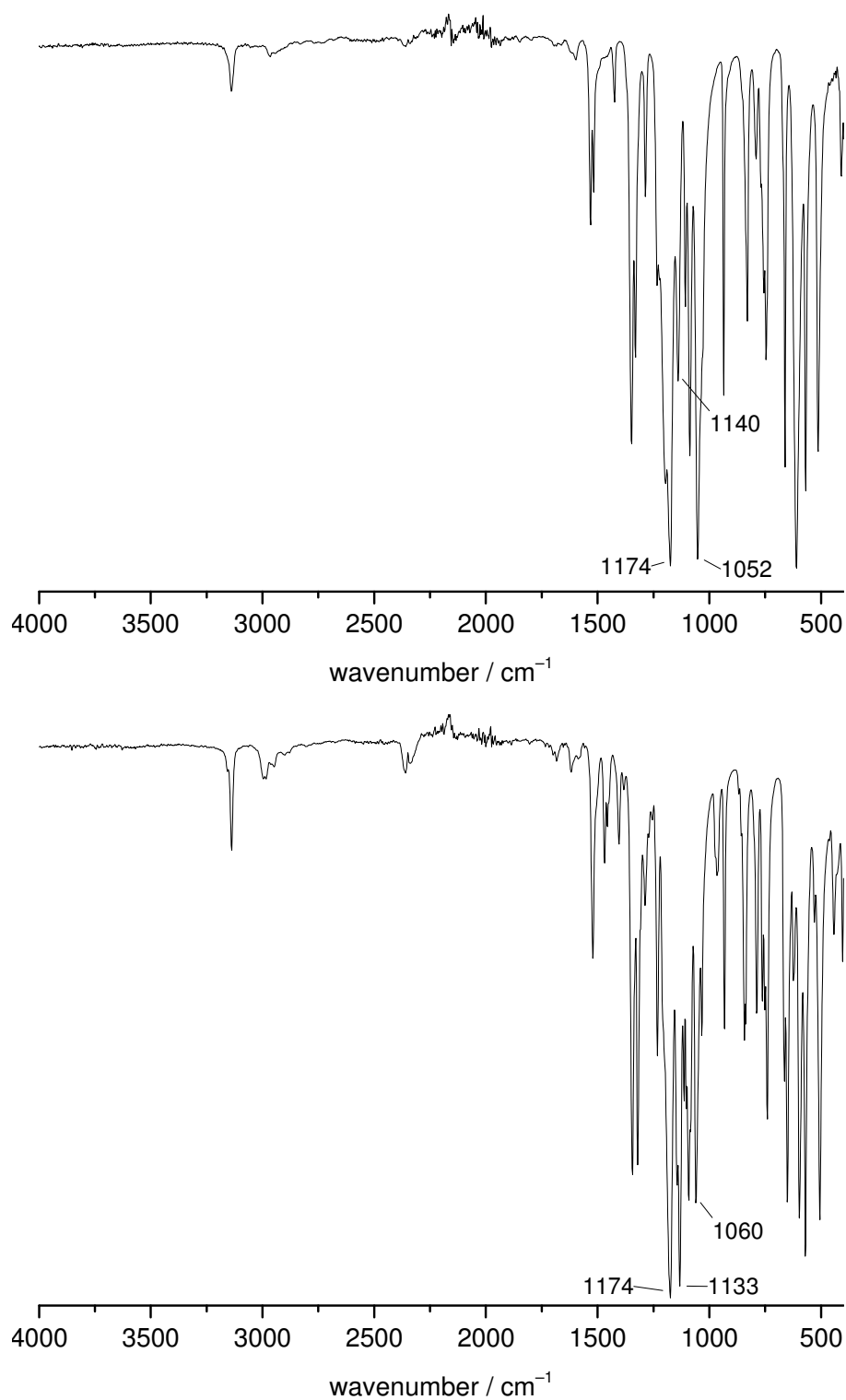


Figure 96: IR spectra of *top*: [Fe(mim)₆](NTf₂)₂·0.5H₂O·0.5EtOH (**33**·0.5H₂O·0.5EtOH) and *bottom*: [Fe(eim)₆](NTf₂)₂·0.5H₂O·0.5EtOH (**34**·0.5H₂O·0.5EtOH).

Owing to their low solubility in common solvents, UV/Vis spectra of these compounds were recorded in propylene carbonate in the range of 300–1100 nm. Both spectra show a broad absorption band at 360 nm ($132 \text{ M}^{-1} \text{ cm}^{-1}$) (**33**·0.5EtOH·0.5H₂O) and 373 nm ($156 \text{ M}^{-1} \text{ cm}^{-1}$) (**34**·0.5EtOH·0.5H₂O) which were assigned to inner-ligand transitions. Additionally, the spectra show rather weak bands at 863 nm ($5 \text{ M}^{-1} \text{ cm}^{-1}$) for the methylimidazole complex (**33**·0.5EtOH·0.5H₂O) and 858 nm ($6 \text{ M}^{-1} \text{ cm}^{-1}$) for the ethylimidazole complex (**34**·0.5EtOH·0.5H₂O) which are presumably provoked by d-d transitions of the iron(II) core (Figure 98). Because of the octahedral coordination sphere, the transitions are - according to the Laporte rule - forbidden and therefore very weak. Due to the pale colour of the compounds and the presence of a d-d transition in the visible region the complexes are presumed to be in the HS state. ^[81] The ligand field splitting for iron(II) HS compounds can be determined easily from the UV-Vis spectrum as the ${}^5\text{T}_{2g} \rightarrow {}^5\text{E}_g$ transition is directly related to $10Dq$ (Figure 97). ^[87] Thus, the ligand field splitting of these compounds calculate to $10Dq = 11600 \text{ cm}^{-1}$ for **33**·0.5EtOH·0.5H₂O and $10Dq = 11700 \text{ cm}^{-1}$ for **34**·0.5EtOH·0.5H₂O, which are typical values for iron(II) in the HS state. ^[87]

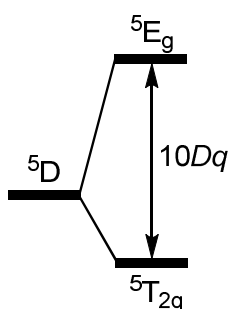


Figure 97: Ligand field splitting of the ground state of an octahedral coordinated iron(II) HS core and relation to $10Dq$.

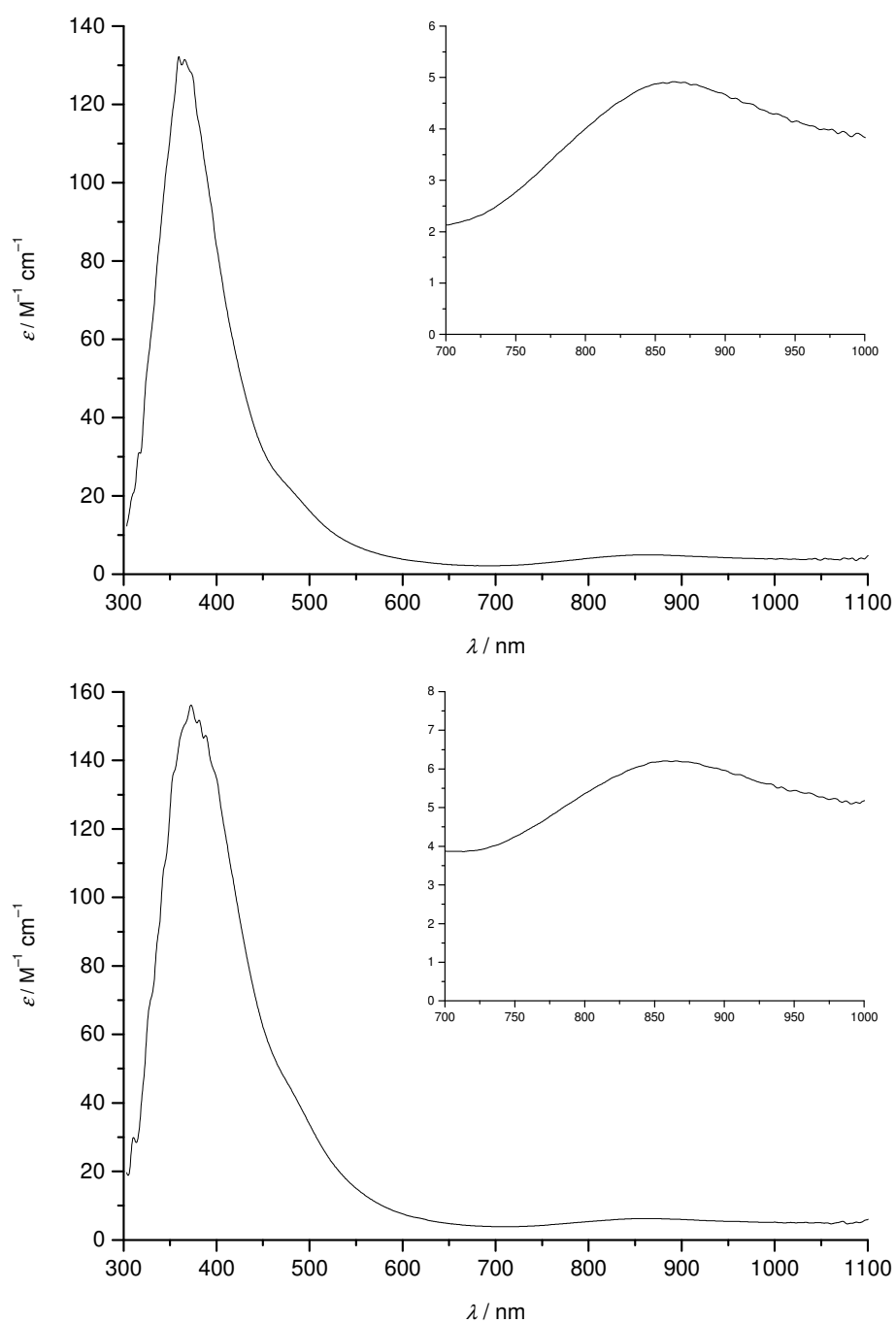


Figure 98: UV/Vis spectra in 10 mm propylene carbonate of *top*: $[\text{Fe}(\text{mim})_6](\text{NTf}_2)_2 \cdot 0.5\text{H}_2\text{O} \cdot 0.5\text{EtOH}$ (**33**·0.5EtOH·0.5H₂O) (inset: enlarged region from 700-1100 nm) and *bottom*: $[\text{Fe}(\text{eim})_6](\text{NTf}_2)_2 \cdot 0.5\text{H}_2\text{O} \cdot 0.5\text{EtOH}$ (**34**·0.5EtOH·0.5H₂O) (inset: enlarged region from 700-1100 nm).

In order to confirm the melting point of the ethylimidazole complex $[\text{Fe}(\text{eim})_6](\text{NTf}_2)_2 \cdot 0.5\text{H}_2\text{O} \cdot 0.5\text{EtOH}$ ($34 \cdot 0.5\text{EtOH} \cdot 0.5\text{H}_2\text{O}$) DSC measurements were carried five times in the heating and the cooling mode. The heating curve of cycle one (Figure 99) clearly shows an endothermic peak at 85 °C ($T_{\text{onset}} = 83$ °C) resulting from the fusion process. Integration of this peak leads to the corresponding fusion enthalpy $\Delta H_{\text{fus}} = 67 \text{ kJ mol}^{-1}$ which is a slightly higher value for an ionic compound consisting of one dication and two mono-anions, than usually observed.^[93–95] The cooling curve (Figure 99) shows an exothermic peak at 51 °C ($T_{\text{onset}} = 50$ °C) resulting from the crystallisation process. Hence the compound's melting and solidifying process shows a hysteresis of 33 K which is in the range of typically observed values for ionic compounds.^[93–95] These results could be reproduced in four subsequent heating and cooling cycles (not shown).

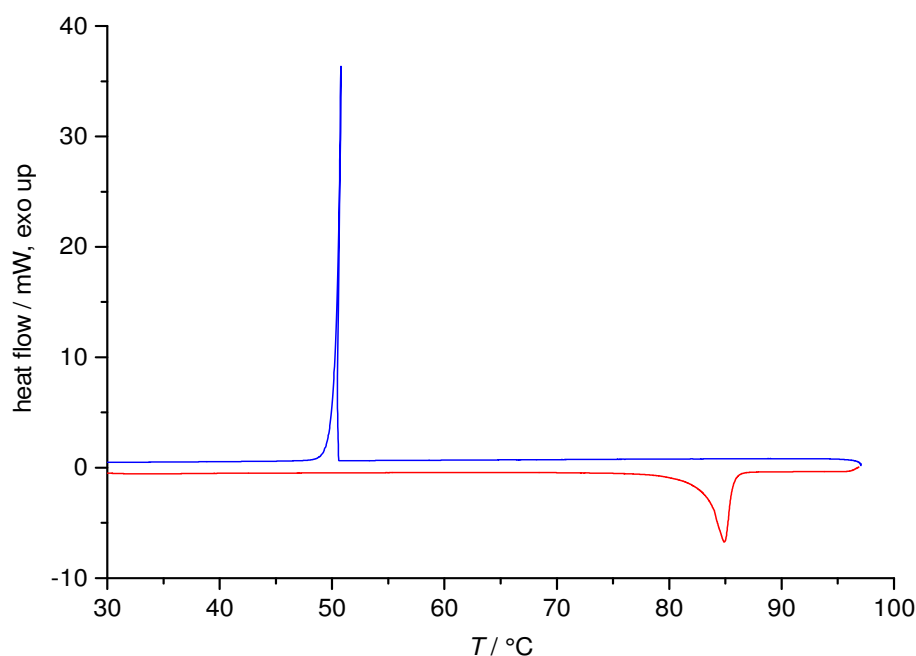
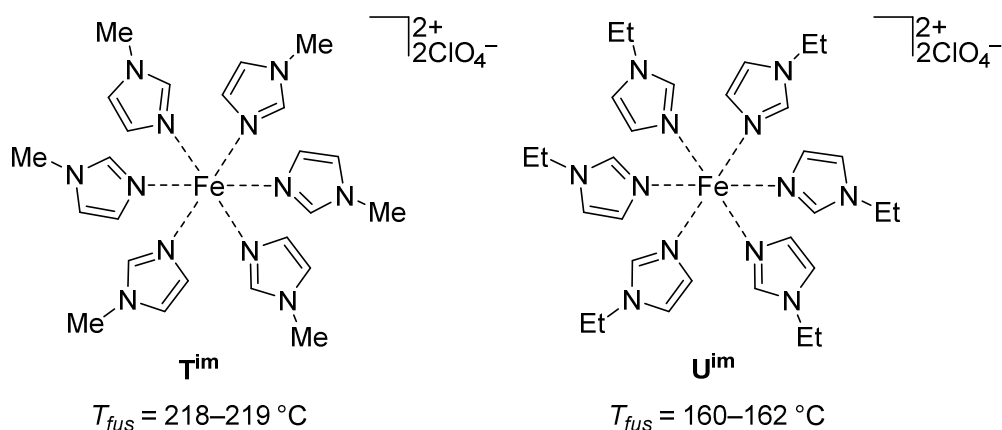


Figure 99: DSC measurements in the heating (red line) and cooling (blue line) mode of $[\text{Fe}(\text{eim})_6](\text{NTf}_2)_2 \cdot 0.5\text{H}_2\text{O} \cdot 0.5\text{EtOH}$ ($34 \cdot 0.5\text{EtOH} \cdot 0.5\text{H}_2\text{O}$) with a scan rate of 2 K min^{-1} .



Scheme 14: Related perchlorate complexes $[\text{Fe}(\text{mim})_6](\text{ClO}_4)_2$ (T^{im}) and $[\text{Fe}(\text{eim})_6](\text{ClO}_4)_2$ (U^{im}) which have been synthesised for the diploma thesis of the author. ^[48,102]

Both herein discussed chromophores already have already been synthesised as the analogue iron(II) perchlorate complexes $[\text{Fe}(\text{mim})_6](\text{ClO}_4)_2$ (T^{im}) and $[\text{Fe}(\text{eim})_6](\text{ClO}_4)_2$ (U^{im}) in the diploma thesis of the author (Scheme 14, Table 12). ^[48,102] The perchlorate complexes exhibit a typical ligand field splitting of $10Dq = 11600 \text{ cm}^{-1}$ (T^{im} and U^{im}) for iron(II) in the HS state. This could be confirmed by measurements of the molar susceptibility in the range of 2–300 K. The methylimidazole complex T^{im} melts at 218–219 °C whereas the ethyl analogue complex melts at 160–162 °C. Hence the same tendency between methyl and ethyl substituent is observed as within the couple of triflimide complexes $\mathbf{33} \cdot 0.5\text{EtOH} \cdot 0.5\text{H}_2\text{O}$ (183 °C dec.) and $\mathbf{34} \cdot 0.5\text{EtOH} \cdot 0.5\text{H}_2\text{O}$ (83 °C) (Table 12).

Table 12: Summary of the compounds discussed in this chapter.

		spin state	$T_{fus} / ^\circ\text{C}$	$10Dq / \text{cm}^{-1}$
$[\text{Fe}(\text{mim})_6](\text{NTf}_2)_2 \cdot 0.5\text{H}_2\text{O} \cdot 0.5\text{EtOH}$	$(\mathbf{33} \cdot 0.5\text{EtOH} \cdot 0.5\text{H}_2\text{O})$	HS	183 (dec.)	11600
$[\text{Fe}(\text{eim})_6](\text{NTf}_2)_2 \cdot 0.5\text{H}_2\text{O} \cdot 0.5\text{EtOH}$	$(\mathbf{34} \cdot 0.5\text{EtOH} \cdot 0.5\text{H}_2\text{O})$	HS	83	11600
$[\text{Fe}(\text{mim})_6](\text{ClO}_4)_2$	T^{im}	HS	218	11500
$[\text{Fe}(\text{eim})_6](\text{ClO}_4)_2$	U^{im}	HS	160	11500

The ethyl substituent possesses additional torsion angles in comparison with the methyl substituent. Thus, enhancing the conformational degrees of freedom of the complex increases its entropy of fusion ΔS_{fus} and therefore lowers its fusion temperature T_{fus} . Besides the complexes with triflimide counterion melt at remarkably lower temperatures than the analogous perchlorate compounds presumably due to the lower coulomb interactions between anions and cation.

2.5 Summary and Outlook

A synthesis for $\text{Fe}(\text{NTf}_2)_2 \cdot 6\text{H}_2\text{O}$ was developed, the compound was structurally characterised via X-ray diffraction analysis and successfully used as starting material for complex syntheses. Together with the thiadiazole ligand L^{td} it forms the 3:1-type LS complex $[\text{Fe}^{\text{II}}(\text{L}^{\text{td}})_3](\text{NTf}_2)_2$ (**12**) that melts at 194 °C, as confirmed by DSC measurements, whereas the related perchlorate **10** and tetrafluoroborate **11** do not melt up to 220 °C and the related chloride **9** even decomposes at 210 °C. The related cobalt(II) perchlorate complex $[\text{Co}^{\text{II}}(\text{L}^{\text{td}})_3](\text{ClO}_4)_2$ (**13**) exhibits a HS state, which indicates that little weakening of the ligand field in the case of the iron(II) complexes with L^{td} could lead to a SCO compound. Indeed, the 2:1-type complex $[\text{Fe}^{\text{II}}(\text{L}^{\text{td}})_2(\text{NCS})_2]$ (**15**) featuring relatively weak coligands NCS^- exhibits a SCO near to rt at $T_{1/2} = 250$ K as confirmed by SQUID measurements. Using the thiazole ligand L^{tz} the 2:1-type HS iron(II) complexes $[\text{Fe}^{\text{II}}(\text{L}^{\text{tz}})_2(\text{NCS})_2]$ (**5**) and $[\text{Fe}^{\text{II}}(\text{L}^{\text{tz}})_2(\text{NCSe})_2]$ (**6**) comprising a relatively rare *cis* coordination of the NCS^- were prepared. Structural characterisation of the related cobalt(II) and nickel(II) isothiocyanato compounds **7** and **8** revealed a similar coordination mode in the latter compounds as well (Table 13).

Table 13: Summary of complexes with L^{tz} and L^{td} .

	L:M	spin state	$T_{\text{fus}} / ^\circ\text{C}$	
$\text{Fe}(\text{NTf}_2)_2 \cdot 6\text{H}_2\text{O}$	-	-	148–151	
$[\text{Fe}^{\text{II}}(\text{L}^{\text{tz}})_2(\text{NCS})_2]$	(5)	2:1	HS	-
$[\text{Fe}^{\text{II}}(\text{L}^{\text{tz}})_2(\text{NCSe})_2]$	(6)	2:1	HS	-
$[\text{Co}^{\text{II}}(\text{L}^{\text{tz}})_2(\text{NCS})_2]$	(7)	2:1	HS	-
$[\text{Ni}^{\text{II}}(\text{L}^{\text{tz}})_2(\text{NCS})_2]$	(8)	2:1	-	-
$[\text{Co}^{\text{II}}(\text{L}^{\text{td}})_3](\text{ClO}_4)_2$	(4)	3:1	HS	>250
$[(\text{L}^{\text{tz}})_2\text{FFe}^{\text{III}}(\mu\text{-O})\text{Fe}^{\text{III}}\text{F}(\text{L}^{\text{tz}})_2](\text{BF}_4)_2$	(1)	4:2	HS	-
$[\text{Fe}^{\text{III}}(\text{L}^{\text{tz}})_2\text{F}_2](\text{BF}_4)$	(2)	2:1	HS	-
$[\text{Cu}^{\text{II}}(\text{L}^{\text{tz}})_2](\text{ClO}_4)_2$	(3)	2:1	-	>220
$[\text{Fe}^{\text{II}}(\text{L}^{\text{td}})_3]\text{Cl}_2$	(9)	3:1	LS	210 (dec.)
$[\text{Fe}^{\text{II}}(\text{L}^{\text{td}})_3](\text{ClO}_4)_2$	(10)	3:1	LS	>220
$[\text{Fe}^{\text{II}}(\text{L}^{\text{td}})_3](\text{BF}_4)_2$	(11)	3:1	LS	>220
$[\text{Fe}^{\text{II}}(\text{L}^{\text{td}})_3](\text{NTf}_2)_2$	(12)	3:1	LS	194
$[\text{Co}^{\text{II}}(\text{L}^{\text{td}})_3](\text{ClO}_4)_2$	(13)	3:1	HS	>220
$[\text{Ni}^{\text{II}}(\text{L}^{\text{td}})_3](\text{ClO}_4)_2$	(14)	3:1	-	>220
$[\text{Fe}^{\text{II}}(\text{L}^{\text{td}})_2(\text{NCS})_2]$	(15)	2:1	SCO	-

The preparation of 3:1-type complexes using L^{tz} is rather demanding as only the cobalt(II) perchlorate $[\text{Co}^{\text{II}}(\text{L}^{\text{tz}})_3](\text{ClO}_4)_2$ (**4**) featuring a HS state could be obtained. Attempts with $\text{Fe}(\text{BF}_4)_2 \cdot 6\text{H}_2\text{O}$ lead to fluoride abstraction and the formation of the dinuclear iron(III) compound $[(\text{L}^{\text{tz}})_2\text{FFe}^{\text{III}}(\mu\text{-O})\text{Fe}^{\text{III}}\text{F}(\text{L}^{\text{tz}})_2](\text{BF}_4)_2$ (**1**) comprising a chromophore that is similar to the one found in certain proteins. Modification of the

reaction set up lead to the formation of the mononuclear iron(III) HS complex $[\text{Fe}^{\text{III}}(\text{L}^{\text{tz}})_2\text{F}_2](\text{BF}_4)$ (**2**) featuring two F^- coligands. Using $\text{Fe}(\text{ClO}_4)_2 \cdot 6\text{H}_2\text{O}$ or $\text{Ni}(\text{ClO}_4)_2 \cdot 6\text{H}_2\text{O}$ did not lead to the formation of any identifiable compound, whereas with $\text{Cu}(\text{ClO}_4)_2 \cdot 6\text{H}_2\text{O}$ complex **3** was obtained featuring two equivalents of L^{tz} (Table 13).

For the preparation of 3:1-type complexes with cationic chromophores the methoxyacetyl substituted ligand L^1 , based on the thiazole L^{tz} , was prepared and the molecular structure of L^1 was investigated by X-ray diffraction analysis. Furthermore, syntheses for the ethyl substituted ligand L^2 and the methoxyethyl substituted ligand L^3 , both based on the imidazole **pi**, were developed. For the preparation of 2:1-type complexes with charge neutral chromophores the ligand L^4NTf_2 , based on the thiadiazole L^{td} , was developed (Figure 100). Besides, the molecular structure of the precursor L^{td} was determined for the first time.

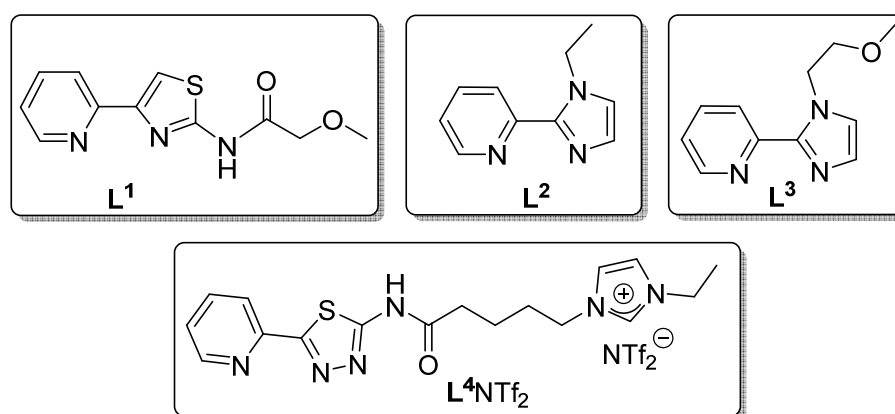


Figure 100: Summary of the ligands developed in this work.

In contrast to its precursor L^{tz} , the methoxyacetyl substituted thiazole ligand L^1 forms a 3:1-type complex using $\text{Fe}(\text{BF}_4)_2 \cdot 6\text{H}_2\text{O}$. No fluoride abstraction is observed. However, the HS complex $[\text{Fe}(\text{L}^1)_3](\text{BF}_4)_2 \cdot 2\text{H}_2\text{O}$ (**16**· $2\text{H}_2\text{O}$) is the only 3:1-type complex obtained with L^1 . Further attempts with iron(II), cobalt(II), or nickel(II) perchlorate resulted in the formation of 2:1-type complexes presumably possessing two molecules of water as coligands. In order to gain more insight into the ligand strength of L^1 the 2:1-type compound $[\text{Fe}(\text{L}^1)_2(\text{NCS})_2] \cdot 0.5\text{H}_2\text{O}$ (**21**· $0.5\text{H}_2\text{O}$) featuring and HS iron(II) was prepared. Hence, the ligand L^1 is too weak to form SCO-complexes. The tetrafluoroborate **16**· $2\text{H}_2\text{O}$ decomposes at 218 °C, whereas the 2:1-type copper perchlorate $[\text{Cu}(\text{L}^1)_2](\text{ClO}_4)_2 \cdot \text{MeOH}$ (**20**· MeOH) melts at 158–160 °C. This indicates that the attachment of methoxyacetyl moiety to ligands can lower the melting point of the resulting

complex, presumably by increasing the fusion entropy, as the related complex with L^{tz} $[Cu^{II}(L^{tz})_2](ClO_4)_2$ (**3**) does not melt up to 220 °C (Table 14).

Table 14: Summary of complexes with L^1 , L^2 , L^3 , L^4 , **mim** and **eim**.

		L:M	spin state	$T_{fus} / ^\circ C$	$T_G / ^\circ C$
$[Fe(L^1)_3](BF_4)_2 \cdot 2H_2O$	(16 ·2H ₂ O)	3:1	HS	218 (dec.)	-
$[Fe(L^1)_2(H_2O)_2](ClO_4)_2$	(17)	2:1	-	221–222	-
$[Co(L^1)_2(H_2O)_2](ClO_4)_2 \cdot H_2O$	(18 ·H ₂ O)	2:1	-	> 220	-
$[Ni(L^1)_2(H_2O)_2](ClO_4)_2$	(19)	2:1	-	> 220	-
$[Cu(L^1)_2](ClO_4)_2 \cdot MeOH$	(20 ·MeOH)	2:1	-	158–160	-
$[Fe(L^1)_2(NCS)_2] \cdot 0.5H_2O$	(21 ·0.5H ₂ O)	2:1	HS	> 220	-
$[Fe(L^2)_3](ClO_4)_2 \cdot H_2O$	(22 ·H ₂ O)	3:1	LS	218 (dec.)	-
$[Fe(L^3)_3](ClO_4)_2$	(27)	3:1	LS	187 (dec.)	-
$[Fe(L^2)_3](BF_4)_2 \cdot H_2O$	(23 ·H ₂ O)	3:1	LS	239	-
$[Fe(L^3)_3](BF_4)_2$	(28)	3:1	LS	175	73
$[Fe(L^2)_3](NTf_2)_2$	(24)	3:1	LS	153	-
$[Co(L^2)_3](ClO_4)_2 \cdot 1.5H_2O$	(25 ·1.5H ₂ O)	3:1	HS	> 235	-
$[Co(L^3)_3](ClO_4)_2$	(29)	3:1	HS	181	66
$[Ni(L^2)_3](ClO_4)_2 \cdot 0.5H_2O$	(26 ·0.5H ₂ O)	3:1	-	> 235	-
$[Ni(L^3)_3](ClO_4)_2$	(30)	3:1	-	189	72
$[Co(L^4)_2][Co(NCS)_4]$	(31)	2:1	HS	-	-
$[Co(L^4)_2(NCS)_2](NTf_2)_2$	(32)	2:1	HS	-	-
$[Fe(mim)_6](NTf_2)_2 \cdot 0.5H_2O \cdot 0.5EtOH$	(33 ·0.5EtOH·0.5H ₂ O)	6:1	HS	183 (dec.)	-
$[Fe(eim)_6](NTf_2)_2 \cdot 0.5H_2O \cdot 0.5EtOH$	(34 ·0.5EtOH·0.5H ₂ O)	6:1	HS	83	-

Synthesis of 3:1-type complexes is much more feasible using the ligands L^2 and L^3 as they form several (**22**·H₂O, **27**, **23**·H₂O, **28**, **24**) 3:1-type coordination compounds with iron(II). However, with $Fe(NTf_2)_2$ only $[Fe(L^2)_3](NTf_2)_2$ (**24**) featuring the ethyl substituted ligand L^2 was obtained. All prepared iron(II) complexes comprise a metal ion in the LS state at rt as their UV/Vis spectra show typical CT bands or as confirmed by Mössbauer spectroscopy in the case of the $[Fe(L^2)_3](NTf_2)_2$ (**24**). As the analogous cobalt(II) complexes $[Co(L^2)_3](ClO_4)_2 \cdot 1.5H_2O$ (**25**·1.5H₂O) and $[Co(L^3)_3](ClO_4)_2$ (**29**) feature the metal ion in the HS state it is very likely that the LS iron(II) compounds switch into a HS state at elevated temperatures. This is supported by the fact that the ligand strength of L^2 and L^3 is similar to the ligand strength of their precursor 2-(2-pyridyl)-imidazole (**pi**) as investigated by UV/Vis spectroscopy. Both of the iron(II) perchlorate compounds **22**·H₂O and **27** decompose at elevated temperatures, whereas both analogous iron(II) tetrafluoroborate complexes are stable before melting at 239 °C (**23**·H₂O) and 175 °C (**28**). The iron(II) triflimide $[Fe(L^2)_3](NTf_2)_2$ (**24**) exhibits the smallest fusion temperature of all herein presented complexes with L^2 or L^3 at 153°C. Thus, a formal exchange of the tetrafluoroborate anion for the triflimide anion results in a decrease of the fusion temperature in the amount of 86 K. When cooled down complex **24** converts into a glass before undergoing cold crystallisation when heated up another

time. Cobalt(II) and nickel(II) perchlorate complexes **25**·1.5H₂O and **26**·0.5H₂O with the ethyl substituted ligand **L**² neither melt nor decompose until 235 °C, whereas the analogous complexes with the methoxyethyl substituted ligand **L**³ melt at 181 °C (**29**) and 189 °C (**30**). Hence, all complexes with the methoxyethyl substituted ligand **L**³ exhibit lower melting points than the analogous complexes with the ethyl substituted ligand **L**².

Synthesis of 2:1-type complexes using the imidazolium ligand **L**⁴NTf₂ is rather demanding. With “Fe(NCS)₂” presumably occurs incomplete complexation as indicated by examination of the red complex solution by HPLC-chromatography and by examination of the red powder obtained from the complex solution by Mössbauer spectroscopy and SQUID measurements. Using “Co(NCS)₂” leads to the formation of the two HS compounds [Fe(**L**⁴)₂][Co(NCS)₄] (**31**) and [Co(**L**⁴)₂(NCS)₂](NTf₂)₂ (**32**) as confirmed by X-ray diffraction analysis of the obtained single crystals. Unfortunately no bulk material could be obtained of those compounds.

Attempts to prepare 6:1-type with Fe(NTf₂)₂·6H₂O complexes using the ligands 1-*n*-ethyltetrazole (**etz**) and 1-*n*-propyltetrazole (**ptz**) did not lead to the formation of any isolable compound. However, with *N*-methylimidazole (**mim**) and *N*-ethylimidazole (**eim**) such complexes could be obtained. The compounds [Fe(**mim**)₆](NTf₂)₂·0.5H₂O·0.5EtOH (**33**·0.5EtOH·0.5H₂O) and [Fe(**eim**)₆](NTf₂)₂·0.5H₂O·0.5EtOH (**34**·0.5EtOH·0.5H₂O) both exhibit the metal ion in the HS state as confirmed by UV/Vis spectroscopy. Complex **33**·0.5EtOH·0.5H₂O decomposes at elevated temperatures, whereas **34**·0.5EtOH·0.5H₂O melts reversibly at a remarkably low temperature of 83 °C as confirmed by DSC measurements.

In conclusion, complex synthesis of 3:1-type complexes with Fe(NTf₂)₂·6H₂O and ligands that are derivatives of 2-(2-pyriyl)-imidazole (**pi**) seems to be the most promising approach for the preparation of SCO ionic liquids or SCO glasses. By preparation of ligands with longer alkyl- or glycol substituents the melting point of the related complexes may even be more decreased. The **pi** moiety also seems to provide an appropriate ligand field splitting which allows related ion(II) complexes to be in the LS state at rt and crossover into the HS state at elevated temperatures. The latter issue could be investigated also with the herein prepared compounds by advanced analysis techniques as *e.g.* high temperature measurements of the magnetic susceptibility.

3 Experimental

3.1 General Remarks

All chemicals and reagents were purchased from commercial sources and used as received. All solvents used were laboratory reagent grade.

NMR spectra were recorded in collaboration with Dr. Harald Scherer and Fadime Bitgül on a Bruker AVANCE II 400 WB spectrometer with a 5 mm ATM BBFO probe head, the decoupler coil tuned to the frequency of ^1H (400.17 MHz, 90° pulse: 14 μs) and the detector coil tuned to the frequency of ^{13}C (100.62 MHz, 90° pulse: 10.2 μs) or on a Bruker Avance DPX 200 spectrometer with a 5 mm QNP probe head (^1H , ^{19}F , ^{31}P , ^{13}C), the decoupler coil tuned to the frequency of ^1H (200.13 MHz, 90° pulse: 15 μs). The detector coil was used for ^{19}F (188.29 MHz, 90° pulse: 13.7 μs) and ^{13}C (50.32 MHz, 90° pulse: 13 μs). ^1H and ^{13}C chemical shifts are given relative to TMS using the residual solvent peak as the reference signal, ^{19}F chemical shifts are given relative to CFCl_3 .

Melting points were determined using a melting point apparatus or in collaboration with Carola Sturm using a Setaram DSC 131 calorimeter calibrated with an indium sample.

Mass spectra were recorded in collaboration with Christoph Warth at the institute of organic chemistry at the University of Freiburg. ESI-MS spectra (spray voltage 4–5 kV) were recorded with a Thermo LCQ Advantage or a Thermo Exactive device injecting 2.5 $\mu\text{l min}^{-1}$ sample solutions into a flow of 100–200 $\mu\text{l min}^{-1}$ MeOH or MeCN and an ion transfer tube temperature of 250–300 °C. APCI-MS spectra (spray-current 5 μA , vaporizer temperature 300–400 °C) were recorded with a Thermo LCQ Advantage or a Thermo Exactive device injecting 2.5 $\mu\text{l min}^{-1}$ sample solutions into a flow of 200–400 $\mu\text{l min}^{-1}$ MeOH or MeCN and a ion transfer tube temperature of 150–180 °C. HR-MS spectra were recorded using a Thermo Exactive device with an Orbitrap analyser in the ESI or APCI mode. EI-MS spectra were recorded using a Thermo TSQ 700 device with an ionisation energy of 70 eV and a source temperature of 200 °C. CI-MS spectra were recorded with a Thermo TSQ 700 device using ammonia as reactive gas and an ionisation energy of 110 eV and a source temperature of 200 °C.

Elemental analysis was carried out in collaboration with Angelika Siegel at the institute of organic chemistry at the University of Freiburg, with Sabine Lude at the KIT Karlsruhe and with Günther Wünsche at the University of Leipzig. Analyses were carried out using a VarioMICRO or an Elementar Vario EL analyser.

IR spectra were recorded over the range 4000–400 cm^{-1} using a Nicolet Magna 760 FTIR spectrometer. Raman spectra were recorded using a Bruker Vertex 70 IR spectrometer equipped with a Bruker RAM II FT Raman unit and a Nd-YAG laser. UV/Vis spectra were recorded over the range 300–1000 nm using an AnalytikJena Specord S 300 VIS spectrometer or over the range of 200–900 nm using a Thermo Scientific Evolution 600 spectrometer.

Mössbauer spectra were recorded in collaboration with Dr. Serhiy Demeshko at the University of Göttingen using a ^{57}Co source in a Rh matrix and an alternating constant acceleration *Wissel* Mössbauer spectrometer operated in the transmission mode and equipped with a *Janis* closed-cycle helium cryostat. Isomer shifts are given relative to iron metal at ambient temperature. Simulation of the experimental data was performed with the *Mfit* program.^[103] The Mössbauer spectrum of **24** was measured in collaboration with Dr. Valeriu Mereacre at the KIT Karlsruhe.

Temperature-dependent magnetic susceptibilities were measured in collaboration with Dr. Serhiy Demeshko at the University of Göttingen with a Quantum Design MPMS XL-5 SQUID magnetometer in the range from 295 (or 300) to 2.0 K at a magnetic field of 0.5 T (or 0.1 T). Magnetic data were simulated using the *julX* program.^[104] The powdered sample was contained in a gel bucket and fixed in a non-magnetic straw. Each raw data file for the measured magnetic moment was corrected for the diamagnetic contribution of the sample holder. The molar susceptibility data were corrected for the diamagnetic contribution. Magnetic measurements also were carried out in collaboration with Frederik Schleife at the University of Leipzig using a Quantum Design MPMS 7AC SQUID Magnetometer and in collaboration with Dr. Yanhua at the KIT Karlsruhe using a Quantum Design MPMSXL SQUID susceptometer.

HPLC chromatography was carried out with a Merck Hitachi device featuring a L-6200A Intelligent Pump, a L-4250 UV-Vis Detector, a D-6000A Interface and a Phenomenex Kinetex 5u C18 100A (250 x 4.60 mm) column and applying flow rates of 0.3 and 0.5 ml min^{-1} and using 100 % MeCN as solvent.

Single crystal X-ray diffraction data were collected in collaboration with Dominic Kaase and Boumahdi Benkmil using a Bruker APEX-II CCD diffractometer with a microfocused sealed tube radiation source, using graphite-monochromated Mo- K_{α} radiation ($\lambda = 0.71073 \text{ \AA}$). The structures were solved in collaborations

with Dominic Kaase, Dr. Julia Klingele, Dr. Daniel Kratzert and Dr. Nils Trapp by direct methods with SHELXS-97^[105] or OLEX2^[106] and refined against F^2 using all data by full-matrix least-squares techniques with SHELXL-97.^[105] All non-hydrogen atoms were refined anisotropically, except for one boron atom in **2**·1.25MeOH and **2**·MeCN. All hydrogen atoms were placed at calculated positions using riding models, except from water solvent molecules in $[\text{Fe}(\text{H}_2\text{O})_6](\text{NTf}_2)_2 \cdot 2\text{H}_2\text{O}$, **10**·0.625MeOH·0.875H₂O, **11**·MeOH·H₂O, **13**·2H₂O and **14**·MeOH·H₂O. Those were located from the difference maps and refined with distance restraints of fixed at that positions. In **5** a disorder is modelled for the NCS-Coligand with an occupation factor of 0.80 for the major part. One ligand of the cobalt(II) perchlorate complex **3**·1.5MeOH·0.25H₂O is modelled with a disordered location with an occupation factor of 0.78 for the *fac* and 0.22 for the *mer* isomer. One ligand of the iron(II) tetrafluoroborate complex **11**·MeOH·H₂O is modelled with a disordered location with an occupation factor of 0.88 for the *mer* and 0.12 for the *fac* isomer. Geometrical restraints were used to make the minor parts “similar” to the major parts. A disorder (occupation factor: 0.56) was modelled for one of the side arms of the cobalt(II) isothiocyanate **31**.

Under the supervision of the author, Christian Göhringer worked during his diploma students internship^[107] on the synthesis of **L^{tz}**, ClC(O)CH₂OMe, **L¹**·HCl and **5**, Selina Leone worked during her bachelor thesis^[108] on the synthesis of **L^{tz}**, ClC(O)CH₂OMe, **L¹**·HCl, **L¹**, **3**, **4**, **6**, **7**, **8**, and **16–21**. Michel Skaisgirski worked during his master thesis^[109] under the supervision of the author on the synthesis of **pi**, **L²**, **L³** and **22–30**. Carla Gotzmann worked during her bachelor thesis^[110] partly under the supervision of the author and prepared compounds **11**, **13** and **14**. Max Schmucker was employed as a student assistant and reproduced under the supervision of the author the compounds Fe(NTf₂)₂·6H₂O, **pyNH**, **L^{td}**, **L⁴Br**, **3**, **4**, **6**, **10**, **11**, **9**, **12** and **15** according to experimental procedures established by the author.

3.2 Organic Ligand Synthesis

3.2.1 Synthesis of L^{tz}

2-(Bromoacetyl)-pyridine hydrobromide (pyBr): Bromine (8.6 g, 54 mmol) was added dropwise at 0 °C to a solution of freshly distilled 2-(Acetyl)pyridine (6.0 g, 50 mmol) and HOAc/HBr (32 %, 184 ml). The mixture was stirred over night at 40 °C before heating it at 75 °C for 1 h. The reaction mixture was allowed to cool down to rt before Et₂O (200 ml) was added. The resulting precipitate was filtered off and washed with Et₂O and acetone. Drying *in vacuo* gave a yellow amorphous powder. Yield: 65 %. IR (diamond, ATR): $\tilde{\nu}$ = 2774, 1725, 1604 (s), 1550, 1522 (s), 1455, 1363, 1301, 1281, 1267, 1226, 1200, 1157, 1096, 1039, 1016 (s), 774 (vs), 716, 636 (s), 619 (vs), 599, 534 cm⁻¹. APCI-MS: *m/z* (rel. abundance, fragment) = 200.0 (100 %, [py⁷⁹Br]⁺), 202.0 (94.9 %, [py⁸¹Br]⁺).

2-Amino-4-(2-pyridyl)-thiazole (L^{tz}): A solution of thiourea (7.38 g, 97 mmol) in water (60 ml) was added to a solution of pyBr (26.7 g, 95 mmol) in water (120 ml). The mixture was stirred for 1 h at rt. The pH was adjusted to 7 with 2M NaOH. The resulting precipitate was filtered off and washed with water. Drying over P₄O₁₀ gave a colourless amorphous powder. Yield: 95 %. ¹H-NMR (200.13 MHz, DMSO-d₆): δ = 8.53 (ddd, 1 H, 6-pyH), 7.81 (m, 2 H, 3-pyH, 4-pyH), 7.25 (s, 1 H, 5-tzH), 7.23 (m, 1 H, 5-pyH), 7.12 (s, 2 H, NH₂) ppm. ¹³C-NMR (50.33 MHz, DMSO-d₆): δ = 168.8 (2-tzC), 152.7 (2-pyC), 149.7 (6-pyC), 147–155 (4-tzC), 137.2 (4-pyC), 122.5 (5-pyC), 120.5 (3-pyC), 105.7 (5-tzC) ppm. IR (diamond, ATR): $\tilde{\nu}$ = 3272, 3107, 1539 (vs), 1472 (vs), 1457, 1420, 1344 (s), 1275, 1058 (s), 1037, 994, 843, 791, 753, 714 (s), 688, 666, 623, 511, 419 cm⁻¹. CI-MS(NH₃): *m/z* (rel. abundance, fragment) = 178.0 (100 %, [L^{tz}H]⁺). Elemental analysis (%) found: C 52.97, H 3.93, N 23.39, S 18.00; calcd. for C₈H_{7.4}N₃O_{0.2}S (180.82 g mol⁻¹) C 47.18, H 3.39, N 31.44, S 17.99.

3.2.2 Synthesis of L¹

Methoxyacetyl chloride: Thionyl chloride (26.2 g, 220 mmol) was added to methoxy acetic acid (18.6 g, 200 mmol). A drop of pyridine was added before stirring the mixture for 1 h at 80 °C. The excess thionyl chloride was removed by a weak flow of argon. Distillation (104 mbar, *T* = 54 °C) of the resulting mixture gave a colourless liquid. Yield: 51 %. ¹H-NMR (200.13 MHz, CDCl₃): δ (ppm) = 4.35 (s, 2 H, CH₂), 3.47 (s, 3 H, CH₃)

2-Methoxy-N-[4-(2-pyridyl)-2-thiazolyl]-acetamide hydrochloride (L¹·HCl): At 0 °C L^{tz} (1.8 g, 10 mmol) was added to a solution of ClC(O)CH₂OMe (1.2 g, 11 mmol) in abs. DCM (50 ml). The mixture was stirred over night at rt. Water (10 ml) was added to the reaction mixture. The resulting precipitate was filtered

off and washed with Et₂O. Drying *in vacuo* gave a beige coloured amorphous powder. Yield: 36 %. ¹H-NMR (200.13 MHz, DMSO-d₆): δ = 12.40 (bs, 1 H, NH), 8.73 (d, 1 H, 6-pyH), 8.40 (s, 1 H, 5-tzH), 8.32 (m, 2 H, 4-pyH, 5-pyH), 7.71 (dd, 1 H, 3-pyH), 4.22 (s, 2 H, CH₂), 3.37 (s, 3 H, CH₃) ppm. ¹³C-NMR (50.33 MHz, DMSO-d₆): δ = 172.2 (C=O), 158.8 (5-tzC), 155.3 (2-tzC), 151.5 (4-tzC), 148.3 (2-pyC), 148.1 (4-pyC), 148.0 (6-pyC), 127.7 (3-pyC), 125.1 (5-pyC), 69.7 (CH₂), 59.8 (CH₃) ppm. IR (diamond, ATR): $\tilde{\nu}$ = 3353, 2885, 1695, 1622, 1601, 1553 (vs), 1506, 1469, 1450, 1274 (s), 1184, 1123 (vs), 1104 (s), 1079, 969 (s), 928, 794, 752, 689, 661 (vs), 614 (s), 491 (s), 421 cm⁻¹. Single crystals, suitable for X-ray diffraction analysis, were obtained by recrystallization from MeOH.

2-Methoxy-N-[4-(2-pyridyl)-2-thiazolyl]-acetamide (L¹): A solution of Na₂CO₃ (0.4 g, 3.8 mmol) in water (5 ml) was added to a solution of L¹·HCl (1.1 g, 3.8 mmol) in water (75 ml). The mixture was stirred for 1.5 h at rt. The resulting precipitate was filtered off and washed with water. Drying over P₄O₁₀ at 20 mbar gave a beige coloured amorphous powder. Yield: 60 %. ¹H-NMR (200.13 MHz, DMSO-d₆): δ = 12.25 (bs, 1 H, NH), 8.60 (ddd, 1 H, 6-pyH), 7.94 (m, 1 H, 3-pyH), 7.88 (m, 1 H, 4-pyH), 7.85 (s, 1 H, 5-tzH), 7.33 (ddd, 1 H, 5-pyH), 4.18 (s, 2 H, CH₂), 3.37 (s, 3 H, CH₃) ppm. ¹³C-NMR (50.33 MHz, DMSO-d₆): δ = 169.1 (C=O), 158.1 (2-tzC), 152.4 (2-pyC), 149.6 (6-pyC), 149.4 (4-tzC), 137.4 (4-pyC), 123.4 (5-pyC), 120.3 (3-pyC), 112.3 (5-tzC), 70.8 (CH₂), 59.2 (CH₃) ppm. IR (diamond, ATR): $\tilde{\nu}$ = 1692 (s), 1554 (s), 1528 (s), 1445, 1419, 1340, 1280, 1192, 1107 (vs), 1063 (s), 990, 771, 749 (vs), 726, 699, 671, 620 (s), 603, 567, 466, 404 cm⁻¹. CI-MS *m/z* (rel. abundance, fragment) = 250.1 (100 %, [L¹·H]⁺). Elemental analysis (%) found: C 52.55, H 4.55, N 16.88, S 12.97; calcd. for C₁₁H₁₁N₃O₂S (249.29 g mol⁻¹): C 53.00, H 4.45, N 16.86, S 12.86.

3.2.3 Synthesis of L^{td}

The material presented in this chapter was included in the following manuscript: Timo Huxel and Julia Klingele, *Cobalt(II) Complexes of a New Imidazolium-Tagged Thiadiazole Ligand With Bis(trifluoromethylsulfonyl)imide or Tetraisoithiocyanato Cobaltate as Counterion*, submitted.

Pyridine-2-carboximidic acid methyl ester (pyNH): 2-Cyanopyridin (26.0 g, 0.25 mol) was added to a suspension of NaOMe (1.40 g, 0.03 mol) in abs. MeOH (225 ml). The mixture was stirred 20 h at rt before adding glacial acetic acid (1.5 ml) and stirring for another 5 min. The solvent was evaporated under reduced pressure and the residue was distilled. The fraction collected at T_{vap} = 113–117 °C and p = 37 mbar was **pyNH**. Yield: 76 %. ¹H-NMR (400.17 MHz, DMSO-d₆): δ = 9.18 (bs, 1 H, NH), 8.69 (ddd, 1 H, 6-pyH), 7.97 (ddd, 1 H, 4-pyH), 7.81 (ddd, 1 H, 3-pyH), 7.55 (ddd, 1 H, 5-pyH), 3.89 (s, 3 H, CH₃) ppm.

^{13}C -NMR (100.62 MHz, DMSO- d_6): δ = 165.6 (C=NH), 149.3 (6-pyC), 146.5 (2-pyC), 137.9 (4-pyC), 127.6 (3-pyC), 128.8 (5-pyC), 53.4 (CH_3) ppm.

2-Amino-5-(2-pyridyl)-1,3,4-thiadiazole (L^{td}): Thiosemicarbazide hydrochloride (21.7 g, 0.17 mol) was added to a solution of **pyNH** (20.4 g, 0.15 mol) in pyridine (120 ml) and the mixture was stirred for 5 h at 110 °C. The resulting suspension was filtrated and the solvent of the filtrate was removed under reduced pressure. The residue was digested in water (150 ml) and filtered off. The residue was washed with water and dried over P_4O_{10} at 20 mbar. A slightly yellow coloured powder was obtained. Yield: 43%. ^1H -NMR (400.17 MHz, DMSO- d_6): δ = 8.58 (d, 1 H, 6-pyH), 8.05 (d, 1H, 3-pyH), 7.90 (ddd, 1 H, 4-pyH), 7.49 (bs, 2 H, NH_2), 7.41 (ddd, 1 H, 5-pyH), ppm. ^{13}C -NMR (100.62 MHz, DMSO- d_6): δ = 170.3 (2-tdC), 159.6 (5-tdC), 149.3 (2-pyC, 6-pyC), 137.1 (4-pyC), 123.9 (5-pyC), 118.8 (3-pyC) ppm. EI-MS m/z (rel. abundance, fragment) = 178.0 (100 %, [L^{td}] $^+$). IR (diamond, ATR): $\tilde{\nu}$ = 3251, 3067 ($\nu_{\text{as}}(\text{NH}_2)$), 2950 ($\nu_{\text{s}}(\text{NH}_2)$), 2693, 1616, 1585, 1563, 1507, 1490 (vs), 1448, 1431 (s), 1335, 1304, 1275, 1248, 1127 (s), 1067, 1008, 895, 779 (s), 739, 713, 619, 603, 577, 507, 451, 404 cm^{-1} . UV/Vis (MeOH): λ_{max} (ϵ) = 202 (8756), 228 (4940), 304 (23436), 314 (25950) nm ($\text{M}^{-1} \text{cm}^{-1}$). Single crystals, suitable for X-ray diffraction analysis, were obtained by recrystallization from MeOH. Elemental analysis (%) found: C 47.46, H 3.46, N 31.72, S 17.78; calcd. for $\text{C}_7\text{H}_6\text{N}_4\text{S}$ (178.21 g mol^{-1}) C 47.18, H 3.39, N 31.44, S 17.99.

3.2.4 Synthesis of L^4NTf_2

The material presented in this chapter was included in the following manuscript: Timo Huxel and Julia Klingele, *Cobalt(III) Complexes of a New Imidazolium-Tagged Thiadiazole Ligand With Bis(trifluoromethylsulfonyl)imide or Tetrakisothiocyanato Cobaltate as Counterion*, submitted.

Pentanoic acid [5-(2-pyridyl)-2-[1,3,4]-thiadiazolyl]-amide-5-bromide (tdBr): At 0 °C ω -bromopentanoic acid chloride (1.32 g, 6.60 mmol) was added dropwise to a suspension of L^{td} (1.07 g, 6.00 mmol) in abs. DCM (60 ml). The resulting suspension was stirred for 24 h at rt. Water (120 ml) was added to the reaction mixture whereupon a precipitate formed. The mixture was filtrated and the residue was washed with water, MeOH and DCM. Drying over P_4O_{10} at 20 mbar gave a colourless powder of **tdBr**·0.5 H_2O . Yield: 76 %. ^1H -NMR (200.13 MHz, DMSO- d_6 , impurity: DCM 5.76 ppm): δ = 12.67 (bs, 1 H, NH), 8.67 (ddd, 1 H, 6-pyH), 8.20 (ddd, 1 H, 3-pyH), 7.99 (ddd, 1 H, 4-pyH), 7.52 (ddd, 1 H, 5-pyH), 3.56 (t, 2 H, $\text{C}(\text{O})\text{CH}_2\text{CH}_2\text{CH}_2\text{CH}_2\text{Br}$), 2.56 (t, 2 H, $\text{C}(\text{O})\text{CH}_2\text{CH}_2\text{CH}_2\text{CH}_2\text{Br}$), 1.85 (m, 2 H, $\text{C}(\text{O})\text{CH}_2\text{CH}_2\text{CH}_2\text{CH}_2\text{Br}$), 1.76 (m, 2 H, $\text{C}(\text{O})\text{CH}_2\text{CH}_2\text{CH}_2\text{CH}_2\text{Br}$) ppm. ^{13}C -NMR (50.32 MHz, DMSO- d_6): δ = 171.4 (C=O), 163.6 (5-tdC), 160.1 (2-tdC), 152.0 (2-pyC), 149.7 (6-pyC), 137.5 (4-pyC), 125.2 (5-pyC), 119.6 (3-pyC), 34.4 ($\text{C}(\text{O})\text{CH}_2\text{CH}_2\text{CH}_2\text{CH}_2\text{Br}$), 33.7 ($\text{C}(\text{O})\text{CH}_2\text{CH}_2\text{CH}_2\text{CH}_2\text{Br}$), 31.4 ($\text{C}(\text{O})\text{CH}_2\text{CH}_2\text{CH}_2\text{CH}_2\text{Br}$),

22.8 (C(O)CH₂CH₂CH₂CH₂Br) ppm. APCI-MS (MeOH): *m/z* (rel. abundance, fragment) = 261. 2 (100 %, [tdBr – Br]⁺), 341.0 (53 %, [td⁷⁹Br·Na]⁺), 343.0 (51 %, [td⁸¹Br·Na]⁺). Elemental analysis (%) found: C 41.37 H 3.61 N 15.99 S 9.00; calcd. for C₁₂H₁₄BrN₄O_{1.5}S (345.74 g mol⁻¹) C 41.15 H 4.03 N 16.00 S 9.15.

Pentanoic acid [5-(2-pyridyl)-2-[1,3,4]-thiadiazolyl]-amide-5-[3-ethyl-1-imidazolium] bromide (L⁴Br):

N-Ethylimidazole (28.4 g, 296 mmol) was added to a solution of tdBr (1.0 g, 2.9 mmol) in THF (300 ml). The mixture was stirred for 24 h at 90 °C. The resulting suspension was filtrated, the residue was washed with Et₂O and dried *in vacuo*. A colourless powder was obtained. Yield: 77 %. M.p. = 220–222 °C. ¹H-NMR (200.13 MHz, DMSO-d₆): δ = 12.67 (bs, 1 H, NH), 9.23 (dd, 1 H, 2-imH), 8.67 (ddd, 1 H, 6-pyH), 8.20 (ddd, 1 H, 3-pyH), 8.00 (ddd, 1 H, 4-pyH), 7.82 (m, 2 H, 4-imH, 5-imH), 7.53 (ddd, 1 H, 5-pyH), 4.20 (t, 2 H, C(O)CH₂CH₂CH₂CH₂N), 4.19 (q, 2 H, NCH₂CH₃), 2.57 (t, 2 H, C(O)CH₂CH₂CH₂CH₂N), 1.85 (m, 2 H, C(O)CH₂CH₂CH₂CH₂N), 1.62 (m, 2 H, C(O)CH₂CH₂CH₂CH₂N), 1.43 (t, 3 H, CH₃) ppm. ¹³C-NMR (50.32 MHz, DMSO-d₆): δ = 171.3 (C=O), 163.5 (5-tdC), 160.0 (2-tdC), 150.2 (2-pyC), 149.7 (6-pyC), 137.5 (4-pyC), 135.5 (2-imC), 125.2 (5-pyC), 122.0 (4-imC, 5-imC), 119.0 (3-pyC), 48.3 (C(O)CH₂CH₂CH₂CH₂N), 43.9 (NCH₂CH₃), 33.8 (C(O)CH₂CH₂CH₂CH₂N), 28.4 (C(O)CH₂CH₂CH₂CH₂N), 20.8 (C(O)CH₂CH₂CH₂CH₂N), 14.7 (CH₃) ppm. ESI-MS (MeOH): *m/z* (rel. abundance, fragment) = 357.1492 (100 %, (L⁴)⁺), 261.0805 (47 %, (L⁴)⁺ – eim), 179.1179 (34 %, [td·H]⁺); 80.9165 (100 %, ⁸¹Br⁻), 78.9185 (94 %, ⁷⁹Br⁻).

Pentanoic acid [5-(2-pyridyl)-2-[1,3,4]-thiadiazolyl]-amide-5-[3-ethyl-1-imidazolium]

bis(trifluoromethylsulfonyl)imide (L⁴NTf₂): A suspension of L⁴Br (0.98 g, 2.24 mmol) and LiNTf₂ (0.64 g, 2.24 mmol) in water (20 ml) was stirred 24 h at rt. The reaction mixture was filtrated and the residue was washed with water until testing the washing solution with AgNO₃ was negative. Drying over P₄O₁₀ at 20 mbar gave a colourless powder. Yield: 89 %. M.p. = 155–157 °C. ¹H-NMR (200.13 MHz, DMSO-d₆): δ = 12.67 (bs, 1 H, NH), 9.18 (dd, 1 H, 2-imH), 8.67 (ddd, 1 H, 6-pyH), 8.20 (ddd, 1 H, 3-pyH), 7.99 (ddd, 1 H, 4-pyH), 7.80 (m, 2 H, 4-imH, 5-imH), 7.52 (ddd, 1 H, 5-pyH), 4.19 (t, 2 H, C(O)CH₂CH₂CH₂CH₂N), q, 2 H, NCH₂CH₃), 2.57 (t, 2 H, C(O)CH₂CH₂CH₂CH₂N), 1.84 (m, 2 H, C(O)CH₂CH₂CH₂CH₂N), 1.63 (m, 2 H, C(O)CH₂CH₂CH₂CH₂N), 1.43 (t, 3 H, CH₃) ppm. ¹³C-NMR (50.32 MHz, DMSO-d₆): δ = 171.3 (C=O), 163.4 (5-tdC), 160.0 (2-tdC), 150.8 (2-pyC), 149.1 (6-pyC), 138.1 (4-pyC), 135.7 (2-imC), 125.5 (5-pyC), 122.3 (4-imC, 5-imC), 119.6 (3-pyC), 48.7 (C(O)CH₂CH₂CH₂CH₂N), 43.3 (NCH₂CH₃), 33.8 (C(O)CH₂CH₂CH₂CH₂N), 28.8 (C(O)CH₂CH₂CH₂CH₂N), 21.2 (C(O)CH₂CH₂CH₂CH₂N), 15.1 (CH₃) ppm. ¹⁹F-NMR (188.31 MHz, DMSO-d₆): –79 (s, CF₃) ppm. ESI-MS (MeOH): *m/z* (rel. abundance, fragment) = 357.1488 (100 %, (L⁴)⁺), 261.0803 (29 %, (L⁴)⁺ – eim), 179.1178 (18 %, [L⁴·H]⁺); 279.9180 (100 %, NTf₂⁻), 146.9608 (25 %, CF₃SO₂N⁻), 77.9652 (19 %, SO₂N⁻). Elemental analysis (%) found: C 35.73, H 3.29, N 15.27, calcd. for C₁₉H₂₁F₆N₇O₅S₃ (637.59 g mol⁻¹) C 35.79, H 3.32, N 15.38. IR (diamond, ATR): $\tilde{\nu}$ = 3156, 2864, 1687, 1561,

1437, 1343, 1329, 1227, 1175 (vs), 1131 (vs), 1052 (s), 1014, 978, 826, 788, 763, 739, 714, 651, 615, 596 (s), 569 (s), 531, 506 (s), 405 cm^{-1} . UV/Vis (MeCN): λ_{max} (ϵ) = 301 (17340) nm ($\text{M}^{-1} \text{cm}^{-1}$).

3.2.5 Synthesis of pi Based Ligands

2-(2-Pyridyl)-imidazole (pi): 2-Pyridinecarbonitrile (10.4 g, 100 mmol) was added to a solution of NaOMe (0.54 g, 10.0 mmol) in abs. MeOH (40 ml). The mixture was stirred for 1 h at 40 °C. The reaction mixture was allowed to cool down before 2,2-dimethoxyethylamine (10.5 g, 100 mmol) and glacial acetic acid (11 ml) were added dropwise. The mixture was stirred for 1 h under reflux. The reaction mixture was allowed to cool down before MeOH (50 ml) and 6M HCl (50 ml) were added. The mixture was stirred for 4 h under reflux. The solvent was removed from the reaction mixture under reduced pressure. The residue was digested in a solution of K_2CO_3 (50 g) in H_2O (50 ml). DCM (50 ml) was added to the resulting suspension. The mixture was filtrated and the organic phase was separated. The aqueous phase was extracted with DCM. The combined organic layers were dried over Na_2SO_4 and the solvent was evaporated under reduced pressure. The residue was recrystallized from EE (50 ml). A beige coloured, amorphous powder was obtained. Yield: 62 %. $^1\text{H-NMR}$ (200.13 MHz, DMSO-d_6): δ = 12.77 (bs, 1 H, 1-imH), 8.58 (d, 1 H, 6-pyH), 8.04 (d, 1 H, 3-pyH), 7.87 (ddd, 1 H, 4-pyH), 7.34 (ddd, 1 H, 5-pyH), 7.22 (s, 1 H, 5-imH or 4-imH), 7.08 (s, 1 H, 5-imH or 4-imH) ppm. $^{13}\text{C-NMR}$ (50.33 MHz, DMSO-d_6): δ = 149.2 (2-pyC), 148.9 (6-pyC), 145.5 (2-imC), 137.1 (4-pyC), 129.5 (4-imC or 5-imC), 123.0 (5-pyC), 119.4 (3-pyC), 118.7 (4-imC or 5-imC) ppm. EI-MS (MeOH) m/z (rel. abundance, fragment) = 145.0 (100 %, (pi) $^+$). IR (diamond, ATR): $\tilde{\nu}$ = 3046, 2983, 2887, 2821, 2743, 1594 (s), 1568, 1479 (vs), 1458 (vs), 1415, 1382, 1308, 1139, 1109 (s), 992, 954 (s), 909, 786 (vs), 758, 736 (vs), 706 (vs), 630 (s), 621, 504, 464, 403 cm^{-1} . Elemental analysis (%) found: C 65.89 H 4.97 N 29.09, calcd. for $\text{C}_8\text{H}_7\text{N}_3$ ($145.16 \text{ g mol}^{-1}$): C 66.19 H 4.86 N 28.95.

2-(2-Pyridyl)-1-ethyl-imidazole (L²): pi (2.61 g, 18.0 mmol) was added to a KOH solution (50 %, 10 ml). Ethyl iodide (2.81 g, 18.0 mmol) was added dropwise and the mixture was stirred under reflux for 6 h. The reaction mixture was extracted with DCM, the combined organic layers were washed with water and dried over Na_2SO_4 . The solvent was removed under reduced pressure. The residue was purified by column chromatography (length: 21 cm, diameter: 5 cm, DCM:MeOH = 9:1). A slightly yellow coloured liquid was obtained. Yield: 72 %. $^1\text{H-NMR}$ (200.13 MHz, DMSO-d_6): δ = 8.61 (ddd, 1 H, 6-pyH), 8.08 (ddd, 1 H, 3-pyH), 7.87 (ddd, 1 H, 4-pyH), 7.34 (ddd, 1 H, 5-pyH), 7.36 (d, 1 H, 5-imH), 7.03 (d, 1 H, 4-imH), 4.58 (q, 2 H, NCH_2CH_3), 1.33 (t, 3 H, CH_3) ppm. $^{13}\text{C-NMR}$ (50.33 MHz, DMSO-d_6): δ = 150.1 (2-pyC), 148.1 (6-pyC), 142.9 (2-imC), 136.6 (4-pyC), 127.8 (4-imC), 123.3 (5-imC), 122.2 (5-pyC), 121.9 (3-pyC), 42.2

(NCH₂CH₃), 16.5 (CH₃) ppm. IR (diamond, ATR): $\tilde{\nu}$ = 2979, 1588 (vs), 1565, 1487 (vs), 1463 (vs), 1438 (s), 1408, 1380, 1355, 1300, 1277, 1257, 1148, 1091 (s), 1051 (s), 1039, 992, 959, 918, 848, 790 (vs), 742 (vs), 708 (vs), 662, 623, 402 cm⁻¹. APCI-MS (MeOH) *m/z* (rel. abundance, fragment) *m/z* = 174.1024 (100 %, [L²·H]⁺). Elemental analysis (%) found: C 69.19 H 6.42 N 24.27, calcd. for C₁₀H₁₁N₃ (173.21 g mol⁻¹): C 69.34 H 6.40 N 24.26. UV/Vis (MeOH): λ_{max} (ϵ) = 290 (12810), 264 (8870), 210 (5360), 204 (4680) nm (M⁻¹ cm⁻¹).

2-(2-Pyridyl)-1-(2-methoxyethyl)-imidazole (L³): pi (2.02 g, 13.9 mmol) was added to a KOH solution (50%, 10 ml). 2-Chloromethyl ethyl ether (1.46 g, 15.4 mmol) was added dropwise and the mixture was stirred under reflux for 3.5 h. Water (10 ml) was added to the reaction mixture, the organic phase was separated and the aqueous phase was extracted with DCM. The combined organic phases were washed with water and dried over Na₂SO₄. The solvent was removed under reduced pressure and the residue was purified by column chromatography (length: 25 cm, diameter: 5 cm, DCM:MeOH = 9:1) A slightly yellow coloured liquid was obtained. Yield: 34 %. ¹H-NMR (200.13 MHz, DMSO-d₆): δ = 8.58 (ddd, 1 H, 6-pyH), 8.09 (ddd, 1 H, 3-pyH), 7.87 (ddd, 1 H, 4-pyH), 7.32 (d, 1 H, 5-imH), 7.34 (ddd, 1 H, 5-pyH), 7.03 (d, 1 H, 4-imH), 4.75 (t, 2 H, NCH₂CH₂OCH₃), 3.65 (t, 2 H, NCH₂CH₂OCH₃), 3.19 (s, 3 H, CH₃) ppm. ¹³C-NMR (50.33 MHz, DMSO-d₆): δ = 151.0 (2-pyC), 149.3 (6-pyC), 143.9 (2-imC), 137.8 (4-pyC), 128.5 (4-imC), 125.5 (5-imC), 123.3 (5-pyC), 122.9 (3-pyC), 72.1 (NCH₂CH₂OCH₃), 58.6 (CH₃), 47.6 (NCH₂CH₂OCH₃) ppm. IR (diamond, ATR): $\tilde{\nu}$ = 2892, 1588 (s), 1566, 1486 (s), 1459 (vs), 1407, 1298, 1277, 1211, 1117 (vs), 1038, 1012, 992, 969, 917, 833, 791 (vs), 743 (vs), 708 (vs), 667, 624, 404 cm⁻¹. APCI-MS (MeOH) *m/z* (rel. abundance, fragment) = 204.1132 (100 %, [L³·H]⁺). Elemental analysis (%) found: C 64.69 H 6.46 N 20.79, calcd. for C₁₁H₁₃N₃O (203.24 g mol⁻¹): C 65.01 H 6.45 N 20.67. UV/Vis (MeCN): λ_{max} (ϵ) = 294 (15850), 266 (12180) nm (M⁻¹ cm⁻¹).

3.3 Complexation Reactions

3.3.1 Complexes with L^{tz}

The material presented in this chapter was published in: T. Huxel, S. Leone, Y. Lan, S. Demeshko, J. Klingele *Eur. J. Inorg. Chem* **2014**, 3114–3124, ^[68] © 2014 WILEY-VCH Verlag GmbH & Co. KGaA, Weinheim.

[(L^{tz})₂FFe^{III}(μ -O)Fe^{III}F(L^{tz})₂](BF₄)₂ (1) a from MeOH: A solution of L^{tz} (142 mg, 800 μ mol) in MeOH (10 ml) was added to a solution of Fe(BF₄)₂·6H₂O (135 mg, 400 μ mol) in MeOH (5 ml). Slow evaporation of the solvent resulted in the formation of a red crystalline solid, which was identified by X-ray diffraction as

complex **1**·1.25MeOH. Filtration, washing with Et₂O and drying *in vacuo* gave bulk material of [(L^{tz})₂FFe^{III}(μ-O)Fe^{III}F(L^{tz})₂](BF₄)₂·2H₂O (**1**·2H₂O). Yield: 37 %. Elemental analysis (%) found: C 35.44, H 2.82, N 15.43; calcd. for C₃₂H₃₂B₂N₁₂O₃S₄F₁₀Fe₂ (1084.22 g mol⁻¹): C 35.45, H 2.97, N 15.50. ESI-MS (MeOH) *m/z* (rel. abundance, fragment) = 178.0436 (100 %, [L^{tz}·H]⁺), 460.0238 (87 %, [Fe(L^{tz})₂FOMe]⁺), 437.0027 (46 %, [Fe₂(L^{tz})₄F₂O]²⁺), 961.0096 (10 %, [[Fe₂(L^{tz})₄F₂O](BF₄)⁺). Single crystals of **1**·1.25MeOH, suitable for X-ray diffraction analysis, and bulk material of **1**·2H₂O were obtained in an analogous reaction but applying a 3:1 ligand to metal ion ratio.

b) from MeCN: Single crystals of **1**·MeCN suitable for X-ray diffraction methods were obtained as follows: A solution of L^{tz} (106 mg, 600 μmol) in MeCN (20 ml) was added to a solution of Fe(BF₄)₂·6H₂O (67.5 mg, 200 μmol) in MeCN (10 ml). Slow evaporation of the solvent resulted in the formation of a red crystalline solid. Solvent free bulk material of **1** was obtained as follows: A solution of L^{tz} (213 mg, 1.20 mmol) in MeCN (30 ml) was added to a solution of Fe(BF₄)₂·6H₂O (135 mg, 400 μmol) in MeCN (5 ml). Slow evaporation of TBME into the reaction mixture resulted in the formation of a red crystalline solid of **1**, which was isolated by filtration, washed with Et₂O and dried *in vacuo*. Yield: 30%. M.p. > 220 °C. Elemental analysis (%) found: C 36.77, H 2.99, N 16.24; calcd. for C₃₂H₂₈B₂N₁₂OS₄F₁₀Fe₂ (1048.19 g mol⁻¹): C 36.67, H 2.69, N 16.01. IR (diamond, ATR): $\tilde{\nu}$ = 3397 (b), 3261 (b), 3125 (b), 1604 (vs), 1566, 1517, 1468 (s), 1447, 1364, 1283, 1225, 1163, 1045 (vs), 1014 (vs), 928, 845, 788 (s), 755 (s), 725, 686, 664, 637, 593, 520, 443, 423, 411 cm⁻¹. ESI-MS (MeOH) *m/z* (rel. abundance, fragment) = 437.0021 (100 %, [Fe₂(L^{tz})₄F₂O]²⁺), 178.0433 (61 %, [L^{tz}·H]⁺), 961.0081 (2 %, [[Fe₂(L^{tz})₄F₂O](BF₄)⁺), 426.9991 (21 %, -HF), 338.4808 (87 %, -L^{tz}, -HF).

[Fe^{III}(L^{tz})₂F₂](BF₄) (2**):** A solution of L^{tz} (142 mg, 800 μmol) in MeOH (10 ml) was added to a solution of Fe(BF₄)₂·6H₂O (135 mg, 400 μmol) in MeOH (5 ml). Vapour diffusion of TBME into the dark red reaction solution resulted in the formation of a red crystalline solid, which was identified by X-ray diffraction as complex **2**·1.5MeOH. Filtration, washing with Et₂O and drying *in vacuo* gave bulk material of [Fe^{III}(L^{tz})₂F₂](BF₄)·1.5H₂O (**2**·1.5H₂O). Yield: 63 %. M.p. > 220 °C. Elemental analysis (%) found: C 34.60, H 3.11, N 14.94, S 11.70; calcd. for C₁₆H₁₇BN₆O_{1.5}F₆S₂Fe (544.10 g mol⁻¹): C 34.19, H 3.05, N 14.95, S 11.41. IR (diamond ATR): $\tilde{\nu}$ = 3594, 3423 (b), 3274 (b), 3132, 1608 (vs), 1567, 1514, 1470 (s), 1449, 1372, 1285, 1228, 1036 (vs), 1017 (vs), 930, 838, 791, 758 (s), 731, 688, 665, 644, 586, 502 (vs), 467, 425, 412 cm⁻¹. ESI-MS (MeOH) *m/z* (rel. abundance, fragment) = 448.0032 (100 %, [Fe(L^{tz})₂F₂]⁺), 178.0433 (35 %, [L^{tz}·H]⁺), 460.0232 (22 %, [Fe(L^{tz})₂FCH₃O]⁺).

[Co^{II}(L^{tz})₃](ClO₄)₂ (3): A solution of Co(ClO₄)₂·6H₂O (73.2 mg, 200 μmol) in MeOH (5 ml) was added to a solution of L^{tz} (106 mg, 600 μmol) in MeOH (10 ml). Slow evaporation of the solvent resulted in the formation of orange coloured crystalline solid, which was identified by for X-ray diffraction as complex **3**·1.5MeOH·0.25H₂O. Filtration and drying *in vacuo* gave bulk material of [Co^{II}(H₂L₃)](ClO₄)₂·H₂O (**3**·H₂O). Yield: 50%. M.p. > 220 °C. Elemental analysis (%) found: C 35.29, H 2.47, N 15.41, S 11.61; calcd. for C₂₄H₂₃N₉O₉S₃Cl₂Co (807.52 g mol⁻¹): C 35.70, H 2.87, N 15.61, S 11.91. IR (diamond ATR): $\tilde{\nu}$ = 3443, 3331, 3116, 1605 (s), 1517, 1468, 1445, 1351, 1284, 1074 (vs), 1018, 919, 846, 789, 753 (s), 713, 686, 666, 644, 620 (vs), 481, 466, 451, 429 cm⁻¹.

[Cu^{II}(L^{tz})₂](ClO₄)₂ (4): A solution of Cu(ClO₄)₂·6H₂O (74.1 mg, 200 μmol) in MeOH (5 ml) was added to a solution of L^{tz} (70.9 mg, 400 μmol) in MeOH (10 ml). The reaction mixture was allowed to stand at rt. After 1 d a dark green crystalline solid of [Cu^{II}(L^{tz})₂](ClO₄)₂ (**4**) had formed, which was collected by filtration, washed with MeOH and dried *in vacuo*. Yield: 60 %. M.p. > 220 °C. Elemental analysis (%) found: C 31.23, H 2.18, N 13.75, S 10.00; calcd. for C₁₆H₁₄N₆O₈S₂Cl₂Cu (616.89 g mol⁻¹): C 31.15, H 2.29, N 13.62, S 10.39. IR (diamond ATR): $\tilde{\nu}$ = 3344, 2160 (s), 2134, 1623 (s), 1604 (s), 1526 (s), 1467, 1047 (vs), 1019 (s), 795, 761, 716, 621 (vs), 480 (s), 420 (s) cm⁻¹. ESI-MS (MeOH): *m/z* (rel. abundance, fragment) = 208.5006 (100 %, [Cu(L^{tz})₂]²⁺), 178.0437 (88 %, [L^{tz}-H]⁺), 271.9919 (55% [Cu(L^{tz})·MeOH]⁺), 415.9939 (37 %, [Cu(L^{tz})(L^{tz}-H⁺)]⁺), 515.9501 (5 %, [[Cu(L^{tz})₂ClO₄]⁺). Crystals obtained by this procedure unfortunately were not of sufficient quality for single crystal X-ray diffraction analysis.

[Fe^{II}(L^{tz})₂(NCS)₂] (5): Under a protective atmosphere of argon, KSCN (38.9 mg, 400 μmol) and a pinch of ascorbic acid were added to a solution of FeSO₄·7H₂O (74.8 mg, 200 μmol) in MeOH (15 ml). After stirring at rt for 5 min, the reaction mixture was filtered. A solution of L^{tz} (70.9 mg, 400 μmol) in MeOH (20 ml) was added under stirring to the clear solution of "Fe(NCS)₂" thus obtained. A brown precipitate formed. The mixture was filtered and the solid residue of [Fe^{II}(L^{tz})₂(NCS)₂] (**5**) was washed with MeOH and dried *in vacuo*. Yield: 76 %. M.p. > 220 °C. Elemental analysis (%) found: C 40.46, H 2.46, N 21.08, S 24.48; calcd. for C₁₈H₁₄N₈S₄Fe (526.45 g mol⁻¹): C 41.07, H 2.68, N 21.28, S 24.36. IR (diamond ATR): $\tilde{\nu}$ = 3270 (b), 3177, 3101, 2026 (vs), 1600 (vs), 1564, 1517 (vs), 1465 (s), 1443 (s), 1356 (s), 1317, 1282, 1257, 1222, 1155, 1103, 1064, 1047, 1012, 923, 885, 841, 788, 749 (vs), 720, 685, 665, 637, 607, 589, 487, 465, 411 cm⁻¹. Single crystals of **5**, suitable for X-ray diffraction analysis, were obtained by this method, but allowing the mixture to stand for 10 d without stirring.

[Fe^{II}(L^{tz})₂(NCSe)₂] (6): Under a protective atmosphere of argon, a solution of FeSO₄·7H₂O (74.8 mg, 200 μmol), KNCS_e (57.6 mg, 400 μmol) and a pinch of ascorbic acid in MeOH (5 ml) was stirred for 5 min at rt

The solvent was removed under reduced pressure and the residue was digested in MeCN (5 ml). The resulting suspension was filtered to obtain a clear MeCN solution of "Fe(NCSe)₂". A solution of L^{tz} (70.9 mg, 400 μmol) in MeCN (10 ml) was added under stirring whereupon a brown precipitate of [Fe^{II}(L^{tz})₂(NCSe)₂] (**6**) formed, which was collected by filtration, washed with Et₂O and dried *in vacuo*. Yield: 45 %. M.p. > 220 °C. Elemental analysis (%) found: C 34.89, H 2.15, N 18.27, S 10.30; calcd. for C₁₈H₁₄N₈S₂Se₂Fe (620.25 g mol⁻¹). IR (diamond ATR): $\tilde{\nu}$ = 3270 (b), 3069 (b), 2038 (vs), 1598 (s), 1513 (vs), 1453, 1351 (s), 1312, 1216, 1149, 1102, 1045, 921, 840, 787, 744, 714 (s), 672, 588, 457, 410 cm⁻¹. Mössbauer at 8 K: *I.S.* 1.15 mms⁻¹, *Q.S.* 1.84 mms⁻¹. Single crystals of **6**, suitable for X-ray diffraction analysis, were obtained by this method, but from MeOH solution and allowing the mother liquor to stand 8 d without stirring.

[Co^{II}(L^{tz})₂(NCS)₂] (**7**): A mixture of CoSO₄·7H₂O (112 mg, 400 μmol) and KSCN (78.0 mg, 800 μmol) in MeOH (15 ml) was stirred for 5 min at rt. The reaction mixture was filtered to obtain a clear solution of "Co(NCS)₂" in MeOH. A solution of L^{tz} (142 mg, 800 μmol) in MeOH (20 ml) was added. The mixture was allowed to stand at rt without stirring. After 10 d a yellow crystalline solid of [Co^{II}(L^{tz})₂(NCS)₂] (**7**) where collected by filtration, washed with MeOH and dried *in vacuo*. Yield: 43 %. M.p. > 220 °C. Elemental analysis (%) found: C 40.60, H 3.00, N 20.87; calcd. for C₁₈H₁₄N₈S₄Co (529.54 g mol⁻¹): C 40.83, H 2.66, N 21.16. IR (diamond ATR): $\tilde{\nu}$ = 3272 (b), 3074, 2023 (bs), 1604 (s), 1558, 1524 (vs), 1465 (s), 1442 (s), 1356 (s), 1287, 1257, 1221, 1104 (s), 1065, 1045 (vs), 1014, 923, 885, 838, 788, 748 (s), 722, 683, 665, 618, 589, 489, 463, 415, 402 cm⁻¹. Single crystals of **7**, suitable for X-ray diffraction analysis, were obtained by this method.

[Ni^{II}(L^{tz})₂(NCS)₂] (**8**): A mixture of NiSO₄·6H₂O (71.2 mg, 200 μmol) and KSCN (38.9 mg, 400 μmol) in MeOH (15 ml) was stirred for 5 min at rt. The reaction mixture was filtrated to obtain a clear MeOH solution of "Ni(NCS)₂". A solution of L^{tz} (38.9 mg, 400 μmol) in MeOH (20 ml) was added. The mixture was allowed to stand at rt without stirring. After 12 d a blue crystalline solid of [Ni^{II}(L^{tz})₂(NCS)₂] (**8**) was collected by filtration, washed with MeOH and dried *in vacuo*. Yield: 35%. M.p. > 220 °C. Elemental analysis (%) found: C 40.50, H 2.27, N 20.98, S 23.78; calcd. for C₁₈H₁₄N₈S₄Ni (529.29 g mol⁻¹): C 40.85, H 2.67, N 21.17, S 24.23. IR (diamond ATR): $\tilde{\nu}$ = 3265 (b), 3074, 2037 (bs), 1602 (s), 1562, 1522 (vs), 1465, 1442 (s), 1358 (vs), 1317, 1282, 1257, 1221, 1153, 1105, 1067, 1047, 1014, 881, 837, 786, 748 (vs), 718 (s), 684, 664, 639, 589, 489, 466, 442, 414 cm⁻¹. Single crystals of **8**, suitable for X-ray diffraction analysis, were obtained by this method.

3.3.2 Complexes with L¹

[Fe(L¹)₃](BF₄)₂ (16): A solution of L¹ (150 mg, 600 μmol) in MeCN (10 ml) was added to a solution of Fe(BF₄)₂·6H₂O (67.5 mg, 200 μmol) in MeCN (5 ml) and stirred for 30 min at rt. The solvent was removed under reduced pressure and the residue was dissolved in acetone (25 ml). Upon adding pentane (15 ml) a yellow precipitate formed. The reaction mixture was filtrated and the residue was washed with acetone. Drying *in vacuo* gave **16**·2H₂O as a yellow coloured amorphous powder. Yield: 67 %. M.p. = 218–220 °C (dec.) Elemental analysis (%) found: C 39.05, H 3.68, N 12.30; calcd. for C₃₃H₃₇F₈B₂N₉O₈S₃Fe (1013.35 g mol⁻¹) C 39.11, H 3.68, N 12.44. IR (diamond, ATR): $\tilde{\nu}$ = 3114, 1697 (s), 1603, 1525 (vs), 1445, 1345, 1290 (s), 1193, 1160, 1114 (s), 1054 (vs), 991, 922, 767 (s), 673, 641, 521, 479, 410 cm⁻¹.

[Fe(L¹)₂(H₂O)₂](ClO₄)₂ (17): A solution of L¹ (74.8 mg, 300 μmol) in MeOH (10 ml) was added to a solution of Fe(BF₄)₂·6H₂O (36.3 mg, 100 μmol) in MeOH (5 ml) and stirred for 30 min at rt. After 1 d at –10 °C a yellow precipitate had formed. The mixture was filtrated and the residue was washed with cold MeOH. Drying *in vacuo* gave **17** as a yellow coloured amorphous powder. Yield: 13 %. M.p. = 221–222 °C Elemental analysis (%) found: C 33.60 H 3.34 N 10.32 S 7.70; calcd. for C₂₂H₂₆N₆O₁₄S₂Cl₂Fe (798.35 g mol⁻¹): C 33.48 H 3.32 N 10.65 S 8.12. ESI-MS (MeOH) *m/z* (rel. abundance, fragment) = 553.0406 (100 %, [**17**(–HClO₄ –ClO₄)⁺]). IR (diamond, ATR): $\tilde{\nu}$ = 1602, 1527 (s), 1096 (vs), 1049 (vs), 1016, 766, 751, 669, 622, 418, 409, 403 cm⁻¹.

[Co(L¹)₂(H₂O)₂](ClO₄)₂·(18): A solution of L¹ (112 mg, 450 μmol) in MeOH (10 ml) was added to a solution of Fe(BF₄)₂·6H₂O (54.9 mg, 150 μmol) in MeOH (5 ml) and stirred for 30 min at rt. After 15 min at 0 °C a pink coloured precipitate had formed. The mixture was filtrated and the residue was washed with cold MeOH. Drying *in vacuo* gave **18**·H₂O as a pink coloured amorphous powder. Yield: 9 %. M.p. > 220 °C Elemental analysis (%) found: C 32.94 H 3.30 N 10.18 S 7.51 calcd. for C₂₂H₂₈N₆O₁₅S₂Cl₂Co (810.45 g mol⁻¹): C 32.60 H 3.48 N 10.37 S 7.91. ESI-MS (MeOH) *m/z* (rel. abundance, fragment) = 556.0389 (100 %, [**18**(–HClO₄ –ClO₄)⁺]). IR (diamond, ATR): = 1711, 1607, 1531 (s), 1468, 1446, 1428, 1344, 1299, 1258, 1195, 1097, 1077 (vs), 1052 (vs), 1022, 924, 848, 765, 730, 676, 644, 621 (s), 576, 465, 444, 437, 420, 414, 408 cm⁻¹.

[Ni(L¹)₂(H₂O)₂](ClO₄)₂ (19): A solution of L¹ (112 mg, 450 μmol) in MeOH (10 ml) was added to a solution of Fe(BF₄)₂·6H₂O (54.9 mg, 150 μmol) in MeOH (5 ml) and stirred for 30 min at rt. After 8 d at –20 °C blue coloured crystals had formed. The mixture was filtrated and the residue was washed with cold MeOH. Drying *in vacuo* gave **19** as a blue coloured microcrystalline powder. Yield: 27 %. M.p. > 220 °C Elemental

analysis (%) found: C 33.45 H 3.34 N 10.53 S 7.69 calcd. for $C_{22}H_{26}N_6O_{14}S_2Cl_2Ni$ ($792.20 \text{ g mol}^{-1}$) C 33.36 H 3.31 N 10.61 S 8.09. ESI-MS (MeOH) m/z (rel. abundance, fragment) = 555.0409 (100 %, $[19(-HClO_4-CIO_4)]^+$). IR (diamond, ATR): = 3238, 1706, 1607, 1532 (vs), 1467, 1448 (vs), 1424, 1346, 1295, 1259, 1222, 1201, 1162, 1054, 1021, 972, 925, 850, 764 (s), 731 (s), 676, 646, 620 (vs), 579, 502, 466, 428, 420, 402 cm^{-1} .

[Cu(L¹)₂](ClO₄)₂ (20): A solution of **L¹** (112 mg, 450 μmol) in MeOH (10 ml) was added to a solution of $Fe(BF_4)_2 \cdot 6H_2O$ (54.9 mg, 150 μmol) in MeOH (5 ml) and stirred for 30 min at rt. After 15 min at 0 °C a green coloured precipitate had formed. The mixture was filtrated and the residue was washed with cold MeOH. Drying *in vacuo* gave **20**·MeOH as a green microcrystalline powder. Yield: 24 %. M.p. = 158–160 °C Elemental analysis (%) found: C 35.08 H 2.91 N 10.53 S 7.95 calcd. for $C_{23}H_{26}N_6O_{13}S_2Cl_2Cu$ ($793.06 \text{ g mol}^{-1}$): C 34.83 H 3.30 N 10.60 S 8.09. ESI-MS (MeOH) m/z (rel. abundance, fragment) = 560.0350 (100 %, $[20(-HClO_4 - ClO_4)]^+$). IR (diamond, ATR): = 3225, 3124, 1676, 1645, 1581, 1534, 1498 (s), 1465, 1224, 1197, 1076 (vs), 962, 925, 845, 796, 766 (s), 711, 669, 621 (vs) 552, 456, 409 cm^{-1} .

[Fe(L¹)₂](NCS)₂ (21): $FeSO_4 \cdot 7H_2O$ (55.6 mg, 200 μmol), KSCN (38.9 mg, 400 μmol) and a pinch of ascorbic acid were suspended in MeOH (10 ml) and stirred for 10 min at rt. The solvent was removed under reduced pressure and the residue was suspended in MeCN (10 ml). Filtration gave a clear solution of “ $Fe(NCS)_2$ ”. A solution of **L¹** (99.7 mg, 400 μmol) in MeCN (10 ml) was added whereupon a yellow solution and a precipitate formed. The mixture was stirred for 10 min at rt and filtered off. The residue was washed with MeCN. Drying *in vacuo* gave **21**·0.5H₂O a yellow coloured amorphous powder. Yield: 54 %. M.p. > 220 °C. Elemental analysis (%) found: C 42.03, H 3.00, N 16.37, S 18.85; calcd. for $C_{24}H_{23}N_8O_{4.5}S_4$ ($679.59 \text{ g mol}^{-1}$) C 42.42, H 3.41, N 16.49, S 18.87. IR (diamond, ATR): $\tilde{\nu}$ = 3300, 2031 (vs), 1708 (s), 1601, 1548 (s), 1530 (vs), 1463, 1440, 1341, 1289 (s), 1195, 1108 (s), 1052, 975, 920, 849, 753 (s), 720, 672 (s), 639, 574, 549, 486, 410 cm^{-1} .

3.3.3 Complexes with L^{td}

[Fe(H₂O)₆](NTf₂)₂: To a suspension of iron powder (559 mg, 10.0 mmol) in degassed water (8.5 ml) was slowly added an aqueous solution of bis(trifluoromethylsulfonyl)imide (80 %, 21.0 mmol). The mixture was stirred at rt for 2 h, before it was filtered. The solvent was removed under reduced pressure. Drying the residue at 80 °C *in vacuo* gave a colourless powder of $Fe(NTf_2)_2 \cdot 6H_2O$. Yield: 75%. M.p. = 115–116 °C. Elemental analysis (%) found: C 7.00, H 1.43, N 3.85; calcd. for $C_4H_{12}N_2O_{14}F_{12}S_4Fe$ ($724.21 \text{ g mol}^{-1}$): C 6.63, H 1.67, N 3.87. ESI-MS (MeCN): m/z (intensity, fragment) = 280.1 (100 % $[(CF_3SO_2)_2N^-]$). Raman: $\tilde{\nu}$ = 3235, 2933, 2847, 2759, 1367, 1240, 1148, 1105, 752 (vs), 659, 559, 425, 332, 290, 243, 193, 127,

99 cm^{-1} . IR (diamond, ATR): $\tilde{\nu}$ = 3530 (b), 1631, 1341 (s), 1322, 1240 (vs), 1194 (vs), 1134 (vs), 1041 (vs), 800, 747, 607 (vs), 571 (vs), 508 (vs) cm^{-1} . Single crystals of $[\text{Fe}(\text{H}_2\text{O})_6](\text{NTf}_2)_2 \cdot 2\text{H}_2\text{O}$, suitable for X-ray diffraction analysis, were obtained in an attempted complexation reaction with 1-ethyltetrazole in DCM at -40°C .

$[\text{Fe}^{\text{II}}(\text{L}^{\text{td}})_3](\text{ClO}_4)_2$ (10): A solution of L^{td} (107 mg, 600 μmol) in MeOH (20 ml) was added to a solution of $\text{Fe}(\text{ClO}_4)_2 \cdot 6\text{H}_2\text{O}$ (72.6 mg, 200 μmol) in MeOH (10 ml). Slow evaporation of the solvent resulted in the formation of a red crystalline solid of $10 \cdot 0.625\text{MeOH} \cdot 0.875\text{H}_2\text{O}$, which was identified by X-ray diffraction analysis. Filtration, washing with TBME and drying *in vacuo* gave bulk material of $10 \cdot 2\text{H}_2\text{O}$. Yield: 80 %. M.p. > 220 $^\circ\text{C}$. Elemental analysis (%) found: C 30.74, H 2.80, N 20.21, calcd. for $\text{C}_{21}\text{H}_{22}\text{N}_{12}\text{O}_{10}\text{S}_3\text{Cl}_2\text{Fe}$ (825.41 g mol^{-1}): C 30.56, H 2.69, N 20.36. ESI-MS (MeCN): m/z (intensity, fragment) = 510.8 (100 %, $[\text{Fe}(\text{L}^{\text{td}})_2\text{ClO}_4]^+$), 179.2 (89 %, $[\text{L}^{\text{td}} \cdot \text{H}]^+$), 295.1 (37 %, $[\text{Fe}(\text{L}^{\text{td}})_3]^{2+}$). IR (diamond, ATR): $\tilde{\nu}$ = 3522, 3323 (b), 3180, 2961, 1603 (s), 1499, (s) 1473 (s), 1417, 1157, 1054 (vs), 930, 853, 791, 771 (s), 745, 719, 678, 620 (s) cm^{-1} . UV/Vis (MeOH): λ_{max} (ϵ) = 210 (8700), 234 (9200), 312 (39200), 324 (32200), 508 (520) nm ($\text{M}^{-1} \text{cm}^{-1}$).

$[\text{Fe}^{\text{II}}(\text{L}^{\text{td}})_3](\text{BF}_4)_2$ (11): A solution of L^{td} (26.7 mg, 150 μmol) in MeOH (5 ml) was added to a solution of $\text{Fe}(\text{BF}_4)_2 \cdot 6\text{H}_2\text{O}$ (17 mg, 50 μmol) in MeOH (5ml). Slow evaporation of the solvent resulted in the formation of a red crystalline solid of $11 \cdot \text{MeOH} \cdot \text{H}_2\text{O}$, which was identified by X-ray diffraction analysis. Filtration, washing with Et_2O and drying *in vacuo* gave bulk material of $11 \cdot 2\text{H}_2\text{O}$. Yield: 52%. M.p. > 220 $^\circ\text{C}$. Elemental analysis (%) found: C 31.59, H 2.88, N 20.80, calcd. for $\text{C}_{21}\text{H}_{22}\text{B}_2\text{N}_{12}\text{F}_8\text{O}_2\text{S}_3\text{Fe}$ (800.12 g mol^{-1}): C 31.52, H 2.77, N 21.01. IR (diamond, ATR): $\tilde{\nu}$ = 3588, 3353, 1604 (s), 1502 (vs), 1474 (vs), 1419, 1340, 1253, 1158, 999 (vs), 854, 773 (s), 745, 719, 678, 519 cm^{-1} . UV/Vis (MeOH): λ_{max} (ϵ) = 208 (8600), 238 (9000), 314 (38600), 502 (1580) nm ($\text{M}^{-1} \text{cm}^{-1}$).

$[\text{Fe}^{\text{II}}(\text{L}^{\text{td}})_3]\text{Cl}_2$ (9): A solution of L^{td} (267 mg, 1.50 mmol) in MeCN (10 ml) was added to a filtrated solution of $\text{FeCl}_2 \cdot 4\text{H}_2\text{O}$ (99.4 mg, 500 μmol) in MeCN (15 ml). A red amorphous solid of **9** formed, which was collected by filtration and dried *in vacuo*. Yield: 52 %. M.p. = 210 $^\circ\text{C}$ (dec.). Elemental analysis (%) found: C 38.33, H 2.74, N 25.23, S 14.36, calcd. for $\text{C}_{21}\text{H}_{18}\text{N}_{12}\text{S}_3\text{Cl}_2\text{Fe}$ (661.39 g mol^{-1}) C 38.14, H 2.74, N 25.41, S 14.54. ESI-MS (MeCN): m/z (intensity, fragment) = 295.0137 (100 %, $[\text{Fe}(\text{L}^{\text{td}})_3]^{2+}$), 446.9658 (87 %, $[\text{Fe}(\text{L}^{\text{td}})_2\text{Cl}]^+$). IR (diamond, ATR): $\tilde{\nu}$ = 3247, 3068, 1601 (s), 1492 (vs), 1473 (vs), 1449, 1432 (s), 1337, 1275, 1152, 1128, 1067, 1030, 1008, 856, 779 (s), 741, 714, 620, 601, 577, 509, 451 (s), 403 cm^{-1} . UV/Vis (MeOH): λ_{max} (ϵ) = 210 (4740), 228 (3840), 314 (12220), 506 (4244) nm ($\text{M}^{-1} \text{cm}^{-1}$).

[Fe^{II}(L^{td})₃](NTf₂)₂ (12): A solution of L^{td} (80.2 mg, 450 μmol) in EtOH (15 ml) was added to a solution of Fe(NTf₂)₂·6H₂O (109 mg, 150 μmol) in EtOH (3 ml). The resulting red solution was stirred for 1.5 h before the solvent was evaporated under reduced pressure. Washing the remaining red solid with Et₂O and drying *in vacuo* gave bulk material of **12**·H₂O. Yield: 47%. M.p. = 195–201 °C. Elemental analysis (%) found: C 25.36 H 1.33 N 16.44, calcd. for C₂₅H₂₀N₁₄S₃F₁₂S₄O₉Fe (1168.77 g mol⁻¹) C 25.69, H 1.72, N 16.78. ESI-MS (MeCN): *m/z* (intensity, fragment) = 691.9148 (100 % [Fe(L^{td})₂NTf₂]⁺). IR (diamond, ATR): $\tilde{\nu}$ = 3330, 3204, 1604, 1505 (s), 1474, 1421, 1342 (s), 1176 (vs), 1128 (vs), 1050 (vs), 858, 770, 740, 721, 651, 598, 569 (s), 507 (s), 466 cm⁻¹. Mössbauer at 80 K: *I.S.* 0.37 mm s⁻¹, *Q.S.* 0.35 mm s⁻¹. UV/Vis (MeOH): λ_{max} (ϵ) = 208 (28600), 238 (19500) 314 (57800), 324 (48100), 504 (960) nm (M⁻¹ cm⁻¹).

[Co^{II}(L^{td})₃](ClO₄)₂ (13): A solution of L^{td} (107 mg, 600 μmol) in MeOH (15 ml) was added to a solution of Co(ClO₄)₂·6H₂O (73 mg, 200 μmol) in MeOH (5 ml). Slow evaporation of the solvent resulted in the formation of brownish amorphous solid. Filtration, washing with MeOH and drying *in vacuo* gave bulk material of **13**·1.5H₂O. Yield: 31%. M.p. > 220 °C. Elemental analysis (%) found C 31.11, H 2.52, N 20.94, S 11.27, calcd. for C₂₁H₂₁N₁₂S₃Cl₂O_{9.5}Co (819.50 g mol⁻¹) C 30.78, H 2.58, N 20.51, S 11.74. IR (diamond, ATR): $\tilde{\nu}$ = 3394, 3316, 3197, 1634, 1603, 1506 (s), 1485 (s), 1457, 1438, 1052 (vs), 1029 (vs), 1012 (s), 930, 778 (s), 742, 717, 643, 620 (s), 494, 430, 419, 408 cm⁻¹. Single crystals of **13**·2H₂O, suitable for x-ray diffraction analysis, were obtained by this method.

[Ni^{II}(L^{td})₃](ClO₄)₂ (14): A solution of L^{td} (107 mg, 600 μmol) in MeOH (15 ml) was added to a solution of NiClO₄·6H₂O (73.1 mg, 200 μmol) on MeOH (5 ml). Slow evaporation of the solvent resulted in the formation of a purple amorphous solid. Filtration, washing with MeOH and drying *in vacuo* gave bulk material of **14**·2H₂O. Yield: 35%. M.p. > 220°C. Elemental analysis (%) found C 30.76, H 2.62, N 20.38, S 11.17, calcd. for C₂₁H₂₂N₁₂S₃Cl₂O₁₀Ni (828.26 g mol⁻¹) C 30.45, H 2.68, N 20.29, S 11.61. IR (diamond, ATR): $\tilde{\nu}$ = 3313, 3188, 1601 (s), 1501 (s), 1478 (s), 1322, 1259, 1158, 1059 (vs), 1028 (s), 930, 777, 743, 718, 621 (s), 447, 412 cm⁻¹. Single crystals of **14**·MeOH·H₂O, suitable for x-ray diffraction analysis, were obtained by this method.

[Fe^{II}(L^{td})₂](NCS)₂ (15): Solid KSCN (29.2 mg, 300 μmol) and a pinch of ascorbic acid was added to a solution of FeSO₄·7H₂O (41.7 mg, 150 μmol) in MeOH (10 ml) and stirred for 5 min at rt. The solvent was removed under reduced pressure and the residue was digested in MeCN (10 ml). The resulting suspension was filtered to obtain a clear MeCN solution of "Fe(NCS)₂". A solution of L^{td} (53.5 mg, 300 μmol) in MeCN (10 ml) was added under stirring whereupon a purple precipitate of [Fe(L^{td})₂](NCS)₂ (**15**) formed, which was collected by filtration, washed with MeCN and dried *in vacuo*. Yield: 73%.

M.p. > 220 °C. Elemental analysis (%) found: C 36.65, H 2.12, N 26.17, S 24.27, calcd. for $C_{16}H_{12}N_{10}S_4Fe$ ($528.43 \text{ g mol}^{-1}$) C 36.37, H 2.29, N 26.51, S 24.27. ESI-MS (MeOH): m/z (intensity, fragment) = 469.9726 (100 %, $[Fe(L^{td})_2NCS]^+$). IR (diamond, ATR): $\tilde{\nu} = 3360, 3247, 3155, 2125, 2070$ (s), 1592 (s), 1499 (vs), 1471 (vs), 1419, 1312, 1293, 1248, 1170, 1155, 1105, 1074, 1056, 1024, 999, 886, 774 (s), 742, 713, 668, 638, 599, 497, 442, 411 (s) cm^{-1} . UV/Vis (MeOH): λ_{max} (ϵ) = 206 (27930), 238 (10070) 312 (33800), 504 (963) nm ($M^{-1} cm^{-1}$).

3.3.4 Complexes with L^4NTf_2

Parts of the material presented in this chapter were included in the following manuscript: Timo Huxel and Julia Klingele, *Cobalt(II) Complexes of a New Imidazolium-Tagged Thiadiazole Ligand With Bis(trifluoromethylsulfonyl)imide or Tetraisoithiocyanato Cobaltate as Counterion*, submitted.

Attempted synthesis of $[Fe(L^4)_2(NCS)_2](NTf_2)_2$: $FeSO_4 \cdot 7H_2O$ (41.7 mg, 150 μmol), KSCN (29.2 mg, 300 μmol) and a pinch of ascorbic acid were suspended in MeOH (10 ml) and stirred for 10 min at rt. The solvent was removed under reduced pressure and the residue was suspended in MeCN (5 ml). Filtration gave a clear solution of " $Fe(NCS)_2$ ". A solution of L^4NTf_2 (191 mg, 300 μmol) in MeCN (20 ml) was added. Immediately a dark red solution formed. The reaction mixture was stirred for 10 min at rt and the solvent was removed under reduced pressure. Drying the residue gave a dark red amorphous powder. Yield: 32%. M.p. = 83–85 °C. Elemental analysis (%) found: C 33.20, H 2.97, 15.49, calcd. for $C_{40}H_{42}F_{12}N_{16}O_{10}S_8Fe$ ($1447.18 \text{ g mol}^{-1}$) C 33.20, H 2.93, N 15.49. IR (diamond, ATR): $\tilde{\nu} = 3153, 2048$ (s), 1695, 1605, 1521 (s), 1450, 1346 (s), 1177 (vs), 1131 (vs), 1050 (vs), 862, 787, 739, 650, 598, 569 (s), 507, 405 cm^{-1} . UV/Vis (MeCN): λ_{max} (ϵ) = 300 (41500), 423 (2720), 510 (6600) nm ($M^{-1} cm^{-1}$). Mössbauer: $I.S. = 0.37 \text{ mm s}^{-1}$, $\Delta E_Q = 0.38 \text{ mm s}^{-1}$.

$[Co(L^4)_2(NCS)_2](X)_2$ ($X = [Co(NCS)_4]$, **31**; $X = NTf_2$, **32**): $CoSO_4 \cdot 7H_2O$ (42.2 mg, 150 μmol) and KSCN (29.2 mg, 300 μmol) were suspended in MeOH abs. (5 ml) and stirred for 10 min at rt. The suspension was filtrated to give a clear purple solution of " $Co(NCS)_2$ ". A solution of L^4NTf_2 (191 mg, 300 μmol) in MeOH (15 ml) was added. The resulting brown solution was allowed to stand. After 3 d blue crystals of $[Co(L^4)_2(NCS)_2][Co(NCS)_4]$ (**31**) had formed, which were identified by means of X-ray diffraction analysis. IR (diamond, ATR): $\tilde{\nu} = 3090, 2927, 2486, 2056$ (vs), 2013 (s), 1987, 1961, 1936, 1673 (s), 1602 (vs), 1519, 1468, 1374, 1276 (s), 1152 (vs), 1007 (vs), 829 (s), 683, 639, 474 cm^{-1} . The mother liquor was allowed to stand. Slow evaporation of the solvent lead to the formation of brown crystals that were identified as $[Co(L^4)_2(NCS)_2](NTf_2)_2$ (**32**) by means of X-ray diffraction analysis. IR (diamond, ATR): $\tilde{\nu} = 3266, 3149,$

2079 (s), 1697, 1601, 1563, 1522 (s), 1483, 1446, 1342 (s), 1327 (s), 1227, 1177 (vs), 1130 (vs), 1053 (vs), 961, 842, 783, 764, 740, 717, 651, 612, 598, 570 (s), 509, 451, 407 cm^{-1} .

3.3.5 Complexes with L^2 and L^3

$[\text{Fe}(\text{L}^2)_3](\text{ClO}_4)_2$ (22**):** A solution of L^2 (109 mg, 630 μmol) in MeOH (10 ml) was added to a solution of $\text{Fe}(\text{ClO}_4)_2 \cdot 6\text{H}_2\text{O}$ (74.3 mg, 205 μmol) in MeOH (5 ml) without stirring. After 24 h a precipitate had formed. The mixture was filtrated, the residue was washed with Et_2O and dried *in vacuo*. A red coloured, amorphous powder of **22**· H_2O was obtained. Yield: 48 %. M.p. = 218–220 °C (dec.) Elemental analysis (%) found: C 45.65 H 4.27 N 15.83, calcd. for $\text{C}_{30}\text{H}_{35}\text{Cl}_2\text{N}_9\text{O}_9\text{Fe}$ (792.42 g mol^{-1}): C 45.47 H 4.45 N 15.91. ESI-MS (MeOH) m/z (rel. abundance, fragment) = 174.1026 (100 %, $[\text{L}^2\cdot\text{H}]^+$), 287.6095 (55 %, $[\text{Fe}(\text{L}^2)_3]^{2+}$), 501.0717 (6 %, $[[\text{Fe}(\text{L}^2)_2]\text{ClO}_4]^+$). IR (diamond, ATR): $\tilde{\nu}$ = 3144, 3124, 2987, 1607, 1535, 1491, 1473 (s), 1445, 1385, 1353, 1311, 1264, 1166, 1073 (vs), 1042, 960, 880, 781 (s), 752 (m), 705 (m), 673, 646, 620 (s), 514, 459, 422 cm^{-1} . UV/Vis (MeOH): λ_{max} (ϵ) = 214 (22090), 264 (23870), (300) (41160), 392 (2310), 498 (6440) nm ($\text{M}^{-1} \text{cm}^{-1}$).

$[\text{Fe}(\text{L}^2)_3](\text{BF}_4)_2$ (23**):** A solution of L^2 (118 mg, 680 μmol) in MeOH (1 ml) was added to a solution of $\text{Fe}(\text{BF}_4)_2 \cdot 6\text{H}_2\text{O}$ (69.2 mg, 205 μmol) in MeOH (1 ml) whereupon a precipitate had formed. The mixture was filtrated, the residue was washed with Et_2O and dried *in vacuo*. A red coloured, amorphous powder of **23**· H_2O was obtained. Yield: 67 %. M.p. = 225–228 °C Elemental analysis (%) found: C 47.18 H 4.42 N 16.62, calcd. for $\text{C}_{30}\text{H}_{35}\text{F}_8\text{B}_2\text{N}_9\text{OFe}$ (767.11 g mol^{-1}): C 46.97 H 4.60 N 16.43. ESI-MS (MeOH) m/z (rel. abundance, fragment) = 174.1023 (100 %, $[\text{L}^2\cdot\text{H}]^+$), 146.0711 (19 %, $[\text{pi}\cdot\text{H}]^+$). IR (diamond, ATR): $\tilde{\nu}$ = 3150, 3129, 2989, 1607, 1536, 1493, 1474 (s), 1446, 1385, 1354, 1313, 1265, 1168, 1106, 1050 (vs), 1034 (vs), 961, 875, 783 (s), 752, 720, 707, 674, 645, 636, 519, 425 cm^{-1} . UV/Vis (MeOH): λ_{max} (ϵ) = 204 (18400), 214 (15800), 268 (29200), 292 (37100), 392 (5920), 494 (5920) nm ($\text{M}^{-1} \text{cm}^{-1}$).

$[\text{Fe}(\text{L}^2)_3](\text{NTf}_2)_2$ (24**):** A solution of L^2 (116 mg, 670 μmol) in MeOH (1 ml) was added to a solution of $\text{Fe}(\text{NTf}_2)_2 \cdot 6\text{H}_2\text{O}$ (145 mg, 206 μmol) in MeOH (1 ml). After 48 h pentane (1 ml) and TBME (200 μml) was added whereupon a precipitate formed. The mixture was filtrated, the residue was washed with Et_2O and dried *in vacuo*. A red coloured, amorphous powder of **24** was obtained. Yield: 70 %. M.p. = 148–151 °C Elemental analysis (%) found: C 35.91 H 2.74 N 13.63, calcd. for $\text{C}_{34}\text{H}_{33}\text{F}_{12}\text{N}_{11}\text{O}_8\text{S}_4\text{Fe}$ (1135.78 g mol^{-1}) C 35.95 H 2.93 N 13.57. ESI-MS (MeOH) m/z (rel. abundance, fragment) = 174.1025 (100 %, $[\text{L}^2\cdot\text{H}]^+$), 287.6096 (71 %, $[\text{Fe}(\text{L}^2)_3]^+$), 682.0414 (23 %, $[[\text{Fe}(\text{L}^2)_2](\text{NTf}_2)]^+$). IR (diamond, ATR): $\tilde{\nu}$ = 3129, 1608, 1538, 1498, 1478, 1449, 1393, 1349 (s), 1330 (s), 1268, 1228, 1178 (vs), 1132 (vs),

1052 (vs), 967, 883, 781 (s), 750, 739, 720, 704, 661, 600 (s), 568 (s), 506 (s), 407 cm^{-1} . UV/Vis (MeOH): λ_{max} (ϵ) = 216 (18440), 262 (21900), 300 (38040), 396 (3034), 494 (5680) nm ($\text{M}^{-1} \text{cm}^{-1}$).

[Co(L²)₃](ClO₄)₂ (25): A solution of L² (105 mg, 605 μmol) in MeOH (2.5 ml) was added to a solution of Co(ClO₄)₂·6H₂O (75.8 mg, 207 μmol) in MeOH (2.5 ml) without stirring. After 20 h orange coloured crystals had formed which were identified as **25**·2MeOH. Filtration, washing with Et₂O and drying *in vacuo* gave bulk material of **25**·1.5H₂O. Yield: 49 %. M.p. >235 °C. Elemental analysis (%) found: C 44.81, H 4.67, N 15.85, calcd. for C₃₀H₃₆Cl₂N₉O_{9.5}Co (804.50 g mol⁻¹): C 44.79, H 4.51, N 15.67. ESI-MS (MeOH) *m/z* (rel. abundance, fragment) = 289.1092 (100 %, [Co(L²)₃]²⁺), 202.5611 (47 %, [Co(L²)₂]²⁺), 174.1025 (25 %, [L²·H]⁺), 504.0711 (11 %, [[Co(L²)₂ClO₄]⁺). IR (diamond, ATR): $\tilde{\nu}$ = 3120, 2985, 1603, 1574, 1490, 1468 (s), 1444, 1387, 1350, 1290, 1264, 1169, 1072 (vs), 1005, 959, 947, 787 (s), 746, 719 (s), 707 (s), 667, 638, 620 (s), 506, 459, 449, 411 cm^{-1} . UV/Vis (MeCN): λ_{max} (ϵ) = 288 (46200), 474 (38), 542 (16) nm ($\text{M}^{-1} \text{cm}^{-1}$).

[Ni(L²)₃](ClO₄)₂ (26): A solution of L² (109 mg, 628 μmol) in MeOH (2.5 ml) was added to a solution of Ni(ClO₄)₂·6H₂O (79.1 mg, 216 μmol) in MeOH (2.5 ml) without stirring. After 20 d crystals had formed. The solution was filtrated, the residue was washed with Et₂O and dried *in vacuo*. A purple coloured, crystalline powder of **26**·0.5H₂O was obtained. Yield: 40 %. M.p. > 235 °C. Elemental analysis (%) found: C 45.93, H 4.60, N 15.93, calcd. for C₃₀H₃₄Cl₂N₉O_{8.5}Ni (786.25 g mol⁻¹) C 45.83, H 4.36, N 16.03. ESI-MS (MeOH) *m/z* (rel. abundance, fragment) = 288.6099 (100 %, [Ni(L²)₃]²⁺), 202.0622 (68 %, [Ni(L²)₂]²⁺), 503.0720 (28 %, [[Ni(L²)₂](ClO₄)⁺). IR (diamond, ATR): $\tilde{\nu}$ = 3142, 3117, 2970, 1606, 1575, 1493, 1472 (s), 1444, 1382, 1353, 1314, 1291, 1263, 1174, 1071 (vs), 1042 (s), 960, 949, 881, 787 (s), 746, 721, 706 (s), 669, 641, 619 (s), 510, 412 cm^{-1} . UV/Vis (MeOH): λ_{max} (ϵ) = 246 (64200), 302 (51100), 530 (21) nm ($\text{M}^{-1} \text{cm}^{-1}$).

[Fe(L³)₃](ClO₄)₂ (27): A solution of L³ (129 mg, 634 μmol) in MeOH (2.5 ml) was added to a solution of Fe(ClO₄)₂·6H₂O (74.1 mg, 204 μmol) in MeOH (2.5 ml) without stirring. After 24 h a red precipitate had formed. The mixture was filtrated, the residue was washed with Et₂O and dried *in vacuo*. A red coloured amorphous powder was **27** obtained. Yield: 55 %. M.p. = 187–190 °C (dec.) Elemental analysis (%) found: C 45.72, H 4.70, N 14.65, calcd. for C₃₃H₃₉Cl₂N₉O₁₁Fe (864.47 g mol⁻¹): C 45.85, H 4.55, N 14.58. ESI-MS (MeOH) *m/z* (rel. abundance, fragment) = 332.6255 (100 %, [Fe(L³)₃]²⁺), 204.1130 (10 %, [L³·H]⁺), 561.0950 (8 %, [[Fe(L³)₂](ClO₄)⁺). IR (diamond, ATR): $\tilde{\nu}$ = 3121, 2889, 1607, 1534, 1471 (s), 1448, 1354, 1305, 1273, 1212, 1165, 1071 (vs), 1011, 959, 832, 781 (s), 746 (s), 721, 703 (s), 674, 646, 620 (s), 494, 457 cm^{-1} . UV/Vis (MeOH): λ_{max} (ϵ) = 262 (24620), 296 (41510), 392 (3387), 496 (6600) nm ($\text{M}^{-1} \text{cm}^{-1}$).

[Fe(L³)₃](BF₄)₂ (28): A solution of L³ (127 mg, 627 μmol) in MeOH (3 ml) was added to a solution of Fe(BF₄)₂·6H₂O (67.8 mg, 201 μmol) in MeOH (3 ml) without stirring. After 96 h at 7 °C a precipitate had formed. The mixture was filtrated, the residue was washed with Et₂O and dried *in vacuo*. A red coloured, amorphous powder of **28** was obtained. Yield: 52 %. M.p. = 170–173 °C. Elemental analysis (%) found: C 47.17, H 4.66, N 14.91, calcd. for C₃₃H₃₉F₈B₂N₉O₃Fe (839.18 g mol⁻¹): C 47.23, H 4.68, N 15.02. ESI-MS (MeOH) *m/z* (rel. abundance, fragment) = 332.6253 (100 %, [Fe(L³)₃]²⁺), 204.1131 (50 %, [L³·H]⁺), 231.0726 (28 %, [Fe(L³)₂]²⁺). IR (diamond, ATR): $\tilde{\nu}$ = 3130, 2895, 2819, 1607, 1536, 1495, 1474 (s), 1451, 1358, 1308, 1273, 1211, 1169, 1027 (vs), 833, 781 (s), 746 (s), 721, 704 (s), 674, 640, 519, 455 cm⁻¹. UV/Vis (MeOH): λ_{max} (ϵ) 262 (23450), 302 (36870), 392 (2929), 496 (5860) nm (M⁻¹cm⁻¹).

[Co(L³)₃](ClO₄)₂ (29): A solution of L³ (80.5 mg, 396 μmol) in MeOH (2.5 ml) was added to a solution of Co(ClO₄)₂·6H₂O (49.5 mg, 135 μmol) in MeOH (2.5 ml) without stirring. After 72 h orange coloured crystals had formed which could be identified as **29** by X-ray diffraction analyses. Filtration of the reaction mixture, washing the residue with Et₂O and drying *in vacuo* gave bulk material of **29**. Yield: 30 %. M.p. = 180–183 °C. Elemental analysis (%) found: C 45.69, H 4.69, N 14.57, calcd. for C₃₃H₃₉Cl₂N₉O₁₁Co (867.56 g mol⁻¹): C 45.69, H 4.53, N 14.53. ESI-MS (MeOH) *m/z* (rel. abundance, fragment) = 334.1245 (100 %, [Co(L³)₃]²⁺), 232.5717 (42 %, [Co(L³)₂]²⁺), 204.1131 (20 %, [L³·H]⁺), 564.0910 (11 %, [[Co(L³)₂](ClO₄)]⁺). IR (diamond, ATR): $\tilde{\nu}$ = 3118, 2893, 2814, 1604, 1574, 1474 (s), 1445, 1392, 1359, 1273, 1211, 1184, 1167, 1070 (vs), 1009 (s), 971, 945, 830, 785 (s), 764, 746, 722, 706 (s), 670, 636, 620 (vs), 548, 411 cm⁻¹. UV/Vis (MeCN): λ_{max} (ϵ) = 266 (28860), 302 (35380), 487 (38), 544 (17) nm (M⁻¹cm⁻¹).

[Ni(L³)₃](ClO₄)₂ (30): A solution of L³ (121 mg, 596 μmol) in MeOH (2.5 ml) was added to a solution of Ni(ClO₄)₂·6H₂O (73.2 mg, 200 μmol) in MeOH (2.5 ml) without stirring. After 72 h a crystalline solid had formed. The mixture was filtrated, the residue was washed with Et₂O and dried *in vacuo*. A purple coloured, crystalline solid of **30** was obtained. Yield: 56 %. M.p. = 188–191 °C. Elemental analysis (%) found: C 45.64, H 4.76, N 14.52, calcd. for C₃₃H₃₉Cl₂N₉O₁₁Ni (867.32 g mol⁻¹): C 45.70, H 4.53, N 14.53. ESI-MS (MeOH) *m/z* (rel. abundance, fragment) = 333.6255 (100 %, [Ni(L³)₃]²⁺), 232.0728 (20 %, [Ni(L³)₂]²⁺), 563.0942 (12 %, [[Ni(L³)₂](ClO₄)]⁺), 204.1133 (10 %, [L³·H]⁺). IR (diamond, ATR): $\tilde{\nu}$ = 3118, 2891, 2814, 1605, 1474 (s), 1445, 1392, 1359, 1273, 1211, 1186, 1168, 1119, 1071 (vs), 1010 (s), 971, 947, 830, 785 (s), 747, 722, 707 (s), 671, 635, 620 (s), 543, 501, 420 cm⁻¹. UV/Vis (MeCN): λ_{max} (ϵ) = 262 (26510), 304 (37440), 538 (15) nm (M⁻¹cm⁻¹).

3.3.6 Complexes with *N*-Alkylimidazoles

[Fe(mim)₆](NTf₂)₂ (33): A solution of *N*-methylimidazole (**mim**) (493 mg, 6.00 mmol) in degassed EtOH (2 ml) was added to a solution of Fe(NTf₂)₂·6H₂O (724 mg, 1.00 mmol) in degassed EtOH (5 ml) whereupon a precipitate formed. The resulting suspension was stirred for 1 h at rt. Filtration, washing with EtOH and drying *in vacuo* gave a colourless powder of **33**·0.5EtOH·0.5 H₂O. Yield: 20 %. M.p. = 183–185 °C (dec.). Elemental analysis (%) found: C 30.22, H 3.94, N 17.47, calcd. for C₂₉H₄₀F₁₂N₁₄O₉S₄Fe (1140.79 g mol⁻¹) C 30.53, H 3.53, N 17.19. ESI-MS (MeOH): *m/z* (rel. abundance, fragment) = 499.9577 (100 %, [Fe(**mim**)₂NTf₂]⁺). IR (diamond, ATR): $\tilde{\nu}$ = 3139, 1532, 1517, 1424, 1349 (s), 1331, 1286, 1233 (vs), 1174, 1140, 1107 (s), 1087, 1052 (vs), 936, 830, 791, 756, 746, 662 (vs), 610 (vs), 569 (s), 514, 410 cm⁻¹. UV/Vis (PC): λ_{max} (ϵ) = 360 (132), 863 (5) nm (M⁻¹ cm⁻¹).

[Fe(eim)₆](NTf₂)₂ (34): A solution of *N*-ethylimidazole (**eim**) (559 mg, 6.00 mmol) in degassed EtOH (2 ml) was added to a solution of Fe(NTf₂)₂·6H₂O (724 mg, 1.00 mmol) in degassed EtOH (5 ml). The Mixture was stirred over night at rt before adding degassed pentane (10 ml) whereupon a precipitate formed. Filtration, washing with pentane and drying *in vacuo* gave a beige powder of **34**·0.5EtOH·0.5H₂O. Yield: 37 %. M.p. = 83–85 °C. Elemental analysis (%) found: C 33.95, H 4.63, N 16.27, calcd. for C₃₅H₅₂F₁₂N₁₄O₉S₄Fe (1224.95 g mol⁻¹) C 34.32, H 4.78, N 16.27. ESI-MS (MeOH): *m/z* (rel. abundance, fragment) = 527.9890 (100 %, [Fe(**eim**)₂NTf₂]⁺). IR (diamond, ATR): $\tilde{\nu}$ = 3138, 1521, 1469, 1457, 1405, 1345 (s), 1321 (s), 1288, 1232, 1175 (vs), 1133 (vs), 1113, 1103, 1092 (s), 1060 (s), 1033, 965, 932, 843, 788, 762, 752, 741, 664, 651 (s), 624, 597 (s), 570, 530, 506, 443, 404 cm⁻¹. UV/Vis (PC): λ_{max} (ϵ) = 372 (156), 858 (6) nm (M⁻¹ cm⁻¹).

4 References

- [1] P. Gütlich, H. A. Goodwin, *Top. Curr. Chem.*, **233**, 1–47.
- [2] O. Kahn, *Science* **1998**, *279*, 44–48.
- [3] a) O. Kahn, J. Kröber, C. Jay, *Adv. Mater.* **1992**, *4*, 718–728; b) J. Zarembowitch, O. Kahn, *New J. Chem.* **1991**, *15*, 181–190;
- [4] a) H. Toftlund, *Coord. Chem. Rev.* **1989**, *94*, 67–108; b) P. Gutlich, Y. Garcia, H. A. Goodwin, *Chem. Soc. Rev.* **2000**, *29*, 419–427; c) S. V. Larionov, *Russ. J. Coord. Chem.* **2008**, *34*, 237–250; d) G. A. Craig, O. Roubeau, G. Aromí, *Coord. Chem. Rev.* **2014**, *269*, 13–31; e) M. A. Halcrow, *Polyhedron* **2007**, *26*, 3523–3576; f) H. A. Goodwin; g) M. A. Halcrow, *Coord. Chem. Rev.* **2009**, *253*, 2493–2514;
- [5] P. Gütlich, A. Hauser, H. Spiering, *Angew. Chem.* **1994**, *106*, 2109–2141.
- [6] P. J. Koningsbruggen, *Top. Curr. Chem.*, **233**, 123–149.
- [7] H. A. Goodwin, *Top. Curr. Chem.* **2004**, *234*, 23–47.
- [8] a) P. Guionneau, M. Marchivie, G. Bravic, J.-F. Létard, D. Chasseau, *Top. Curr. Chem.*, **234**, 97–128; b) M. A. Halcrow, *Chem. Soc. Rev.* **2011**, *40*, 4119;
- [9] B. Weber, E. Kaps, J. Weigand, C. Carbonera, J.-F. Létard, K. Achterhold, F. G. Parak, *Inorg. Chem.* **2008**, *47*, 487–496.
- [10] T. M. Pfaffeneder, S. Thallmair, W. Bauer, B. Weber, *New J. Chem.* **2011**, *35*, 691.
- [11] B. Weber, W. Bauer, T. Pfaffeneder, M. M. Dîrtu, A. D. Naik, A. Rotaru, Y. Garcia, *Eur. J. Inorg. Chem.* **2011**, *2011*, 3193–3206.
- [12] J. Klingele, D. Kaase, M. H. Klingele, J. Lach, S. Demeshko, *Dalton Trans.* **2010**, *39*, 1689–1691.
- [13] J. Klingele, D. Kaase, M. H. Klingele, J. Lach, *Dalton Trans.* **2012**, *41*, 1397–1406.
- [14] J. Klingele, D. Kaase, M. Schmucker, Y. Lan, G. Chastanet, J.-F. Létard, *Inorg. Chem.* **2013**, *52*, 6000–6010.
- [15] P. Hemmerich, B. Prijs, H. Erlenmeyer, *Helv. Chim. Acta* **1958**, *41*, 2058–2065.
- [16] G. Aromí, L. A. Barrios, O. Roubeau, P. Gamez, *Coord. Chem. Rev.* **2011**, *255*, 485–546.
- [17] M. Klingele, *Coord. Chem. Rev.* **2003**, *241*, 119–132.
- [18] J. Klingele, D. Kaase, M. Schmucker, L. Meier, *Eur. J. Inorg. Chem.* **2013**, 4931–4939.
- [19] F. Bentiss, M. Lagrenée, O. Mentré, P. Conflant, H. Vezin, J. P. Wignacourt, E. M. Holt, *Inorg. Chem.* **2004**, *43*, 1865–1873.
- [20] F. Bentiss, M. Lagrenée, J. P. Wignacourt, E. M. Holt, *Polyhedron* **2002**, *21*, 403–408.

-
- [21] J. Klingele, D. Kaase, J. Hilgert, G. Steinfeld, M. H. Klingele, J. Lach, *Dalton Trans.* **2010**, 39, 4495–4507.
- [22] a) D. Kaase, C. Gotzmann, S. Rein, Y. Lan, S. Kacprzak, J. Klingele, *Inorg. Chem.* **2014**, 53, 5546–5555;
b) J. Klingele, D. Kaase, T. Huxel, C. Gotzmann, Y. Lan, *Polyhedron* **2013**, 52, 500–514;
- [23] J. Klingele, S. Dechert, F. Meyer, *Coord. Chem. Rev.* **2009**, 253, 2698–2741.
- [24] A. T. Baker, H. A. Goodwin, A. D. Rae, *Inorg. Chem.* **1987**, 26, 3513–3519.
- [25] E. König, G. Ritter, H. A. Goodwin, *Chem. Phys.* **1973**, 1, 17–26.
- [26] J. K. Beattie, R. A. Binstead, R. J. West, *J. Am. Chem. Soc.* **1978**, 100, 3044–3050.
- [27] A. Bhattacharjee, V. Ksenofontov, H. A. Goodwin, P. Gütlich, *J. Phys.: Condens. Matter* **2009**, 21, 026011.
- [28] B. J. Childs, D. C. Craig, M. L. Scudder, H. A. Goodwin, *Inorg. Chim. Acta* **1998**, 274, 32–41.
- [29] E. König, G. Ritter, H. A. Goodwin, *Chem. Phys. Lett.* **1976**, 44, 100–103.
- [30] G. Ritter, E. Koenig, W. Irlner, H. A. Goodwin, *Inorg. Chem.* **1978**, 17, 224–228.
- [31] R. N. Sylva, H. A. Goodwin, *Aust. J. Chem.* **1967**, 20, 479.
- [32] B. J. Childs, D. C. Craig, K. A. Ross, M. L. Scudder, H. A. Goodwin, *Aust. J. Chem.* **1994**, 47, 891–902.
- [33] B. J. Childs, J. M. Cadogan, D. C. Craig, M. L. Scudder, H. A. Goodwin, *Aust. J. Chem.* **1997**, 50, 129.
- [34] L. Farkas, E. Kasztreiner, F. Andradi, J. Borsi, I. Elekes, I. Polgari, Ger. Pat., DE2453147 (A1), **1975**.
- [35] J. D. Crane, A. McLaughlin, *Acta Cryst.* **2004**, E60, o129–o130.
- [36] B. Chiswell, F. Lions, B. S. Morris, *Inorg. Chem.* **1964**, 3, 110–114.
- [37] R. J. Dosser, W. J. Eilbeck, A. E. Underhill, P. R. Edwards, C. E. Johnson, *J. Chem. Soc., A* **1969**, 810.
- [38] Y. Sasaki, T. Shigematsu, *Bull. Chem. Soc. Jpn.* **1973**, 46, 3438–3442.
- [39] Goodgame, David M. L., Machado, A. A. S. C., *Inorg. Chem.* **1969**, 8, 2031–2033.
- [40] K. A. Reeder, E. V. Dose, L. J. Wilson, *Inorg. Chem.* **1978**, 17, 1071–1075.
- [41] W. L. Driessen, van der Voort, P.H., *Inorg. Chim. Acta* **1977**, 21, 217–222.
- [42] W. Hibbs, A. M. Arif, J. van Koningsbruggen, Petra, J. S. Miller, *Cryst. Eng. Comm.* **1999**, 1, 12.
- [43] W. Hibbs, van Koningsbruggen, Petra J., A. M. Arif, W. W. Shum, J. S. Miller, *Inorg. Chem.* **2003**, 42, 5645–5653.
- [44] A. Bhattacharjee, van Koningsbruggen, P J, W. Hibbs, J. S. Miller, P. Gütlich, *J. Phys.: Condens. Matter* **2007**, 19, 406202.
- [45] P. L. Franke, J. G. Haasnoot, A. P. Zuur, *Inorg. Chim. Acta* **1982**, 59, 5–9.
- [46] N. Hassan, P. Weinberger, K. Mereiter, F. Werner, G. Molnar, A. Bousseksou, M. Valtiner, W. Linert, *Inorg. Chim. Acta* **2008**, 361, 1291–1297.

-
- [47] K. Nishiyama, M. Oba, A. Watanabe, *Tetrahedron* **1987**, *43*, 693–700.
- [48] T. Huxel, S. Riedel, J. Lach, J. Klingele, *Z. Anorg. Allg. Chem.* **2012**, *638*, 925–934.
- [49] Barbara Kirchner (Ed.) *Topics in Current Chemistry, Vol. 290*, Springer, Berlin / Heidelberg, **2010**.
- [50] S. H. Strauss, *Chem. Rev.* **1993**, *93*, 927–942.
- [51] U. Preiss, S. Bulut, I. Krossing, *J. Phys. Chem. B* **2010**, *114*, 11133–11140.
- [52] M. E. Williams, H. Masui, J. W. Long, J. Malik, R. W. Murray, *J. Am. Chem. Soc.* **1997**, *119*, 1997–2005.
- [53] M. E. Williams, H. Masui, R. W. Murray, *J. Phys. Chem. B* **2000**, *104*, 10699–10706.
- [54] M. Okuhata, Y. Funasako, K. Takahashi, T. Mochida, *Chem. Commun.* **2013**, *49*, 7662.
- [55] a) M.-E. Moret, A. B. Chaplin, A. K. Lawrence, R. Scopelliti, P. J. Dyson, *Organometallics* **2005**, *24*, 4039–4048; b) C. Barthes, C. Lepetit, Y. Canac, C. Duhayon, D. Zargarian, R. Chauvin, *Inorg. Chem.* **2013**, *52*, 48–58; c) M. J. Bravo, I. Favier, N. Saffon, R. M. Ceder, G. Muller, M. Gómez, M. Rocamora, *Organometallics* **2014**, *33*, 771–779;
- [56] H. Schottenberger, K. Wurst, Horvath, Ulrike E. I., S. Cronje, J. Lukasser, J. Polin, J. M. McKenzie, H. G. Raubenheimer, *Dalton Trans.* **2003**, 4275–4281.
- [57] V. O. Nyamori, M. Gumede, M. D. Bala, *J. Organom. Chem.* **2010**, *695*, 1126–1132.
- [58] a) Y. Gao, B. Twamley, J. M. Shreeve, *Inorg. Chem.* **2004**, *43*, 3406–3412; b) R. Balasubramanian, W. Wang, R. W. Murray, *J. Am. Chem. Soc.* **2006**, *128*, 9994–9995;
- [59] G. H. Frischat, *Chem. Unserer Zeit* **1977**, *11*, 65–74.
- [60] G. Molnar, L. Salmon, W. Nicolazzi, F. Terki, A. Bousseksou, *J. Mat. Chem. C* **2014**, *2*, 1360–1366.
- [61] M. B. Duriska, S. M. Neville, B. Moubaraki, J. D. Cashion, G. J. Halder, K. W. Chapman, C. Balde, J.-F. Létard, K. S. Murray, C. J. Kepert et al., *Angew. Chem. Int. Ed.* **2009**, *48*, 2549–2552.
- [62] A. B. Gaspar, M. Seredyuk, P. Gütlich, *J. Mol. Struct.* **2009**, *924-926*, 9–19.
- [63] E. Coronado, G. Minguez Espallargas, *Chem. Soc. Rev.* **2013**, *42*, 1525–1539.
- [64] A. Taurins, A. Blaga, *J. Heterocyclic Chem.* **1970**, *7*, 1137–1141.
- [65] G. B. Barlin, L. P. Davies, S. J. Ireland, Ngu, M. M. L., *Aust. J. Chem.* **1989**, *42*, 1735–1748.
- [66] G. Hegar, Ger. Pat., DE1925654 (A1), **1969**.
- [67] F. C. Schaefer, G. A. Peters, *J. Org. Chem.* **1961**, *26*, 412–418.
- [68] T. Huxel, S. Leone, Y. Lan, S. Demeshko, J. Klingele, *Eur. J. Inorg. Chem.* **2014**, 3114–3124.
- [69] D. M. Kurtz, *Chem. Rev.* **1990**, *90*, 585–606.
- [70] K. S. Murray, *Coord. Chem. Rev.* **1974**, *12*, 1–35.

-
- [71] a) E. Y. Tshuva, S. J. Lippard, *Chem. Rev.* **2004**, *104*, 987–1012; b) S. V. Kryatov, E. V. Rybak-Akimova, S. Schindler, *Chem. Rev.* **2005**, *105*, 2175–2226; c) E. I. Solomon, T. C. Brunold, M. I. Davis, J. N. Kemsley, S.-K. Lee, N. Lehnert, F. Neese, A. J. Skulan, Y.-S. Yang, J. Zhou, *Chem. Rev.* **2000**, *100*, 235–350;
- [72] J. Reedijk, *Comments Inorg. Chem.* **1982**, *1*, 379–389.
- [73] S. Taktak, S. V. Kryatov, T. E. Haas, E. V. Rybak-Akimova, *J. Mol. Catal. A: Chem.* **2006**, *259*, 24–34.
- [74] K. S. Min, A. M. Arif, J. S. Miller, *Inorg. Chim. Acta* **2007**, *360*, 1854–1858.
- [75] R. K. Egdal, A. Hazell, C. J. McKenzie, *Acta Cryst.* **2002**, *E58*, m10.
- [76] N. Raffard, V. Balland, J. Simaan, S. Létard, M. Nierlich, K. Miki, F. Banse, E. Anxolabéhère-Mallart, J.-J. Girerd, *C. R. Chimie* **2002**, *5*, 99–109.
- [77] T. Kojima, R. A. Leising, S. Yan, L. Que, *J. Am. Chem. Soc.* **1993**, *115*, 11328–11335.
- [78] Dao Feng Xiang, Xiang Shi Tan, Si Wei Zhang, Yu Han, Kai Bei Yu, Wen Xia Tang, *Polyhedron* **1998**, *17*, 2095–2100.
- [79] M.-N. Collomb, A. Deronzier, K. Gorgy, J.-C. Leprêtre, J. Pe'caut, *New J. Chem.* **1999**, *23*, 785–790.
- [80] S. Brooker, P. D. Croucher, *Chem. Commun.* **1997**, 459–460.
- [81] E. Wiberg, N. Wiberg, *Lehrbuch der Anorganischen Chemie*, Walter de Gruyter, Berlin, **1995**.
- [82] P. Gütllich, *Chem. unserer Zeit* **1971**, *5*, 131–141.
- [83] Gütllich, Philipp, Bill, Eckhard, Trautwein, Alfred X., *Mössbauer Spectroscopy and Transition Metal Chemistry*, Springer, Berlin / Heidelberg, **2011**.
- [84] I. Rey, P. Johansson, J. Lindgren, J. C. Lassègues, J. Grondin, L. Servant, *J. Phys. Chem. A* **1998**, *102*, 3249–3258.
- [85] C. Baer, J. Pike, *J. Chem. Educ.* **2010**, *87*, 724–726.
- [86] P. Eiden, *Inauguraldissertation*, Albert-Ludwigs-Universität, Freiburg, **2011**.
- [87] A. Hauser, *Adv. Polym. Sci.* **2004**, *233*, 49–58.
- [88] H. E. Gottlieb, V. Kotlyar, A. Nudelman, *J. Org. Chem.* **1997**, *62*, 7512–7515.
- [89] Günter Zeppenfeld, *Organikum. Organisch-chemisches Praktikum*, Barth Verlagsgesellschaft mbH, Leipzig, **1993**.
- [90] M. E. Voss, C. M. Beer, S. A. Mitchell, P. A. Blomgren, P. E. Zhichkin, *Tetrahedron* **2008**, *64*, 645–651.
- [91] K. Nakamoto, *Infrared and Raman Spectra of Inorganic and Coordination Compounds. Part A: Theory and Applications in Inorganic Chemistry*, John Wiley & Sons, Inc., Hoboken, New Jersey, **2009**.
- [92] G. Stupka, L. Gremaud, A. F. Williams, *Helv. Chim. Acta* **2005**, *88*, 487–495.

-
- [93] M. Kärnä, M. Lahtinen, P.-L. Hakkarainen, J. Valkonen, *Aust. J. Chem.* **2010**, *63*, 1122.
- [94] M. Kärnä, M. Lahtinen, A. Kujala, P.-L. Hakkarainen, J. Valkonen, *J. Mol. Struct.* **2010**, *983*, 82–92.
- [95] M. K. Kärnä, M. K. Lahtinen, J. U. Valkonen, *J. Chem. Eng. Data* **2013**, *58*, 1893–1908.
- [96] F. Bentiss, M. Lagrenée, H. Vezin, J.-P. Wignacourt, E. M. Holt, *Polyhedron* **2004**, *23*, 1903–1907.
- [97] dos Santos, Marcelo R., J. R. Diniz, A. M. Arouca, A. F. Gomes, F. C. Gozzo, S. M. Tamborim, A. L. Parize, Suarez, Paulo A. Z., Neto, Brenno A. D., *ChemSusChem* **2012**, *5*, 716–726.
- [98] R. Tan, D. Yin, Y. Ningya, J. Yong, Z. Haihong, Y. Dulin, *J. Catal.* **2008**, *255*, 287–295.
- [99] a) K. Ambrose, B. B. Hurisso, R. D. Singer, *Can. J. Chem.* **2013**, *91*, 1258–1261; b) S. Sonar, K. Ambrose, A. D. Hendsbee, J. D. Masuda, R. D. Singer, *Can. J. Chem.* **2012**, *90*, 60–70;
- [100] P. U. Naik, G. J. McManus, M. J. Zaworotko, R. D. Singer, *Dalton Trans.* **2008**, 4834–4836.
- [101] K.-M. Song, H.-Y. Gao, F.-S. Liu, J. Pan, L.-H. Guo, S.-B. Zai, Q. Wu, *Catal. Lett.* **2009**, *131*, 566–573.
- [102] T. Huxel, *Diplomarbeit*, Albert-Ludwigs-Universität, Freiburg, **2010**.
- [103] E. Bill, *Mfit program*, Max-Planck Institute for Chemical Energy Conversion, Mülheim/Ruhr, Germany.
- [104] E. Bill, *JulX program*, Max-Planck Institute for Chemical Energy Conversion, Mülheim/Ruhr, Germany.
- [105] G. M. Sheldrick, *Acta Cryst.* **2008**, *A64*, 112–122.
- [106] O. V. Dolomanov, L. J. Bourhis, R. J. Gildea, J. A. K. Howard, H. Puschmann, *J. Appl. Cryst.* **2009**, *42*, 339–341.
- [107] C. Göhringer, *Protokoll Forschungspraktikum*, Albert-Ludwigs-Universität, Freiburg, **2011**.
- [108] L. Leone, *Bachelorarbeit*, Albert-Ludwigs-Universität, Freiburg, **2012**.
- [109] M. Skaisgirski, *Masterarbeit*, Albert-Ludwigs-Universität, Freiburg, **2014**.
- [110] C. Gotzmann, *Bachelorarbeit*, Albert-Ludwigs-Universität, Freiburg, **2011**.

5 Appendix

5.1 NMR Spectra

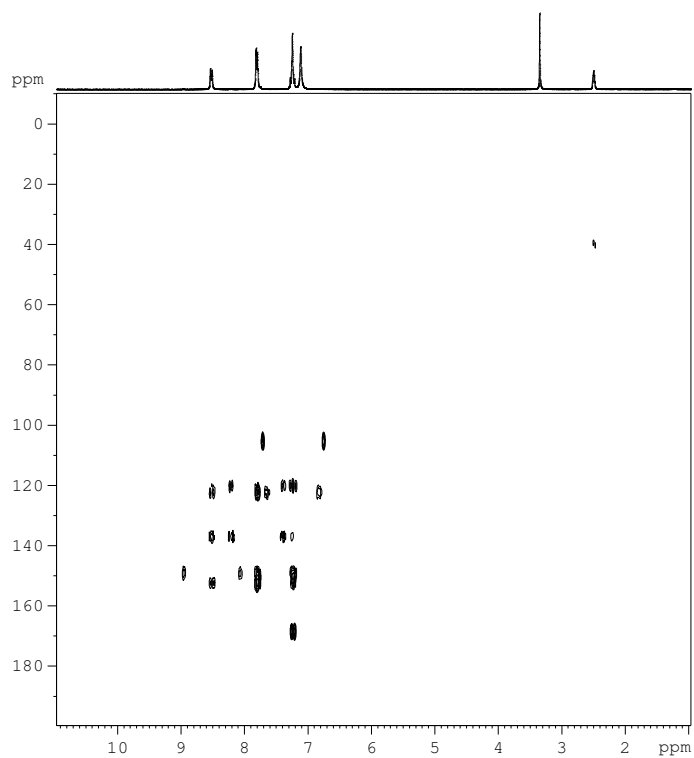


Figure 101: ^1H , ^{13}C -HMBC correlation (200.13 MHz, optimised for 7 Hz) of the thiazole ligand L^{tz} in DMSO-d_6 at 298 K.

NMR Spectra

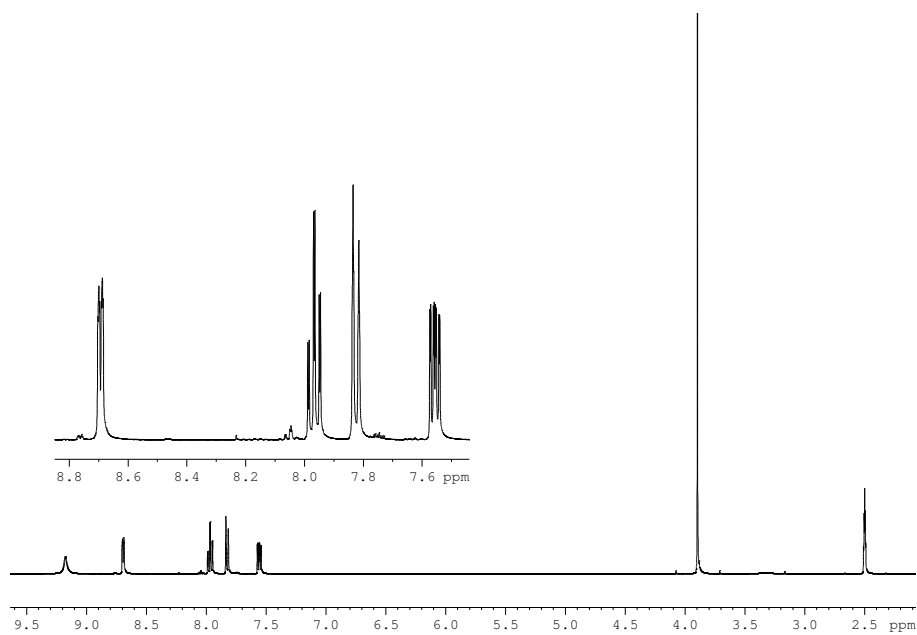


Figure 102: ^1H -NMR spectrum (400.17 MHz) of the imidoester **pyNH** in DMSO-d_6 at 298 K.

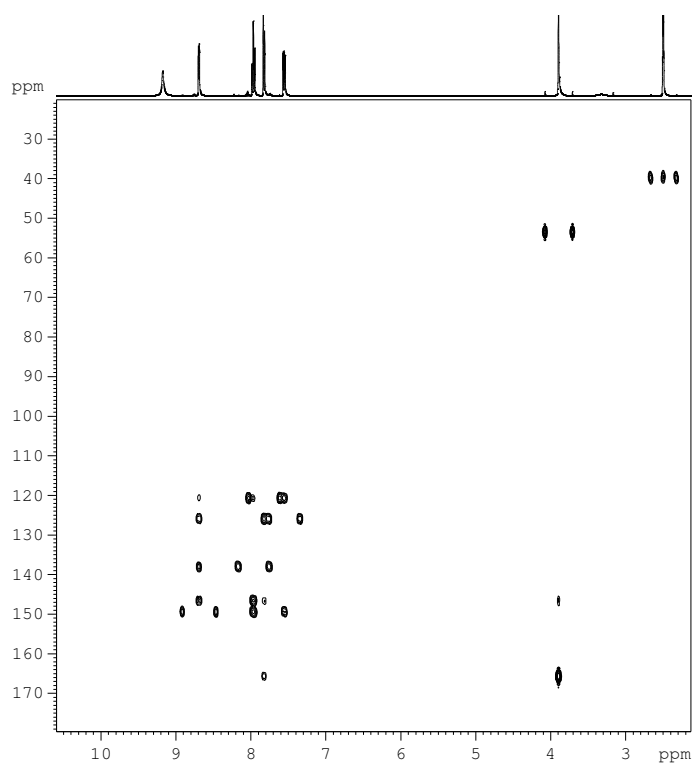


Figure 103: ^1H , ^{13}C -HMBC correlation (400.17 MHz, optimised for 8 Hz) of the imidoester **pyNH** in DMSO-d_6 .

NMR Spectra

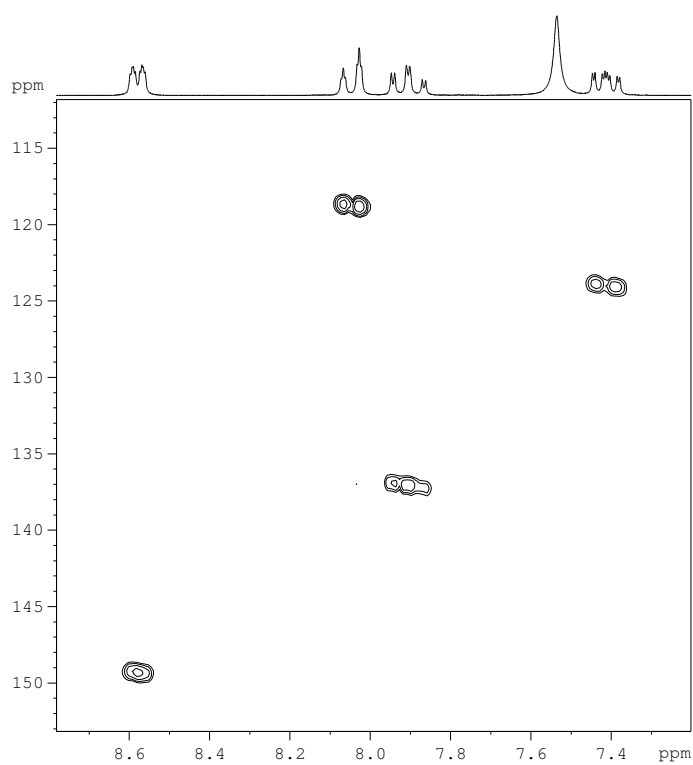


Figure 104: ^1H , ^{13}C -HMQC correlation (200.13 MHz, optimised for 150 Hz) of the thiadiazole ligand L^{td} in DMSO-d_6 298 K.

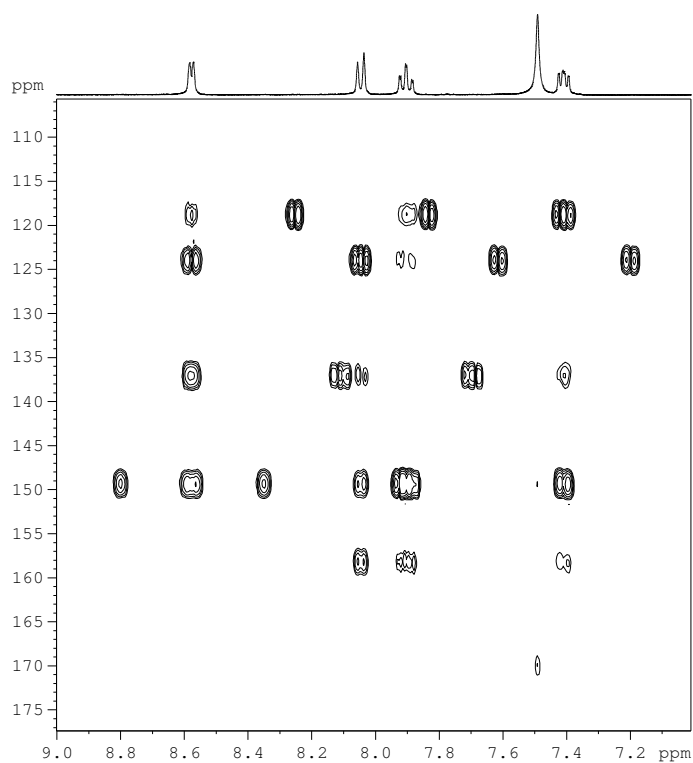


Figure 105: ^1H , ^{13}C -HMBC correlation (400.17 MHz, optimised for 145 Hz) of the thiadiazole ligand L^{td} in DMSO-d_6 298 K.

NMR Spectra

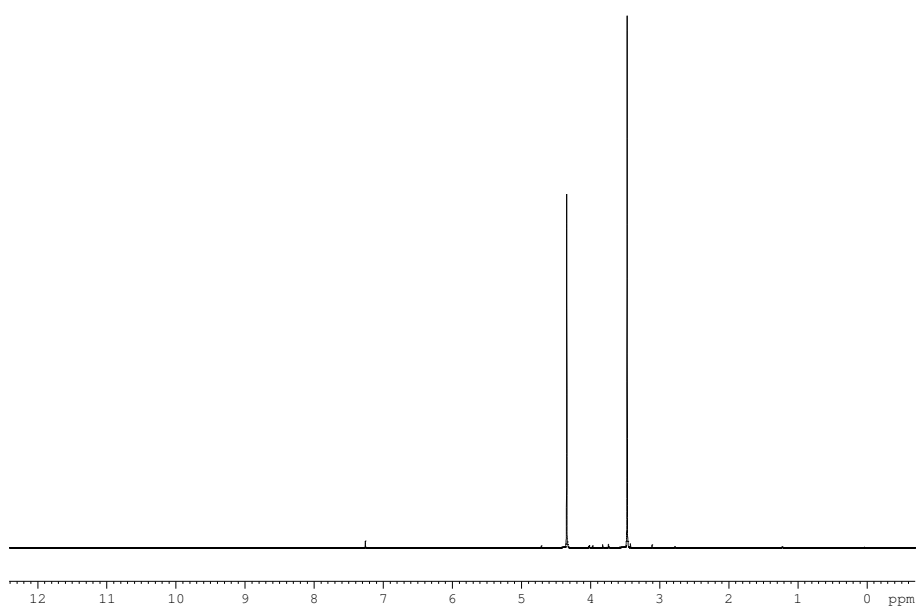


Figure 106: ¹H-NMR spectrum (200.13 MHz) of ClC(O)CH₂OMe in CDCl₃ at 298 K.

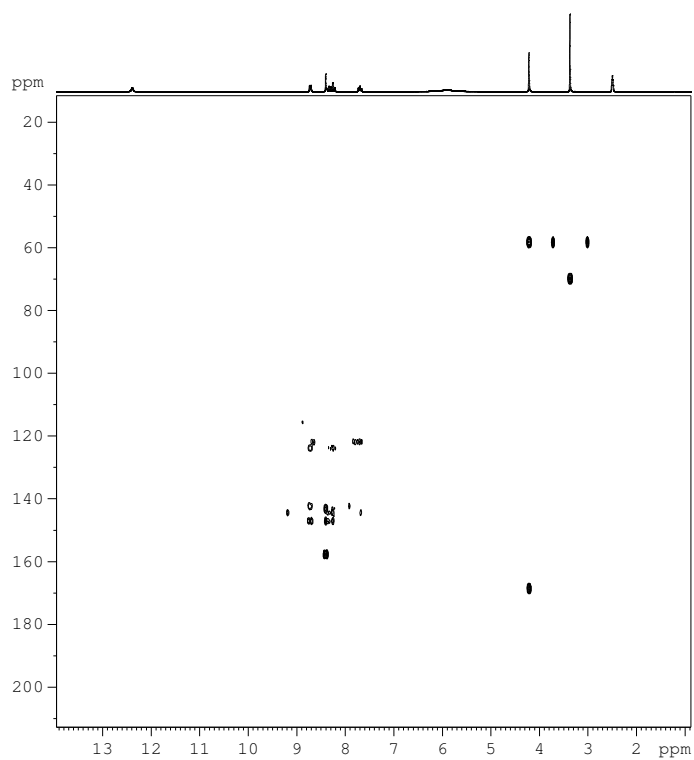


Figure 107: ¹H, ¹³C-HMBC correlation (200.13 MHz, optimised for 8 Hz) of the hydrochloride of the expanded thiazole ligand L¹-HCl in DMSO-d₆ at 298 K.

NMR Spectra

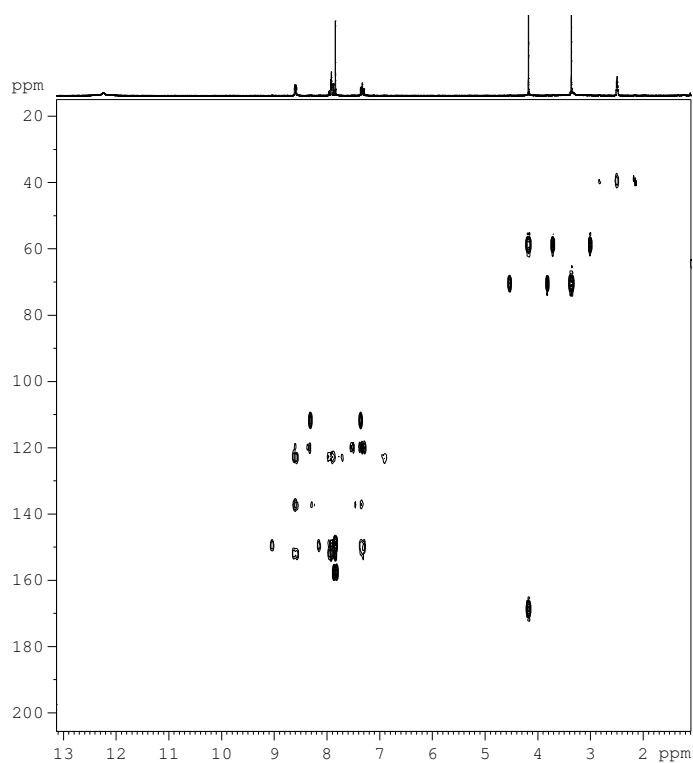


Figure 108: ^1H , ^{13}C -HMBC correlation (200.13 MHz, optimised for 7 Hz) of the expanded thiazole ligand L^1 in DMSO-d_6 at 298 K.

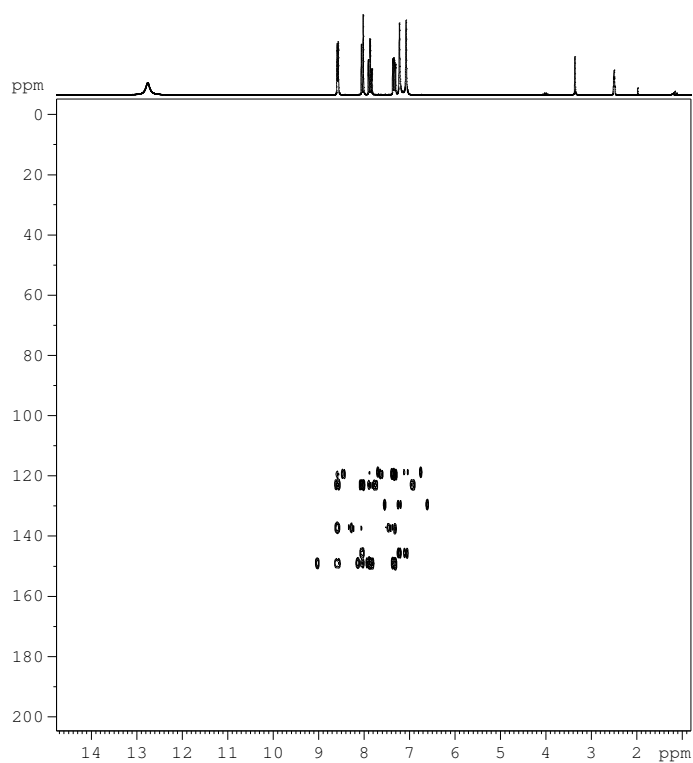


Figure 109: ^1H , ^{13}C -HMBC correlation (200.13 MHz, optimised for 7 Hz) of 2-(2-pyridyl)-imidazole (pi) in DMSO-d_6 at 298 K.

NMR Spectra

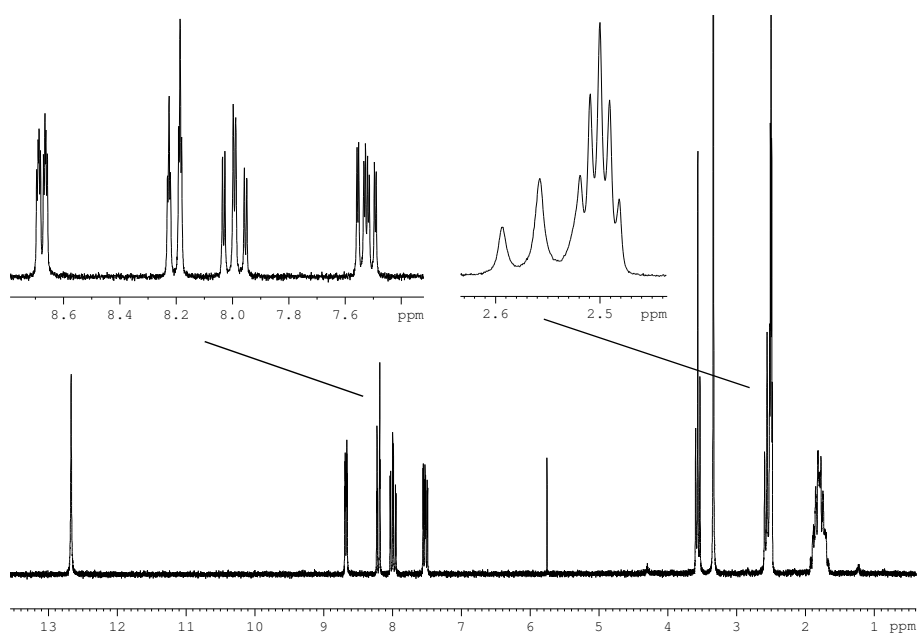


Figure 110: ^1H -NMR spectrum (200.13 MHz) of the precursor **tdBr** in DMSO-d_6 at 298 K.

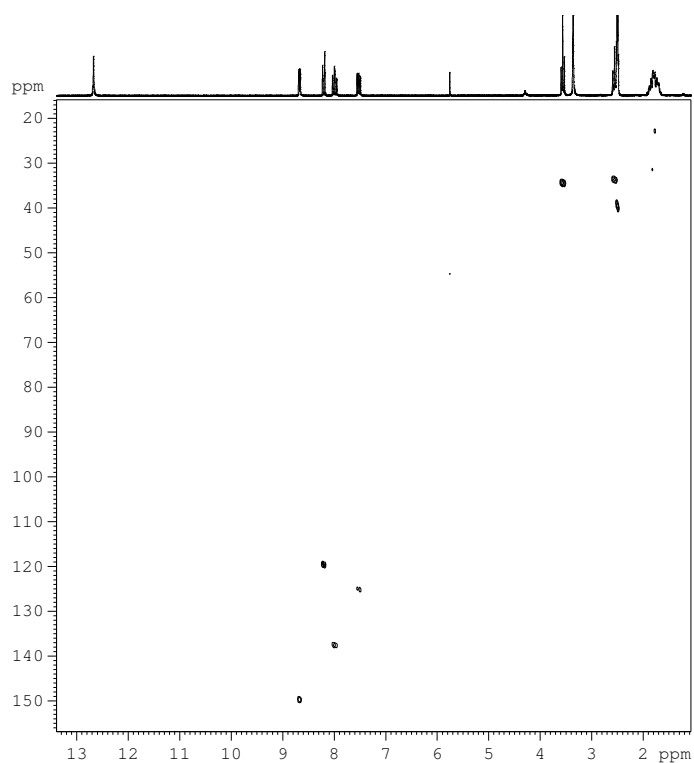


Figure 111: ^1H , ^{13}C -HMQC correlation (200.13 MHz, optimised for 150 Hz) of the precursor **tdBr** in DMSO-d_6 at 298 K.

NMR Spectra

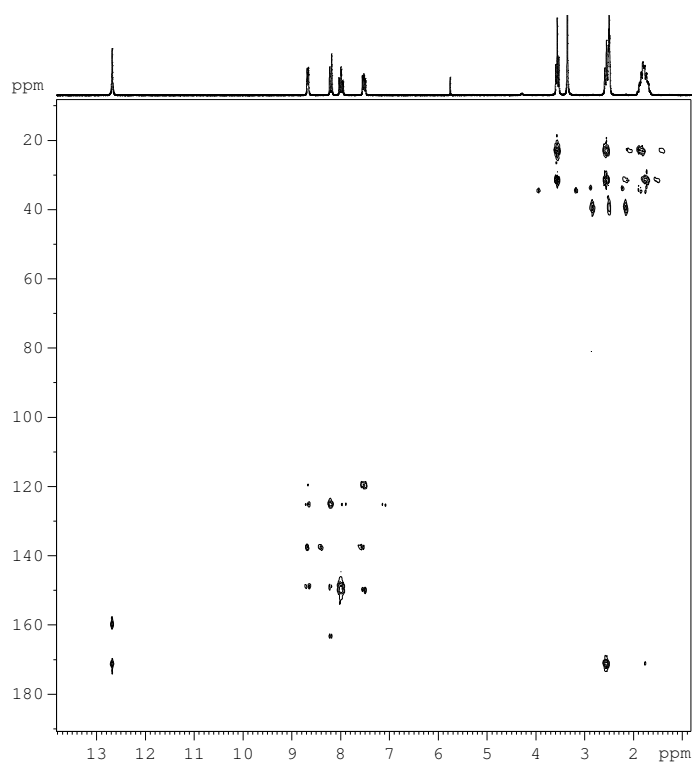


Figure 112: ^1H , ^{13}C -HMBC correlation (200.13 MHz, optimised for 7 Hz) of the precursor **tdBr** in DMSO-d_6 at 298 K.

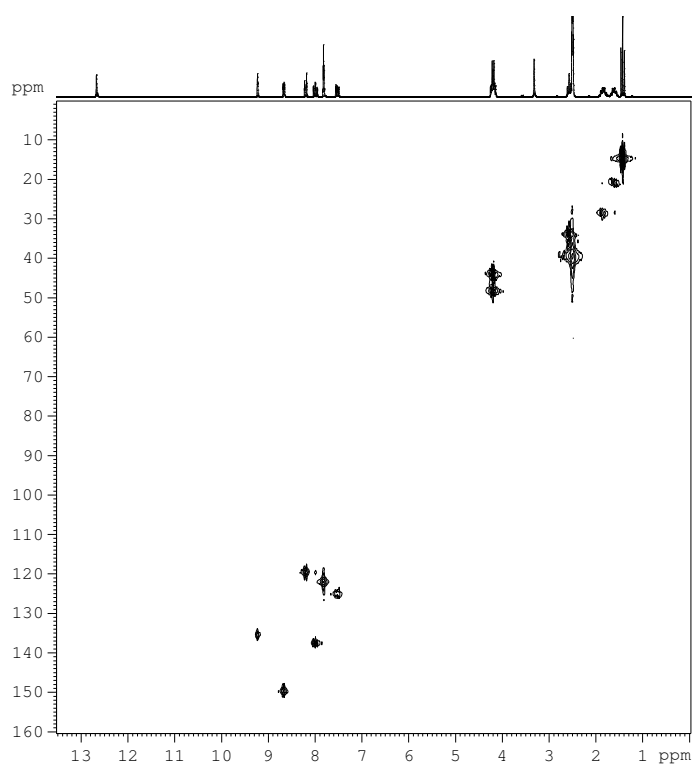


Figure 113: ^1H , ^{13}C -HMQC correlation (200.13 MHz, optimised for 150 Hz) of the imidazolium bromide ligand **L⁴Br** in DMSO-d_6 at 298 K.

NMR Spectra

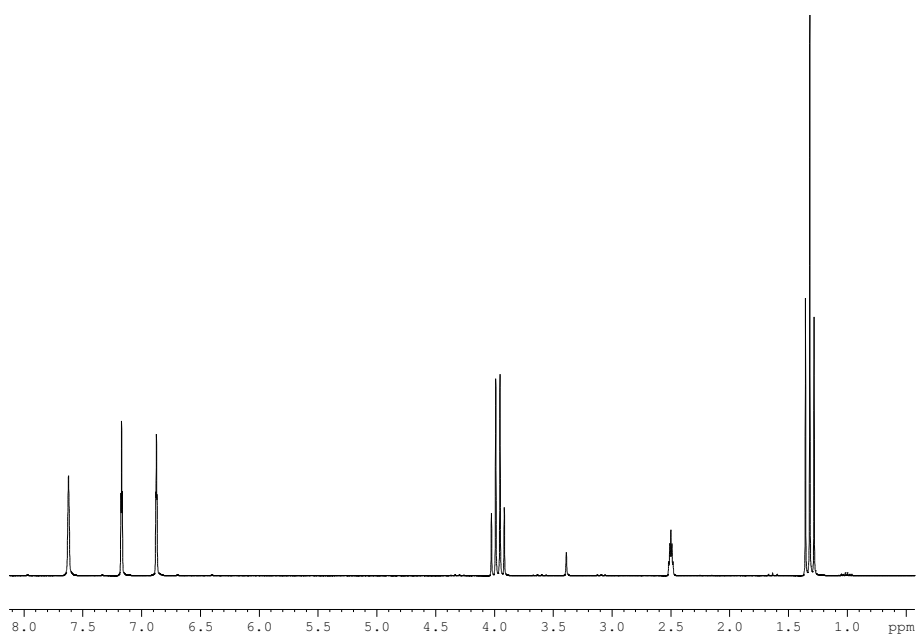


Figure 114: ^1H -NMR spectrum (200.13 MHz) of *N*-ethylimidazole in DMSO-d_6 at 298 K.

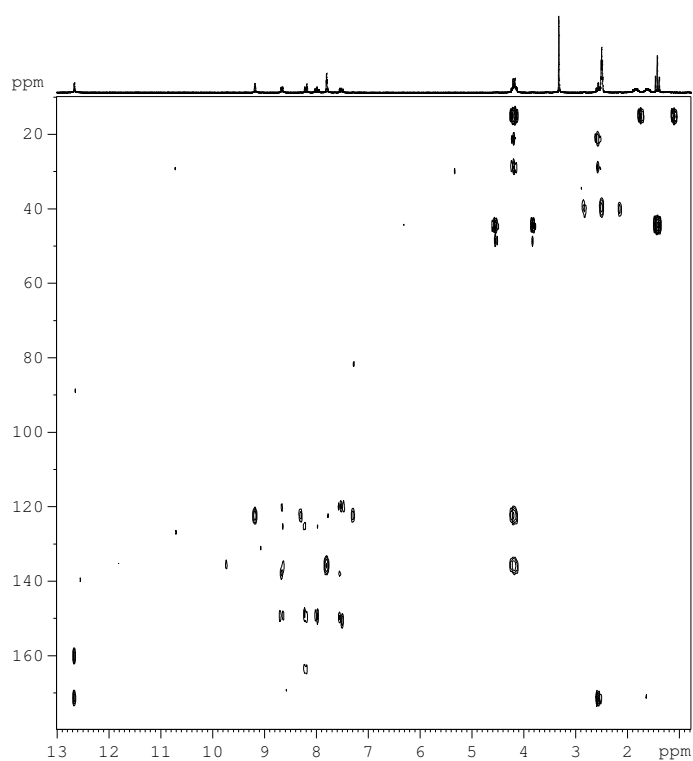


Figure 115: ^1H , ^{13}C -HMBC (200.13 MHz, optimised for 7 Hz) correlation the imidazolium triflimide ligand L^4NTf_2 in DMSO-d_6 at 298 K.

5.2 Mass Spectra

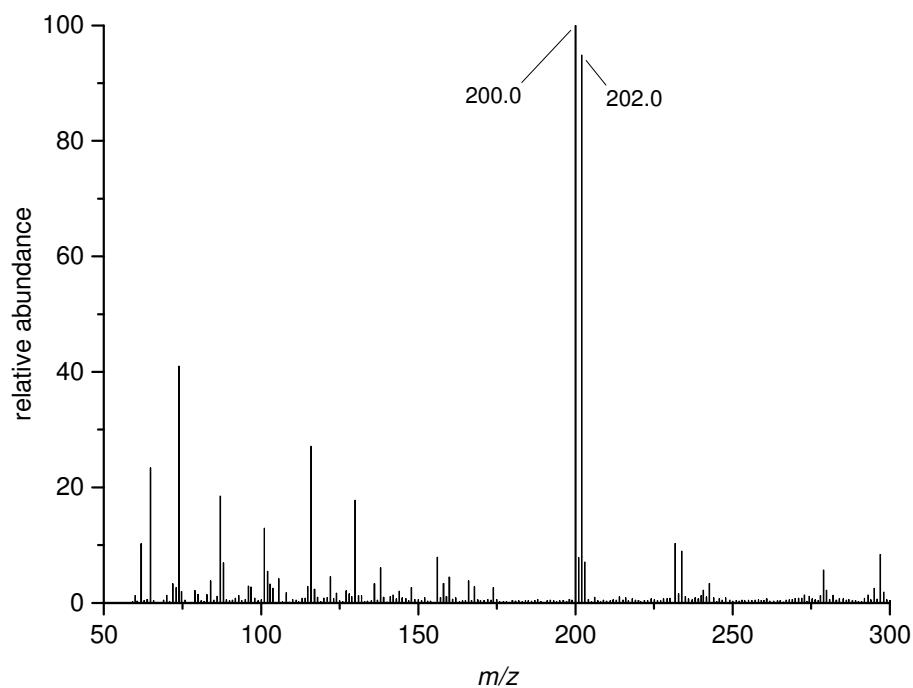


Figure 116: APCI mass spectrum of 2-(bromoacetyl)-pyridine hydrobromide (pyBr).

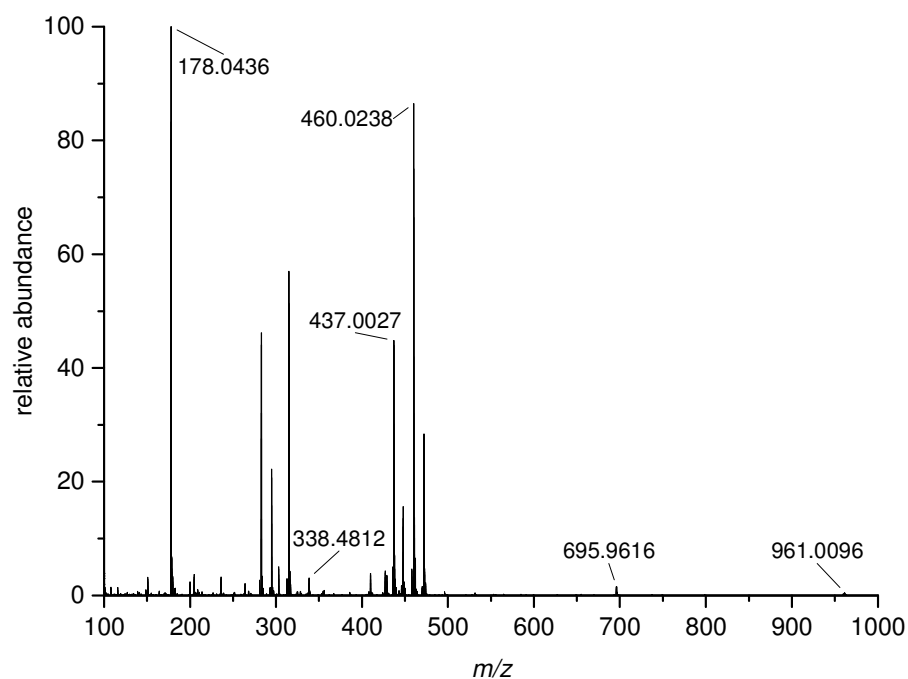


Figure 117: ESI-MS spectrum of $[(L^{tz})_2Fe^{III}(\mu-O)Fe^{III}(L^{tz})_2](BF_4) \cdot 1.25H_2O$ (1·1.25MeOH)

Mass Spectra

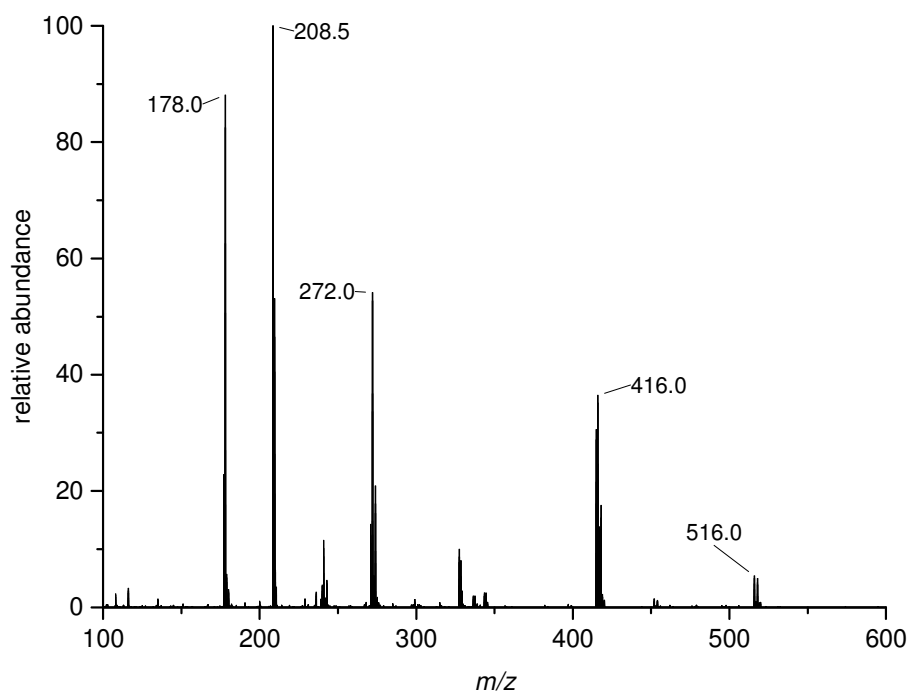


Figure 118: ESI-MS mass spectrum of $[\text{Cu}^{\text{II}}(\text{L}^{\text{Lz}})_2](\text{ClO}_4)_2$ (4).

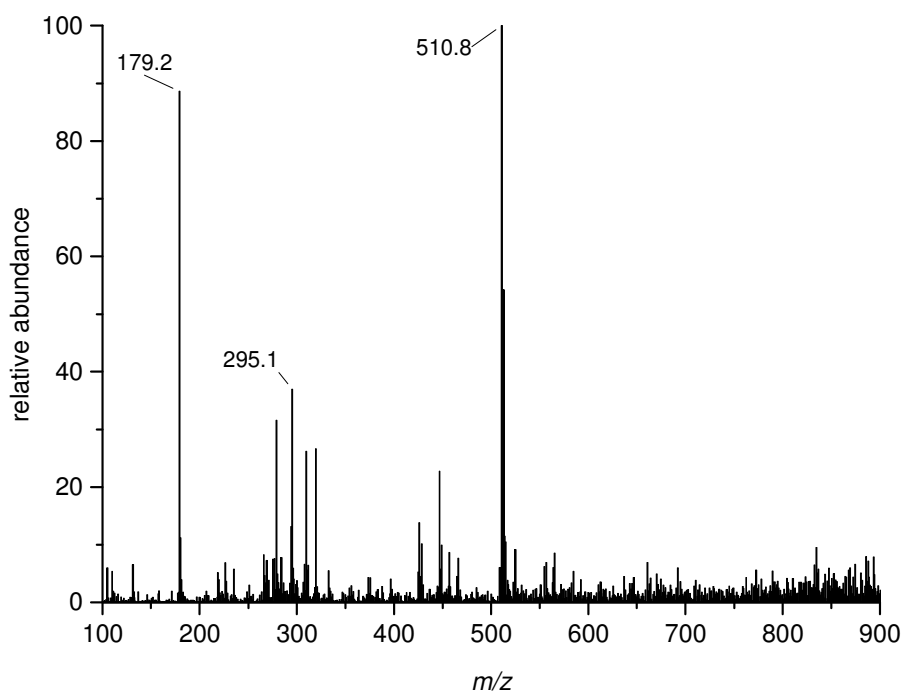


Figure 119: ESI-MS spectrum of $[\text{Fe}^{\text{II}}(\text{L}^{\text{td}})_3](\text{ClO}_4)_2 \cdot 2\text{H}_2\text{O}$ (10·2H₂O).

Mass Spectra

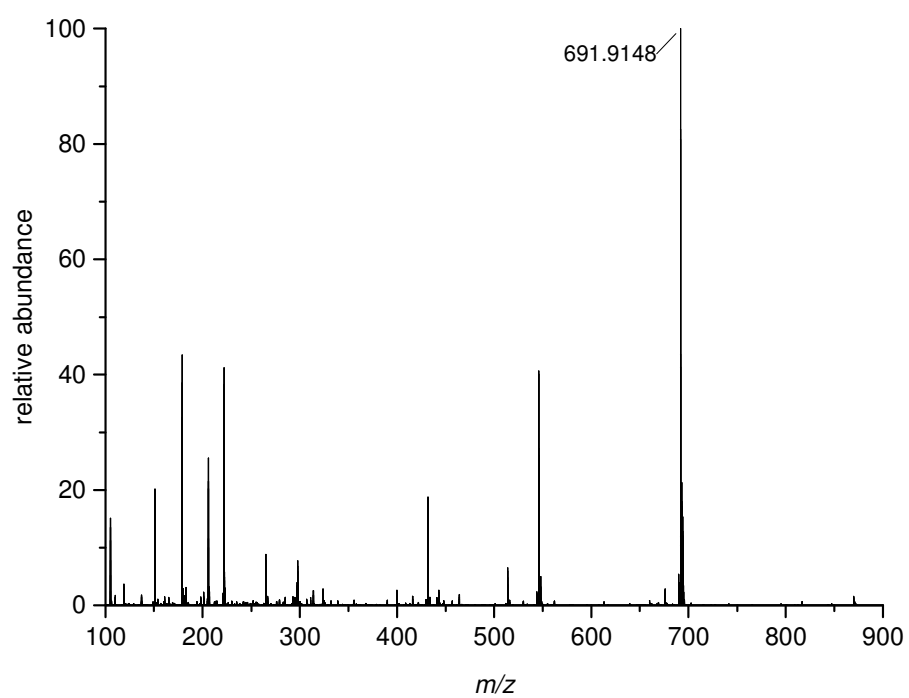


Figure 120: ESI-MS spectrum of $[\text{Fe}(\text{L}^{\text{td}})_3](\text{NTf}_2)_2 \cdot \text{H}_2\text{O}$ (**12**· H_2O).

5.3 Vibrational Spectra

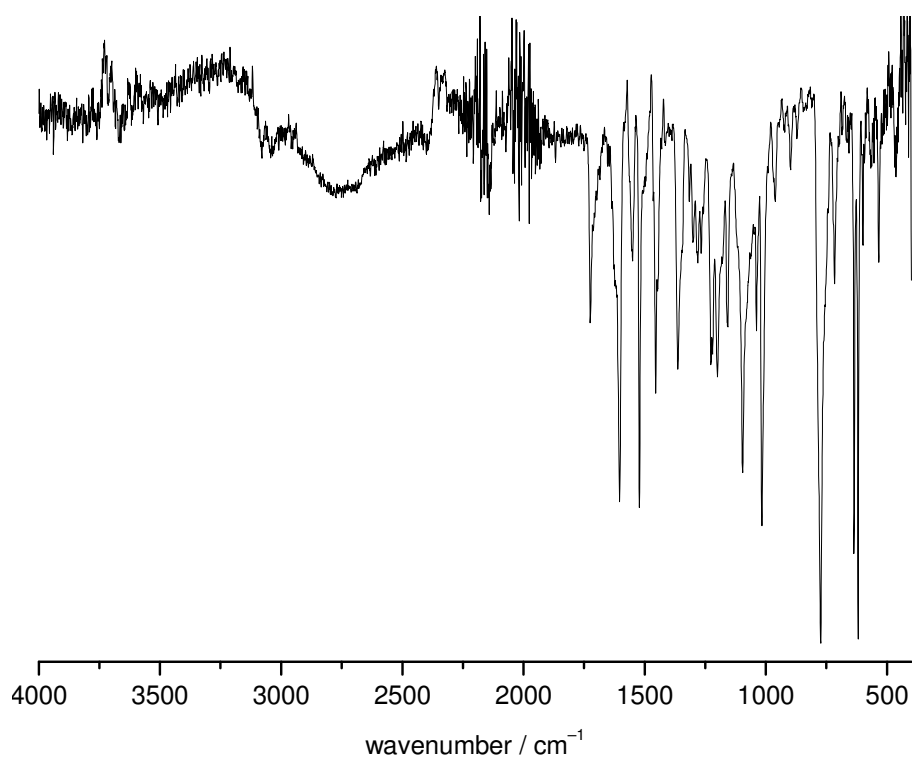


Figure 121: IR spectrum of 2-(bromoacetyl)-pyridine hydrobromide (**pyBr**).

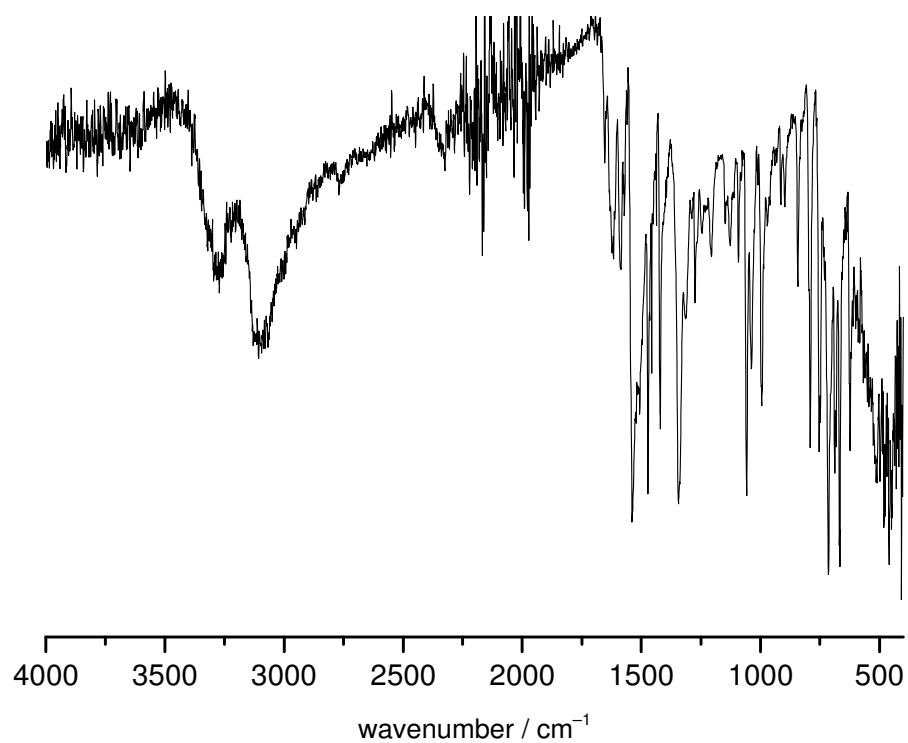


Figure 122: IR spectrum of the thiazole ligand L^{tz} .

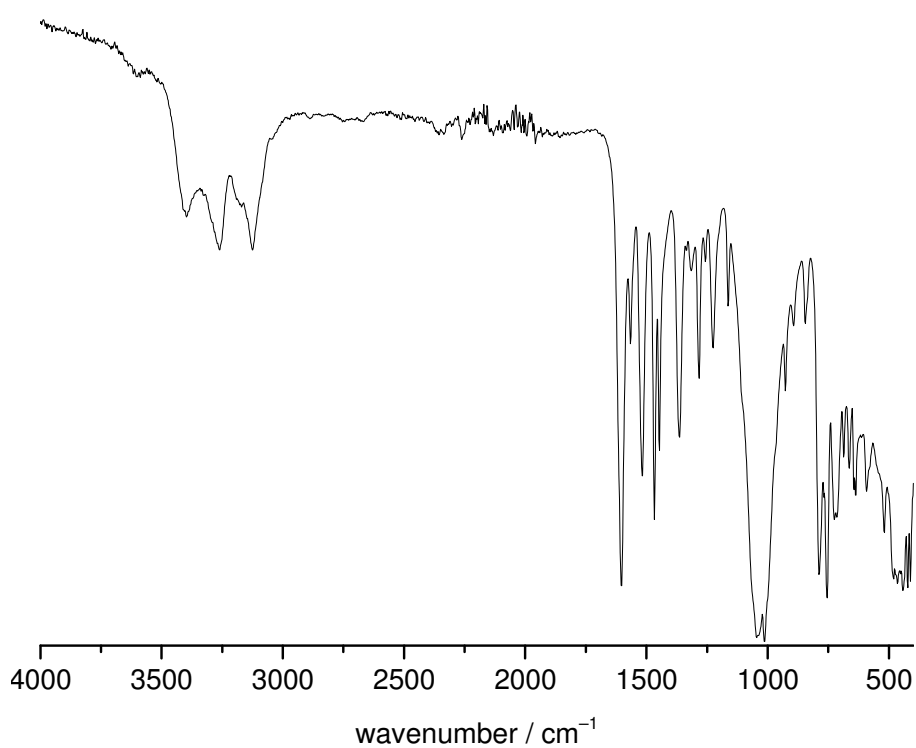


Figure 123: IR spectrum of $[\text{Fe}^{\text{III}}(L^{tz})_2(\text{F})_2](\text{BF}_4) \cdot 1.25\text{MeOH}$ ($2 \cdot 1.25\text{MeOH}$).

Vibrational Spectra

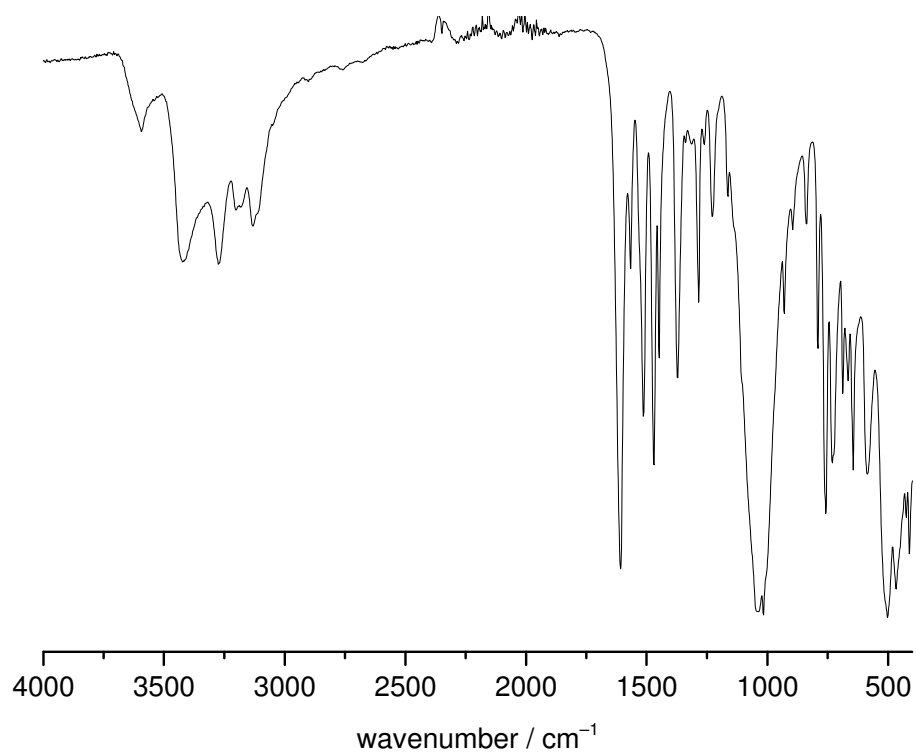


Figure 124: IR spectrum of $[\text{Fe}^{\text{III}}(\text{L}^{\text{tz}})_2(\text{F})_2](\text{BF}_4) \cdot 1.25\text{MeOH}$ ($2 \cdot 1.25\text{MeOH}$).

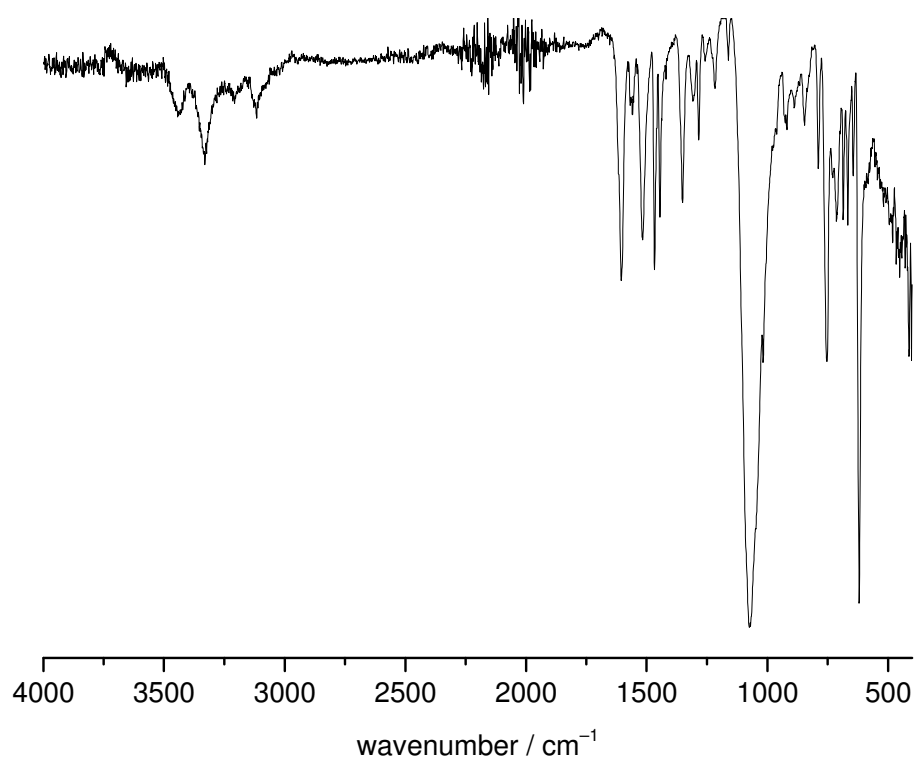


Figure 125: IR spectrum of $[\text{Co}^{\text{II}}(\text{L}^{\text{tz}})_3](\text{ClO}_4)_2 \cdot \text{H}_2\text{O}$ ($3 \cdot \text{H}_2\text{O}$).

Vibrational Spectra

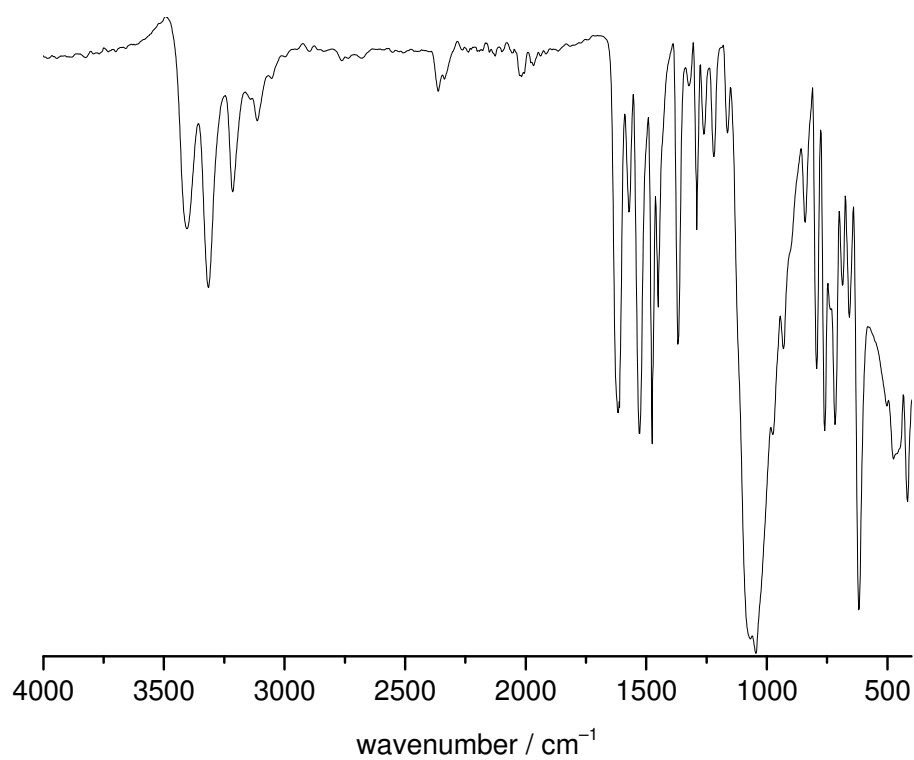


Figure 126: IR spectrum of $[\text{Cu}^{\text{II}}(\text{L}^{\text{tz}})_2](\text{ClO}_4)_2$ (**4**).

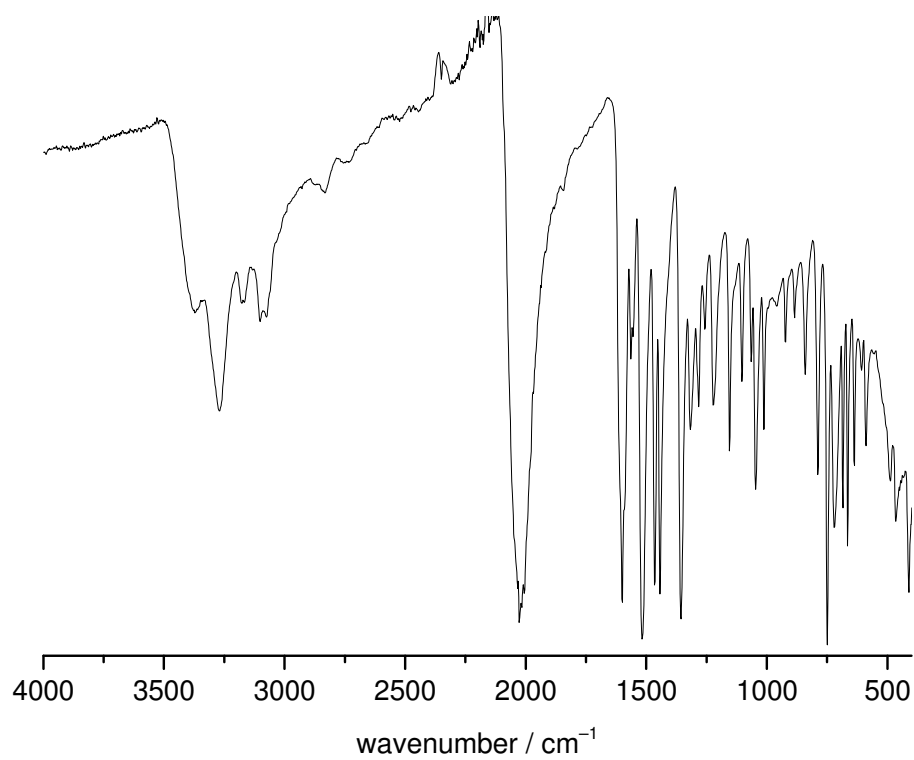


Figure 127: IR spectrum of $[\text{Fe}^{\text{II}}(\text{L}^{\text{tz}})_2(\text{NCS})_2]$ (**5**).

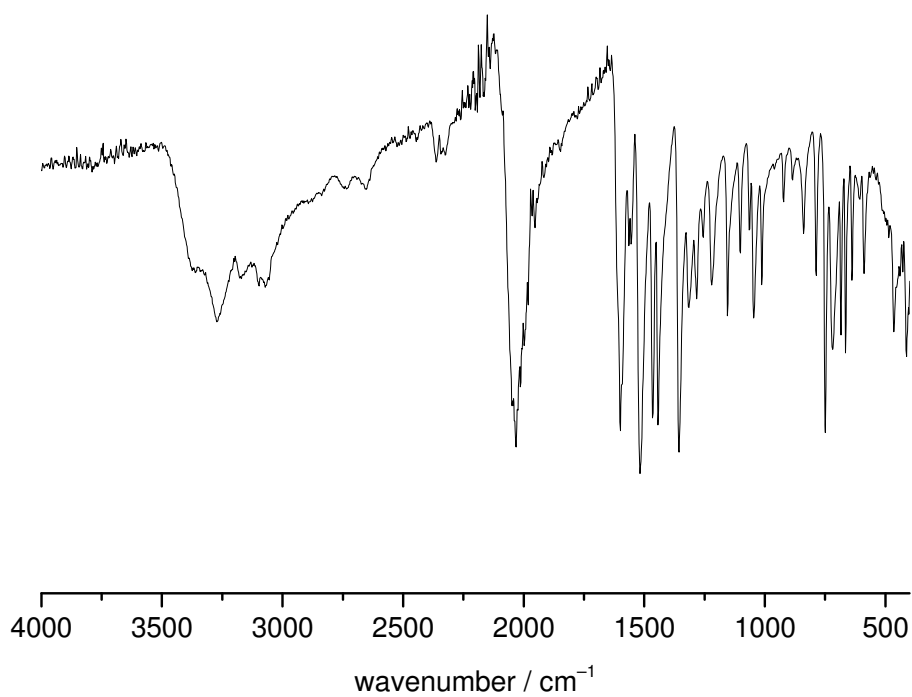


Figure 128: IR spectrum of $[\text{Fe}^{\text{II}}(\text{L}^{\text{tz}})_2(\text{NCSe})_2]$ (**6**).

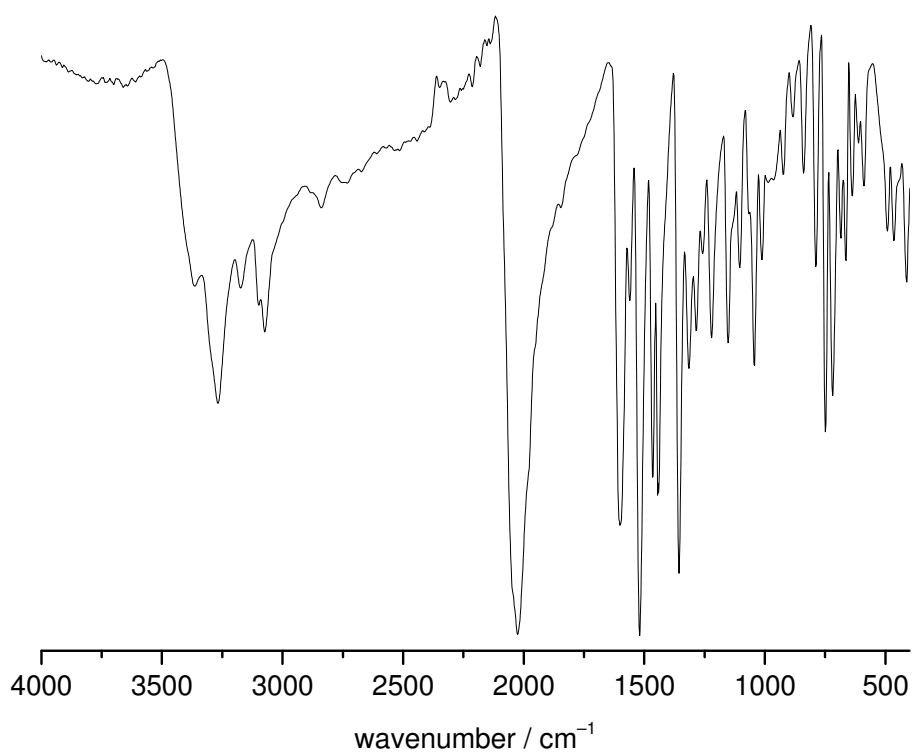


Figure 129: IR spectrum of $[\text{Co}^{\text{II}}(\text{L}^{\text{tz}})_2(\text{NCS})_2]$ (**7**).

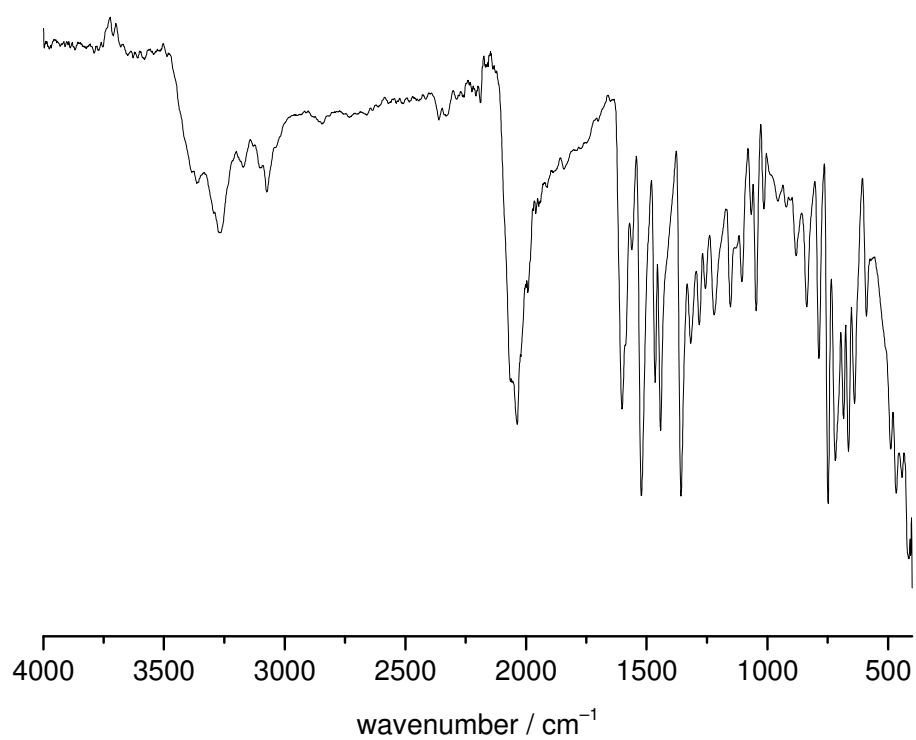


Figure 130: IR spectrum of $[\text{Ni}^{\text{II}}(\text{L}^{\text{tr}})_2(\text{NCS})_2]$ (**8**).

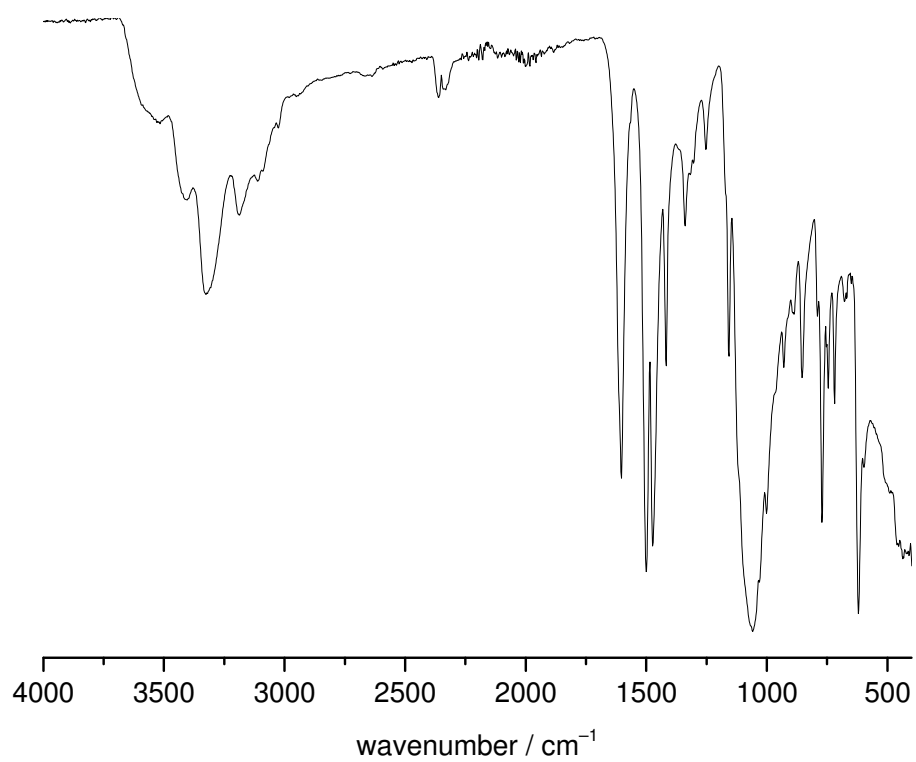


Figure 131: IR spectrum of $[\text{Fe}^{\text{II}}(\text{L}^{\text{td}})_3](\text{ClO}_4)_2 \cdot 2\text{H}_2\text{O}$ (**10**·2H₂O).

Vibrational Spectra

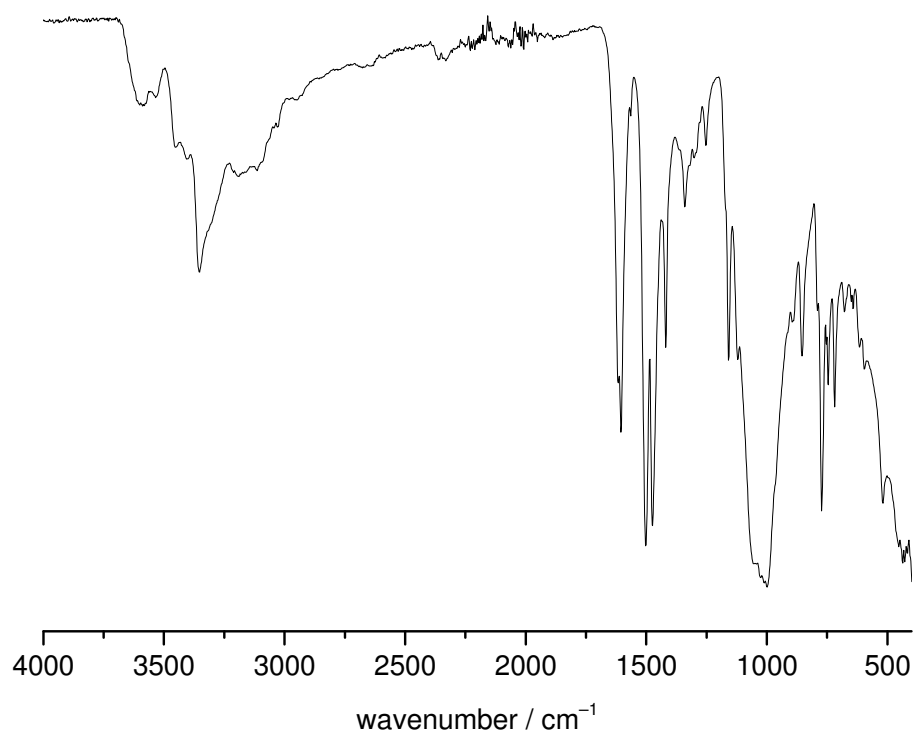


Figure 132: IR spectrum of $[\text{Fe}^{\text{II}}(\text{L}^{\text{td}})_3](\text{BF}_4)_2 \cdot 2\text{H}_2\text{O}$ (**11**·2H₂O).

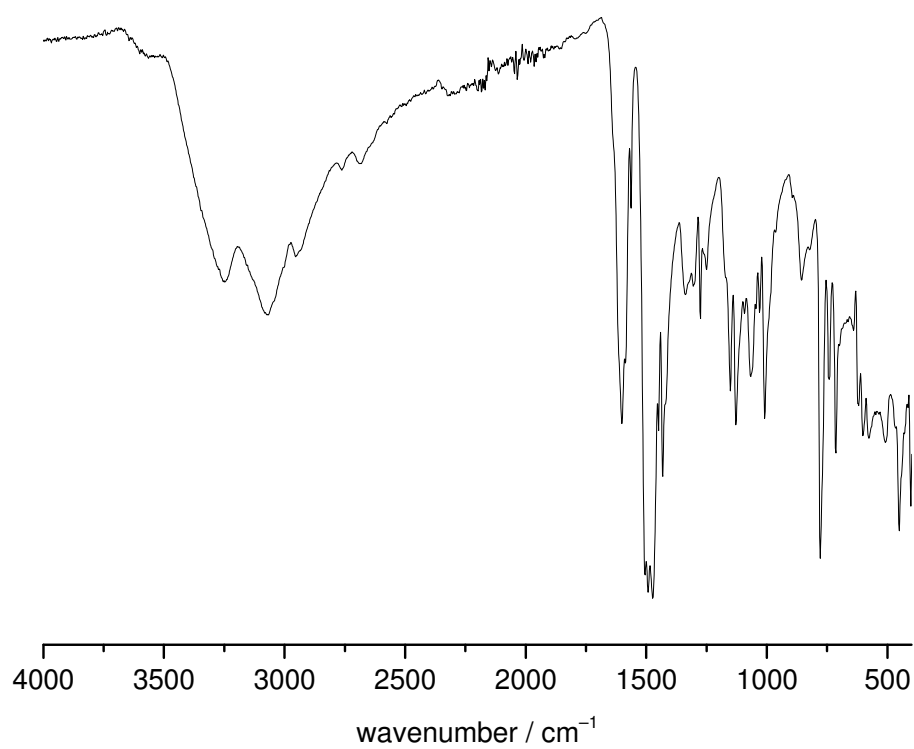


Figure 133: IR spectrum of $[\text{Fe}(\text{L}^{\text{td}})_3]\text{Cl}_2$ (**9**).

Vibrational Spectra

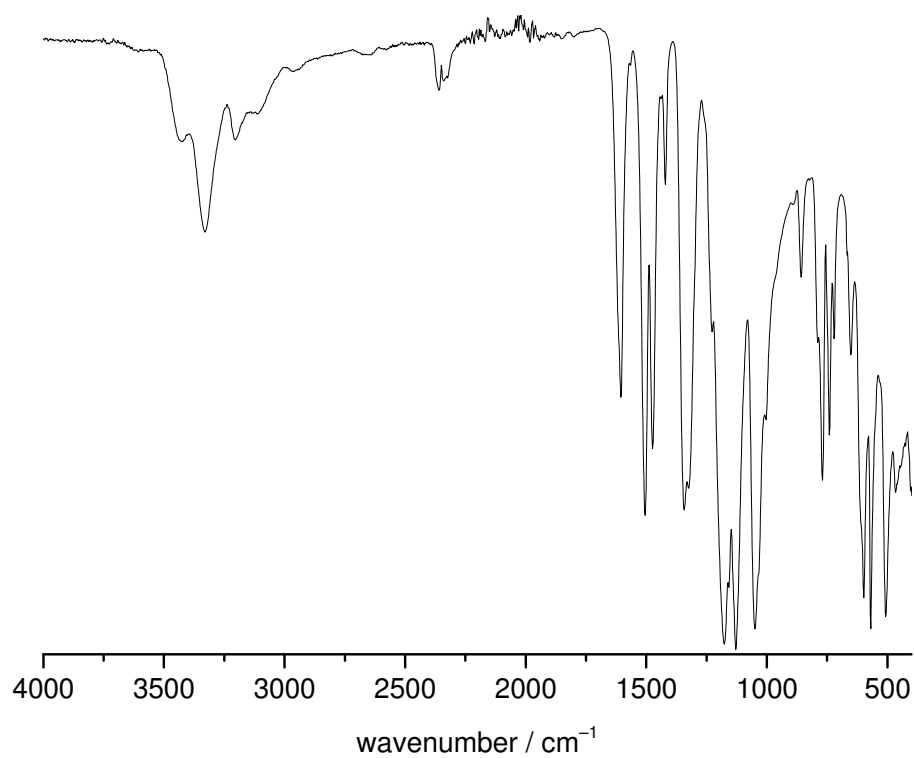


Figure 134: IR spectrum of $[\text{Fe}(\text{L}^{\text{td}})_3](\text{NTf}_2)_2 \cdot \text{H}_2\text{O}$ (**12**· H_2O).

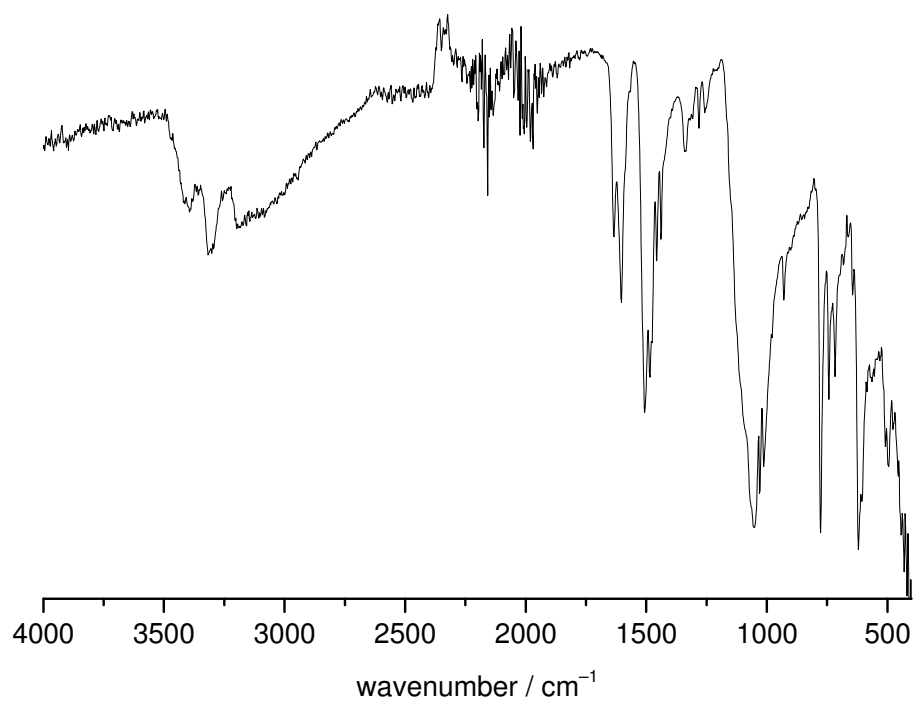


Figure 135: IR spectrum of $[\text{Co}^{\text{II}}(\text{L}^{\text{td}})_3](\text{ClO}_4)_2 \cdot 1.5\text{H}_2\text{O}$ (**13**· $1.5\text{H}_2\text{O}$).

Vibrational Spectra

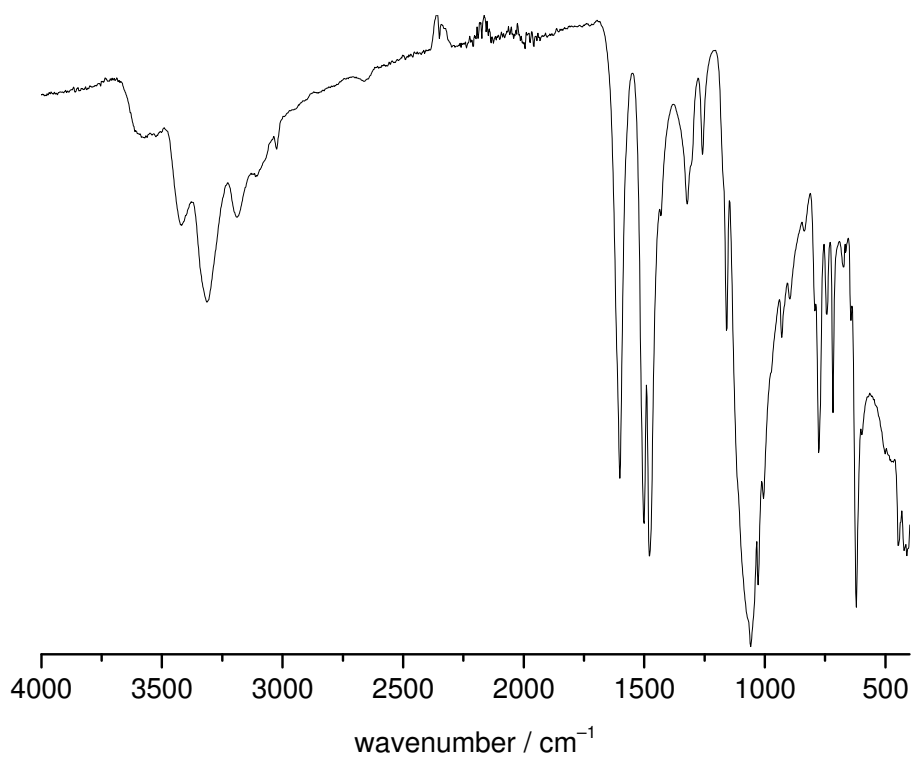


Figure 136: IR spectrum of $[\text{Ni}^{\text{II}}(\text{L}^{\text{td}})_3](\text{ClO}_4)_2 \cdot 2\text{H}_2\text{O}$ (**14**·2H₂O).

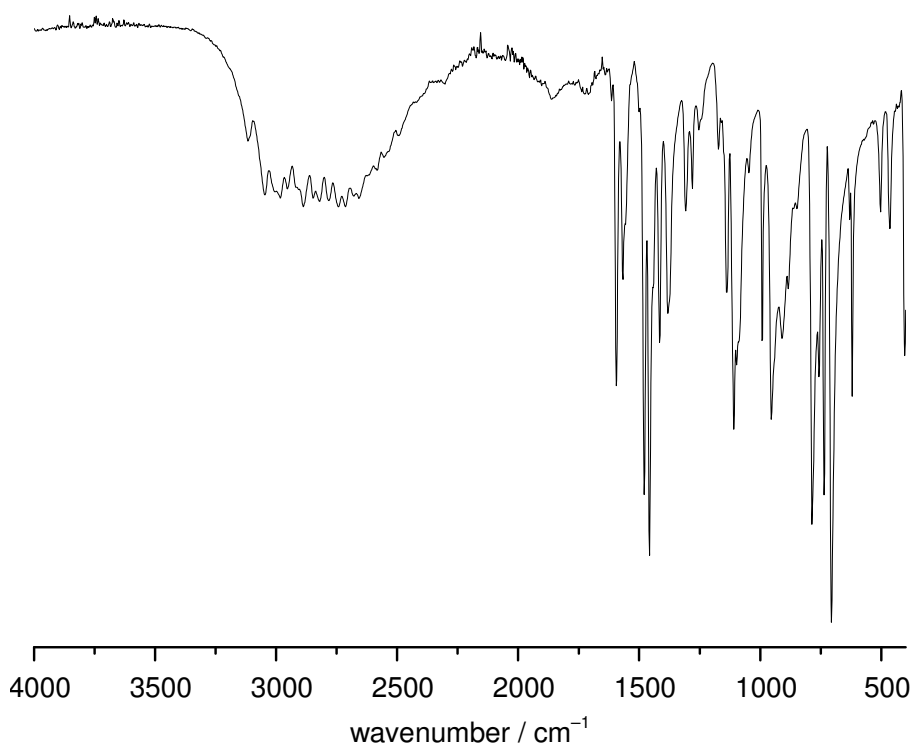


Figure 137: IR spectrum of 2-(2-pyridyl)-imidazole (**pi**).

Vibrational Spectra

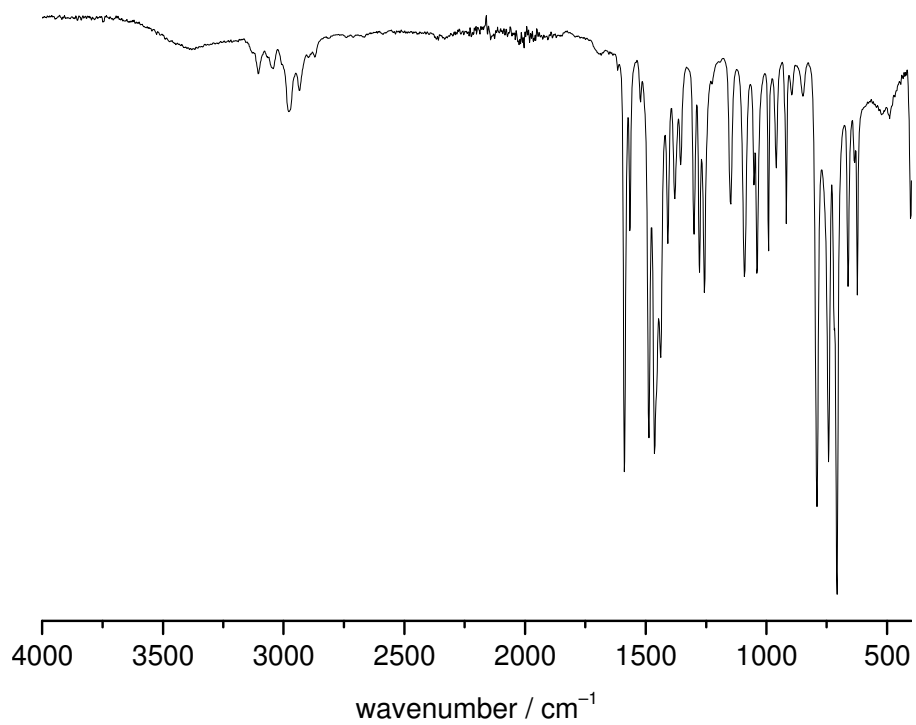


Figure 138: IR spectrum of the ethyl substituted ligand L^2 .

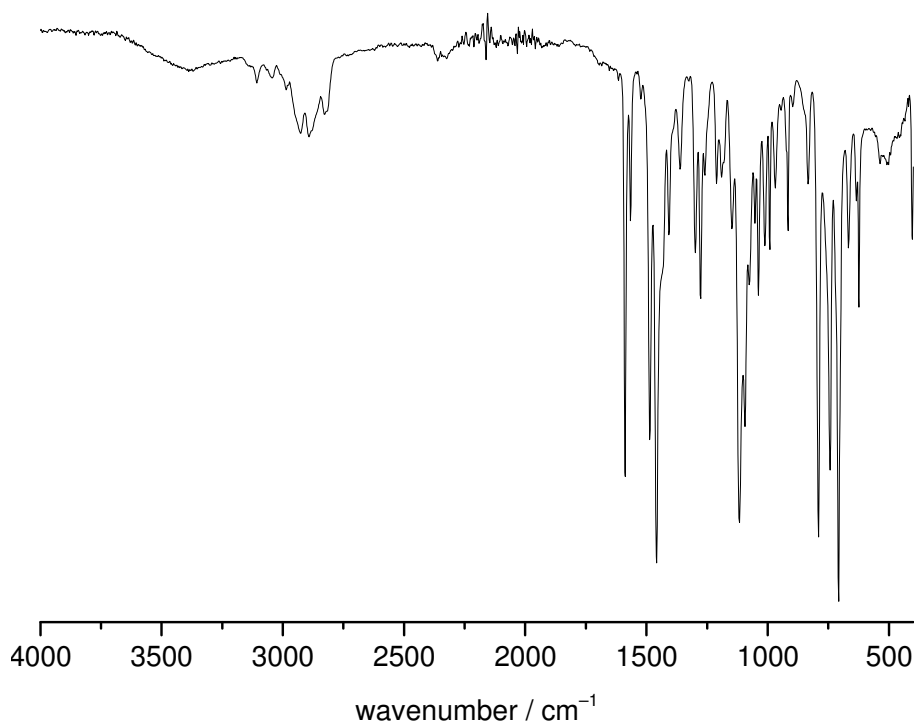


Figure 139: IR spectrum of the methoxy substituted ligand L^3 .

5.4 UV/Vis Spectra

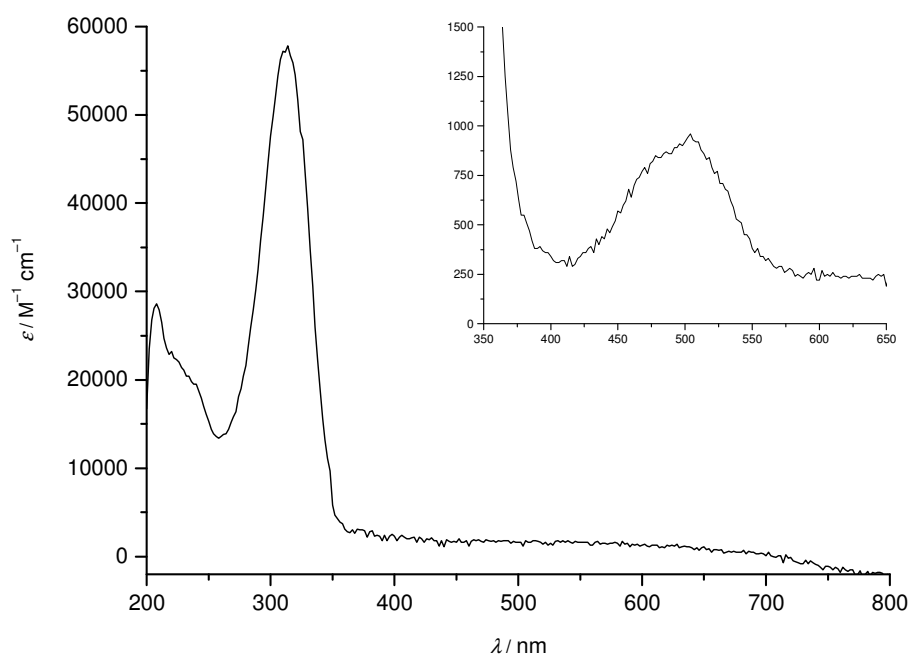


Figure 140: UV/Vis spectrum of $[\text{Fe}(\text{L}^{\text{td}})_3](\text{NTf}_2)_2 \cdot \text{H}_2\text{O}$ (**12**· H_2O) in 0.01 mM MeOH (inset: 0.1 mM).

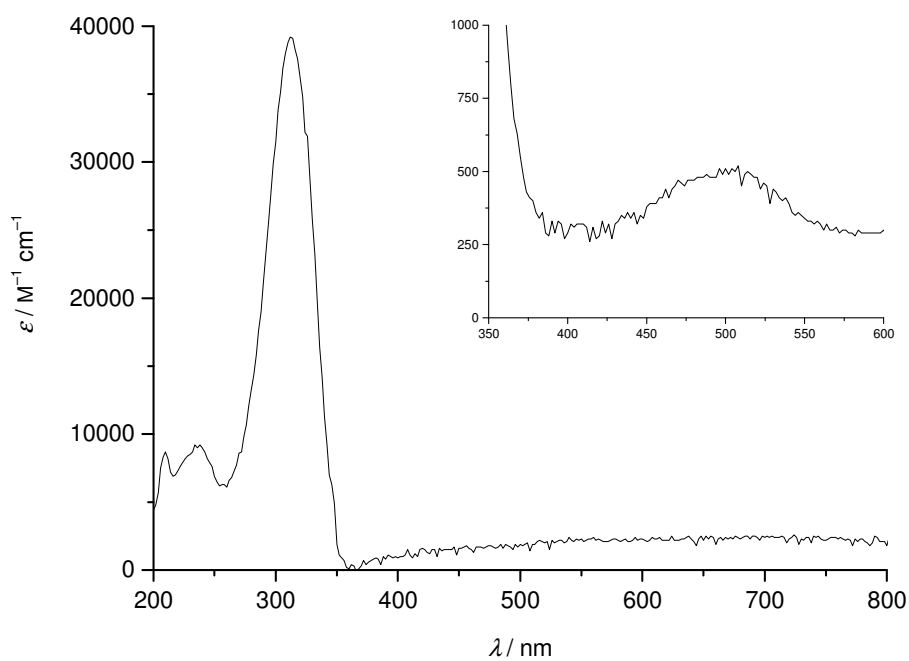


Figure 141: UV/Vis spectrum of $[\text{Fe}(\text{L}^{\text{td}})_3](\text{ClO}_4)_2 \cdot 2\text{H}_2\text{O}$ (**10**· $2\text{H}_2\text{O}$) in 0.01 mM MeOH (inset: 0.1 mM).

UV/Vis Spectra

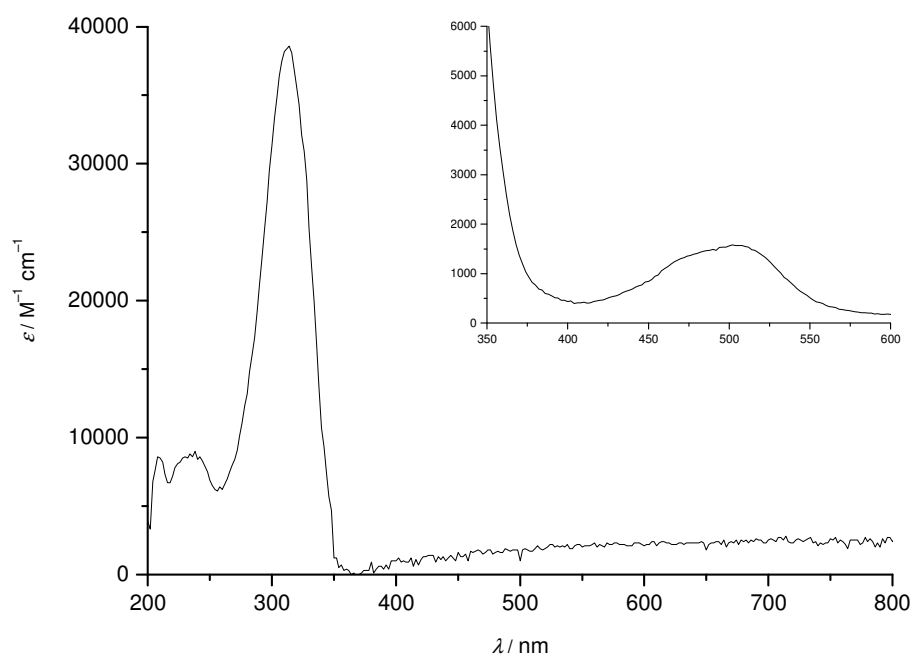


Figure 142: UV/Vis spectrum of $[\text{Fe}(\text{L}^{\text{td}})_3](\text{BF}_4)_2$ (**11**) in 0.01 mm MeOH (inset: 0.2 mm).

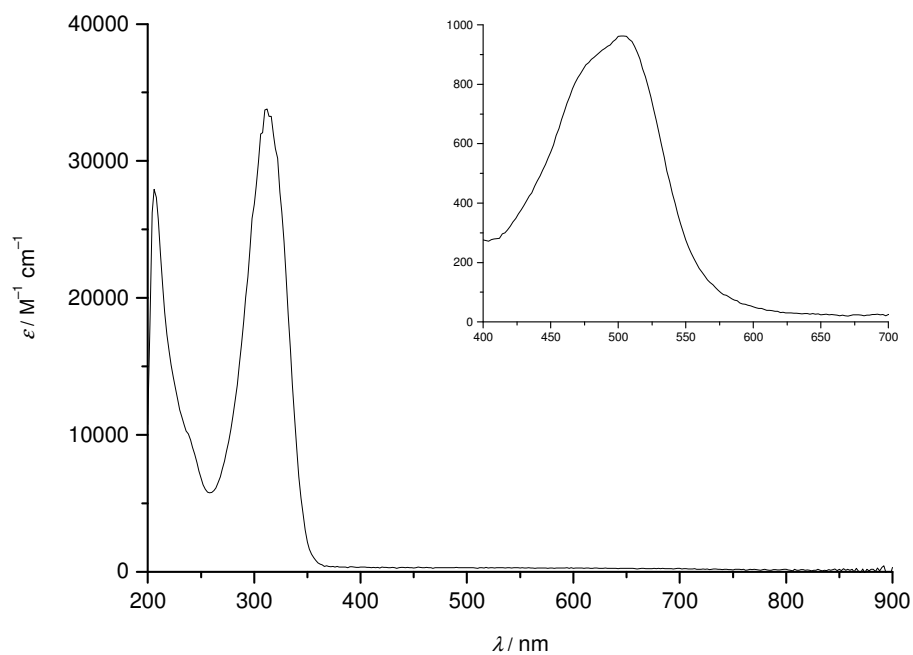


Figure 143: UV/Vis spectrum of $[\text{Fe}(\text{L}^{\text{td}})_2(\text{NCS})_2]$ (**15**) in 0.1 mm MeOH (inset: 1mm).

5.5 X-Ray Data

Table 15: Crystallographic data for L^{td} and $L^1 \cdot HCl \cdot H_2O$

	L^{td}	$L^1 \cdot HCl \cdot H_2O$
empirical formula	$C_7H_6N_4S$	$C_{12}H_{10}ClN_2O_3S$
formula weight / $g\ mol^{-1}$	178.22	297.73
crystal system	Orthorhombic	monoclinic
space group	$Pca2_1$	Pc
$a / \text{\AA}$	27.2816(18)	7.7170(9)
$b / \text{\AA}$	5.2973(4)	9.0506(11)
$c / \text{\AA}$	10.7706(8)	9.6881(11)
$\alpha / ^\circ$	90.00	90.00
$\beta / ^\circ$	90.00	102.663(6)
$\gamma / ^\circ$	90.00	90.00
$V / \text{\AA}^3$	1556.55(19)	660.19(13)
Z	8	1
$\rho_{\text{calcd.}} / g\ cm^{-3}$	1.521	0.749
μ / mm^{-1}	0.357	0.226
temperature / K	100(2)	100(2)
$F(000)$	736	153.00
crystal colour and shape	colourless needle	colourless plate
crystal size / mm^3	0.18 x 0.09 x 0.03	0.45 x 0.18 x 0.07
$\vartheta_{\text{min.}} / ^\circ; \vartheta_{\text{max.}} / ^\circ$	1.89; 27.84	4.50; 59.76
h	-33 \rightarrow 35	-10 \rightarrow 10
k	-6 \rightarrow 6	-11 \rightarrow 12
l	-11 \rightarrow 14	-13 \rightarrow 13
reflections collected	14040	5910
independent reflections	3218 [$R_{\text{int}} = 0.0435$]	3196 [$R_{\text{int}} = 0.0368$]
completeness to $\vartheta_{\text{max.}} / \%$	99.2	98.6
data; restraints; parameters	3218; 5; 229	3196; 2; 180
GOOF	1.021	1.073
$R1; wR2 [I > 2\sigma(I)]$	0.0366; 0.0783	0.0498; 0.1206
$R1; wR2$ (all data)	0.0466; 0.0830	0.0598; 0.1273
max. peak; hole / $e\ \text{\AA}^{-3}$	0.376; -0.341	0.71; -0.66

X-Ray Data

Table 16: Selected short contacts [Å] for [Fe^{III}(L^{tz})₂F₂](BF₄)·1.5H₂O (2·1.5H₂O).

	2·1.5H ₂ O		2·1.5H ₂ O
N3–H…F1	2.742	N33–H…F11E ^[a]	2.949
N3–H…F24A ^[a]	2.891	N33–H…F24D ^[a]	3.009
N3–H…F28A ^[a]	3.055	F13…H–O50	2.841
N13–H…F2	2.747	O50–H…O60	2.757
N13–H…F22B ^[a]	3.105	F14D…H–O60 ^[a]	2.889
N13–H…F25B ^[a]	3.051	N23F…H–O60 ^[a]	3.068
N13–H…O70B ^[a]	2.859	F27…H–O70 ^[a]	2.796
N23–H…F3	2.701	F21…H–O70 ^[a]	3.352
N23–H…F21C ^[a]	2.947	O70–H…O50G ^[a]	2.796
N23–H…F24A ^[a]	2.891	C _{tz1} …C _{py2A} ^[b]	3.582
N23–H…F27A ^[a]	2.836	C _{py1} …C _{tz2A} ^[b]	3.678
N33–H…F4	2.747	C _{py3} …C _{tz4B} ^[b]	3.675
N33–H…F23D ^[a]	3.267	C _{py4} …C _{tz3B}	3.695

^[a] Symmetry operations used to generate equivalent atom: A) $x - 0.5, 0.5 - y, z$; B) $1.5 - x, y - 0.5, 1 - z$; C) $1.5 - x, y + 0.5, 1 - z + 2$; D) $x - 0.5, 1.5 - y, z$; E) $1.5 - x, y + 0.5, 1 - z$; F) $x - 0.5, 1.5 - y, z - 1$; G) $1 - x, 1 - y, 1 - z$; F21–F24 belong to the major part of the disordered BF₄⁻ anion, F25–F28 to the corresponding minor part.

^[b] C_{py1}: centroid{C1/C2/C3/C4/C5/N1}; C_{py2}: centroid{C11/C12/C13/C14/C15/N11}; C_{py3}: centroid{C21/C22/C23/C24/C25/N21}; C_{py4}: centroid{C31/C32/C33/C34/C35/N31}; C_{tz1}: centroid{C6/C7/S1/C8/N2}; C_{tz2}: centroid{C16/C17/S11/C18/N12}; C_{tz3}: centroid{C26/C27/S21/C28/N22}; C_{tz4}: centroid{(36/C37/S31/C38/N31)}; Symmetry operations used to generate equivalent atoms: A) $x - 0.5, -y + 0.5, z$; B) $x - 0.5, 1.5 + y, z$.

Table 17: Selected short contacts [Å] for [Fe^{II}(L^{tz})₂(NCS)₂] (5), [Fe^{II}(L^{tz})₂(NCSe)₂] (6), [Co^{II}(L^{tz})₂(NCS)₂] (7) and [Ni^{II}(L^{tz})₂(NCS)₂] (8).

	5 ^[a]	6 ^[b]	7 ^[c]	8 ^[d]
S1…S1A	3.276(2)	3.310(3)	3.278(2)	3.258(1)
S20…S20A	3.445(7)	-/-	3.426(2)	3.418(1)
S25…S25A	3.31(3)	-/-	-/-	-/-
Se20…Se20A	-/-	3.413(1)	-/-	-/-

^[a] symmetry operations used to generate equivalent atoms: A) $-x, y, -z$; B) $1.5 - x, 0.5 - y, -z$; S(25) belongs to the minor part of the disordered NCS⁻ coligand (occupation 20 %).

^[b] symmetry operations used to generate equivalent atoms: A) $1 - x, 1 - y, 1 - z$; B) $0.5 - x, 0.5 - y, -z$.

^[c] symmetry operations used to generate equivalent atoms: A) $0.5 - x, 0.5 - y, 1 - z$; B) $2 - x, -y, 1 - z$.

^[d] symmetry operations used to generate equivalent atoms: A) $2 - x, 1 - y, 1 - z$; B) $1.5 - x, 0.5 - y, -z$.

X-Ray Data

Table 18: Crystallographic data for $[\text{Fe}^{\text{III}}_2(\text{L}^{\text{tz}})_4\text{F}_2(\mu\text{-O})](\text{BF}_4)_2 \cdot 1.25\text{MeOH}$ (**1**·1.25MeOH) and **1**·MeCN.

	1 ·1.25MeOH	1 ·MeCN
empirical formula	$\text{C}_{33.25}\text{H}_{33}\text{B}_2\text{F}_{10}\text{Fe}_2\text{N}_{12}\text{O}_{2.25}\text{S}_4$	$\text{C}_{34}\text{H}_{31}\text{B}_2\text{F}_{10}\text{Fe}_2\text{N}_{13}\text{O}\text{S}_4$
formula weight [g mol^{-1}]	1088.28	1089.28
crystal system	triclinic	triclinic
space group	$P\bar{1}$	$P\bar{1}$
a [Å]	12.4176(3)	12.5635(3)
b [Å]	12.9143(3)	12.8848(3)
c [Å]	14.4965(3)	14.7272(4)
α [°]	73.8052(10)	73.4374(16)
β [°]	77.1380(10)	75.5033(16)
γ [°]	75.8103(10)	74.3244(15)
V [Å ³]	2134.46(8)	2160.97(9)
Z	2	2
$\rho_{\text{calcd.}}$ [g cm^{-3}]	1.693	1.674
μ [mm^{-1}]	0.970	0.956
temperature [K]	100(2)	100(2)
$F(000)$	1101	1100
crystal colour and shape	red block	red block
crystal size [mm^3]	$0.10 \times 0.10 \times 0.02$	$0.10 \times 0.04 \times 0.01$
$\vartheta_{\text{min.}} / \vartheta_{\text{max.}}$ [°]	2.62 / 26.63	1.71 / 27.56
h	-15 → 15	-16 → 16
k	-16 → 16	-16 → 16
l	-18 → 18	-19 → 17
reflections collected	34350	35446
independent reflections	8943 [$R_{\text{int}} = 0.0401$]	9889 [$R_{\text{int}} = 0.0562$]
completeness to $\vartheta_{\text{max.}}$ [%]	99.4	99.1
data / restraints / parameters	8943 / 16 / 625	9889 / 27 / 584
GOOF	1.016	1.054
$R1 / wR2$ [$I > 2\sigma(I)$]	0.0441 / 0.1008	0.0889 / 0.2306
$R1 / wR2$ (all data)	0.0692 / 0.1132	0.1533 / 0.2732
max. peak / hole [$\text{e}\text{\AA}^{-3}$]	0.871 / -0.982	1.319 / -0.950

X-Ray Data

Table 19: Crystallographic data for [Fe^{III}(L^{tz})₂F₂](BF₄)·1.5H₂O (**2**·1.5H₂O) and [Co^{II}(L^{tz})₃](ClO₄)₂·1.5MeOH·0.25H₂O (**3**·1.5MeOH·0.25H₂O)

	2 ·1.5H ₂ O	3 ·1.5MeOH·0.25H ₂ O
empirical formula	C ₃₂ H ₃₄ B ₂ F ₁₂ Fe ₂ N ₁₂ O ₃ S ₄	C ₁₀₂ H ₁₁₀ Cl ₈ Co ₄ N ₃₆ O ₃₉ S ₁₂
formula weight [g mol ⁻¹]	1124.27	3368.30
crystal system	monoclinic	monoclinic
space group	<i>P</i> ₂ <i>1/a</i>	<i>P</i> ₂ <i>1/c</i>
<i>a</i> [Å]	14.3006(7)	13.2344(3)
<i>b</i> [Å]	15.3720(8)	13.5942(3)
<i>c</i> [Å]	20.3389(10)	21.6852(4)
α [°]	90	90
β [°]	91.8178(12)	120.0990(10)
γ [°]	90	90
<i>V</i> [Å ³]	4468.8(4)	3375.34(12)
<i>Z</i>	4	1
$\rho_{\text{calcd.}}$ [g cm ⁻³]	1.671	1.657
μ [mm ⁻¹]	0.936	0.920
temperature [K]	100(2)	100(2)
<i>F</i> (000)	2272	1722
crystal colour and shape	red block	orange block
crystal size [mm ³]	0.20 × 0.20 × 0.06	0.39 × 0.38 × 0.25
$\vartheta_{\text{min.}} / \vartheta_{\text{max.}}$ [°]	2.83 / 29.54	2.00 / 33.14
<i>h</i>	-19 → 19	-20 → 16
<i>k</i>	-21 → 21	-20 → 11
<i>l</i>	-28 → 28	-33 → 32
reflections collected	42957	52175
independent reflections	11822 [<i>R</i> _{int} = 0.0376]	12818 [<i>R</i> _{int} = 0.0309]
completeness to $\vartheta_{\text{max.}}$ [%]	94.8	99.7
data / restraints / parameters	11822 / 48 / 650	12818 / 56 / 643
GOOF	1.020	1.082
<i>R</i> 1 / <i>wR</i> 2 [<i>I</i> > 2 σ (<i>I</i>)]	0.0430 / 0.0967	0.0657 / 0.1809
<i>R</i> 1 / <i>wR</i> 2 (all data)	0.0756 / 0.1130	0.0844 / 0.1936
max. peak / hole [eÅ ⁻³]	0.777 / -0.447	1.100 / -0.991

X-Ray Data

Table 20: Crystallographic data for [Fe^{II}(L^{tz})₂(NCS)₂] (**5**) and [Fe^{II}(L^{tz})₂(NCSe)₂] (**6**).

	5	6
empirical formula	C ₁₈ H ₁₄ FeN ₈ S ₄	C ₁₈ H ₁₄ FeN ₈ S ₂ Se ₂
formula weight [g mol ⁻¹]	526.46	620.26
crystal system	monoclinic	monoclinic
space group	C2/c	C2/c
<i>a</i> [Å]	7.9878(6)	8.070(2)
<i>b</i> [Å]	13.4551(9)	13.616(5)
<i>c</i> [Å]	20.4399(4)	20.831(7)
α [°]	90	90
β [°]	96.453(4)	98.348(18)
γ [°]	90	90
<i>V</i> [Å ³]	2182.9(2)	2264.8(13)
<i>Z</i>	4	4
$\rho_{\text{calcd.}}$ [g cm ⁻³]	1.602	1.819
μ [mm ⁻¹]	1.098	4.088
temperature [K]	100(2)	100(2)
<i>F</i> (000)	1072	1216
crystal colour and shape	yellow block	yellow block
crystal size [mm ³]	0.20 × 0.18 × 0.04	0.06 × 0.05 × 0.03
$\vartheta_{\text{min.}} / \vartheta_{\text{max.}}$ [°]	2.01 / 27.80	1.98 / 27.53
<i>h</i>	-10 → 10	-10 → 10
<i>k</i>	-17 → 17	-13 → 16
<i>l</i>	-26 → 26	-27 → 23
reflections collected	18050	13823
independent reflections	2563 [<i>R</i> _{int} = 0.0382]	2498 [<i>R</i> _{int} = 0.1057]
completeness to $\vartheta_{\text{max.}}$ [%]	99.0	96.6
data / restraints / parameters	2563 / 0 / 151	2498 / 0 / 141
GOOF	1.029	1.017
<i>R</i> 1 / <i>wR</i> 2 [<i>I</i> > 2 σ (<i>I</i>)]	0.0456 / 0.1002	0.0445 / 0.0773
<i>R</i> 1 / <i>wR</i> 2 (all data)	0.0601 / 0.1089	0.1218 / 0.0952
max. peak / hole [eÅ ⁻³]	0.593 / -0.933	1.258 / -1.393

X-Ray Data

Table 21: Crystallographic data for [Co^{II}(L^{tz})₂(NCS)₂] (**7**) and [Ni^{II}(L^{tz})₂(NCS)₂] (**8**).

	7	8
empirical formula	C ₁₈ H ₁₄ CoN ₈ S ₄	C ₁₈ H ₁₄ NiN ₈ S ₄
formula weight [g mol ⁻¹]	529.54	529.32
crystal system	monoclinic	monoclinic
space group	<i>C2/c</i>	<i>C2/c</i>
<i>a</i> [Å]	7.9091(2)	7.9071(2)
<i>b</i> [Å]	13.5735(4)	13.6455(3)
<i>c</i> [Å]	20.9755(5)	20.1318(4)
α [°]	90	90
β [°]	105.6744(14)	96.6467(12)
γ [°]	90	90
<i>V</i> [Å ³]	2168.07(10)	2157.55(8)
<i>Z</i>	4	4
$\rho_{\text{calcd.}}$ [g cm ⁻³]	1.622	1.630
μ [mm ⁻¹]	1.201	1.311
temperature [K]	100(2)	100(2)
<i>F</i> (000)	1076	1080
crystal colour and shape	yellow plate	blue block
crystal size [mm ³]	0.11 × 0.10 × 0.03	0.09 × 0.08 × 0.03
$\vartheta_{\text{min.}} / \vartheta_{\text{max.}}$ [°]	2.99 / 24.58	2.99 / 27.49
<i>h</i>	-9 → 9	-10 → 10
<i>k</i>	-15 → 15	-17 → 17
<i>l</i>	-24 → 24	-26 → 26
reflections collected	12769	18722
independent reflections	1822 [<i>R</i> _{int} = 0.0319]	2472 [<i>R</i> _{int} = 0.0306]
completeness to $\vartheta_{\text{max.}}$ [%]	99.9	99.7
data / restraints / parameters	1822 / 0 / 141	2472 / 0 / 141
GOOF	1.069	1.038
<i>R</i> 1 / <i>wR</i> 2 [<i>I</i> > 2 σ (<i>I</i>)]	0.0407 / 0.0923	0.0356 / 0.0829
<i>R</i> 1 / <i>wR</i> 2 (all data)	0.0538 / 0.0995	0.0451 / 0.0880
max. peak / hole [eÅ ⁻³]	0.875 / -0.618	0.888 / -0.562

X-Ray Data

Table 22: Crystallographic data for $[\text{Fe}(\text{H}_2\text{O})_6](\text{NTf}_2)_2 \cdot 2\text{H}_2\text{O}$, $[\text{Fe}^{\text{II}}(\text{L}^{\text{td}})_3](\text{ClO}_4)_2 \cdot 0.625\text{MeOH} \cdot 0.875\text{H}_2\text{O}$ (**10**·0.625MeOH·0.875H₂O) and $[\text{Fe}^{\text{II}}(\text{L}^{\text{td}})_3](\text{BF}_4)_2 \cdot \text{MeOH} \cdot \text{H}_2\text{O}$ (**11**·MeOH·H₂O).

	$[\text{Fe}(\text{H}_2\text{O})_6](\text{NTf}_2)_2 \cdot 2\text{H}_2\text{O}$	10 ·0.625MeOH·0.875H ₂ O	11 ·MeOH·H ₂ O
empirical formula	$\text{C}_4\text{H}_{16}\text{F}_{12}\text{FeN}_2\text{O}_{16}\text{S}_4$	$\text{C}_{86.5}\text{H}_{89}\text{Cl}_8\text{Fe}_4\text{N}_{48}\text{O}_{38}\text{S}_{12}$	$\text{C}_{22}\text{H}_{24}\text{B}_2\text{F}_8\text{FeN}_{12}\text{O}_2\text{S}_3$
formula weight [g mol^{-1}]	760.28	3300.78	814.18
crystal system	tetragonal	triclinic	triclinic
space group	$P4_2/n$	$P-1$	$P-1$
a [Å]	20.079(8)	12.7321(3)	10.2651(2)
b [Å]	20.079(8)	13.1146(3)	12.6910(2)
c [Å]	6.313(3)	23.7264(6)	13.1681(2)
α [°]	90	99.3930(10)	97.9275(8)
β [°]	90	98.7940(10)	94.5975(9)
γ [°]	90	100.8100(10)	112.0130(8)
V [Å ³]	2545.2(19)	3769.82(16)	1558.88(5)
Z	4	1	2
$\rho_{\text{calcd.}}$ [g cm^{-3}]	1.984	1.454	1.735
μ [mm^{-1}]	1.077	0.769	0.780
temperature [K]	100(2)	123(2)	100(2)
$F(000)$	1520	1680	824
crystal colour and shape	colourless plate	red block	red block
crystal size [mm^3]	$0.66 \times 0.18 \times 0.05$	$0.22 \times 0.11 \times 0.05$	$0.34 \times 0.19 \times 0.11$
$\vartheta_{\text{min.}} / \vartheta_{\text{max.}}$ [°]	1.43 / 29.57	1.66 / 24.71	2.14 / 39.13
h	-25 → 25	-14 → 14	-17 → 18
k	-27 → 26	-15 → 15	-22 → 18
l	-5 → 8	-27 → 27	-21 → 21
reflections collected	13107	46110	52085
independent reflections	3518 [$R_{\text{int}} = 0.0316$]	12825 [$R_{\text{int}} = 0.0417$]	15728 [$R_{\text{int}} = 0.0294$]
completeness to $\vartheta_{\text{max.}}$ [%]	98.4	99.8	99.4
data / restraints / parameters	3518 / 34 / 203	12825 / 94 / 952	15728 / 34 / 513
GOOF	1.074	1.040	1.038
$R1 / wR2$ [$I > 2\sigma(I)$]	0.0313 / 0.0885	0.0850 / 0.2363	0.0478 / 0.1277
$R1 / wR2$ (all data)	0.0332 / 0.0899	0.1189 / 0.2640	0.0611 / 0.1350
max. peak / hole [e Å^{-3}]	0.513 / -0.436	2.022 / -1.086	1.236 / -1.102

X-Ray Data

Table 23: [Co^{II}(L^{td})₃](ClO₄)₂·2H₂O (**13**·2H₂O) and [Ni^{II}(L^{td})₃](ClO₄)₂·MeOH·H₂O (**14**·MeOH·H₂O).

	13 ·2H ₂ O	14 ·MeOH·H ₂ O
empirical formula	C ₂₁ H ₂₂ Cl ₂ CoN ₁₂ O ₁₀ S ₃	C ₂₂ H ₂₄ Cl ₂ N ₁₂ NiO ₁₀ S ₃
formula weight [g mol ⁻¹]	828.52	842.32
crystal system	triclinic	triclinic
space group	<i>P</i> -1	<i>P</i> -1
<i>a</i> [Å]	10.4856(2)	10.5904(2)
<i>b</i> [Å]	12.9656(3)	12.9279(3)
<i>c</i> [Å]	13.2252(3)	13.2859(3)
α [°]	100.4674(13)	101.3009(10)
β [°]	92.1018(12)	92.3890(9)
γ [°]	112.6290(12)	113.9924(8)
<i>V</i> [Å ³]	1620.67(6)	1614.59(6)
<i>Z</i>	2	2
$\rho_{\text{calcd.}}$ [g cm ⁻³]	1.698	1.733
μ [mm ⁻¹]	0.960	1.034
temperature [K]	100(2)	100(2)
<i>F</i> (000)	842	860
crystal colour and shape	yellow block	pink block
crystal size [mm ³]	0.07 × 0.05 × 0.03	0.58 × 0.33 × 0.15
$\vartheta_{\text{min.}} / \vartheta_{\text{max.}}$ [°]	1.58 to 23.84	1.77 / 36.21
<i>h</i>	-11 → 11	-15 → 17
<i>k</i>	-14 → 14	-21 → 19
<i>l</i>	-15 → 15	-20 → 20
reflections collected	22343	39778
independent reflections	4965 [<i>R</i> _{int} = 0.0610]	13211 [<i>R</i> _{int} = 0.0185]
completeness to $\vartheta_{\text{max.}}$ [%]	99.7	99.2
data / restraints / parameters	4965 / 27 / 468	13211 / 0 / 456
GOOF	1.027	1.034
<i>R</i> 1 / <i>wR</i> 2 [<i>I</i> > 2 σ (<i>I</i>)]	0.0722 / 0.1860	0.0298 / 0.0784
<i>R</i> 1 / <i>wR</i> 2 (all data)	0.1109 / 0.2109	0.0356 / 0.0816
max. peak / hole [e Å ⁻³]	1.270 / -0.740	1.289 / -0.670

X-Ray Data

Table 24: Crystallographic data for $[\text{Co}(\text{L}^2)_3](\text{ClO}_4)_2 \cdot 1.5\text{H}_2\text{O}$ (**25**·1.5H₂O) and $[\text{Co}(\text{L}^3)_3](\text{ClO}_4)_2$ (**29**).

	25 ·1.5H ₂ O	29
empirical formula	C ₃₂ H ₄₁ Cl ₂ CoN ₉ O ₁₀	C ₃₃ H ₃₉ Cl ₂ CoN ₉ O ₁₁
formula weight / g mol ⁻¹	841.57	867.56
crystal system	monoclinic	triclinic
space group	<i>P</i> 2 ₁ / <i>n</i>	<i>P</i> -1
<i>a</i> / Å	8.5392(2)	8.9130(2)
<i>b</i> / Å	28.2904(6)	12.8828(3)
<i>c</i> / Å	15.8193(4)	17.9445(5)
α / °	90	71.1580(10)
β / °	95.9320(11)	89.3090(10)
γ / °	90	72.0760(10)
<i>V</i> / Å ³	3801.12(15)	1846.66(8)
<i>Z</i>	4	2
$\rho_{\text{calcd.}}$ / g cm ⁻³	1.471	1.560
μ / mm ⁻¹	0.659	0.683
temperature / K	100(2)	100(2)
<i>F</i> (000)	1748	898
crystal colour and shape	orange block	orange block
crystal size / mm ³	0.22 x 0.05 x 0.02	0.08 x 0.05 x 0.05
$\vartheta_{\text{min.}}$ / °; $\vartheta_{\text{max.}}$ / °	1.48; 26.37	1.20; 29.58
<i>h</i>	-10 → 10	-12 → 12
<i>k</i>	-35 → 35	-17 → 17
<i>l</i>	-19 → 16	-24 → 24
reflections collected	49914	46099
independent reflections	7764 [<i>R</i> _{int} = 0.0417]	10248 [<i>R</i> _{int} = 0.0190]
completeness to $\vartheta_{\text{max.}}$ / %	99.7	99.0
data; restraints; parameters	7764; 0; 491	10248; 0; 505
GOOF	1.072	1.026
<i>R</i> 1; <i>wR</i> 2 [<i>I</i> > 2 σ (<i>I</i>)]	0.0436; 0.0927	0.0495; 0.1292
<i>R</i> 1; <i>wR</i> 2 (all data)	0.0605; 0.0990	0.0556; 0.1337
max. peak; hole / e Å ⁻³	0.483; -0.542	1.305; -0.934

X-Ray Data

Table 25: Crystallographic data for $[\text{Co}^{\text{II}}(\text{L}^4)(\text{NCS})_2][\text{Co}(\text{NCS})_4]$ (**31**) and $[\text{Co}^{\text{II}}(\text{L}^4)(\text{NCS})_2](\text{NTf}_2)_2$ (**32**).

	31	32
empirical formula	$\text{C}_{40}\text{H}_{42}\text{Co}_2\text{N}_{18}\text{O}_2\text{S}_8$	$\text{C}_{40}\text{H}_{42}\text{CoF}_{12}\text{N}_{16}\text{O}_{10}\text{S}_8$
formula weight / g mol^{-1}	1181.26	1450.31
crystal system	monoclinic	triclinic
space group	$P2_1/n$	$P-1$
$a / \text{\AA}$	9.3730(7)	10.6565(3)
$b / \text{\AA}$	39.204(3)	17.1343(5)
$c / \text{\AA}$	14.1288(11)	17.7652(5)
$\alpha / ^\circ$	90	118.1340(11)
$\beta / ^\circ$	96.292(2)	91.6530(13)
$\gamma / ^\circ$	90	97.9010(14)
$V / \text{\AA}^3$	5160.5(7)	2817.02(14)
Z	4	2
$\rho_{\text{calcd.}} / \text{g cm}^{-3}$	1.520	1.710
μ / mm^{-1}	1.022	0.711
temperature / K	100(2)	100(2)
$F(000)$	2424	1474
crystal colour and shape	blue block	brown block
crystal size / mm^3	$0.10 \times 0.08 \times 0.05$	$0.14 \times 0.12 \times 0.10$
$\vartheta_{\text{min.}} / ^\circ; \vartheta_{\text{max.}} / ^\circ$	1.54; 24.71	1.31; 30.60
h	-11 \rightarrow 11	-15 \rightarrow 15
k	-45 \rightarrow 45	-24 \rightarrow 24
l	-16 \rightarrow 16	-25 \rightarrow 25
reflections collected	79000	75970
independent reflections	8750 [$R_{\text{int}} = 0.0595$]	17243 [$R_{\text{int}} = 0.0191$]
completeness to $\vartheta_{\text{max.}} / \%$	99.7	99.2
data; restraints; parameters	8750; 64; 619	17243; 0; 784
GOOF	1.090	1.030
$R1; wR2 [I > 2\sigma(I)]$	0.0578; 0.1125	0.0340; 0.0916
$R1; wR2$ (all data)	0.0828; 0.1221	0.0421; 0.0979
max. peak; hole / e \AA^{-3}	0.932; -1.138	1.048; -0.464